THE UNIVERSITY OF HULL

Radio frequency excited carbon dioxide laser processing of carbon fibre reinforced composites: experimental and theoretical analyses of the fume content and expansion dynamics

being a Thesis submitted for the
degree of Doctor of Philosophy

in the Faculty of Science & Engineering
Department of Physics & Mathematics

by

Matthew B. Leach, BSc.

July 2014

Abstract

In this thesis a detailed analysis of long pulse CO_2 laser interactions with carbon fibre reinforced polymer composites (CFRPs) is presented. In particular, the fume dynamics and the fume contents are determined. Knowledge of both of these aspects of laser processing of CFRPs is important for the development of specialist fume extraction and treatment systems. The study has been conducted in a progressive manner; firstly the individual components of the composite have been characterised in respect of their thermal and optical properties, then their individual interaction with laser light quantified, and finally the whole composite has been subject to the same laser processing tests. The materials are PAN-based carbon fibres (T300, Toray Carbon Fibers America Inc.), an epoxy resin (RS-M135, PRF Composite Materials) and a $50:50$ combination by volume as a complete CFRP from Goodfellow Cambridge Ltd.

The laser processing of CFRP is known to be a challenge due to the vastly differing thermal and optical properties between the components of the composite. Despite this, it has been studied widely due to its highly desirable properties in high-technology industries and drilling with an assortment of laser sources has proved it to be a viable option. The contribution of this work is to put aspects of the laser interaction on a firmer experimental and theoretical basis in the medium irradiance regime. In particular, there is little published work on the origin and composition of fume from laser processed CFRPs and this thesis documents studies that address this knowledge gap.

The fume from the carbon dioxide laser ablation of CFRPs has been found to be primarily phenol, CO_2, CO, water, methane and an aldehyde which is most likely formaldehyde. Specific regimes under which carbon fibres can be released from the surface of both the bare carbon fibre weave and the CFRP have been identified. Predominantly, this is when the fibre is cut in two places using the laser beam in a scanning mode of operation as would be used for trepanning holes, for example. A method of tracking the motion of the ejected fibres in a time resolved way using fast imaging has been shown, but also in a non-time resolved fashion by observing the incandescent streaks from them. The evidence suggests that fibres cannot be released from a single ablation site unless they are near the edge of the material, and also that any fibres released when using PAN fibres and a Gaussian beam are unlikely be thinned to the point where they are hazardous to human health. This is due to a concomitant swelling of the fibre at moderate fluences which increases its size significantly. They could however be a source of debris on the surface of the sample.

By using time-resolved interferometry, the sensitivity of the plume image capture system was improved over the typical shadowgraphic method to the point that gas phase decomposition can be observed very early on in the laser interaction. This technique can be applied to finding the moment during the laser interaction at which carbon fibre or epoxy resin starts to decompose. The two materials produce very different fume compositions and the results vary significantly over a piece of CFRP as the thickness of the epoxy over-layer changes due to the woven carbon fibre structure beneath. A theoretical model has been used to analyse the data and is shown to give good agreement with the time-to-onset of thermal decomposition as a function of laser irradiance as well as closely predicting the threshold laser fluence. The time-resolved images of the plume have also been used to plot the progression of the ejecta with time so that their velocity can be measured thus informing the conditions required for efficient extraction.

The fluence threshold for laser-induced damage to carbon fibre weave was measured and was found to have a threshold $1.5\times$ higher when the fibre orientation was perpen-

dicular to the polarization of the laser as opposed to parallel. This result was supported by calculations of the reflectivity of the fibre at the laser wavelength, which found that $1.6\times$ more energy was absorbed by fibres that are perpendicular to the polarization of the laser. As there is a large array of fibre types, matrix compositions and laser sources, the work presented here is detailed in such a way as to allow these techniques to be applied to other systems in the future.

Acknowledgements

I would first like to thank my supervisor, Howard Snelling for never being too busy (despite having too much to do) to answer questions, provide support and take the time to explain, demonstrate and assist - and never losing patience!

I would next like to thank the technical support within the department: Rob Farley, Graham Randerson, Gordon Sowersby and Dave Stavenau for their input in my getting my experiments running. I will also thank the other members of the department for their willingness to share equipment, knowledge and ideas throughout the laboratory and tea room. I am also indebted to technical and academic staff members from other departments for their generosity in offering me their time to further my work, particularly Mark Anderson, Ian Dobson, Julia Malle, Nigel Parkin, Garry Robinson, Tony Sinclair and Kevin Welham.

I'd like to thank my family, partner and close friends for their help and support outside of the laboratory.

Finally I would like to thank both Andy Easey and Purex International Ltd. for sponsoring the project, and PRF Composite Materials for generously providing me with samples.

Contents

Abstract **ii**

Acknowledgments **v**

Table of Contents **viii**

1 Introduction **1**

2 Literature Review **5**

2.1 Introduction 5

2.2 Laser processing of polymers 8

2.3 Laser processing of carbon fibre composites 12

2.4 Fume analysis of carbon fibre composites 16

2.5 High magnification ultra-fast time resolved imaging 17

2.6 Michelson interferometry 18

2.7 Arrhenius equation 22

3 Laser Systems **24**

3.1 Introduction 24

3.2 RF CO_2 laser 25

3.3 Dye laser system 31

3.4 Conclusions 37

4 Material Characterisation **39**

4.1 Introduction 39

4.2 Sample preparation and analysis 41

4.3 Thermo-gravimetric analysis to determine the decomposition characteristics of CFRP 45

4.4 Thermo-gravimetric analysis to determine the activation energy of RS-M135 epoxy resin 48

4.5 Differential scanning calorimetry to determine the specific heat capacity of the materials 52

4.6 Lees' disc method to determine the thermal conductivity of the samples 55

4.7 Determination of the reflectance of CFRP and its constituents 57

4.8 FT-IR spectroscopy to measure the optical absorption coefficient of RS-M135 epoxy resin 67

4.9 Summary 69

4.10 Conclusions 73

5 Laser Processing of CFRPs Part I: Thresholds and Ablation Products **75**

5.1 Introduction 75

5.2 Determination of the fluence threshold of CFRP and its constituents . 76

5.3 Fume content of laser processed CFRPs 90

5.3.1 Isokinetic sampling & GC-MS 90

5.3.2 FT-IR gas-phase fume analysis 92

5.3.3 Particle fume capture 100

5.4 Conclusions 103

6 Laser Processing of CFRPs Part II: Fume dynamics **105**

6.1 Introduction 105

6.2 Shadowgraphy 106

6.2.1 Experimental arrangement 106

6.2.2 Results & analysis 118

6.2.3 Discussion 123
6.3 Time resolved interferometry 124
6.3.1 Experimental arrangement 124
6.3.2 Results & analysis 129
6.3.3 Discussion 148
6.4 Conclusions 149

7 Laser Processing of CFRPs Part III: Theoretical Analysis 151
7.1 Polymer decomposition model 151
7.2 Results and Discussion 154
7.3 Conclusions 160

8 Conclusions 161
8.1 Conclusions 161
8.2 Future work 165

Appendix A: CFRP and Carbon Fibre Weave Laser Processing Results 167

Appendix B: Interferometer Parts List and Setup Procedure 170

Glossary 175

References 180

Chapter 1

Introduction

Carbon fibre reinforced polymer composites (CFRP) are materials of increasing interest due to their high strength and stiffness to weight ratio, fatigue properties, corrosion resistance and that they can be tailored to specific applications.[1] Mechanical machining of CFRPs is challenging and can cause problems such as fibre pull-out and delamination of the composite.[2, 3] Laser machining offers a solution to these problems and can increase the speed, flexibility and economic viability of the process[4], but it also has its own challenges such as the need to consider the vastly different thermal and optical properties of the materials and also the anisotropic nature of the thermal conductivity. This results in the heat affected zone (HAZ) needing careful consideration.[5] CFRPs have been successfully processed with various lasers, and are now finding industrial applications.[6, 7, 8]

At the present time, the fume from the laser processing of CFRPs has not been studied comprehensively. In this thesis radio frequency excited (RF) CO_2 laser processing of CFRP is studied with a particular emphasis on analysing the fume. The RF CO_2 laser was chosen due to its abundance in industry. This stems from its low cost, compact size, flexibility, low noise and also its wavelength of 10.59μm is absorbed strongly in many materials, including some polymers.[8, 4]

For this thesis the mechanical, thermal and optical characteristics of carbon fibre weave, epoxy resin matrix and CFRP have been studied in order to fully characterise them and draw conclusions from a laser processing point of view. The separate materials have then been laser irradiated and the damage sites examined. The resultant fume has been simultaneously captured to understand what is being released during the interaction; the fluence thresholds and thermal damage areas for the materials have also been measured. The plume from the laser processing has been observed directly with fast imaging techniques: shadowgraphy and time resolved interferometry (TRI).[9] From this the contents of the fume have been visualised and conclusions drawn about their content. The trajectory has been mapped out so that it can be considered from a fume extraction point of view; the point at which the material starts to decompose is also found giving us another method of finding the fluence threshold. Finally, theoretical models are presented and measured parameters from earlier are used to successfully predict a fluence threshold and time before material is released from the surface of the epoxy resin.

The objective of this thesis is to study the laser processing of CFRPs, with an emphasis on the resultant fume. Due to the large number of CFRPs, and also the wide range of applications and laser processing techniques, the results are presented in a general way, with a view to being applied to specific materials and processes in the future. To achieve this, we have focussed on one specific study, which is RF CO_2 laser processing of T300 carbon fibres in an RS-M135 epoxy resin matrix.

The structure of the thesis is as follows. In the literature review a summary of previous work relating to the laser processing of polymers, carbon fibre weave and CFRPs is presented and the industrial context is explained in more detail. Past experiments examining the products of thermal degradation of epoxy resins and the hazards related to the fume from CFRPs in mechanical processing and fires are discussed. Previous fast imaging techniques are reviewed and concepts which are important to this thesis such as the Arrhenius equation[10] and Michelson interferometry[11] are also explained.

In chapter 3 the parameters of the laser systems are measured. The pulse energy, pulse duration, wavelength, spot size and polarization of the RF CO_2 laser are measured so that the irradiance and fluence interacting with the sample is known. Temporal measurements relating to the delay between the trigger input of the laser and the optical output are performed; this is very important for meaningful time resolved experiments as the delay can be significant. A dye laser is used in the fast imaging experiments, so its wavelength, linewidth and pulse duration are measured. The pulse duration defines the time resolution of the imaging system, and the linewidth is an important parameter in determining the coherence length of the laser and hence the visibility of fringes in the Michelson interferometer.

In chapter 4 the CFRP is examined from a mechanical point of view in order to predict how the laser will interact with it. The preparation of the samples is also discussed. The activation energy for thermal decomposition, specific heat capacity, thermal conductivity, reflectivity and the optical absorption coefficient of the specific epoxy resin matrix used in the composite are measured. The values are compared to literature where possible. The properties of the carbon fibres used are generally covered in literature, so a review of these parameters is presented. The parameters discussed in this chapter are used to analyse the laser processing of the CFRP, and are also used to analyse the process theoretically.

In chapter 5 the carbon fibre weave, epoxy resin matrix and CFRP is processed with an RF CO_2 laser, and the damage sites are examined and thresholds are measured. The effect of polarization on the laser processing of the fibres at 10.59μm is also discussed and shows good agreement with predictions made in chapter 4. In this chapter the fume is captured and analysed using techniques such as scanning electron microscopy (SEM), Fourier transform infra-red spectroscopy (FT-IR) and gas chromatography-mass spectrometry (GC-MS). These techniques are used to to examine particulate ejecta, gas phase fume and condensed vapour.

Chapter 6 uses Shadowgraphy and time resolved interferometry (TRI) to examine the

particulate and gas phase fume as it is released from the surface. The trajectory of the fume is analysed which also gives us the time delay before the ejecta start to leave the sample. The technique is used to find the regimes under which fibres are released from the surface of carbon fibre weave and CFRP, in both a time resolved and non-time resolved manner.

Chapter 7 gives theoretical calculations of the decomposition of the epoxy resin using the parameters measured in chapter 4; the threshold fluence is successfully predicted using this analysis, and also the time until the fume starts to leave the surface.

Finally, a summary of the findings is given in chapter 8, and also future work is suggested.

Chapter 2

Literature Review

2.1 Introduction

CFRP is a synthetic composite material made from carbon fibres confined within a polymer matrix, most commonly epoxy resins,[12] see figure 2.1. The purpose of this composite is to create a material with properties superior to that of its individual components. Within the composite the polymer matrix provides the bulk of the material, it also holds the reinforcement together.[12] An increase in the amount of polymer matrix within the composite will increase the impact toughness of the material.[13] The

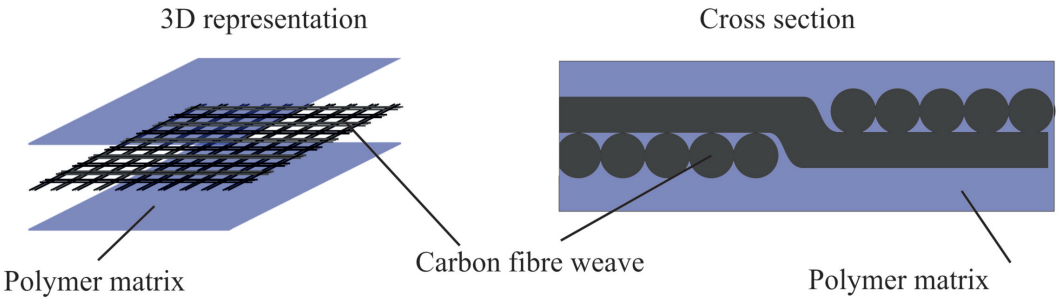

Figure 2.1: A diagram showing the construction of a CFRP with a bi-directional plain weave, with fibre orientations of 0°/90° demonstrated with a 3D representation and also a cross section. A carbon fibre weave is reinforced with an epoxy resin matrix. This results in a thin layer of epoxy resin above the fibres, and also acts as a matrix surrounding the fibres.

carbon fibre reinforcement increases the strength and stiffness in the direction of the fibres. The reinforcement has a higher strength; when a load is applied to the composite the lower strength matrix deforms to spread the load across the fibres.[12] The fibre configuration may be unidirectional, bi-directional or multi-directional, depending on which direction requires the greatest stiffness.[1] The result of constructing the material in this way is that it provides good specific stiffness and strength to weight performances. It also means that the material can be tailored to fit a specific need, i.e. favouring stiffness in a certain direction at the expense of an increase in weight, or vice versa. CFRPs have a greatly increased fatigue life and are corrosion resistant compared to metals used in manufacturing.[1]

The features outlined above mean that CFRPs are very desirable for applications ranging from sports equipment to weight and strength critical aerospace projects,[14] for example the next generation Airbus A350 XWB which takes advantage of CFRPs in over 50% of the materials used, increasing the service intervals from 6 years to 12 years, and reducing the need for fatigue and corrosion related maintenance checks.[15]

Mechanical machining of fibre reinforced composite materials faces a number of challenges. The most significant problem is delamination, in addition to other damage caused by matrix cracking and fibre pull-out.[16, 2, 17, 3] Delamination of the composite is when the layers of the material come apart due to mechanical stresses or thermal damage. This can result in poor assembly tolerances and performance deterioration[18]; mechanical drilling-associated delamination is responsible for 60% of parts rejections in the aircraft industry.[19] Delamination can be caused by the stiff fibres surrounded by a more pliable matrix being pulled out as the matrix shears, rather than the fibres themselves shearing.[19] Delamination can also be caused by high temperatures generated in the cutting process. The thermal damage to a fibre/polymer matrix can be significantly higher than damage to a metal undergoing similar machining. This is because the matrix often has a relatively low thermal conductivity when compared to metals commonly used in industry, meaning that the heat cannot easily be transferred from the drilling site leading to high temperatures. In addition to this the matrix will

usually start to decompose at lower temperatures than metals.[16]

Mechanical machining of CFRP can also cause high tool wear. The primary cause of tool wear is the high temperature generated during drilling due to the the abrasiveness of the composite material.[3, 16] An increased tool wear rate means that the process becomes more costly, but also a worn tool will generate higher thrust forces, which means that the delamination factor of the process increases with tool wear.[16] Solutions to these problems can be found by adjusting the cutting speed and feed rate; the optimum parameters are usually specific to the material and can be found experimentally but theoretical models have also been suggested.[3, 16, 20] Water jets can be used to drill CFRPs, but they also have their problems such as causing delamination, the need for a guide hole to be drilled for them to start, and the disposal of waste cutting products, thus limiting their flexibility.[21]

Laser drilling is a solution to many of these problems, particularly the speed, flexibility and ease of automation of the cutting equipment and no tool wear.[4, 22] Fibre pull out is also eliminated. However, laser drilling composites is a complex problem due to the vastly different thermal and optical properties of the matrix compared to the reinforcement, which means that the response to elevated temperatures, i.e. melting and vaporization, will vary significantly between the constituents. In addition to this the fibrous nature of CFRPs means that heat flow in the direction of the fibres is greatly increased due to the high conductivity along the fibres compared to through the matrix.[5] Despite the complications, CFRPs have been successfully processed by lasers.

Extensive work on the laser processing of polymers has been undertaken, a brief review of the field is presented in section 2.2 because it relates to the laser interaction with the composite matrix. Previous work on laser processing of CFRPs and carbon fibres is discussed in greater detail in section 2.3. At this time the fume from laser processed CFRPs has not been studied in detail, however a review of any past work relating to the fumes from mechanical machining of carbon fibres and thermal degradation of epoxy

resin matrices are presented in section 2.4. One of the key analysis techniques presented in this thesis is time resolved, high magnification, fast-photography with extensive work using time resolved interferometry; previous work on fast photography is examined in section 2.5 and the concepts behind Michelson interferometry are discussed in section 2.6. Finally the Arrhenius equation predicts the temperature dependence of a reaction rate, which is important when considering thermal modelling of decomposition pathways. Details of this type of analysis are outlined in section 2.7.

2.2 Laser processing of polymers

Early work on the surface modification of polymers used ultraviolet (UV) lasers to advance photo-lithography using a KrF excimer laser with a wavelength of 248nm to expose a photo-resist followed by chemical etching.[23] At a similar time a shorter wavelength (193nm ArF excimer) was used so that 'self-developing photoetching' could be observed by increasing the photon energy.[24] This type of etching, or ablation, is generally referred to as photochemical because the driving mechanism for the ablation is primarily due to the breaking of bonds; for photochemical etching the photon energy must be greater than the bond dissociation enthalpy[25] which is commonly $1.5 - 11$eV per bond for simple molecules[26], and an excimer laser's photon energy can range from $3.5 - 10$eV. A XeCl excimer laser at a wavelength of 308nm was also used to directly etch polymers with a lower photon energy, which meant that the interaction was primarily a thermal process.[27] Since these early publications, UV ablation of polymers has been studied and reviewed extensively.[28, 29, 30, 31, 32, 33]

Infra-red (IR) laser processing of polymers means that the photon energy itself is not sufficient to break bonds, so the interaction will be photothermally driven by the absorbed IR light (negating phenomena such as two photon absorption). However, pulsed IR lasers such as the transversely excited atmospheric pressure (TEA) CO_2 laser have advantages over UV excimer lasers, such as higher pulse energy, greater efficiency

and the advantage of not using toxic gases. Due to the longer wavelength the resolution achievable with IR lasers is reduced in comparison to UV sources.[34] Despite the majority of work being focussed on UV lasers, pulsed IR sources have been shown to both assist UV ablation[35] and produce good results ablating polymers independently.[34, 36, 37, 38, 39, 40]

The commercial interest in long pulse IR lasers, such as radio frequency (RF) CO_2 lasers has increased due to their compact size, high power (and therefore processing speed), sealed operation and low cost.[41, 42] Due to their wavelength of $9.4 - 10.6\mu m$ they are also generally absorbed strongly in materials which are transparent to other common wavelengths, such as $1.06\mu m$.[43] RF CO_2 lasers are the most common for industrial marking, cutting and drilling of polymers for these reasons.[44] It has been found that polymers can be cut or drilled with these lasers, but the process must be optimized for the specific material in order to obtain a high quality result.[45, 22, 46, 47, 48] The main quality factor to be considered while laser processing is the heat affected zone (HAZ) and the parameters which affect it include the laser pulse energy, scanning speed and assist gas pressure.[49]

When laser processing with long pulse CO_2 lasers, the interaction will be dominated by photothermal processes due to its low photon energy, as discussed above. When polymers are laser-processed in this way, one of three mechanisms can be identified.[43] The first is 'fusion cutting', where material made molten by the laser is removed by a high pressure assist gas; this mechanism can take place in polymers which can melt, i.e. thermoplastics such as polythene, polypropylene and polycarbonate.[43] The second is 'vaporization cutting', where the surface is heated to sufficiently high temperature to become gas phase; the pressure of the vapour will then blow ejecta out of the hole. This mechanism is achieved with thermoplastics by limiting the assist gas pressure to avoid blowing material away and poly(methyl methacrylate) is frequently cut in this manner to increase the cut edge quality.[4, 43] The final mechanism is cutting via thermally induced chemical degradation, which is the mechanism for thermosetting polymers because they cannot melt. This process is caused by thermal degradation at elevated

temperatures, and tends to produce a carbonaceous 'smoke'; polymers such as epoxy resins will be cut in this way.[43]

In order to achieve cutting using any of the methods discussed above, the required energy per unit volume must be delivered to the material. If all of the energy is reflected then none will be deposited, similarly if the material is transparent to the wavelength of light then no energy will be absorbed. It follows that absorption is one of the most important aspects of laser processing; a high absorption coefficient, α, means that energy is deposited in a smaller volume, so the energy density is higher.[50, 27, 33] The reflectivity can be used to calculate the intensity of the laser light incident on the surface that goes into the sample. After this, the Beer-Lambert law models optical absorption (equation 2.1).[51, 27, 33]

$$I_T = I_0 e^{-\alpha z} \tag{2.1}$$

where I_T is the light intensity after it has passed through the sample sample, I_0 is the initial intensity and z the distance into the sample. From this is is clear that the intensity will drop exponentially as it propagates further into the medium, as is shown in figure 2.1. The distance over which the intensity falls to I_0/e is called the optical absorption length, $1/\alpha$.

The other significant mechanism involved in determining the deposited energy per unit volume is thermal diffusion, i.e. the heat being conducted from the volume where the energy is deposited (so far governed by the spot size and the optical absorption length). This can be characterised in terms of a thermal diffusion length, δ (equation 2.2).[25, 50]

$$\delta = 2\sqrt{D_H \tau} \tag{2.2}$$

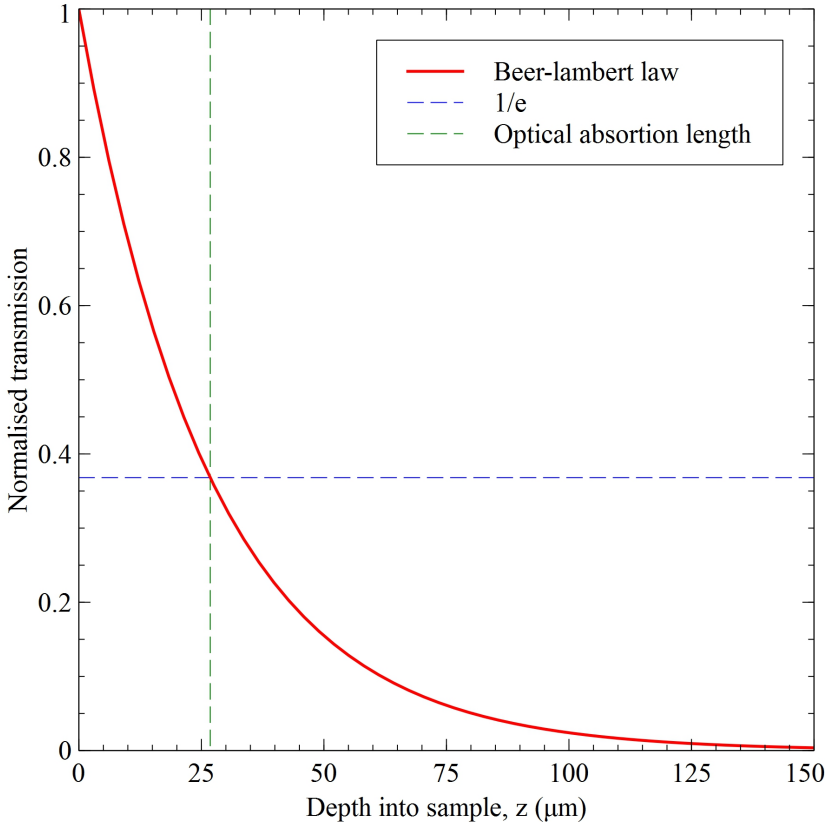

Figure 2.2: An example of the Beer-Lambert law of optical absorption; the optical absorption length is shown on the graph where the intensity drops to $1/e$. The intersection with the Beer-Lambert line is the value of $1/\alpha$.

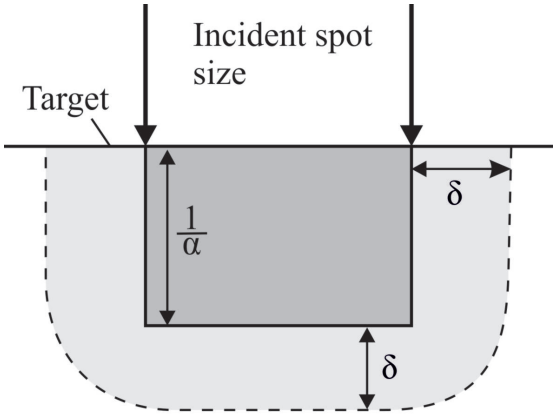

Figure 2.3: A diagram showing the cross section of a laser interaction. The optical absorption depth ($1/\alpha$) and spot size define the initial deposition volume. The subsequent thermal diffusion length depends on the laser pulse duration and the thermal diffusivity, and is shown as δ.

$$D_H = K/\rho c_p \tag{2.3}$$

where D_H is the thermal diffusivity (equation 2.3) and τ is the pulse duration. The thermal diffusion length tells us how far the laser energy conducts to from where it is deposited, i.e. where the temperature distribution falls to $1/e$ (figure 2.3), and will increase with longer pulse durations and increased thermal diffusivity.

2.3 Laser processing of carbon fibre composites

Laser processing CFRPs is a complicated problem, because the graphite fibres and the epoxy resin have very different thermal and optical properties, which means that the absorption and diffusion properties discussed in section 2.2 need to be considered in greater detail. The heat flow along the direction of the fibres is larger when compared to the transverse value and the direction of the fibres may be unidirectional, bidirectional,

multidirectional; these two factors led to an anisotropy in the conductivity of the CFRP, which may also vary across the material.[5]

For unidirectional fibres, the conductivity in the direction of the fibres can be estimated by the rule of mixtures (equation 2.4).[52]

$$K^p_{CFRP} = V_m K_m + V_f K^p_f \tag{2.4}$$

where K^p_{CFRP}, K_m and K^p_f are the conductivities of the unidirectional CFRP parallel to the direction of the fibres, the resin matrix and the carbon fibres respectively. V_m and V_f and the volumetric fractions of the matrix and fibres which make up the CFRP. Epoxy resins generally have a relatively low thermal conductivity, of the order of $0.17 - 0.23 \mathrm{W\,m^{-1}\,K^{-1}}$.[52, 53] In contrast to this carbon fibres have conductivities up to three orders of magnitude higher, ranging around $7 - 360 \mathrm{W\,m^{-1}\,K^{-1}}$, the large variation being due to different crystal structures.[52] From this it is clear that the conductivity will increase greatly in the direction of the fibres with an increased volumetric fraction.

The conductivity perpendicular to the fibres is a much more complex problem. The first consideration is the conductivity across the fibre, which is generally lower than along it, and can be around $2.0 - 2.4 \mathrm{W\,m^{-1}\,K^{-1}}$. The second is the lower conductivity of the matrix between the fibres. A model has been proposed to predict the conductivity perpendicular to the fibres; however it only serves as a guideline due to the random nature of the geometric arrangement of the fibres, and should be backed up with experimental data.[52] Experimentally it is found that there is a slight increase in the conductivity of the CFRP perpendicular to the fibres when compared to pure epoxy resin; however, it is still very low ($\sim 0.5 \mathrm{W\,m^{-1}\,K^{-1}}$ for a 50:50 fibre:matrix ratio) when compared to both the CFRP and carbon fibres parallel to their orientation.[52] It should be noted that the conductivity into the sample (normal to the surface) will be similar, or identical, to the conductivity perpendicular to the direction of the fibres, as is clear from examining the structure of the composite (figure 2.1).

Early work on the laser machining of CFRPs was successful with excimer lasers, but the fibres were generally found to have a much higher fluence threshold for ablation than the matrix.[54] A PEEK/carbon fibre composite was ablated with a XeCl excimer laser; the threshold of the fibres was found to be much greater than that of the PEEK, allowing 'fibre stripping' by selective ablation. The thermal damage with this laser was small due to the short pulse. Fibres were observed thinning before fracturing catastrophically due to thermal or mechanical stresses. The surface recession rate was also predicted by calculating the temperature rise in the fibres and using a vaporization model.[6]

Along with the need to consider the different thermal and optical properties of the materials, the primary complication for industrial laser cutting of CFRPs is the HAZ,[55, 5] which can cause the recession and decomposition of the surrounding matrix and delamination. It has been found that the wavelength of a laser has no impact on the tensile strength of the CFRPs, only the way the laser's parameters affect the HAZ, which subsequently governs any loss in strength.[56] Another complication is fibre swelling[5], which can occur with PAN based fibres such as Toray T300[57]. A detailed study has shown that the swelling is caused by the rapid volatilization of non-carbon impurities due to the large laser induced thermal gradients. The swelling in PAN fibres can be reduced by heat treatment which drives off impurities in the same way as the laser, but at a smaller temperature gradient, thus reducing swelling.[58]

In early experiments it was found that a Nd:YAG laser could be used to perforate CFRPs in order to reduce skin friction drag. However, the technique produced a large amount of damage to the matrix which meant the tensile strength was reduced.[59] Later, Nd:YAG lasers were found to be capable of producing a HAZ which yielded a tensile strength loss similar to that of mechanical milling (though in the latter case the strength loss is due to mechanical stresses).[56, 60] A Nd:YVO_4 diode pumped solid state laser with a UV wavelength was used in a process development to cut CFRPs with minimal HAZ. By trepanning concentric rings with a fast cutting speed, fibres were chopped at either end, meaning that heat within the chopped fibre could not

be conducted to the surrounding matrix. Models have also been formulated for this process.[7, 61, 62] It has been found that minimizing the HAZ for CW laser processing can be achieved by increasing the scan or cutting speed of the process.[63] Drilling with concentric rings, or 'laser spiral drilling' has also been shown to reduced the HAZ using a fibre laser and in addition use of an assist gas can reduce the thermal damage, but increases the amount of debris around the laser drilled hole.[21] Fibre laser drilling has also been modelled theoretically, and has predicted hole sizes in agreement with experimental results.[5]

The interest in laser cutting CFRPs with CO_2 lasers is primarily due to high assembly costs when producing aerospace products; industrial laser systems can help to reduce these costs due to their high speed, flexibility/automation and low noise/dust.[8, 4] The other advantage is the high absorption in matrices compared to shorter wavelengths (UV excluded).[64, 65] In earlier papers replicating industrial laser processing it was found that the CO_2 laser significantly reduced the tensile strength of a material[66], and produced inferior cuts with a larger HAZ compared to Nd:YAG which matched mechanical milling.[56] However, experiments have successfully optimized the CO_2 laser cutting of CFRPs in order to minimize the HAZ.[67] In a more recent experimental study of CO_2 laser cutting of CFRPs it was concluded that while CO_2 laser cutting of CFRPs is difficult, and a HAZ is unavoidable, acceptable results (i.e. matching mechanical methods) can be achieved with careful consideration of the cutting parameters, and the damage was minimized so that the integrity of the sample was not comprised.[8] CO_2 lasers have also been found to be suitable for cutting carbon fibre weaves (without a matrix), and can also be used to join the ends of the fibres together in the same step.[68]

2.4 Fume analysis of carbon fibre composites

The velocity and momentum of fume from laser ablated carbon fibre weave were measured, by filming the ablation and measuring the reaction force from the ablated sample. It was concluded that the high velocity and momentum of the plume could be a challenge for fume extraction units.[69] No literature directly related to the fume content from laser ablation of CFRPs has been found; however below are summaries of literature related to the thermal decomposition of epoxy resins and carbon fibres, and also the mechanical machining of carbon fibres.

The fume from the thermal decomposition of a bisphenol A based epoxy resin has been investigated by using thermo gravimetric analysis (TGA) to decompose materials, the fume was then analysed using techniques such as Fourier transform infra-red spectrometry (FT-IR) and gas-chromatography mass-spectrometry.[70] The primary constituents for an epoxy resin fume were found to be water, CO_2 and phenols.[71] Previous experiments of a similar kind found quantities of CO and methane, and also CO_2, small quantities of ethylene, a trace of an aldehyde which was thought to be formaldehyde, acrolein, acetone, allyl alcohol and water. Phenol and cresol based compounds were also noted.[72]

It is known that fibres which have diameters of $< 3\mu m$ are respirable, meaning they can bypass the lungs defences against such particles, and the body would be unable to metabolize them.[73] Due to the hazardous nature of breathing in asbestos-like fibres, an investigation into the production and hazards of PAN carbon fibres was undertaken. It was found that respirable particles were difficult to produce using equipment that would produce a large quantity of hazardous fibres when used with asbestos. Of this low concentration of respirable fume, less than 1% of it was fibrous in nature.[74] Carbon fibres are generally larger than 3µm, but it was suspected that if the CFRP was exposed to a fire they could thin due to oxidation and become hazardous. It was concluded that respirable fibres could be generated in a fire, but high quantities of

oxygen were necessary.[73]

2.5 High magnification ultra-fast time resolved imaging

Ultra-fast imaging is a technique where a visible laser pulse is used to define the duration of exposure of an image. This means that the exposure can be $<$ 5ns, which is much faster than a camera's shutter speed or flash gun. There are two primary configurations for this. The first uses a camera in a conventional manner, i.e. focussed onto the area of interest, a fast laser pulse illuminates the site and reflected light exposes the sensor. This is how a camera's flash gun works, but a laser is a much shorter and higher intensity source of light. The second technique is commonly referred to as shadowgraphy, where a short duration collimated laser pulse is directed through an area of interest, and objects, such as the ablated material, cast a shadow onto the camera sensor or film.[75] Shadowgraphy is one of the primary methods used in this thesis for observing the ablation plume in a time resolved manner.

Very early experiments using lasers to expose cameras formed the basis for fast photography.[76] Ultra-fast imaging was later applied to laser ablation to build on previous time resolved transmission, reflection and photoacoustic experiments to deduce the mechanism by which polymers decompose under UV irradiation.[77, 78, 79] The crater evolution with time for an XeCl excimer laser ablating polyimide was observed using fast imaging by splitting the XeCl laser pulse so that part of it ablated the material and another part pumped a dye laser. An optical delay line was used to control the temporal position of the image. The processing and imaging were through the same UV microscope objective and along the same optical axis.[80] The technique was also achieved by reflecting light from the sample and into the camera at a small angle, as opposed to on axis, in order to observe the damage with respect to time for excimer laser processed PMMA.[81] High speed imaging of plumes from polymer and tissue targets was used to analyse the fume products and dynamics during UV excimer laser

ablation. The illumination laser was not directed through the sample and into the camera, but grazed the target to expose the plume.[82]

Shadowgraphy by directing a visible laser pulse through a plume from behind (normal to the surface) and into a camera to create a shadow on the sensor is the technique most relevant to this thesis. This was applied to a laser induced plume by using two excimer lasers, one to ablate the sample and the other to pump the dye laser; this was used to analyse the products of the PMMA ablation and the fume velocity.[81] Shadowgraphy has also been used to analyse the dynamics of thin Al film removal while minimizing the damage to the substrate by understanding the release mechanism.[83]

2.6 Michelson interferometry

Interferometry with a continuous wave source (CW) has been used in a time resolved fashion to probe the refractive index of a laser induced plume; the interaction was performed in one of the arms of a Michelson interferometer, and the output during the ablation pulse was recorded along with the optical emission of the plume.[84] Imaging with time resolved interferometry (TRI) is described, and has been shown to have an increase in sensitivity over shadowgraphy for the observation of ablation products by performing the interaction in an arm of the interferometer and directing its output into a camera.[9]

An interferometer is a device which extracts information from two waves by superimposing them. In this section a Michelson interferometer which extracts information from two electromagnetic waves using a 'divison of amplitude' technique is discussed.[11, 85]

Interference fringes are formed when two electromagnetic waves are superimposed. In a Michelson Interferometer the two electromagnetic waves originate from a single source of light. The light is split 50:50 using a beamsplitter. The two waves are each

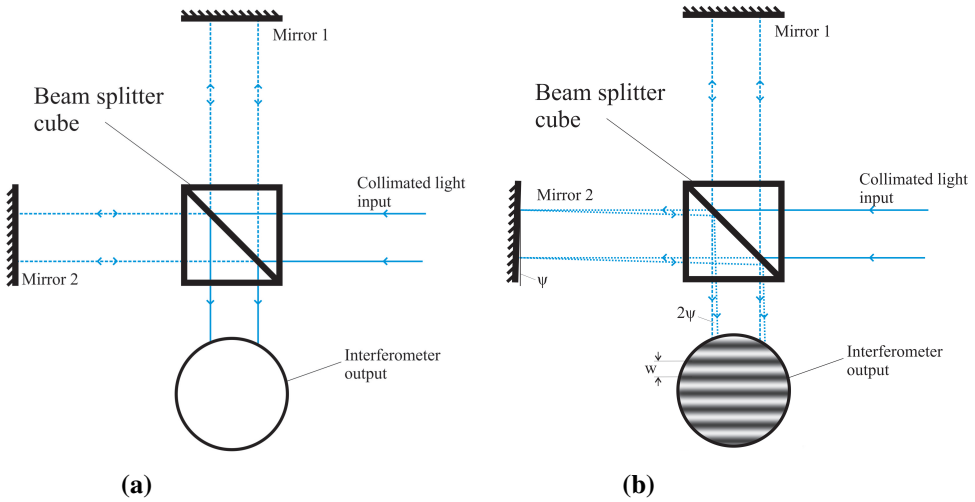

Figure 2.4: (a) shows an interferometer which is set up so the mirrors are both perpendicular to the input beam of light. (b) shows the same setup with one of the mirrors tilted at a small angle, interference fringes can be seen at the output.

reflected from a mirror and are recombined using the beamsplitter, as shown in figure 2.4 (a beamsplitter cube is shown). If both mirrors are perpendicular to the beams of light, as shown in figure 2.4a, the two beams are recombined at the beamsplitter and the output is identical to the input when the path difference is zero. If mirror 2 is moved so that it is at a small angle, ψ, as shown in figure 2.4b, the light path from this mirror will be at an angle of 2ψ with respect to the path from mirror 1 at the interferometer output. This small angle results in interference fringes with a spacing w. For small angles the fringe spacing is given by equation 2.5.[85]

$$w = \frac{\lambda}{2\psi} \tag{2.5}$$

The visibility of the fringes, $V_{visibility}$, is defined from the light intensity at the fringe maxima, I_{max}, and at the minima, I_{min}, using equation 2.6.[85, 86]

$$V_{visibility} \equiv \frac{I_{max} - I_{min}}{I_{max} + I_{min}} \tag{2.6}$$

If the source of light is perfectly monochromatic the two paths of light will form in-

terference fringes (regardless of the difference in optical path lengths) with very high contrast because the waves will be fully constructive and destructive, so that the maxima will be bright and the minima will be entirely black. It is clear from equation 2.6 that if the fringe minima are black then $I_{min} = 0$, and therefore $V_{visibility} = 1$.[85]

However, in reality light is not perfectly monochromatic, so cannot be represented by a pure sine wave. The coherence time, τ_c, is the length of time which an incoherent source of light is observed to be a 'perfect' sine wave,[86] and can be approximated with equation 2.7.[87]

$$\tau_c \approx \frac{1}{\Delta\nu} \tag{2.7}$$

where $\Delta\nu$ is the frequency bandwidth of the light source. The coherence time is related to the coherence length, l_c,which is the length over which the wave is observed to be an uninterrupted sine wave (equation 2.8).[87]

$$l_c = c\tau_c \tag{2.8}$$

where c is the speed of light. This can be approximated in terms of peak wavelength, λ_0, and the linewidth, $\Delta\lambda$ (equation 2.9).

$$l_c \approx \frac{\lambda_0^2}{\Delta\lambda} \tag{2.9}$$

When the arm lengths of a Michelson interferometer are within $l_c/2$ of each other, fringes can be observed. The fringes will then shift if the optical path length in the arm changes; this technique can be used to observe a change in refractive index within the arm due to changes in a temperature or in the gas atmosphere (for example), and the refractive index can be extracted.

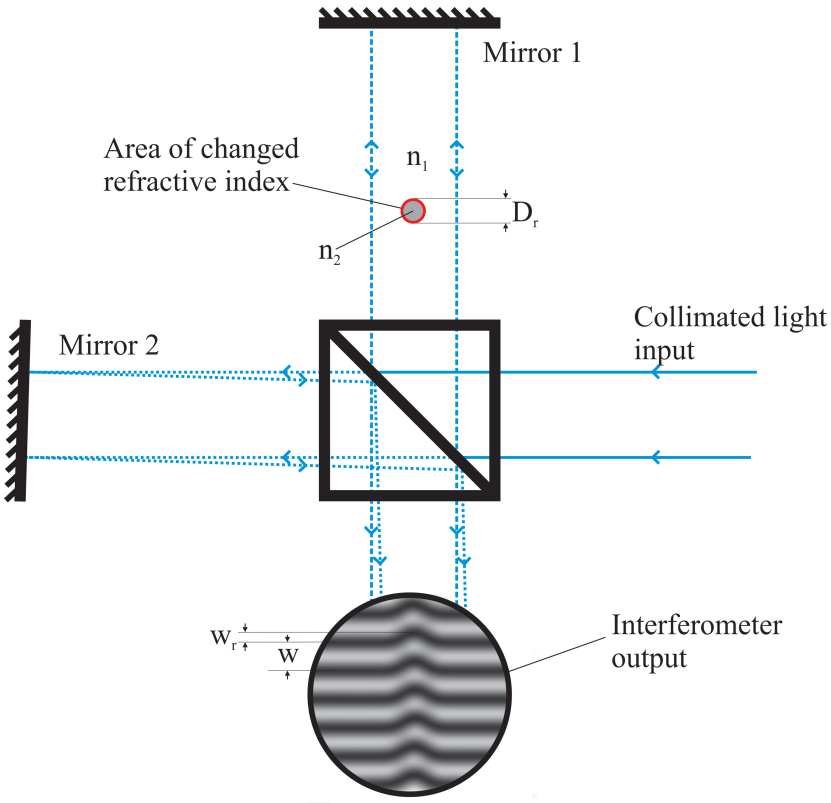

Figure 2.5: A diagram demonstrating the effect of a column of diameter D_r, with a changed refractive index, n_2 as observed in the interferometer fringes.

Figure 2.5 shows an interferometer with a circular column of changed refractive index, with a diameter, D_r. In the diagram there is an example of the output which this would yield; the fringes have a disturbance where the region of changed refractive index is, with a peak fringe displacement w_r. It follows that the number of fringes displaced at the peak is w_r/w. The optical path length change in units of wavelengths can then be equated to the number of fringes displaced by comparison with equation 2.5. This is shown in equation 2.10. D_r can be used as the path length at the peak fringe shift, due to the region being circular.

$$\frac{2[(n_1 \times D_r) - (n_2 \times D_r)]}{\lambda} = \frac{w_r}{w} \tag{2.10}$$

From equation 2.10 it can be seen that the direction of the number of fringe shifts, w_r/w, i.e. positive or negative will affect the refractive index calculated. This must be

calibrated for a specific system, as it is possible to set the direction of the fringe shifts with an increase or decrease by changing the alignment of the mirrors.

2.7 Arrhenius equation

Models of polymer decomposition, whether by laser or by other heat sources, have often employed an Arrhenius law to describe the process.[30, 36] For laser heating, it is important to include this in any analysis as the ablation of the epoxy is likely to be dependent on the heating rate in that strong over-heating can occur for high irradiances.[88, 89, 90]

The rate that a chemical reaction proceeds with depends on the the concentration of reactants, and the rate constant, κ. The rate constant is temperature dependent, and can be described with the Arrhenius equation, see equation 2.11.[91, 10]

$$\kappa = \Lambda e^{-E_a/\overline{R}T} \tag{2.11}$$

where Λ is the pre-exponential factor, E_a is the activation energy, $\overline{R}$ is the gas constant and T is temperature. The units for the pre-exponential factor are the same as the units for the rate constant, and for a first order reaction the units for both are s^{-1}. From this equation it can be shown if a plot of $\ln \kappa$ against $1/T$ yields a straight line then the gradient is $-E_a/\overline{R}$.[91]

The activation energy is the minimum energy reactants must have to allow the reaction to take place. The progress of a reaction can be described with the reaction co-ordinate, which summarizes the change in interatomic distances and bond angles. For a reaction to proceed the molecules must have enough energy to overcome a 'barrier', which has a height of E_a (figure 2.6). When a molecule is at the peak of the potential energy curve, it is in the transition state; in this configuration a small amount of energy is required to pass the barrier. Once the barrier has been passed the potential energy falls

as the atoms in the molecules rearrange in clusters to form products. The fraction of molecules which have sufficient energy to overcome the barrier, i.e. $> E_a$, is given by $e^{-E_a/\overline{R}T}$, which comes from the Boltzmann distribution.[92]

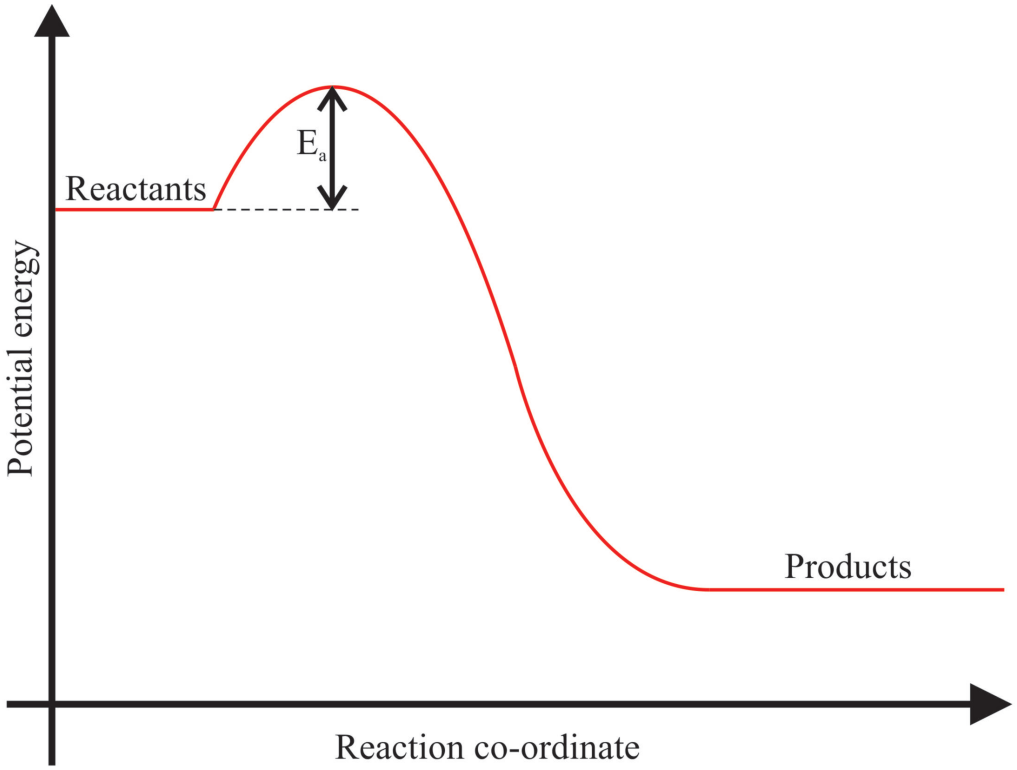

Figure 2.6: A graph demonstrating that a reaction with an increasing reaction co-ordinate must overcome the activation energy (E_a) barrier in order to form the reaction products.

Chapter 3

Laser Systems

3.1 Introduction

In this thesis a radio frequency excited waveguide carbon dioxide (RF CO_2) laser is used to process CFRP and its constituents in order to determine the processing parameters, the fume contents and the fume dynamics. As a starting point, this chapter describes the characterisation of this laser in terms of its pulse duration, energy and polarization.

Timing between the laser interaction and the exposure of the camera is important for the time-resolved techniques described in chapter 6. This, combined with the fact that radio frequency excited lasers often exhibit a delay between receiving an 'enable' signal and the optical (laser) output, requires the pulse characteristics of the laser system as a whole to be characterised. This chapter quantifies these temporal features.

The imaging systems in this thesis require a fast, visible pulse of light; in our experiments this is produced with a dye laser. Its pulse duration defines the exposure time of the system and therefore determines the upper velocity of fume which can be resolved on an imaging system. The coherence length of the dye laser is relevant to setting up a Michelson interferometer because it defines the region over which fringes are observ-

able; it is governed by the wavelength and linewidth of the dye laser. These parameters are measured in this chapter.

3.2 RF CO_2 laser

A Universal Laser Systems OEM ULR 30W RF CO_2 laser[93] was used to process materials throughout this thesis. The laser was a sealed tube with a CO_2 gas mixture electrically excited with a radio frequency electric field. The output was continuous wave (CW) in time with a Gaussian transverse profile. The optical pulse duration could be modulated via a TTL input; when the TTL pulse was high, the laser was enabled. It was air cooled and had an external power supply. The laser was triggered using one TTL output of a Farnell PG102 dual pulse generator.

The wavelength of the laser was measured using a CO_2 spectrum analyser from Optical Engineering Inc. The emission was from the 001-100 transition, and the strongest line was at P20 (10.59μm) with a much weaker emission at P22 (10.61μm). For the purposes of calculations throughout this thesis it is assumed that the 10.59μm laser transition dominates all interactions.

The laser pulse duration was measured using a gold doped germanium (Ge:Au) detector from Santa Barbara Research Corporation, orientated as shown in figure 3.1. The Ge:Au was liquid nitrogen cooled and insulated in a vacuum dewar with a Ge window to expose the detector to laser light. The detector had a -90V bias provided by a battery pack to reduce electrical noise pick-up. Light from the RF CO_2 laser was scattered off a brushed Al plate towards the detector. The output from the detector was monitored on an Agilent InfiniiVision DSO-X 3052A 500MHz, 4GSa/s oscilloscope[94]; a compromise was sought between sensitivity (high impedance) and rise time (faster at low impedance), and a 22kΩ resistor in parallel with the oscilloscope 1MΩ input was found to fulfil these criteria.

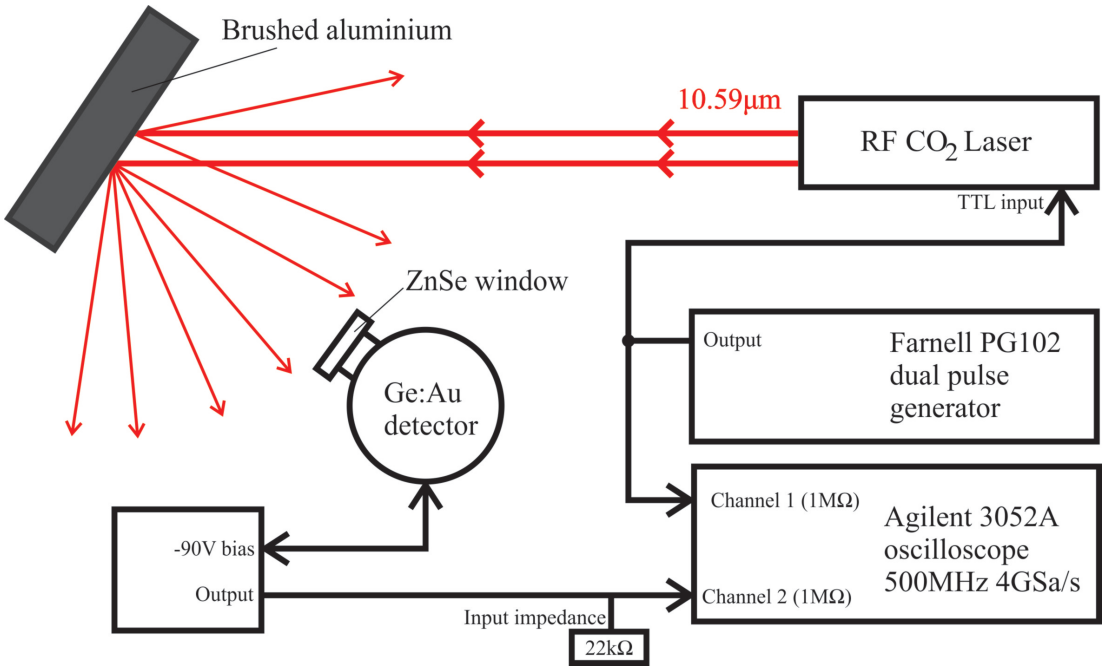

Figure 3.1: The pulse duration of the RF CO_2 laser was measured by scattering light onto a liquid nitrogen cooled Ge:Au detector using a brushed aluminium plate.

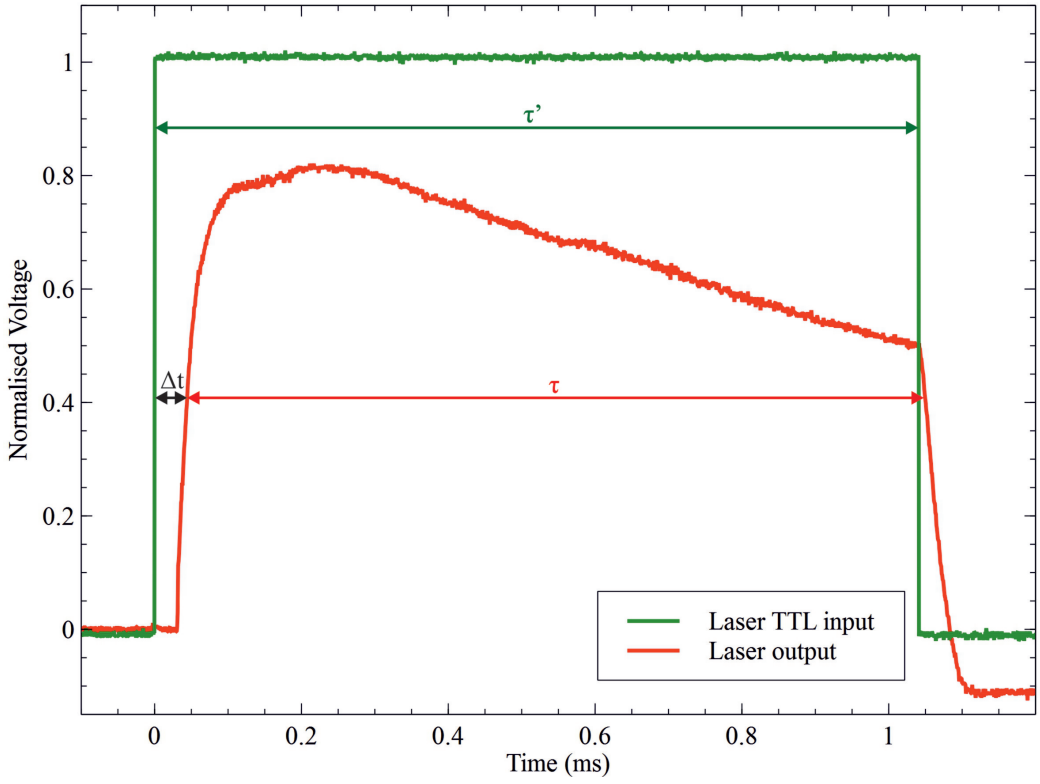

Figure 3.2: A graph of the RF CO_2 laser pulse compared to the input TTL pulse, measured using a -90V biased Ge:Au detector. The graph is annotated to show the pulse duration of the laser τ compared to the TTL trigger pulse duration, τ' and also the delay between the start of these two pulses, Δt.

The input TTL pulse duration was adjusted until the laser output was as close to 1ms as possible; this was the setup used throughout the thesis (figure 3.2). It can be seen from this that there is a delay between the start of the TTL control pulse which enables the RF CO_2 laser, and the start of the optical output. This is defined as Δt. The delay also affects the pulse duration of the laser, τ, compared to the TTL input pulse duration, τ'.

To measure the parameters precisely and test for reproducibility 100 pulses were recorded on the oscilloscope at a pulse repetition rate (*PRR*) of 0.5Hz, chosen to match the *PRR* of the experiments in this thesis. The averages and standard deviations of the 100 pulses were calculated and from this τ' was measured to be 1.0408ms with a standard deviation of 57ns, τ was measured as 1.012ms at the full width half maximum (FWHM) with a standard deviation of 2.6µs and Δt was measured to be 41.5µs with a standard deviation of 1.2µs.

The laser was directed onto the target site via an Au coated mirror, and a 125mm ZnSe lens was used to focus the laser. The focus was found by ablating ink covered card at various distances from the lens, and examining the ablation sites under a microscope. The position with the smallest and most circular spot was chosen and maintained throughout this thesis.

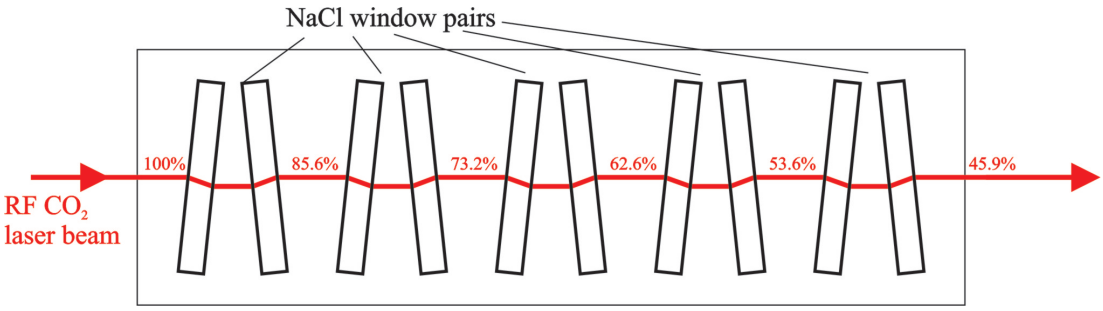

Figure 3.3: A diagram of the NaCl attenuators used to adjust the power of the RF CO_2 laser. The NaCl windows were used in pairs so that the beam was not translated. Five pairs of windows were available, which meant that six different power levels could be selected.

The RF CO_2 laser pulse energy was attenuated using a series of NaCl windows at $\pm 6^\circ$ to the plane perpendicular to the optical axis of the laser (figure 3.3). The windows were used in pairs to avoid displacing the beam from the original optical axis. The reflectivity of each window at a wavelength of 10.59μm (combined from both surfaces) was calculated from the Fresnel equations[95, 96, 87] to be $\sim 7.5\%$, based on a refractive index of 1.49065[97, 96]. Five pairs of NaCl windows were available, giving theoretical transmission (and hence energies) of 100%, 85.6%, 73.2%, 62.6%, 53.6% and 45.9%.

The pulse energy was measured by setting the RF CO_2 laser to a particular *PRR*, and measuring the average power after the optical elements in the system. The average power was measured using a Coherent 201 power meter with a Coherent 205 20W power meter head[98]. The average power was plotted against the *PRR*, and the gradient gave the energy per pulse. It should be noted that this calibration was performed before each set of results at specific pulse energies in later chapters; however an example of the calibration used in section 6.3.2 is shown in figure 3.4 and the pulse energy was calculated from this graph. The measured energy was compared to theoretical values, and the results are shown in figure 3.5.

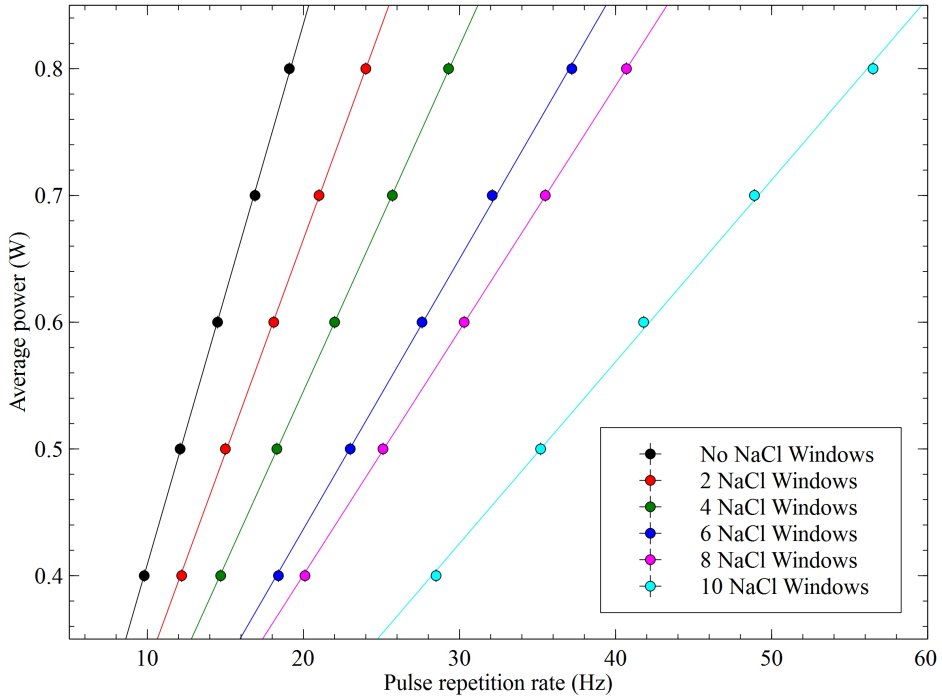

Figure 3.4: A graph of the average power with respect to the PRR for the RF CO_2 laser attenuated with differing numbers of NaCl windows. These calibrations were used in the work presented in figure 6.18.

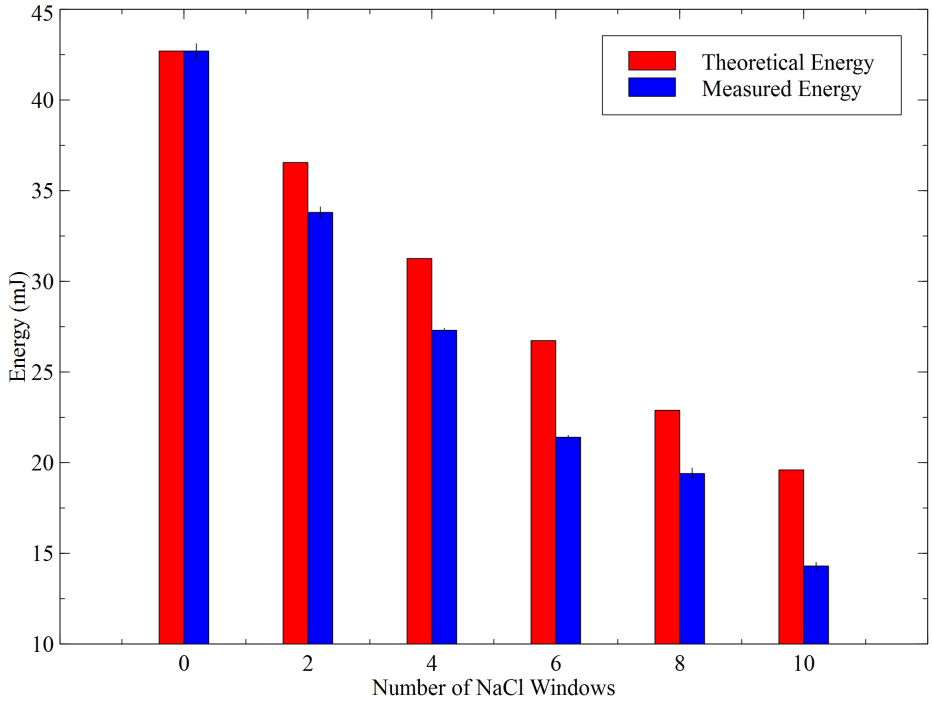

Figure 3.5: A graph showing the RF CO_2 laser pulse energy calculated from figure 3.4. The pulse energy is compared to theoretical values deduced using the Fresnel equations and the refractive index of NaCl (1.49065)[97] at 10.59µm.

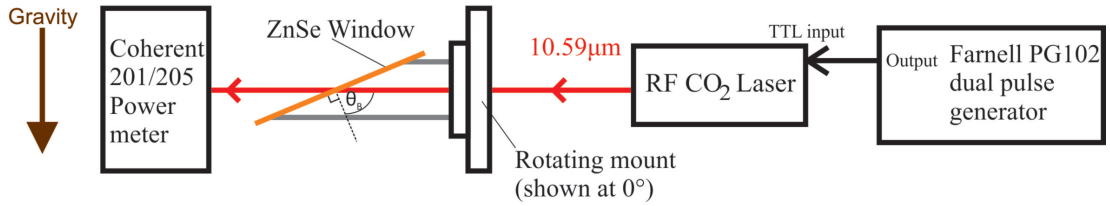

Figure 3.6: A diagram of the setup to analyse the polarization of the RF CO_2 laser. The laser light was directed through a ZnSe window which was mounted at Brewster's angle, and onto a power meter. The rotation angle of the ZnSe window could be adjusted.

The polarization of the RF CO_2 laser was analysed by directing the laser through a ZnSe window at Brewster's angle[99] and onto the Coherent power meter (figure 3.6). The RF CO_2 laser was set at a *PRR* of 10Hz and the power was recorded. The ZnSe window was then rotated in 45° increments while noting the average power. Figure 3.6 shows the configuration which is defined as the 0° position. Looking from the power meter, towards the laser, and rotating the ZnSe window clockwise is defined as a positive angle increase. The results are shown in table 3.1.

From the results shown in table 3.1, it can be seen that at 0° and 180° little power was lost from the control reading with no window in the beam line. At 90° and 270° there was a significant loss in transmitted power. At 45°, 135°, 225° and 315° around half of the power was lost.

At Brewster's angle some s-polarized light will be reflected, but p-polarized light will not.[100] From the results above, it can be deduced that when the ZnSe window is in the 0° or 180° position, the light incident on the ZnSe window is p-polarized, and therefore could not be reflected. The slight drop in power from the control result with no window could be due to a small uncertainty in the rotation of the window or in the angle at which the ZnSe window is mounted. It could also be due to absorption either in the window, or in dust and dirt which had accumulated on the window. When the window was at 90° and 270° the reflectance, and therefore the drop in power, significantly increased. This supported the earlier statement, because at these angles the incident light on the window would be s-polarized, and would be reflected. In terms

Table 3.1: A table showing the power which was transmitted through a ZnSe window, placed at Brewster's angle of incidence, at various degrees of rotation about the optical axis of the laser.

ZnSe window rotation	Average power (W)
No Window	0.40
0°	0.37
45°	0.24
90°	0.13
135°	0.27
180°	0.38
225°	0.27
270°	0.14
315°	0.25

of the laser, the direction of the polarization was 'vertical', i.e. parallel to the direction of gravity.

3.3 Dye laser system

A dye laser consists of a dye solution, which is optically excited with an external source. The output wavelength is governed by the dye chosen, the solvent which the dye is dissolved in and finally the wavelength of the pump source.

The dye laser used here held the dye solution in a quartz cuvette, giving a gain length of 10mm, and required 4ml of dye solution. The dye was laser pumped with a Lumonics Excimer-500 laser[101] with a XeCl gas mixture (HCl, Xe and a He buffer) giving a wavelength of 308nm, and a pulse energy of $\sim$ 30mJ. The light from the XeCl laser was directed using two Al mirrors and was then focussed onto the cuvette using a quartz cylindrical lens with a focal length of $\sim$ 15mm. The focus could be optimized by changing the cuvette's distance from the lens with a micrometer stage. The cuvette was held such that the sides were not perfectly perpendicular to the lasing path so that a laser cavity was not formed between the quartz walls.

Coumarin 120 (also known at Coumarin 440[102]) was the chosen dye with methanol for the solvent. This yields a laser output with a wavelength of $418-498$nm, and a peak wavelength of 444nm when pumped with an N_2 laser; similar results can be expected with a XeCl pump laser, however the concentration of the dye may need to be higher due to a lower absorption at this wavelength.[102] The dye concentration for an N_2 laser was recommended to be of the order 5×10^{-3}M.[102] To find the optimum absorption for our setup two concentrations of the dye were mixed, one at 3×10^{-3}M and another at 13.5×10^{-3}M. The lower concentration dye was added to the cuvette, and then the concentrated solution was added in small quantities until the 308nm light was observed to be absorbed strongly so a thin line of fluorescence was visible.

A grating was used for the 'rear' optic. The grating was in an adjustable mount so that it could be set at a particular angle of incidence and the alignment could be adjusted. This meant that the laser could be tuned to give a narrower linewidth compared to a mirror. This was important as laser dyes typically fluoresce over a broad band of wavelengths[100]; it was particularly important when using this laser in a Michelson interferometer as the linewidth is inversely proportional to the coherence length, see section 2.6. The front optic was an uncoated glass window which was also adjustable to align the cavity. The glass window will give $\sim 8\%$ reflectance at a wavelength of 440nm.

The diffraction grating had a groove density of 1200grooves/mm. Its blaze wavelength was 500nm. The grating equation can describe the response of a diffraction grating to various wavelengths and angles of incidence (equation 3.1)[86] .

$$d_g(\sin\theta_i+\sin\theta_m)=m\lambda \tag{3.1}$$

where d_g is the line spacing, the angle of incidence on the grating is θ_i, the angle of diffraction at a particular order m is θ_m and λ is the wavelength of the light. By setting $\theta_i=\theta_m=\theta_L$, then the light is diffracted at the same angle as the incident light; this is

called the Littrow condition[103] and equation 3.1 can be rearranged to equation 3.2.

$$2d_g \sin\theta_L = m\lambda \tag{3.2}$$

For the dye laser the diffraction grating was set to the Littrow condition for 440nm, which is 15.3°. This is close to the optimum wavelength for the grating (the blaze wavelength)[104].

The approximate theoretical linewidth, $\Delta\lambda_t$, was calculated from the cavity linewidth equation (equation 3.3)[105].

$$\Delta\lambda_t = \frac{\Delta\Theta}{\left(\partial\theta_m/\partial\lambda\right)} \tag{3.3}$$

where $\Delta\Theta$ is the divergence full angle of the laser and $\left(\partial\theta_m/\partial\lambda\right)$ is the total dispersion of the system. For this dye laser the significant dispersion was from the diffraction grating; in Littrow configuration this is given by equation 3.4.

$$\frac{\partial\theta_m}{\partial\lambda} = \frac{2\tan\theta_m}{\lambda} \tag{3.4}$$

An Ophir Beamstar-V-PCI beam profiling system[106] was used to measure the spot diameter of the dye laser at the front mirror as 1.1mm, with a half angle divergence of 1.7mrad. This gives a theoretical linewidth of 2.7nm; this means that the theoretical coherence length is 72µm. This is a relatively short coherence length, but is suitable for use in an interferometer with a high quality optomechanical system.

The dye laser wavelength and linewidth was measured using an Ocean Optics USB4000 spectrometer.[107] The spectrometer used a 1200mm^{-1} grating with a blaze wavelength of 750nm. It had a slit width of 50µm with a height of 1000µm. The detector in the spectrometer was a Toshiba TCD1304AP CCD-array which had dimensions of 8µm

height by 200µm width, with 3648 pixels along the width. An optional L4 cylindrical lens was specified to focus the light from the slit with a height of 1000µm onto the pixels which had a height of 8µm. The spectrometer had a spectral wavelength range of $399 - 720$nm and a resolution of 1nm FWHM.

The edge of the dye laser beam was directed into the spectrometer so as to not saturate the detector. The software was set to an integration time of 500ms and the dye laser was set to a *PRR* of 2Hz. This meant that there was just one pulse per scan. The alignment was adjusted to give a good signal to noise ratio. The resultant Coumarin 120 dye laser spectrum is shown in figure 3.7.

From figure 3.7b the peak wavelength, λ_0, was measured to be 440nm. The linewidth, $\Delta\lambda$ at the FWHM was measured to be 2.3nm. This means that the coherence length of the Coumarin 120 dye laser is 84.2µm, as discussed in section 2.6. These figures are broadly consistent with the predicted values, especially as the linewidth is approaching the limit resolvable by the system.

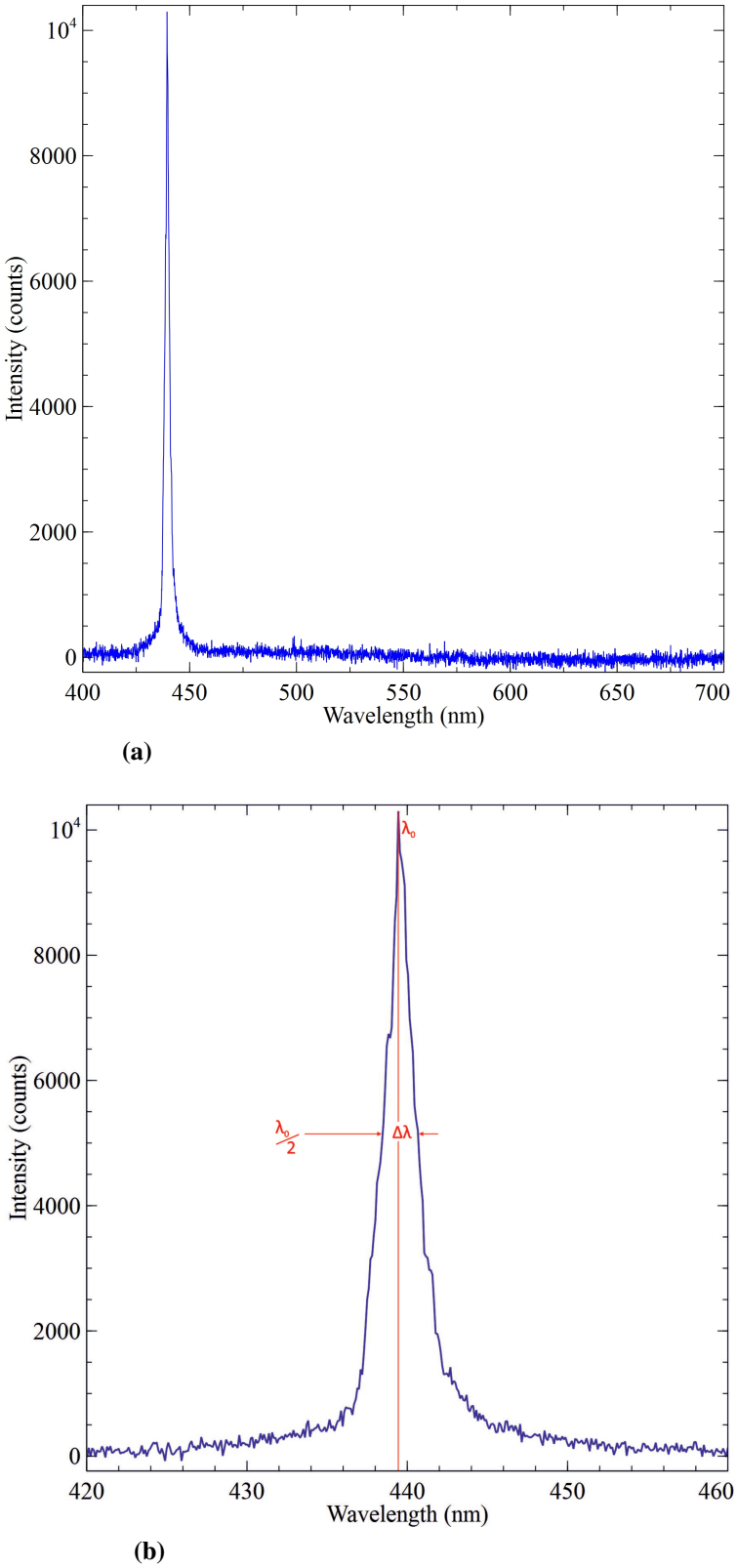

Figure 3.7: The Coumarin 120 dye laser spectrum is shown in 3.7a. In figure 3.7b the scale has been adjusted to analyse the peak. The peak wavelength is labelled as λ_0 on the graph. The linewidth, $\Delta\lambda$, is calculated at the FWHM (i.e. the width of the emission at half the intensity at λ_0).

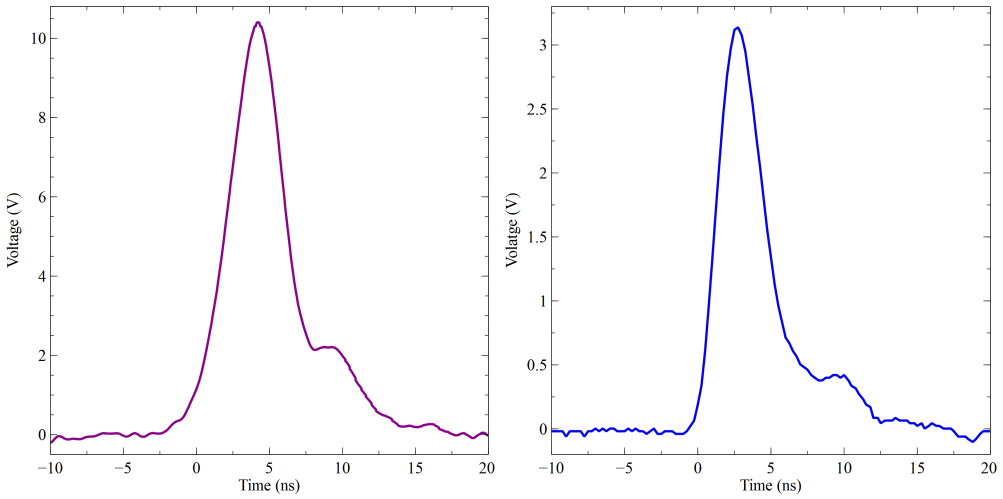

(a) XeCl laser pulse **(b)** Dye laser pulse

Figure 3.8: Plots of the pulse durations of the XeCl pump laser and the Coumarin 120 dye laser, recorded using a reverse biased FND-100Q photodiode and an oscilloscope. Note that time 0 is where the oscilloscope was triggered.

The pulse duration of the XeCl pump laser and the dye laser were measured with a reverse biased FND-100Q photodiode[108]. The photodiode has a typical junction capacitance of 8.5pF. It was coupled to the Agilent 500MHz oscilloscope with a 50Ω input impedance. In this configuration the bandwidth of the photodiode was 370MHz, which yielded a rise time of 0.9ns. It is important to note that the photodiode had a quartz window which meant that UV light would be transmitted with minimal fluorescence.

The pulse duration results are shown in figure 3.8. The pulse durations were each taken as an average of 20 samples, using the oscilloscope. The XeCl laser had a pulse duration of 4.4 ± 0.1ns. The Coumarin 120 dye laser has a pulse duration of 3.6 ± 0.2ns, which is defined as τ_{exp}. These are FWHM values for the pulse. It can be seen that the XeCl laser has a slight 'tail' on the end of the pulse, which is propagated through to the dye laser pulse; however the intensity is much lower than the primary pulse.

3.4 Conclusions

RF CO_2 laser

The RF CO_2 laser wavelength was measured to be primarily 10.59μm, with a smaller emission at 10.61μm. For the purposes of this thesis this wavelength will be referred to as 10.59μm as this is the strongest output and is the expected wavelength for an RF CO_2 laser in industry.

The pulse timings for the RF CO_2 laser have been recorded, and are presented in table 3.2.

Table 3.2: A table of the RF CO_2 laser parameters quantified in this chapter.

	Mean	Uncertainty
RF CO_2 laser wavelength (μm)	10.59	–
Delay between TTL and laser, Δt (μs)	41.5	1.2
RF CO_2 laser duration, τ (μs)	1012	2.6
TTL duration (RF CO_2 laser input), τ' (μs)	1040.8	0.06

Table 3.2 shows that the variation in the output from the TTL pulse generator is very small and is $<$ 60ns. The pulse generator was set to a pulse duration of 1040.8 ± 0.06μs throughout the experiments presented in this thesis. The laser output using this input was 1.012ms which is the value which will be used in calculations, however this will be referred to as a '1ms' pulse in this thesis. The delay between the TTL input and the laser output was also recorded; this was important because it would be used to determine how long the laser had been interacting with the material during time resolved experiments.

Dye laser

Table 3.3: A table of the parameters measured for the Coumarin 120 dye laser pumped with a 308nm XeCl excimer laser.

	Mean	Uncertainty
Dye laser peak wavelength, λ_0 (nm)	440	-
Dye laser linewidth, $\Delta\lambda$ (nm)	3.6	-
Coherence length of dye laser (μm)	84.2	-
Dye laser pulse duration, τ_{exp} (ns)	3.6	0.2
Dye laser divergence, $\Delta\Theta$ (mrad)	3.4	-

Table 3.3 shows the parameters for the dye laser which have been measured in this chapter. The linewidth was measured to be 2.3nm with a peak wavelength of 440nm, resulting in a coherence length of the of 84.2μm; these show good agreement with the predicted values. The coherence length is relatively short, and when setting up a Michelson interfereometer the distance between each mirror and the beamsplitter must be each be within half this distance of each other in order to observe fringes; this is achieveable with good quality optical mounts. The peak wavelength is in the visible spectrum, therefore it is suitable for both visual observations (indirect), and observations using a standard camera sensor. The pulse duration defines the effective exposure of a fast imaging system and here this is many orders of magnitude higher than the shutter duration of a typical camera or its flashgun. This means that objects travelling quickly can be captured with no blurring, as is discussed further in chapter 6.

Chapter 4

Material Characterisation

4.1 Introduction

In this thesis it has been chosen to focus on a carbon/epoxy composite sheet material (referred to as CFRP), with a thickness of 0.25mm (tolerance of $\pm 20\%$) supplied by Goodfellow Cambridge Limited, part no. C 423025.[109] The composite consisted of Toray Industries Inc.[57] T300 carbon fibre in a bi-directional plain weave, with a 'tow' size of 3K, i.e. 3000 fibres within each tow; the tows are the groups which are woven. The weave is encapsulated within a matrix of PRF Composites' RS-M135 epoxy resin system, represented in figure 4.1. The carbon fibre to epoxy resin volume fraction was 50%.[109] T300 is Toray's baseline carbon fibre for aerospace applications, and is a PAN based fibre.[57] The RS-M135 resin is an ultra-low viscosity, bisphenol based, laminating, epoxy system, formulated for use in manufacturing various composite materials.[110]

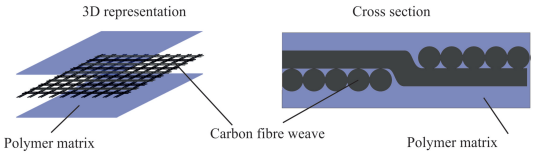

Figure 4.1: A representation of a simple carbon fibre plain weave, with just one layer of fibres. In reality each group of fibres here would be a 'tow' of many hundreds or thousands of fibres.

To study the material fully, in addition to the sheets of the carbon/epoxy composite, separate sheets of T300 carbon weave (Goodfellow part no. C 003531) were obtained, and also PRF Composites generously supplied a sample quantity of the three part RS-M135 epoxy resin system so that various samples for experimentation could be created.

This work presented in this thesis uses an RF CO_2 laser at a wavelength of 10.59μm. In order to describe how the light couples into the material the optical properties were required, such as the absorption coefficient and reflectivity at 10.59μm. Due to the low photon energy of the infra-red light, photothermal decomposition is likely when the materials are laser processed, as opposed to photochemical decomposition. In order to analyse the thermal decomposition, the thermal properties of the materials were required, such as the activation energy for thermal decomposition, specific heat capacity and thermal conductivity.

The thermal and optical properties for the T300 carbon fibre are well documented in literature, so most of the properties relevant to this thesis could be found. The RS-M135 epoxy resin system's documentation primarily covers the mechanical properties and mixing/casting techniques relevant to specifying a resin for a specific application. The experiments presented in this chapter were required to obtain the thermal and optical properties of the resin.

In this chapter the sample preparation is discussed first. This consists of mixing, casting and polishing pure RS-M135 epoxy resin disks, and comparison of the surface of this epoxy with the surface of the CFRP. The preparation of sheets of pre-made CFRP and T300 carbon fibres into manageable samples is also explained. Then, techniques to measure the activation energy for thermal decomposition, specific heat capacity, thermal conductivity, reflectivity and the optical absorption coefficient for the RS-M135 epoxy resin system are presented. These are then compared to referenced values where available.

4.2 Sample preparation and analysis

The carbon/epoxy composite sheet is thin enough that it can be cut easily with shears or scissors. The T300 weave can also be cut easily; however, due to the lack of a matrix, it will fall apart if it is not secured at the edges. In order to maintain the shape and structure of the weave pattern, sample areas were marked out with thin strips of adhesive insulation tape. The samples could then be cut along these strips. This gave the sections of fibre weave a border of tape which held them together. The CFRP and carbon fibre weave samples were then attached to microscope slides to avoid contamination and to keep them flat. This was particularly important for the fibre weave as it was not rigid. This also allowed the samples to be labelled and handled easily.

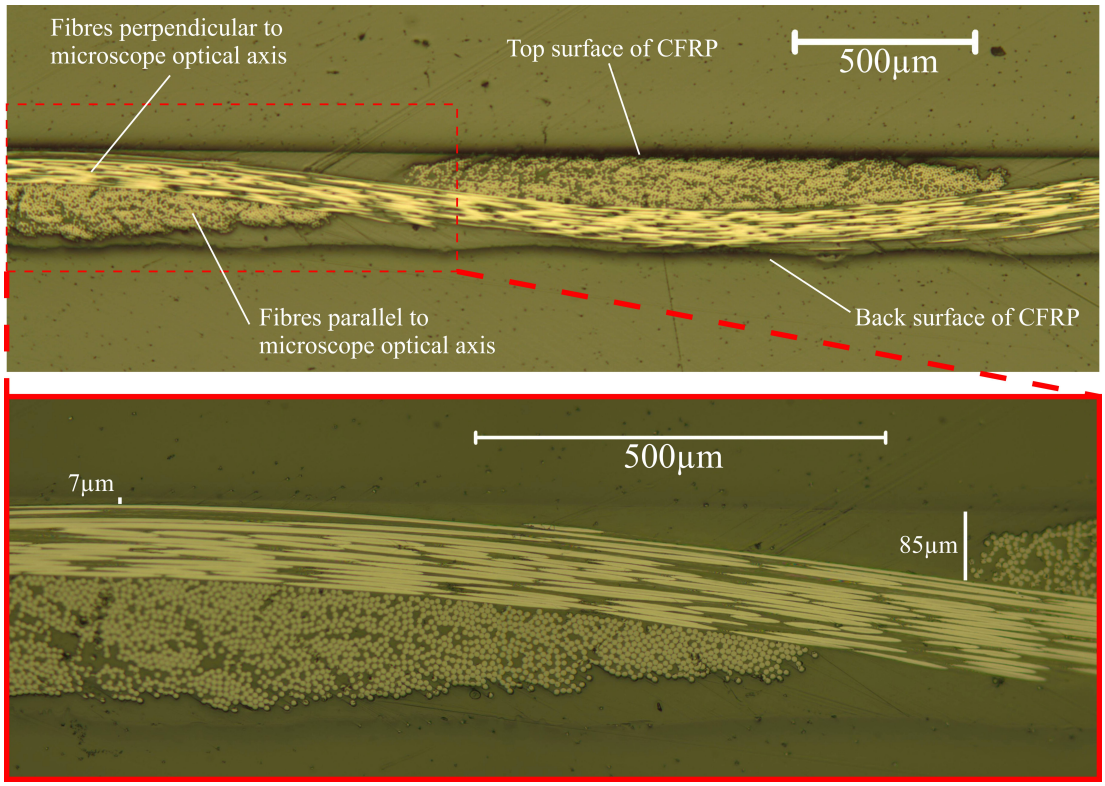

Figure 4.2: Micrographs of the cross sections of CFRP potted in an epoxy resin at magnifications of 50× and 200×. The top and back faces of the sample can seen along with the two directions of the carbon fibres in the plain weave (also known as the warp and weft). The variation in epoxy thickness on top of the fibres is clearly visible and two measurements of this thickness at different points are shown.

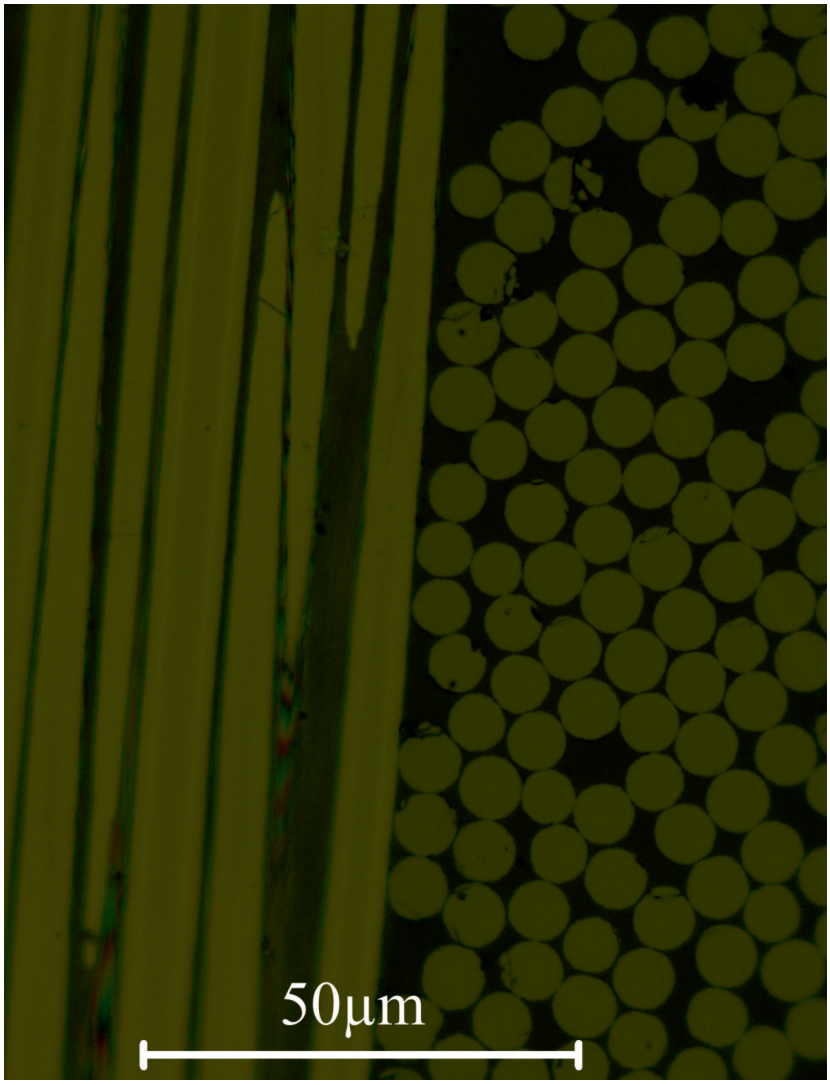

Figure 4.3: A micrograph of the cross section of CFRP with a magnification of 1000×. The epoxy between the fibres can clearly be seen, and the spacing between the fibres varies. The fibres can also be measured as $6.5 - 7.1$µm, as expected from the specification.

The CFRP sheet was analysed by cutting a section and 'potting' it perpendicular to the surface of an epoxy resin. The sample was then ground flat and parallel using a P600 grit sheet on a Buehler Metaserv cross section polisher with a Motopol 12 AutoHead.[111] On the side to be examined, this was followed with a P2500 grit sheet and then a TexMet pad with a 3µm diamond paste, and then a 0.05µm alumina polishing suspension on a new pad. The polished cross section was examined under an optical microscope (figure 4.2). The micrograph clearly shows the 'shiny' top surface which is relatively flat where it has been cast against a smooth surface, and the rougher

back surface which has a 'dull' appearance. Also, the tow of fibres running perpendicular to the optical axis of the microscope which go 'over and under' the tow which is parallel to the optical axis is visible; this is expected from the warp and weft of the plain weave. The weave means that the thickness of the epoxy on top of the carbon fibres varies significantly, and can range from $7-85\mu m$ in the example shown, and has been observed to be as thick as $100\mu m$ in other parts of the sample. Elsewhere in the composite there are gaps in the fibre weave where the epoxy goes through the full thickness of the sample.

A higher magnification micrograph is displayed in figure 4.3, this shows that the epoxy is amongst both layers of fibres with no gaps between them. It can also be seen that the distribution of fibres is somewhat random, which would make the thermal conductivity perpendicular to their direction difficult to predict, as discussed in section 2.3. The diameter of the fibres were measured and they were confirmed as having a diameter between $6.5-7.1\mu m$, as expected from the specification.

The RS-M135 matrix is a three part epoxy resin system. The resin was mixed at a resin:hardener ratio of $100:30\ (\pm 1)$ by weight. The hardener used was either a fast hardener (RS-MH134), a slow hardener (RS-MH137), or a combination of both.[110] By using a combination of hardeners the pot life can be tailored to specific needs. In the composite a 70% RS-MH137 and 30% RS-MH134 mix was used giving a pot life of around 2 hours.

To make the epoxy resin samples for experimentation, the hardener ratio that was utilised in manufacturing the composite was replicated. The constituents of the epoxy resin system were mixed thoroughly in a clean glass beaker and poured into 40mm diameter circular moulds with removable bases. The mixture was then degassed in a vacuum chamber at approximately 6mbar until the bubbles on the surface of the liquid had stopped being generated from the gases in the mixture and had mostly burst. The chamber pressure was then brought up to atmospheric pressure and the samples were allowed to cure in the chamber. It was important to not degas the mixture too quickly

as it will overflow. In addition, if the pressure in the chamber is too low the epoxy will boil, which can reintroduce gases into the resin mixture.

Once the samples had fully hardened, the solid epoxy disks could be pushed out through the removable base of the mould. A release agent was not required. The discs were then polished using a rotating lapping machine. The process started by grinding the discs flat and parallel using a P1200 grit sheet with the Buehler Metaserv. The discs were then polished on one side in stages starting with a 6µm diamond paste, then a 1µm diamond paste, and finally ending with a 0.06µm colloidal silica slurry.

The surface finish of the polished epoxy disks was compared to the surface of the CFRP from Goodfellow using a Veeco WYKO 1100 optical profiling system, running Vision32 software[112]. A vertical scanning white light interferometric (VSI) technique was used to profile the surface with a 2.5× objective lens and a 1× field of view. The results are shown in figure 4.4.

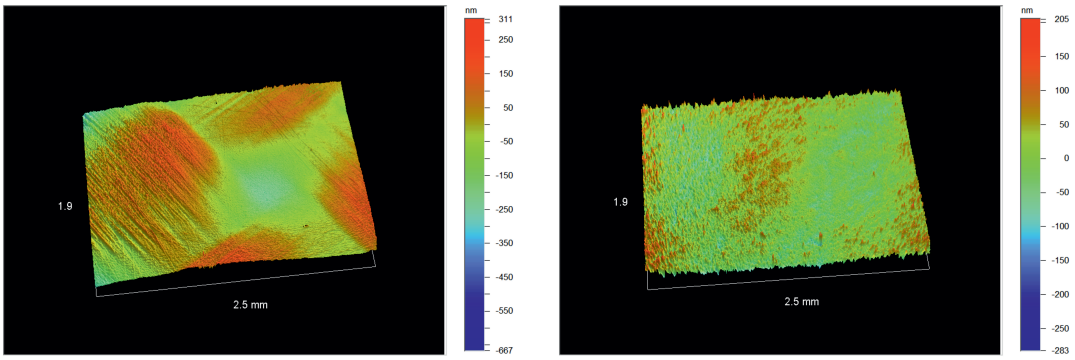

(a) **(b)**

Figure 4.4: 3D optical profiles of the surface of the CFRP from Goodfellow (4.4a) and the cast and polished epoxy resin (4.4b), profiled with a Veeco WYKO 1100 white light interferometer with a 2.5× objective lens and a 1× field of view. The surface roughnesses for these materials are shown in table 4.1.

Table 4.1: A table showing the surface roughness values measured with a Veeco WYKO 1100.

	CFRP	Epoxy
R_a (nm)	60.08	29.22
R_q (nm)	77.22	36.65

From figure 4.4b the 3D surface profile of the CFRP compared to the cast epoxy disks is shown. The surface roughness of the materials is shown in table 4.1. The surface roughness value, R_a is the average peak and trough deviation from the mean whereas R_q is the root mean square of the surface roughness. Single, large variations from the mean will affect R_q more significantly than R_a.

The two samples have visibly different finishes in figure 4.4; the surface roughness of the epoxy looks to be uniform across the sample and is likely to be due to the polishing process alone, whereas the CFRP's main surface defects are due to the influence of the carbon fibre weave. It can be seen that R_a and R_q are both are acceptably low for the two samples, with the polished epoxy being slightly less rough compared to the CFRP.

4.3 Thermo-gravimetric analysis to determine the decomposition characteristics of CFRP

Thermo-gravimetric analysis (TGA) is a technique to determine the thermal decomposition properties and the phase transition details for a material within a particular gas environment. For these experiments a Mettler Toledo TGA/DSC 1 was used. The instrument consists of a furnace with a controlled atmosphere. A sample is put into an alumina crucible which is then placed into the furnace and heated at a specific rate up to a particular temperature. The furnace can also be held isothermally for specified time periods. As the temperature program is running, the weight of the sample is recorded. The output consists of a plot of temperature and time on the x-axis and weight on the y-axis.[70]

Small sections of the samples were cut and placed into alumina crucibles and weighed; note that insulating tape was not used in preparing the T300 weave for this experiment as it would affect the result; also the fibres do not need to be held together in a weave. The CFRP and the T300 carbon fibres were analysed by TGA at a heating rate of $30\text{K}\,\text{min}^{-1}$. The results are shown in figure 4.5. These results are taken directly from the Mettler Toledo STARe thermal analysis software. The software will also give a first derivative of the curve, and this is plotted below the mass data on a common time/temperature axis. Note that the default units for temperature in the software are degrees Celsius; however, in this thesis kelvin will be used.

Figure 4.5a shows the TGA curve for T300 carbon fibres, analysed in a nitrogen atmosphere. It can be seen that there is very little weight loss up to the maximum temperature which the furnace reaches, around 1200K. This is to be expected as graphitic carbon sublimes at $3895 - 4020$K.[113] The small weight change could be due to the loss of water or other contaminants that had been adsorbed to the fibres. At higher temperatures the weight starts to decrease slightly again. This could be due to oxygen being present as adsorbed gas on the fibres therefore allowing a small amount of oxidation to take place. Examining the fibres when they have been removed from the furnace, there was no obvious evidence of any decomposition.

Figure 4.5b shows the TGA curve for T300 carbon fibres, analysed in a bottled air atmosphere. On this graph it can be seen that the fibres are decomposing from around 900K onwards. Note that the vertical ranges of the plots in figures 4.5a and 4.5b are very different; there is substantially more mass loss in figure 4.5b. This is due to oxidation from the oxygen in the bottled air. Examining the fibres when they have been removed from the furnace, the fibres have not fully decomposed, but they have broken up into fine pieces.

Figure 4.5c shows the TGA curve for the CFRP, analysed in a nitrogen atmosphere. From figures 4.5a and 4.5b, it is clear that the carbon fibre weave should not decompose significantly unless there is oxygen present. No evidence of decomposition at higher

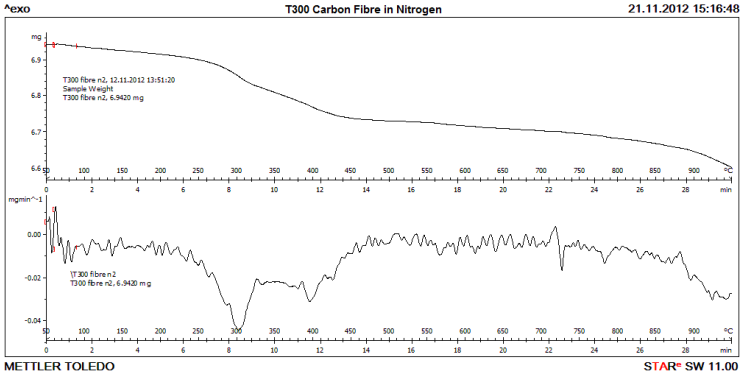

(a) T300 carbon fibres in nitrogen.

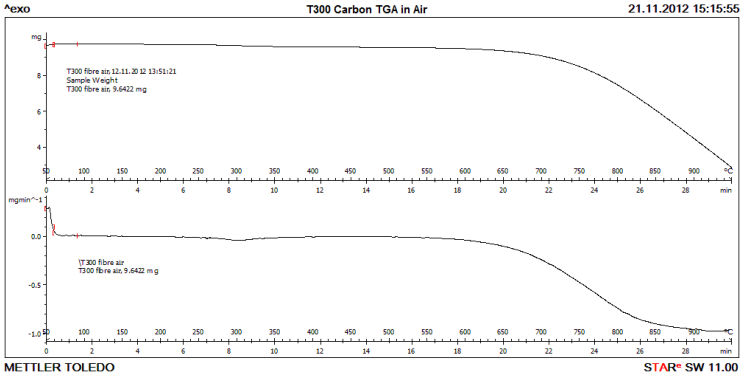

(b) T300 carbon fibres in air.

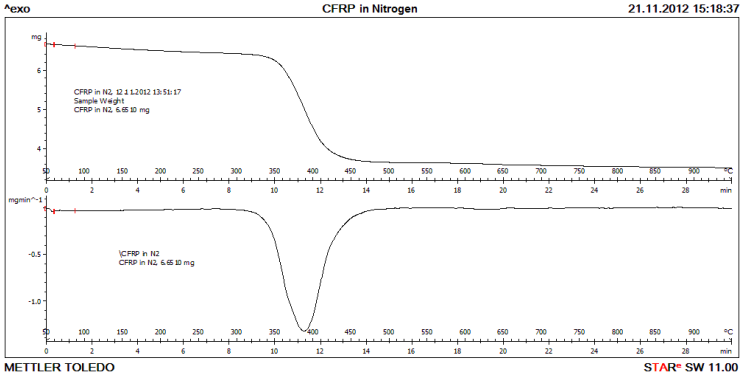

(c) CFRP in nitrogen.

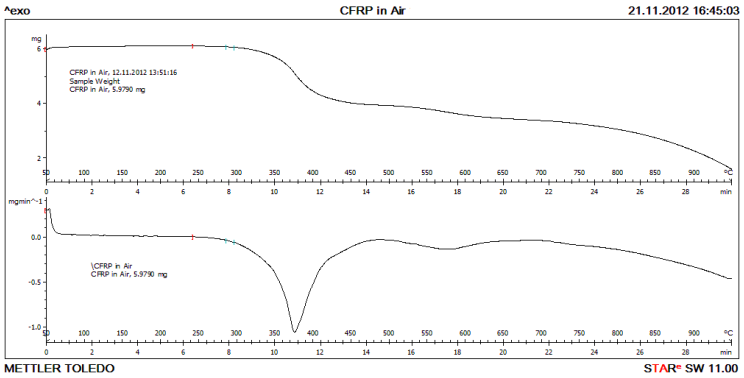

(d) CFRP in air.

Figure 4.5: Thermo-gravimetric analysis of carbon fibre composite and the T300 fibres used in its manufacture, analysed in nitrogen and air.

temperatures was observed, which would suggest that there is very little, if any, oxygen adsorbed to the fibres or encapsulated in the composite in any way. Therefore, it can be deduced that this graph is demonstrating the decomposition characteristics in nitrogen for the epoxy matrix. A significant decomposition of the epoxy which peaks between $450-470$K is clear on the graph. Examining the remains after they have been removed from the furnace, bare fibres are visible, and the sample looks identical to the bare fibres which had been heated in a nitrogen atmosphere. The weave and structure was fully intact.

Figure 4.5d shows the TGA curve for the CFRP, analysed in a bottled air atmosphere. Here the epoxy decomposition dominates the weight loss and occurs at a slightly lower temperature ($440-455$K) with the addition of the oxygen atmosphere. At higher temperatures the carbon was observed to decompose as before. This is to be expected from the previous graphs because the epoxy has fully decomposed by this point, leaving bare fibres. The remains were examined after they were removed from the furnace and the samples were found to be similar to the bare fibres decomposed in air.

4.4 Thermo-gravimetric analysis to determine the activation energy of RS-M135 epoxy resin

Thermal decomposition of polymers is a rate-limited process with an activation energy. Knowledge of this energy level allows the response of the material to various heating rates to be predicted. In this section the activation energy of the epoxy used as the matrix in the CFRP is determined. A material's activation energy, E_a, can be determined using the isoconversional method, assuming a first order reaction, as introduced by Doyle, Ozawa and Flynn & Wall.[114, 115, 116] From the Arrhenius equation, it can be shown that plotting a graph of $\log\chi$ against ${}^{1}/_{T_D}$, the gradient is:

$$gradient = \zeta\frac{E_a}{R} \tag{4.1}$$

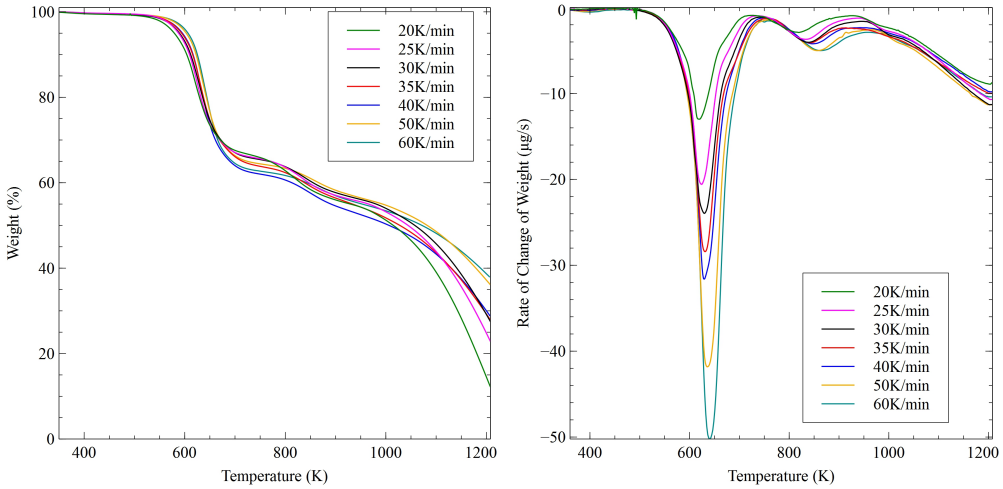

(a) A normalised TGA curve for CFRP.

(b) The first derivative of the CFRP decomposition curves.

Figure 4.6: Thermo-gravimetric analysis of carbon fibre composite at various heating rates, used to calculate the activation energy.

where χ is the heating rate ($\mathrm{K\,s^{-1}}$), E_a is the activation energy ($\mathrm{J\,mol^{-1}}$), $\overline{R}$ is the gas constant, ζ is a constant to be determined and T_D is the decomposition temperature (K) at a particular degree of decomposition.

The carbon fibre composite sheet was cut into small uniform sections and placed into alumina crucibles. TGA was performed at various heating rates. Normalised curves are shown in figure 4.6a and the derivative of the curves is shown in figure 4.6b.

The composite was chosen over the cast epoxy for this analysis because it was easier to get small, uniform samples for the decomposition. Because the sample is a composite, it is necessary to extract the data which relates to the epoxy resin in order to determine its activation energy. From figure 4.6b the temperature where the first significant decomposition occurs is clear. Comparing this graph with the results in section 4.3, it can be deduced that this is the epoxy decomposition. This allowed a plot of the fractional mass remaining, $(1-\gamma)$, against temperature to be made (figure 4.7). It can be seen that γ represents the fractional degree of decomposition.

A graph of $\log \chi$ against $1/T_D$ can then be plotted for a particular degree of decomposi-

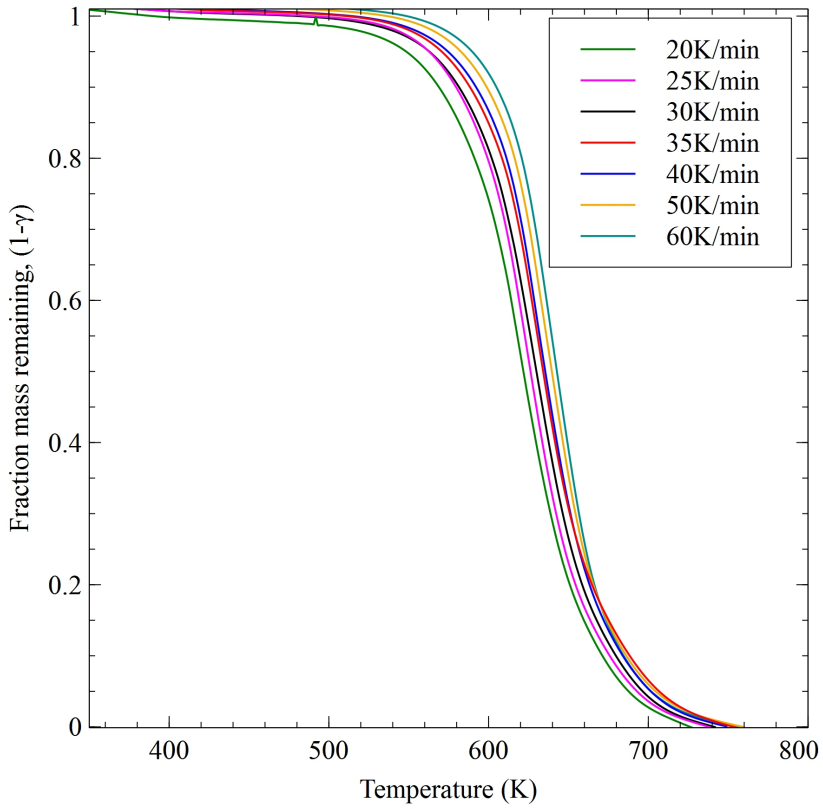

Figure 4.7: A graph of the fractional mass of epoxy in a CFRP remaining against temperature for decomposition at various heating rates, extracted from figure 4.6.

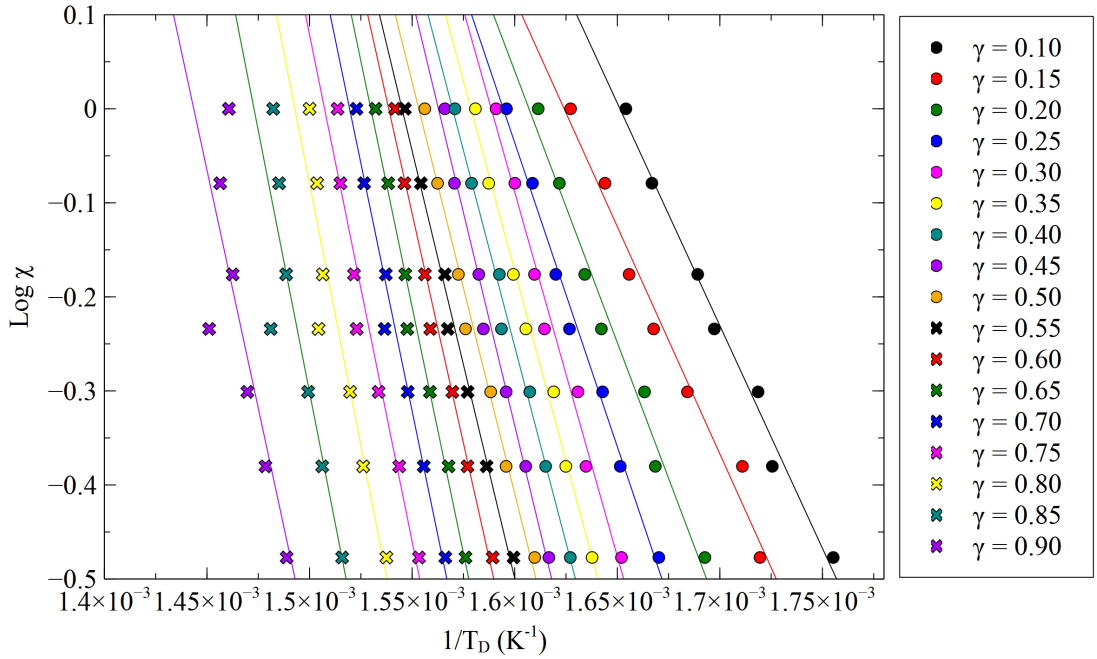

Figure 4.8: Plots of $\log \chi$ against $1/T_D$ with T_D determined at various degrees of decomposition, γ.

tion. Graphs have been plotted for values of γ between 0.1 and 0.9 in figure 4.8.

Once the gradient is determined from figure 4.8, equation 4.1 can be used to calculate E_a at that particular value of γ. The constant to be determined, ζ, arises from the simplification of a temperature integral. A standard value of ζ was proposed by Doyle[114], assuming the it is the same for all values of $E_a/\bar{R}T_D$, though it can deviate significantly from this, particularly at small values of $E_a/\bar{R}T_D$. However, a correction factor can be applied by using an iterative technique. The standard value of ζ is tried, and the value of $E_a/\bar{R}T_D$ is calculated using it. A lookup table[117, 116] is then used based on $E_a/\bar{R}T_D$ and a new value of ζ is obtained from it. This process continues until the value of ζ does not change.

E_a can then be plotted against γ (figure 4.9). From this it is seen that there is a plateau region between $\gamma = 0.3$ and $\gamma = 0.6$, where E_a has the same average value as an average of all of the values shown. The uncertainty was calculated from the plateau region. The average value of E_a has been estimated in this way to be $156 \pm 13 \text{kJ mol}^{-1}$. It can be seen on figure 4.9 that the average activation energy is around the value which was calculated for 50% decomposition. This is also around the region of peak decomposition

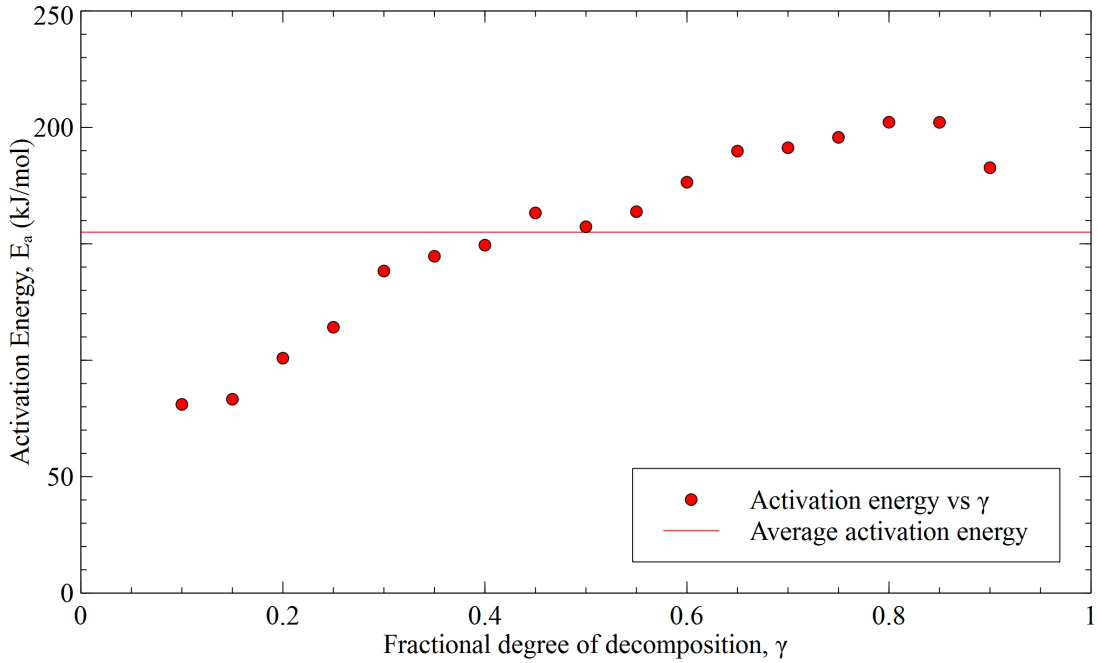

Figure 4.9: A graph showing the activation energy against fractional degree of decomposition. The average activation energy is also shown.

seen in figure 4.6b.

4.5 Differential scanning calorimetry to determine the specific heat capacity of the materials

Differential scanning calorimetry (DSC) is a technique which measures the differential heat flow in and out of a sample, relative to a reference material, with respect to its temperature. This allows us to determine the heat required to change the temperature of a sample and calculate its specific heat capacity, c_P ($\mathrm{J\,kg^{-1}\,K^{-1}}$). The technique can also be used to characterise the materials in other ways, such as locating glass transition temperatures. The system has a chamber with a purge gas inlet and a heated disk with thermal contacts for two aluminium pans to sit upon. The temperatures of the pans are monitored by two thermocouples. The differential heat flow can be measured because it is directly proportional to differences in the output from the two thermocouple junctions.[70]

The specific heat capacity for the epoxy was measured by DSC using a Mettler Toledo TGA/DSC 1 with a DSC-30 heat flux calorimeter controlled by a Mettler TC15 thermal analysis controller running STARe software. The epoxy resin was mixed as in section 4.2, then degassed and directly cast in aluminium DSC pans. A DSC analysis was run with a heating rate of $10\,\mathrm{K\,min^{-1}}$ from 273K to 523K. These values were chosen because it was appropriate to calculate c_p from room temperature (300K), and the system takes some time to settle, so it is better to start the process below the temperature of interest. The upper limit of 523K was set to avoid decomposing the material inside the DSC, while measuring as wide a range as possible. No purge gas was present. Heat flow graphs for weighed samples of epoxy were obtained in addition to various metals used as reference materials, (figure 4.10).

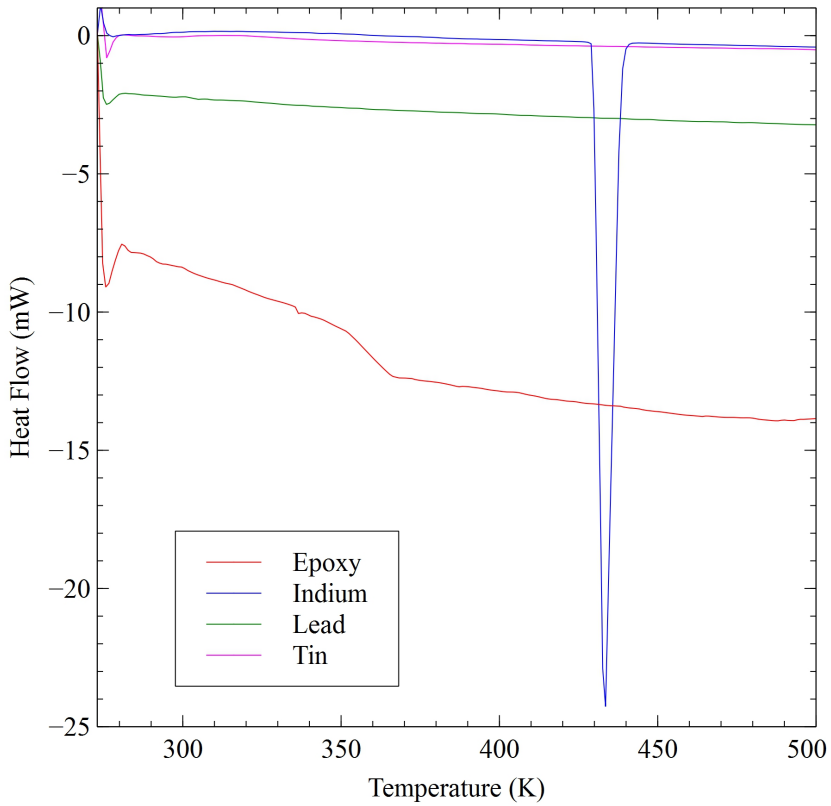

Figure 4.10: DSC traces for weighed samples of epoxy and three reference metals, measured using a Mettler Toledo TGA/DSC 1.

Figure 4.10 shows the heat flow curves for RS-M135 epoxy resin. The endotherm in the graph at 360K is the glass transition. The graph also also shows indium, tin and lead, which are used as reference samples. These were chosen as references because

they have relatively consistent specific heat capacities over the temperature range of interest and are well documented in literature.[118] The melting point of indium at $430-440$K can clearly be seen in the graph.

Equation 4.2 shows that the specific heat capacity with respect to temperature, $c_P(T)$, is equal to the heat flow, $^{dQ}/_{dt}$ (W), divided by the heating rate, $^{dT}/_{dt}$ (K s^{-1}), and the sample mass, m_s (kg). A calibration function $G(T)$ is required and is determined from the reference samples using their documented heat capacities. It should be noted that $G(T)$ is a temperature dependent function, so will change over the measured temperature range.

$$c_P(T) = \frac{^{dQ}/_{dt}}{^{dT}/_{dt} \cdot m_s} G(T) \tag{4.2}$$

A value for $G(T)$ was calculated for each of the 3 reference metals by inserting their specific heat capacity and values from figure 4.10 into equation 4.2. Values of $G(T)$ were then calculated at small temperature intervals for each of the metals being used as a reference. The average value of $G(T)$ was then calculated for each interval. This function was then used with the heat flow graph for the epoxy resin to calculate the specific heat capacity at particular temperatures in small steps across the range, (figure 4.11).

Figure 4.11 shows that at room temperature the specific heat capacity of the epoxy is around 1450J kg^{-1} K^{-1}. At 400K the specific heat capacity has increased to around 2000J kg^{-1} K^{-1}. It should be noted that the specific heat capacity has not been calculated for the region around the melting point of indium as $G(T)$ cannot be calculated here.

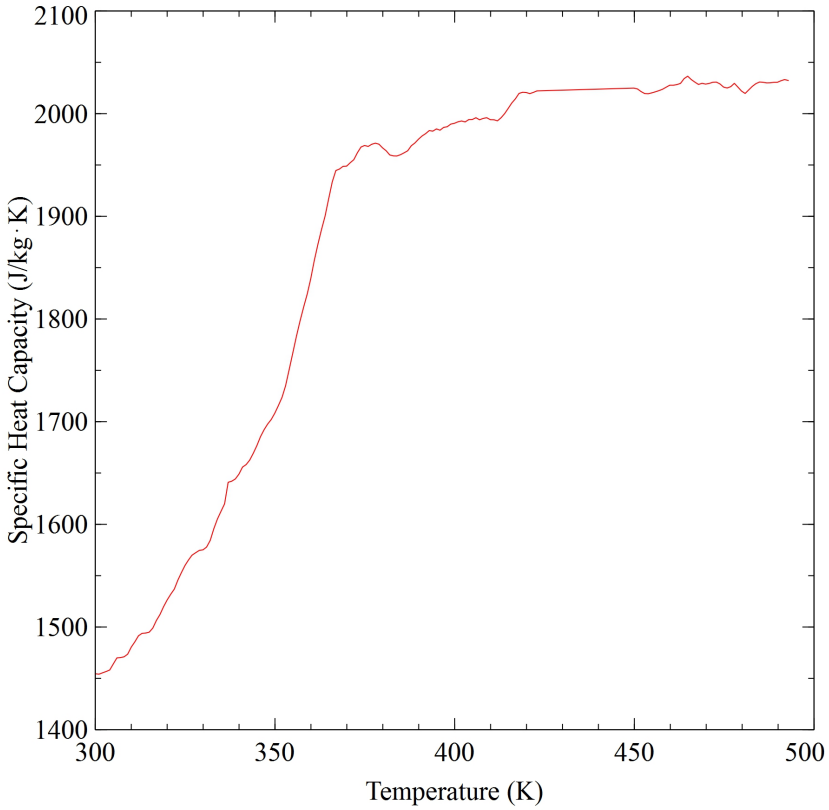

Figure 4.11: A graph of the specific heat capacity against temperature for RS-M135 epoxy resin.

4.6 Lees' disc method to determine the thermal conductivity of the samples

The thermal conductivity of a cast pellet of epoxy was measured using the Lees' disc method; this method is suitable for materials with a low thermal conductivity.[119] The experimental setup is shown in figure 4.12. The apparatus consists of 3 copper discs, (A, B and C), a copper heater disc element and an epoxy disc, all of which have the same diameter. The disks were setup in the arrangement shown and clamped by 2 small insulating pads. The temperatures of the copper disks were monitored by thermocouples linked to data logging software. The current drawn by the heating disk, I, at a particular voltage, V, was monitored, which means that the power being delivered to the system could be calculated simply as $V \times I$.

If the system is heated at a particular power using the heater disk, heat will be con-

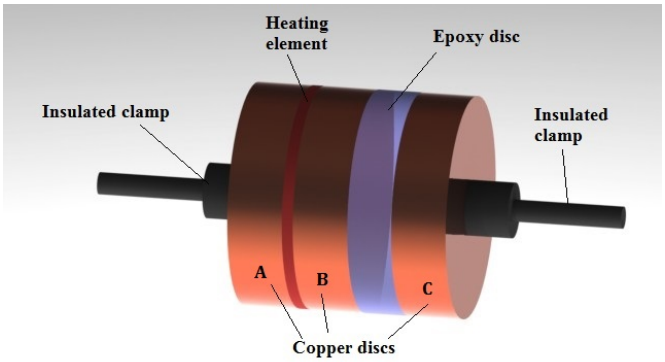

Figure 4.12: Experimental setup for Lees' disks method of determining the thermal conductivity of a material.

ducted to discs A & B. The heat in disc B will conduct through the epoxy sample to disc C. Due to Newton's law of cooling[120], the heat loss from the copper discs is proportional to the temperature difference between the disks and their surroundings. The system will reach a steady state temperature when the power into the system is equal to the power losses to the environment due to convection and radiation from the heater disc and the 3 copper discs. It is assumed that there is no heat loss from the edges of the sample and no heat loss from the wires to the heater. From this, when the system is at equilibrium, equation 4.3 can be written.

$$V \cdot I = \xi [A_A(T_A - T_0) + A_B(T_B - T_0) + A_C(T_C - T_0) + A_H(T_H - T_0)] \tag{4.3}$$

where A_A, A_B & A_C are the surface areas exposed to the environment of copper disks A, B & C (m^2), T_A, T_B & T_C are the temperatures of copper discs A, B and C (K), T_0 is the ambient temperature in the room measured with a thermometer (K), A_H is the area exposed to the environment for the heater disc (m^2) and T_H is the temperature of the heater disc (K). Equation 4.3 can then be used to calculate ξ, the heat transfer coefficient ($W\,m^{-2}\,K^{-1}$).

Equation 4.4 is Fourier's 1-D law of heat conduction.[121, 122, 123]

$$\frac{dQ}{dt} = -K \cdot A \frac{dT}{dx} \tag{4.4}$$

where $^{dQ}/_{dt}$ is the heat flow through the epoxy sample (W) which has cross sectional area A (m^2), the temperature gradient across the epoxy is $^{dT}/_{dx}$ ($K\,m^{-1}$) and K is the thermal conductivity ($W\,m^{-1}\,K^{-1}$). The can be rewritten as:

$$\xi \cdot A_C(T_C - T_0) = K \cdot A\frac{(T_B - T_C)}{d} \tag{4.5}$$

where d is the thickness of the epoxy sample disk (m), measured with a micrometer in several places across the surface.

Using the measured value for ξ and the values from the equilibrium state, the thermal conductivity of the RS-M135 epoxy resin was measured as $0.20 \pm 0.03 W\,m^{-1}\,K^{-1}$.

4.7 Determination of the reflectance of CFRP and its constituents

A Fourier transform infra-red spectrometer (FT-IR)[70] is a device which directs a wide spectrum of mid infra-red light through a chamber and onto a detector at the other side. It then uses a Fourier transform to convert the collected data to a spectrum. A Thermo-Nicolet NEXUS 670 FT-IR[124] was used with a Perkin-Elmer variable angle specular reflectance accessory[125] to measure the reflectance of the samples. The specular reflectance accessory diverts the path of the infra-red light off two mirrors and onto the surface of the sample to be analysed. The specular reflectance from the sample is then directed back to its original path and onto the detector of the FT-IR via another two mirrors. The angle of incidence onto the sample can be adjusted between 20° and 80° to the normal, see figure 4.13.

The instrument was used to measure the reflectance of the surface of the CFRP, the cast epoxy disks and the bare carbon fibre weave. The surface roughness for the CFRP and cast epoxy disks was very low as discussed in section 4.2, which meant that the

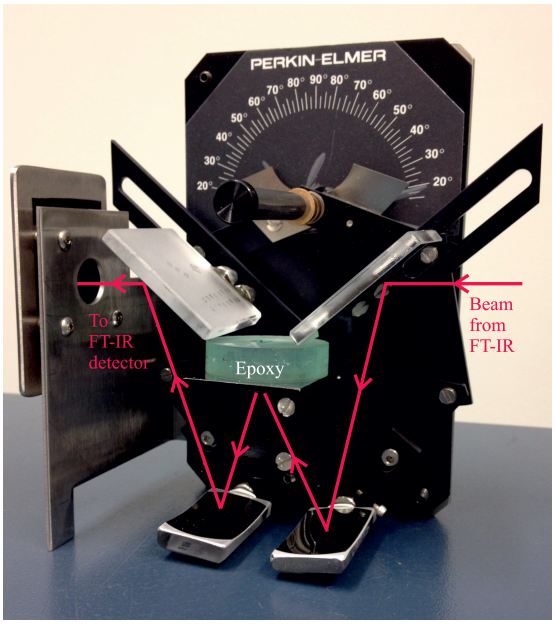

Figure 4.13: A Perkin-Elmer variable angle specular reflectance accessory to be used on a Thermo-Nicolet NEXUS 670 FT-IR. The line shows the path of the infra-red beam being directed onto the surface of the sample to be analysed at a particular angle of incidence (20° shown), and then back to its original path to the detector.

reflections would be specular with little scattering. An angle of 20° on the specular reflectance accessory was used for the measurements, as according to the Fresnel equations[87] it can be assumed that it deviates little from a normal reflectance spectrum. An Al mirror was used as a background reference and was taken to be a uniform reflector across the mid to far infra-red spectrum.[126, 127] The samples used were big enough to fill the full diameter of the infra-red beam. Figure 4.14 shows average reflectance spectra for the CFRP and carbon fibre weave samples, and also for the cast epoxy discs. The CFRP and the carbon fibre weave results were taken twice and an average spectrum was calculated. Four epoxy discs were cast and polished, so that the average spectrum of the four is shown.

From figure 4.14 it can be seen that the thick cast epoxy samples have a very similar reflectance spectrum to the composite. In general, the reflectivity of the CFRP is slightly higher. This could be due to a contribution to the reflectivity from the carbon weave in the areas where the epoxy is very thin; it is shown later in section 4.8 that the thick-

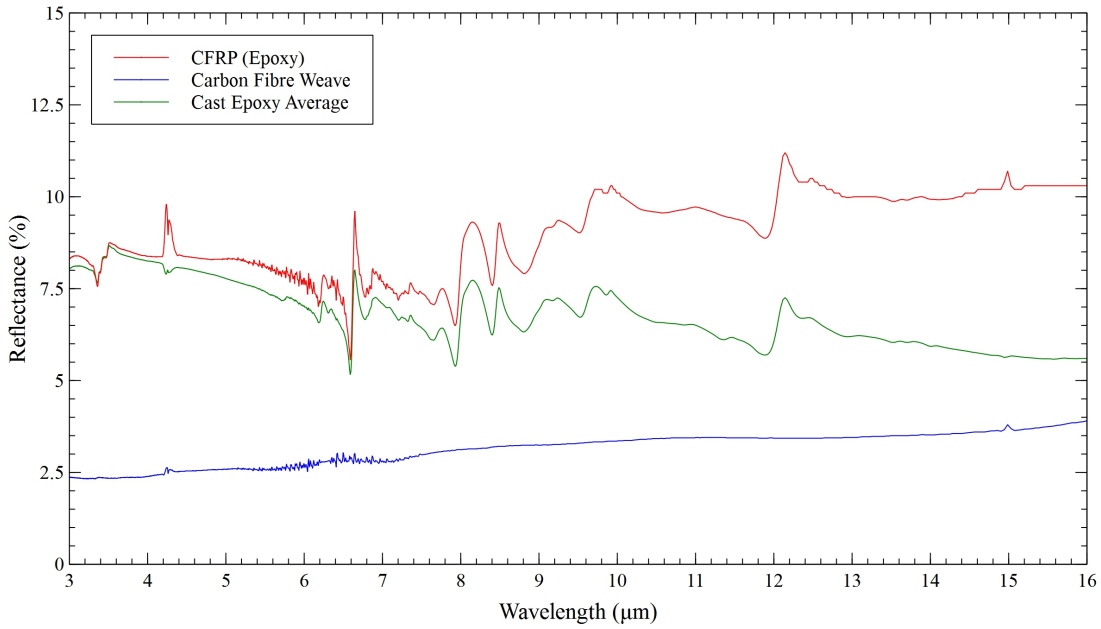

Figure 4.14: An FT-IR reflectance spectrum for cast epoxy, CFRP and carbon fibre weave at a 20° angle of incidence.

Table 4.2: A table of the optical properties of graphite at 10.59μm.[128] The complex refractive index of the ordinary ray is $\tilde{n_o} = n_o - ik_o$, the complex refractive index of the extraordinary ray is $\tilde{n_e} = n_e - ik_e$.

	n	k
Ordinary ray (n_o,k_o)	6.96	7.38
Extraordinary ray (n_e,k_e)	2.399	3.00×10^{-5}

ness of the epoxy above the fibres is thinner in places than the absorption depth for a wavelength of 10.59μm. The variation between the samples was taken into account when calculating uncertainties. The reflectivity for epoxy at a wavelength 10.59μm was $8.0 \pm 1.5\%$.

The reflectivity of the carbon fibre weave at a wavelength 10.59μm was $3.4 \pm 0.1\%$; however, the sample has gaps in the weave and some of the reflections will not reach the sensor due to the cylindrical nature of the fibres, so this measurement is not an accurate representation. The properties of graphite are well defined (table 4.2)[128], and the reflectivity for a fibre has been demonstrated in literature[129] by using equations for reflectance in uniaxial crystals.[130] The T300 fibre is a PAN fibre, thus it can be

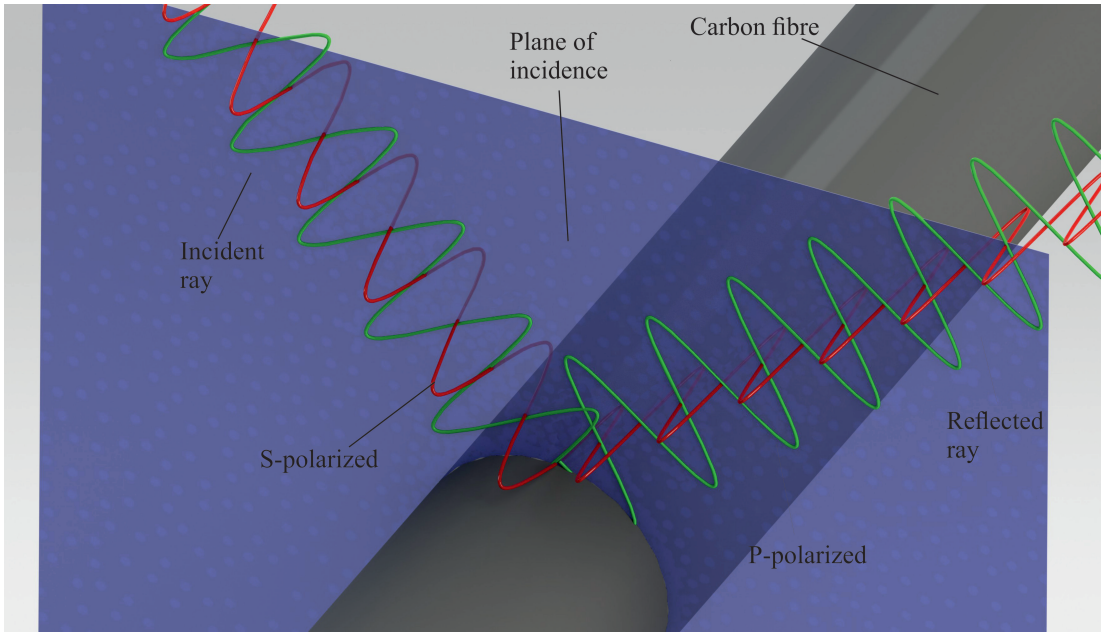

Figure 4.15: A diagram showing the plane of incidence (blue) of light incident on a carbon fibre. The polarization of the red wave is parallel to the direction of the fibres, however it is perpendicular to the plane of incidence, and therefore s-polarized. The polarization of the green wave is perpendicular to the direction of the fibres, but parallel to the plane of incidence, and therefore p-polarized.

treated as concentric rings of graphite when observed in cross section[129, 131, 52], so light incident at a point on the fibre is equivalent to being incident on a basal plane at a particular angle. In this situation the optic axis of the graphite (normal to the surface of a basal plane) lies in the plane of incidence of the light, and the polarization with respect to the plane of incidence is the same as the polarization with respect to the basal plane; thus formulae for r_{ss} and r_{pp} can be written, which are the amplitude reflection coefficients for s and p-polarized light respectively in this configuration (equations 4.6 and 4.7).[130] It should be noted that when the direction of the fibres is perpendicular to the polarization, the incident light on the fibres is p-polarized, and when the direction of the fibres is parallel to the polarization, the incident light is s-polarized (figure 4.15).

$$r_{ss} = \frac{n_1 \cos\theta_i - \tilde{n_o}\sqrt{1-(\frac{n_1}{\tilde{n_o}}\sin\theta_i)^2}}{n_1 \cos\theta_i + \tilde{n_o}\sqrt{1-(\frac{n_1}{\tilde{n_o}}\sin\theta_i)^2}} \tag{4.6}$$

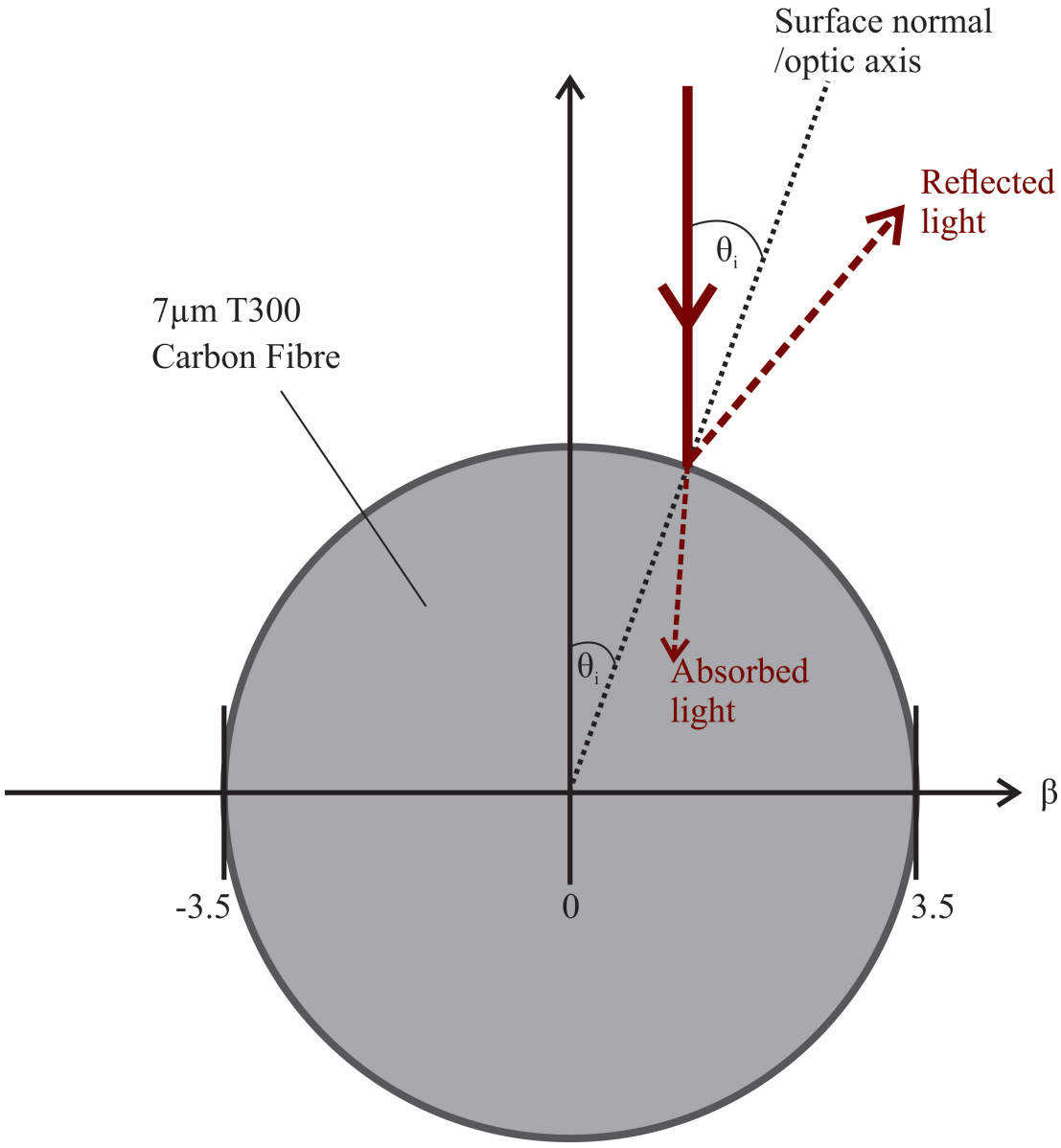

Figure 4.16: A diagram representing the angle of incidence, θ_i of a ray of light onto a carbon fibre, with respect to the radial co-ordinate, β.

$$r_{pp} = \frac{\frac{\sqrt{1-(\frac{n_1}{\tilde{n_e}}\sin\theta_i)^2}}{\tilde{n_o}} - (\frac{\cos\theta_i}{n_1})}{\frac{\sqrt{1-(\frac{n_1}{\tilde{n_e}}\sin\theta_i)^2}}{\tilde{n_o}} + (\frac{\cos\theta_i}{n_1})} \tag{4.7}$$

where n_1 is the refractive index of air, $\tilde{n_o} = n_o - ik_o$ is the complex refractive index for the ordinary ray, $\tilde{n_e} = n_e - ik_e$ is the complex refractive index for the extraordinary ray and θ_i is the angle of incidence on the fibre. This means for s and p-polarized light the reflectance from the fibres (R_s and R_p) at a particular angle of incidence can be calculated with equations 4.8 and 4.9 respectively.

$$R_s = |r_{ss}|^2 \tag{4.8}$$

$$R_p = |r_{pp}|^2 \tag{4.9}$$

A cross section of a 7µm diameter carbon fibre is shown in figure 4.16. From this diagram it can be written that $\theta_i = \arcsin(\beta/\beta_f)$, where β is the radial co-ordinate and β_f is the fibre radius. Using this with equations 4.8 and 4.9, and the data in table 4.2 the fibre reflectivity for the polarization with respect to the fibre direction has been plotted in figure 4.17a. The light absorbed by the fibre when the polarization is parallel, $(1-R_s)$, and the light absorbed when the polarization is perpendicular to the fibres, $(1-R_p)$, is plotted in figure 4.17b.

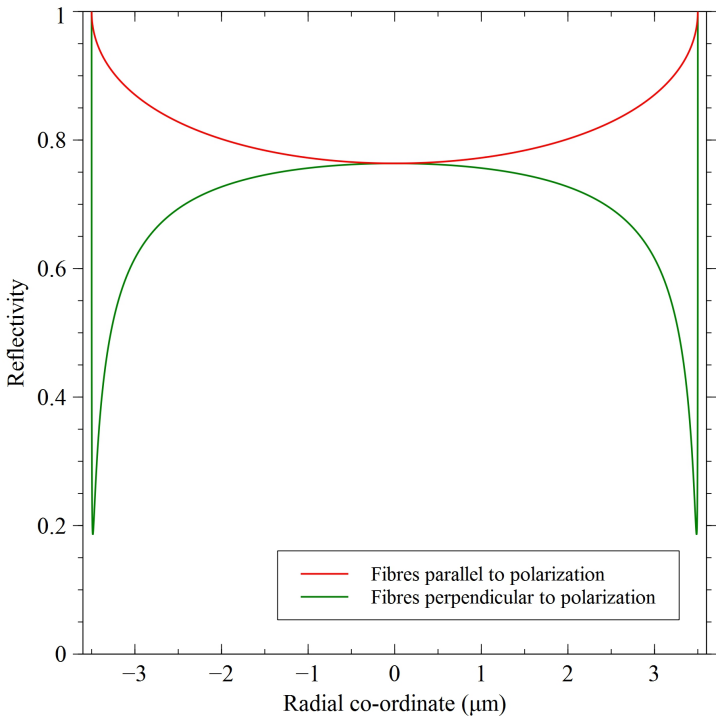

(a) Reflectivity plot

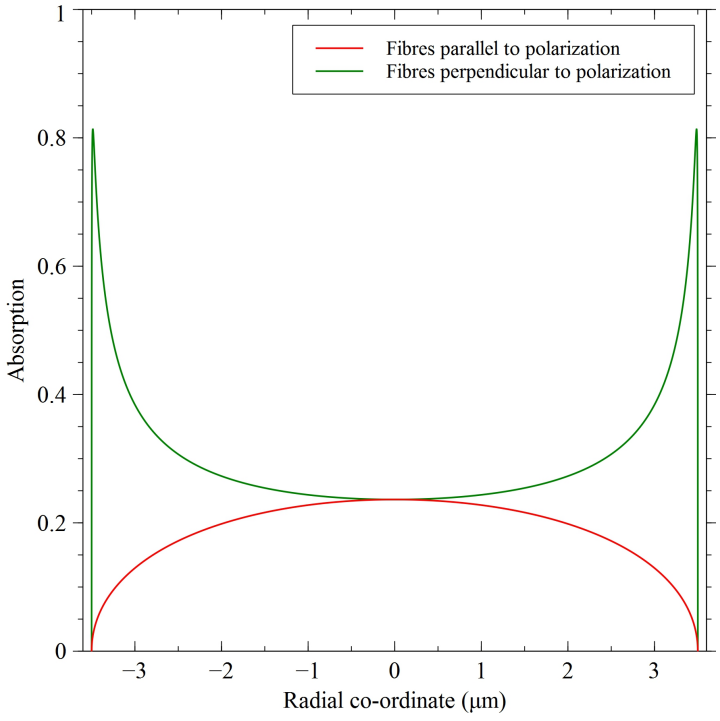

(b) Absorption plot

Figure 4.17: Plots of the reflectivity and absorption with respect to the radial coordinate for 10.59μm light incident on T300 carbon fibres, for polarization parallel and perpendicular to the fibre direction.

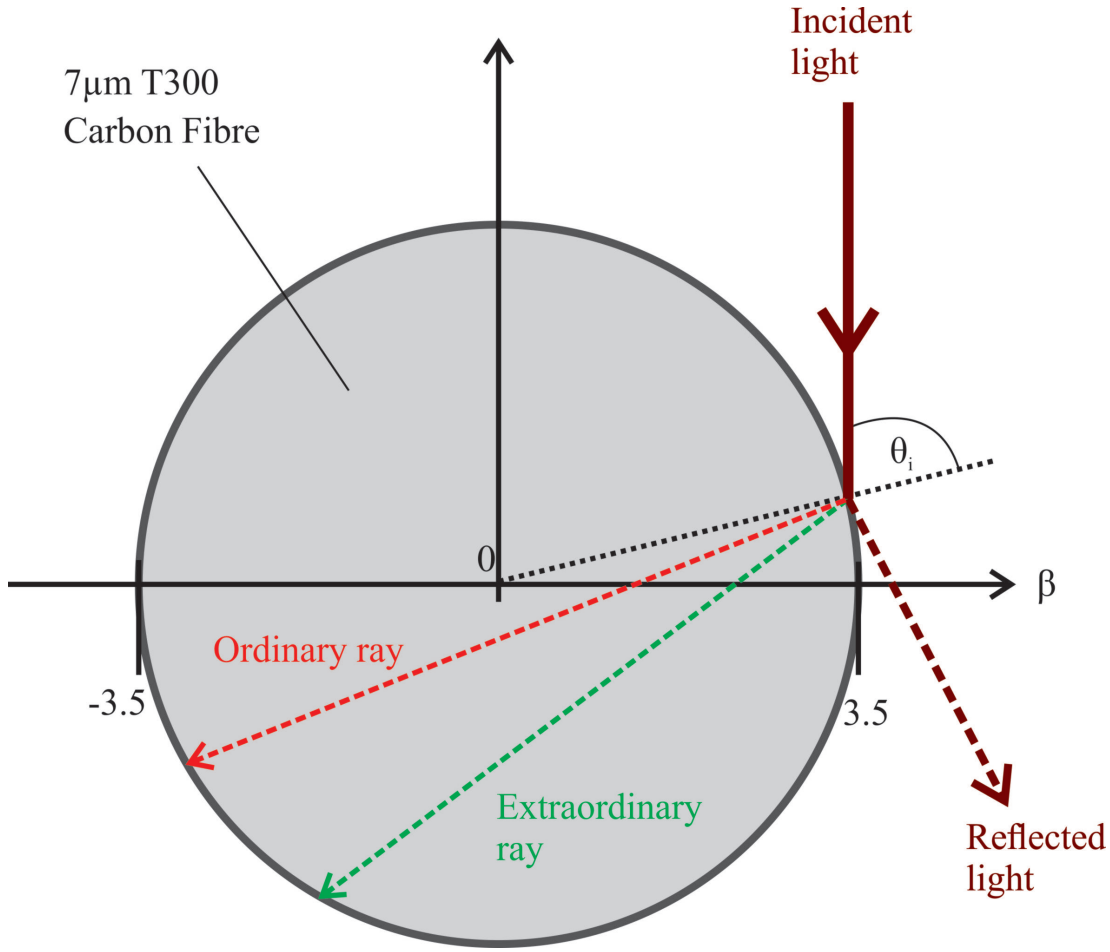

Figure 4.18: The path of light through a fibre for a large angle of incidence (i.e. close to the edge of the fibre) for the ordinary and extraordinary rays. Angles shown in the figure are to scale.

It has been assumed that any light which is not reflected by the carbon fibre will be absorbed, which can be justified by calculating the path length of the light through the fibre (from air with a refractive index of unity). The angle of refraction, θ_r, for a material exhibiting absorption (i.e. having a complex refractive index) is given by equation 4.10.[132]

$$\sin\theta_r = \frac{\sqrt{2}\sin\theta_i}{\sqrt{n^2+k^2+\sin^2\theta_i+\sqrt{(n^2-k^2-\sin^2\theta_i)^2+4n^2k^2}}} \tag{4.10}$$

where θ_i is the angle of incidence, and n and k are the real and imaginary components

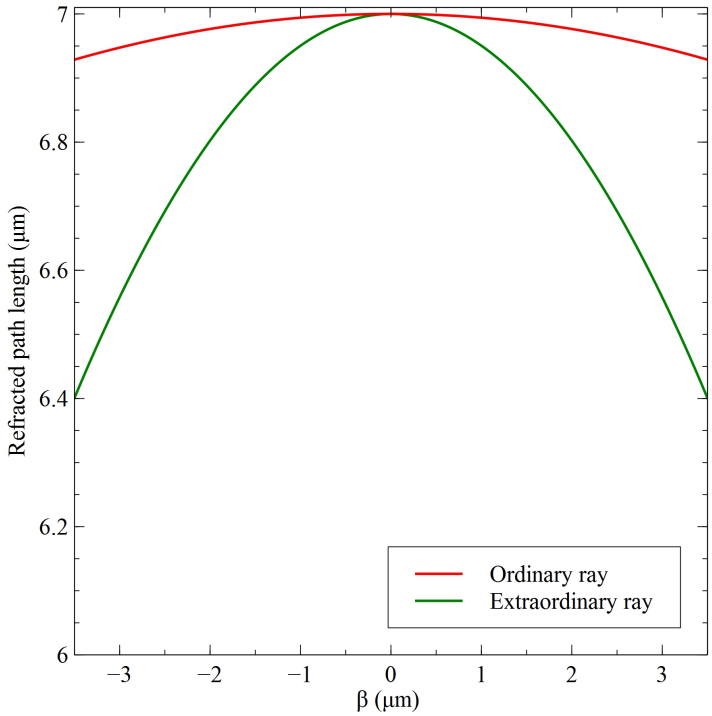

Figure 4.19: The path length through a fibre with respect to the its radial co-ordinate for the ordinary and extraordinary rays.

of the complex refractive index $\tilde{n}$. Knowing the angle of refraction, the path length through the fibre can be calculated with $l_{chord} = 2\beta_f \cos\theta_r$, as demonstrated in figure 4.18. The path length through the fibre is plotted in figure 4.19 for the ordinary and extraordinary rays using the optical properties shown in table 4.2. It can be seen from figure 4.19 that the optical path length through the fibre is always close to the diameter of the fibre due to the high refractive index. This means that the ordinary ray will dominate due to its large extinction coefficient, which yields an absorption depth of ~ 114nm; this is much smaller than any path length through the fibre in figure 4.19, so it can be assumed that any energy which is not reflected is absorbed and not transmitted by the fibre.

Table 4.3: A table of the average reflectance across the diameter of a T300 carbon fibre at a wavelength of 10.59μm.

Polarization:	Perpendicular to fibres	Parallel to fibres
Average reflectivity	69.5%	81.1%

An average reflectivity value across the fibre for each configuration yields the results shown in table 4.3. This shows that the reflectivity is significantly higher when the polarization is parallel to the direction of the fibres, compared to when it is perpendicular to it. In other words 1.6× more light is absorbed when the fibres are perpendicular to the direction of the fibres.

It has been recognised that a full treatment of the coupling of laser light to the fibres requires numerical solution of Maxwell's equations as the fibre diameter is of the order of one wavelength. However, preliminary work using bespoke software has not indicated any significant departures from the conclusions drawn here.

4.8 FT-IR spectroscopy to measure the optical absorption coefficient of RS-M135 epoxy resin

The FT-IR used in section 4.7 was used in a transmission configuration; materials are placed in the beam path of the instrument after taking a background with an empty sample chamber, light is directed though the sample and the absorbance spectrum is obtained. The instrument was chosen because the spectral range includes the RF CO_2 laser wavelength (10.59µm)

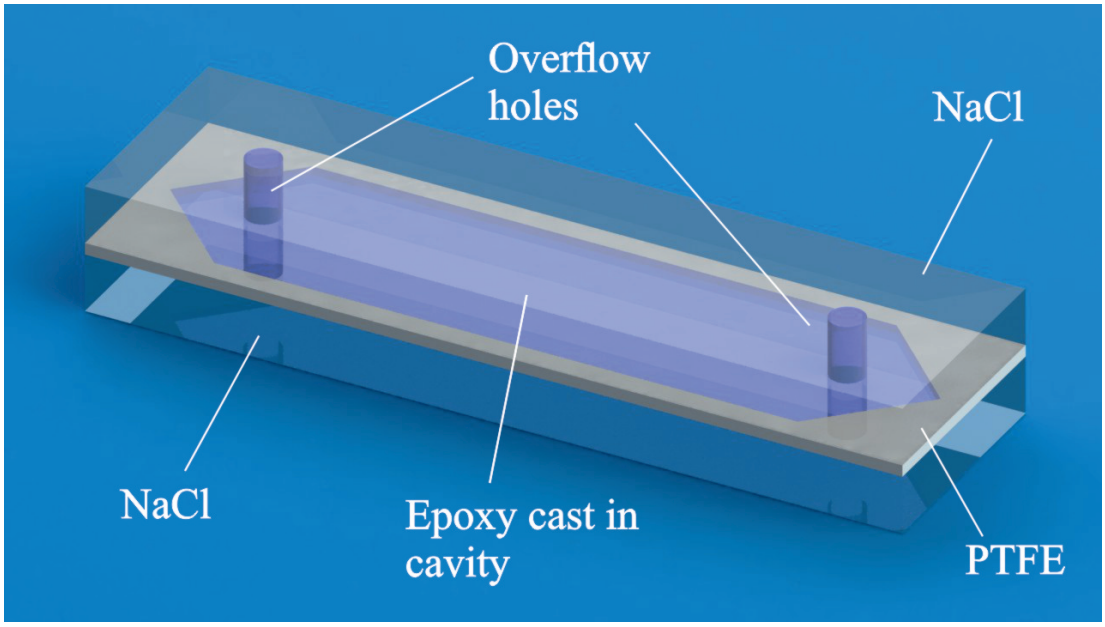

Figure 4.20: Two optical grade NaCl windows separated with a 115±1µm PTFE film gasket, leaving a cavity which has been used to cast epoxy. There are two holes in the top NaCl window which allow excess epoxy to escape without being forced through the PTFE gasket. When the epoxy has hardened and the NaCl windows have been removed, a 116 ± 1µm film of epoxy remains.

In order to get an FT-IR transmission spectrum for the epoxy, which has a relatively high absorption coefficient, a thin, uniform film was required. The epoxy was mixed as described in section 4.2 and degassed and then cast between two optical grade NaCl windows separated with a 115 ± 1µm PTFE film gasket (figure 4.21). The NaCl windows had two small holes to allow excess epoxy to flow into when the windows were pressed together. The windows were compressed together and the epoxy was left to

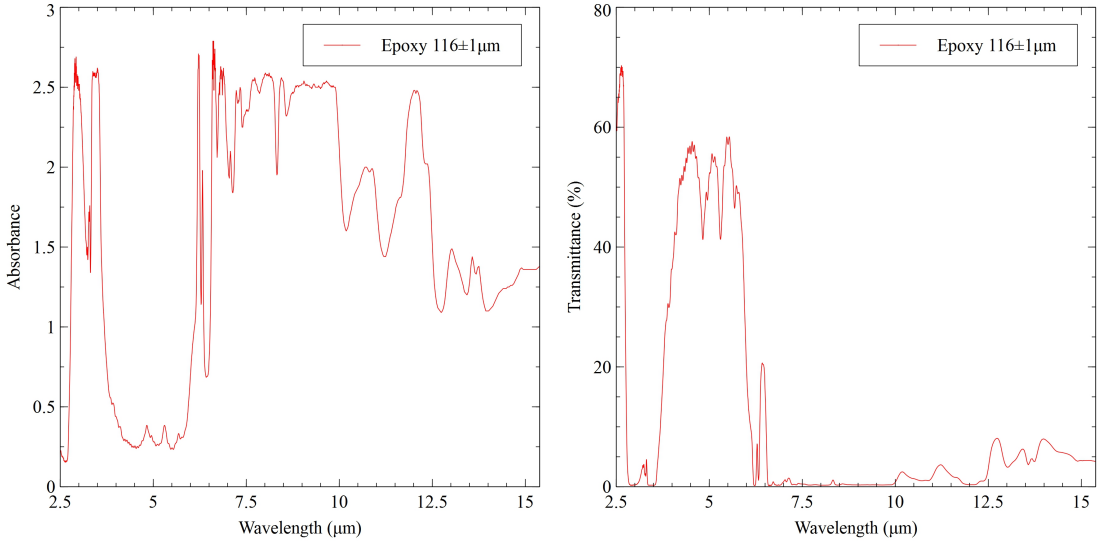

(a) Absorption spectrum.

(b) Transmission spectrum.

Figure 4.21: Absorption and transmission spectra for a 116 ± 1µm film of RS-M125 epoxy resin film, obtained using a Thermo-Nicolet NEXUS 670 FT-IR.

harden. Once the epoxy had hardened, the NaCl windows were dissolved in water. This produced a 116 ± 1µm film of epoxy, measured with a micrometer in several places across its surface. This film was thin enough to allow a spectrum with a measurable absorbance at a wavelength of 10.59µm to be obtained. Figure 4.21 shows the acquired spectrum in absorbance units and processed to transmission percentage.

The Beer-Lambert law for optical absorption is:[51]

$$I_T = I_0 e^{-\alpha z} \tag{4.11}$$

where I_T is the light intensity after it has passed through the sample, I_0 is the initial intensity, α is the optical absorption coefficient (m^{-1}) and z is the sample thickness (m). This can be written this in terms of transmission fraction, T_{trans}, with the reflectance, R, (measured in section 4.7) subtracted:

$$\ln\left(\frac{T_{trans}}{(1-R)^2}\right) = -\alpha z \tag{4.12}$$

From this, the optical absorption coefficient at 10.59μm was calculated to be $37.3 \pm 0.7 \times 10^3 \mathrm{m}^{-1}$. This means the optical absorption length ($1/\alpha$) at this wavelength is 26.8 ± 0.5μm. It should be noted that in some areas of the CFRP the depth of the epoxy on top of the carbon fibres is less than this absorption length.

4.9 Summary

Epoxy characteristics

The results from the measurements performed on RS-M135 epoxy resin are presented in table 4.4 and compared to values taken from literature for similar epoxy resins. There are many types of epoxy, so the values found in literature were for 'unfilled' epoxy or pure epoxy. Specifically, bisphenol based epoxy resins were sought.

Table 4.4: A summary of the measured values for RS-M135 epoxy resin compared to the values for similar materials found in literature.

	Measured value	Literature value
Activation energy ($\mathrm{kJ\,mol^{-1}}$)	155 ± 13	44 – 227[133, 134, 135, 136, 137]
Specific heat capacity ($\mathrm{J\,kg^{-1}\,K^{-1}}$)	1450 – 2000	1110 – 2110[118]
Thermal conductivity ($\mathrm{W\,m^{-1}\,K^{-1}}$)	0.20 ± 0.03	0.17 – 0.21[53]
Density ($\mathrm{kg\,m^{-3}}$)	1150 ± 10	1180 – 1200[110]
Thermal diffusivity ($\mathrm{m^2\,s^{-1}}$)	$8.7 \pm 1.4 \times 10^{-8}$	-
Thermal diffusion length for 1ms pulse (μm)	19	-
Reflectivity (%)	8.0 ± 1.5	-
Absorption coefficient ($\mathrm{m^{-1}}$)	$37.3 \pm 0.7 \times 10^3$	-
Absorption depth (μm)	26.8 ± 0.5	-

The activation energy falls within the literature values; however, the references give a very wide range of results. This is due to a number of factors. The references are for unfilled epoxies, but there are many types. There are also different methods and definitions to determine the activation energy. The most relevant reference to compare our work to is Chiang[137], who uses the Ozawa/Flynn & Wall method and finds a value for a bisphenol based pure unfilled epoxy which falls within our experimental uncertainty.

The specific heat capacity given for a general epoxy by Kaye & Laby[118] follows a similar trend to our graph. At 273K they quote 1110J kg^{-1} K^{-1}, rising to 1520J kg^{-1} K^{-1} at 373K and finally 2110J kg^{-1} K^{-1} at 473K. For the heat rise models in chapter 6 the specific heat capacity was simplified to 2000J kg^{-1} K^{-1} as the graph increases to this value with temperature, and then stays approximately constant.

The thermal conductivity for a general epoxy resin given by Kaye & Laby as $0.17 - 0.21$W m^{-1} K^{-1}.[53] The value measured in this thesis was between these values.

The RS-M135 epoxy system datasheets gave the density of the cured resin as $1180 - 1200$kg m^{-3}.[110] This was checked against our samples with a simple experiment; a cast epoxy disc was measured with callipers, the volume was calculated and the disc was weighed, this yielding the density with $^{volume}/_{mass}$. The measured density was 1150 ± 10kg m^{-3}. The literature value is close to the measured value but falls outside our experimental uncertainty. This could be due to the crudeness of the method used to calculate the volume, which assumes a perfect cylinder, or due to air bubbles in the sample reducing the density. Because of this, the literature value was chosen for the heat rise models in chapter 6.

The thermal diffusivity of the epoxy resin was calculated using equation 2.3 with measured values. The thermal diffusivity was measured to be $8.7 \pm 1.4 \times 10^{-8}$m^2 s^{-1}. From this the heat diffusion length for a 1ms pulse could be obtained from equation 2.2 and was found to be 19µm.

The reflectivity and absorption coefficients could not be found for epoxy in the literature and so were measured here. The reflectance at 10.59μm was found to be $8.0 \pm 1.5\%$, the differences between the cast epoxy block and the CFRP were taken into account when the uncertainties were calculated. The absorption in a thin film of epoxy was measured at a wavelength 10.59μm, yielding an absorption coefficient of $37.3 \pm 0.7 \times 10^3 \mathrm{m}^{-1}$; this means that the absorption length in the epoxy at this wavelength is 26.8 ± 0.5μm.

The large range of accepted values in the literature, particularly for the activation energy, and the various types of epoxy available highlights the need to take such measurements in order to characterise the material.

Carbon fibre characteristics

The properties of the T300 carbon fibre are presented in table 4.5. Most of the properties were found in the datasheet for the fibre.[57] The graphite sublimation temperature was also found in literature.[113] The conductivity across the carbon fibres is not given in the specification sheet, however the conductivity across a T300 carbon fibre was found in literature.[52]

The thermal diffusivity of the carbon fibres in both directions was calculated using equation 2.3 with values found in literature, and from this the heat diffusion length could be obtained from equation 2.2. The themal diffusivity in the direction of the fibres was found to be $7.95 \times 10^{-6} \mathrm{m}^2\,\mathrm{s}^{-1}$, yielding a heat diffusion length for a 1ms pulse of 178μm. Across the fibres the thermal diffusivity was found to be $1.52 \times 10^{-6} \mathrm{m}^2\,\mathrm{s}^{-1}$, yielding a heat diffusion length for a 1ms pulse of 78μm. It should be noted that the heat diffusion length across the fibres is not a realistic estimate in a woven sheet of carbon fibre because there will either be air gaps between individual fibres in a tow which will insulate them, or the contact point will be minimal due to their cylindrical shape.

Table 4.5: A table of the thermal and optical properties of T300 carbon fibre. Note that the reflectances have been modelled for a wavelength of 10.59μm. It should also be noted that the thermal diffusion length across the fibre is not a realistic estimate beyond the edges of the fibres, as there will be air gaps or small contact areas between fibres in a woven tow which will insulate them.

	Value
Specific heat capacity	$749.96\,\mathrm{J\,kg^{-1}\,K^{-1}}$[57]
Thermal conductivity in direction of fibres	$10.46\,\mathrm{W\,m^{-1}\,K^{-1}}$[57]
Thermal conductivity across fibres	$2.0\,\mathrm{W\,m^{-1}\,K^{-1}}$[52]
Density	$1760\,\mathrm{kg\,m^{-3}}$[57]
Sublimation temperature	$3895-4020\,\mathrm{K}$[113]
Thermal diffusivity in direction of fibres	$7.95\times10^{-6}\mathrm{m^2\,s^{-1}}$
Thermal diffusivity across fibres	$1.52\times10^{-6}\mathrm{m^2\,s^{-1}}$
Thermal diffusion length in direction of fibres for 1ms pulse	178μm
Thermal diffusion length across fibres for 1ms pulse	78μm
Average reflectance for polarization parallel to fibres	81.1%
Average reflectance for polarization perpendicular to fibres	69.5%

The reflectances were modelled assuming a graphite fibre, with the optic axis normal to the surface[130, 129]; the data in table 4.2 was used for these calculations.[128] This shows an increase in absorbed light of $\sim 1.6\times$ when the polarization is perpendicular to the fibres compared to parallel.

Table 4.6: A table of estimates for some thermal properties of CFRP in the direction of the fibres, and perpendicular to their direction.

CFRP:	Parallel to direction of fibres	Perpendicular to direction of fibres
Thermal conductivity ($W\,m^{-1}\,K^{-1}$)	5.33	0.5
Thermal diffusivity ($m^2\,s^{-1}$)	2.66×10^{-6}	2.50×10^{-7}
Thermal diffusion length for 1ms pulse (μm)	103	32

4.10 Conclusions

As discussed previously, the carbon fibres and the epoxy matrix have very different thermal and optical properties. The optical absorption depth into a carbon fibre is very small[129], so the most significant optical property is the high reflectivity for the fibres; light which is not reflected will be absorbed. The epoxy resin absorbs 10.59μm light strongly and the absorption depth is 26.8 ± 0.5μm; however, in section 4.2 it was found that the depth of epoxy above the fibres varies between $7 - 100$μm, which means that the laser light can interact with the fibres through the epoxy matrix and the reflected light from the fibres will then be absorbed by the epoxy, further complicating the interaction. In addition to this it was found that polarization significantly impacts the reflectivity and therefore absorption of pure carbon fibres, and this would be expected to be true when the fibres are within the matrix as well.[1]

The thermal conductivity of the epoxy resin is relatively low compared to metals, which generally have conductivities $2 - 3$ orders of magnitude higher.[138] This means that with pure epoxy resin there will be little thermal diffusion across or into the sample for short laser pulses; it can be seen in table 4.4 that the thermal diffusion length is 19μm for a 1ms pulse, so the energy will be confined to a smaller volume than a ma-

[1] Due to the high refractive indices of the carbon fibre, an epoxy matrix boundary as opposed to air does not significantly impact the reflectance, using a typical refractive index for epoxy resin of ~ 1.5 for the mid-IR.

terial of higher conductivity. The presence of the carbon fibres, which have a higher conductivity, particularly in the direction of the fibres, will mean that CFRP has an increased conductivity over pure epoxy resin. Using equation 2.4, the conductivity of CFRP in the direction of the fibres can be calculated as 5.33W m^{-1} K^{-1}. The conductivity of CFRP perpendicular to the fibres cannot be modelled easily, but from literature a slight increase over pure epoxy is expected, and this can be estimated as 0.5W m^{-1} K for a 50:50 matrix to fibre ratio.[52]

From these thermal conductivities the diffusivity of CFRP in each direction can be estimated using the ratio of matrix to fibres for the other parameters, and a thermal diffusion length can then be obtained. These results are presented in table 4.6. From this it can be seen that the thermal diffusion length for a 1ms pulse is relatively short perpendicular to the direction of the fibres at 32μm, and similar to that of the pure epoxy resin. The thermal diffusion length in the direction of the fibres is much higher at 103μm, therefore it would be expected that there would be a larger damage width in this orientation.

Chapter 5

Laser Processing of CFRPs Part I: Thresholds and Ablation Products

5.1 Introduction

In this chapter the laser processing of carbon fibre composites using an RF CO_2 laser is explored. First, the laser power is vaired to measure the fluence threshold of the materials and observe the effects of RF CO_2 laser irradiation of CFRPs to ensure that the laser is coupling to the materials and ablating them. Then, fume capture techniques are used to analyse the fume content; first isokinetic sampling and gas chromatography-mass spectrometry (GC-MS) is used to analyse the vapour phase material; Fourier transform infra-red spectroscopy (FT-IR) is then used to evaluate the permanent gas-phase fume; finally larger particle fume is captured and viewed using a scanning electron microscope (SEM).

5.2 Determination of the fluence threshold of CFRP and its constituents

Background

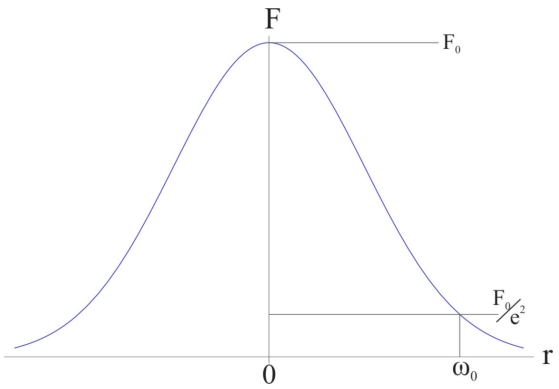

Figure 5.1: A diagram of the spatial fluence distribution for a Gaussian laser beam. F is the fluence with respect to the radial position, r. The peak fluence is F_0 and the spot size is ω_0.

In this section the laser energy threshold, i.e. the energy required to damage a material, is measured, and this is then converted to a fluence threshold by determining the spot size of the focussed laser beam. In section 3.2 the laser was focussed and the pulse energy was measured; however, to determine the spot size the fluence distribution of the laser output must be considered. The spatial fluence distribution of a Gaussian beam can be described using equation 5.1.

$$F(r) = F_0 \cdot e^{-2r^2/{\omega_0}^2} \tag{5.1}$$

where $F(r)$ is the fluence as a function of the radial co-ordinate, r. F_0 is the peak fluence and ω_0 is the spot size (radius), as shown in figure 5.1.

To find the size of the laser-induced damage $F(r) = F_T$ is set and the equation is re-arranged for r^2, i.e. the radius squared when the fluence drops to the threshold fluence,

F_T. This yields equation 5.2.

$$r^2 = \frac{1}{2}{\omega_0}^2 \ln\left(\frac{F_0}{F_T}\right) \tag{5.2}$$

Now, r^2 can be substituted for ${}^{D^2}/_4$, where D is the beam diameter at the threshold, i.e. the damage diameter of the material. The *area* which the pulse energy, E, is delivered to is common to F_0 and F_T, i.e. $F_0 = {}^{E}/_{area}$ and $F_T = {}^{E_T}/_{area}$, where E_T is the energy threshold. Therefore ${}^{F_0}/_{F_T} \equiv {}^{E}/_{E_T}$ can be substitued and then rewritten as equation 5.3.

$$D^2 = 2{\omega_0}^2 \ln\left(\frac{E}{E_T}\right) \tag{5.3}$$

It follows from equation 5.3 that if a graph of D^2 as a function of $\ln E$ is plotted, the gradient is $2{\omega_0}^2$ and the x-intercept (i.e. where $D = 0$) is $\ln E_T$.

The spot size is very important to this thesis, as it it used to calculate the energy per unit area and power per unit area (fluence and irradiance). It is also a relatively small size, resulting in a potentially large fractional error. In order to minimize the uncertainties, cast epoxy resin was chosen to measure the spot size, as it has a uniform surface. The CFRP had fibres close to the surface which meant that they could interfere with the damage diameter because they are highly conductive, and also they cause the epoxy thickness to vary.

Epoxy resin

Cast epoxy resin was processed using the RF CO_2 laser at various pulse energies, with a number of repeats for each pulse energy. The pulse duration was set to 1.012ms, as described in chapter 3, and remained at this value throughout the experiments. The damage sites were observed and measured using an optical microscope, as shown in figure 5.2.

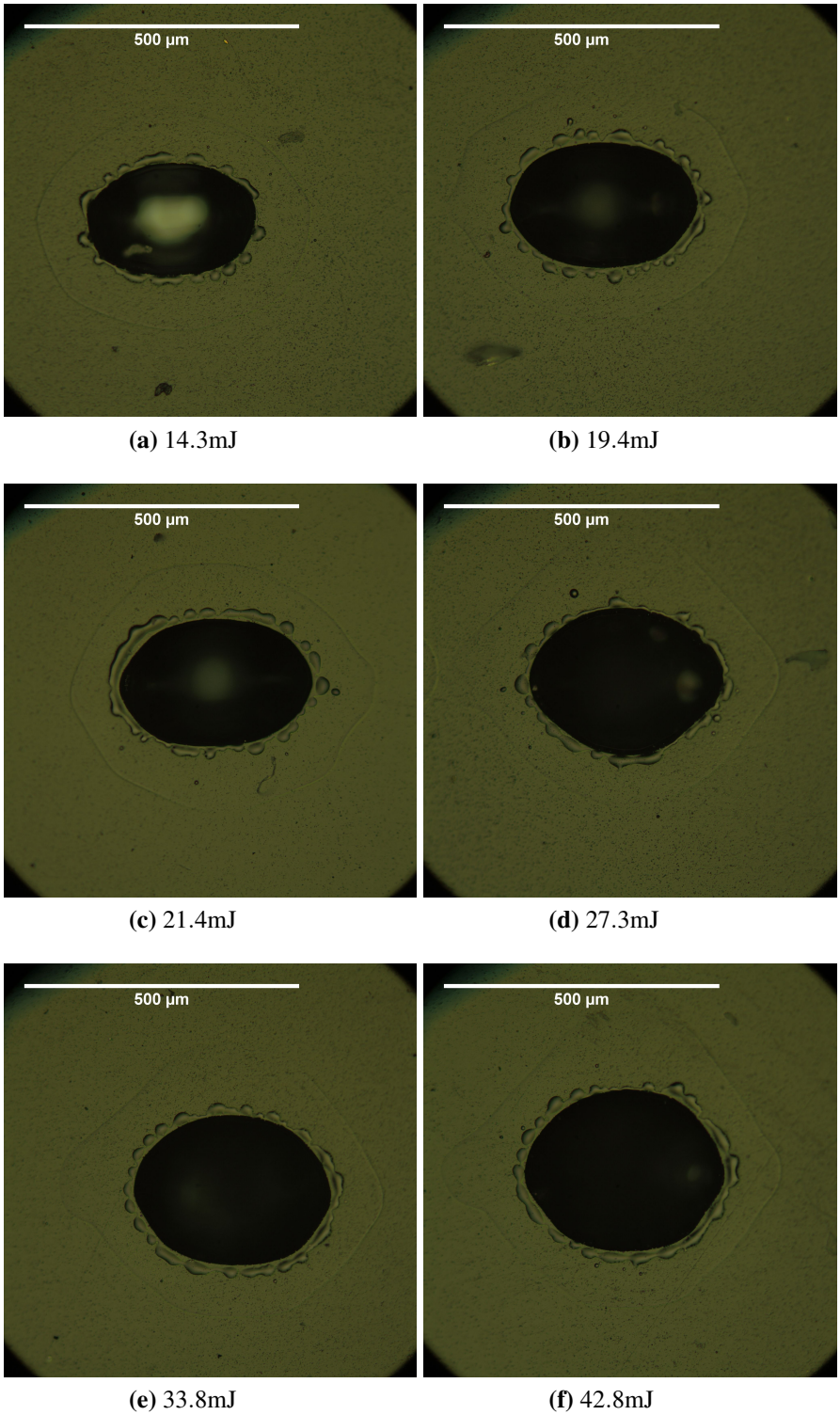

(a) 14.3mJ **(b)** 19.4mJ

(c) 21.4mJ **(d)** 27.3mJ

(e) 33.8mJ **(f)** 42.8mJ

Figure 5.2: Micrographs of RF CO_2 laser ablation sites on a cast and polished epoxy resin block at various 1ms pulse energies.

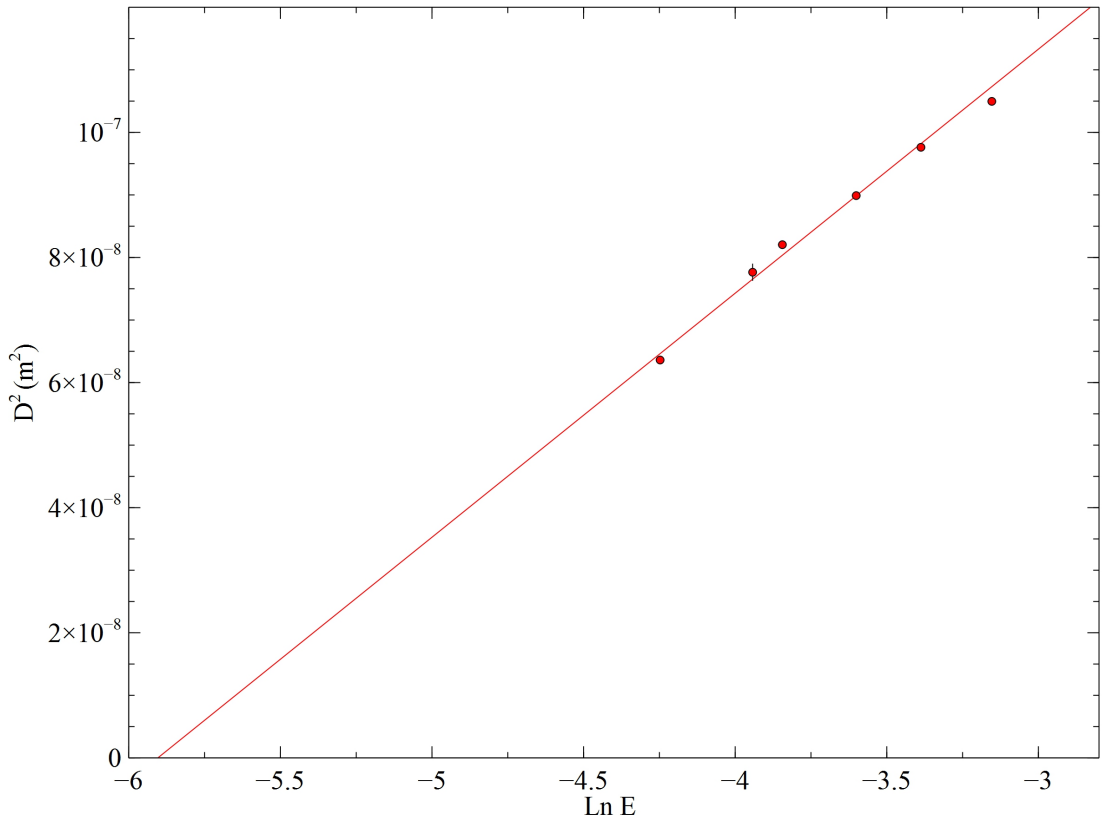

Figure 5.3: A graph of the damage diameter of cast epoxy resin squared against the natural logarithm of the laser pulse energy, according to equation 5.3.

It can be seen in figure 5.2 that the damage sites are not circular, so the beam radius is different in the different planes; this is defined as the 'horizontal' (in the micrographs) as the X-axis and the 'vertical' as the Y-axis. The difference in damage diameter between the axes is due to the raw beam from the RF CO_2 laser being elliptical. To account for this, the damage area was measured by tracing the circumference of the damage site on the microscope software, which would then display the area of the enclosed section. From this the effective damage diameter was calculated. For each laser pulse this measurement was repeated five times. The result was plotted as defined by equation 5.3 in figure 5.3.

The information presented in table 5.1 can be extracted from the gradient and x-axis intercept of the plot in figure 5.3.

As the laser to lens and lens to sample distance remained constant for all the work presented in this thesis, the effective spot radius of $136 \pm 3\mu m$ is applied throughout.

Table 5.1: A table showing the calculated spot size (radius) for the RF CO_2 laser, and also the threshold energy and fluence for ablation as determined from figure 5.3 for a 1ms pulse.

	Value	Uncertainty
Spot Size (μm)	136	3
E_T (mJ)	2.47	0.17
F_T (J cm^{-2})	4.2	0.5

T300 carbon fibre

Measuring the threshold fluence for laser-induced damage to the T300 carbon fibre weave is a more complex problem because it is not a simple surface. It is made from fibres which vary in direction, so the surface is not flat because of the fibre weave, and, when considering the fibres alone, there is no matrix to hold them rigidly.

The carbon fibre weave was prepared as described in section 4.2. The samples were then processed with the RF CO_2 laser at various pulse energies, at many sites across the samples to ensure that variations in the fibre weave could be accounted for. The sample was arranged so that the fibres would be parallel to the incident laser polarization or perpendicular to the polarization, depending on which part of the fibre weave was ablated. The polarization of the laser was parallel to the X-axis of the system, as described in section 3.2, which is horizontal on the high magnification images presented here. When the ablation sites were observed, a significant difference between those irradiated with different polarization directions was noticed. This can be demonstrated with the two SEM images in figure 5.4.

Figure 5.4 shows micrographs of two RF CO_2 laser ablation sites, each processed with the same fluence, 31.5 ± 2.7J cm^{-2}, and a spot radius of 136μm. It can be seen immediately that the damage in figure 5.4a, where the polarization is parallel to the fibre orientation, is significantly less extensive than when the polarization is perpendicular to the fibre orientation, as shown in figure 5.4b. Figure 5.4a shows some damage to the fibres in the irradiation site, however the fibres are still continuous. In the centre of

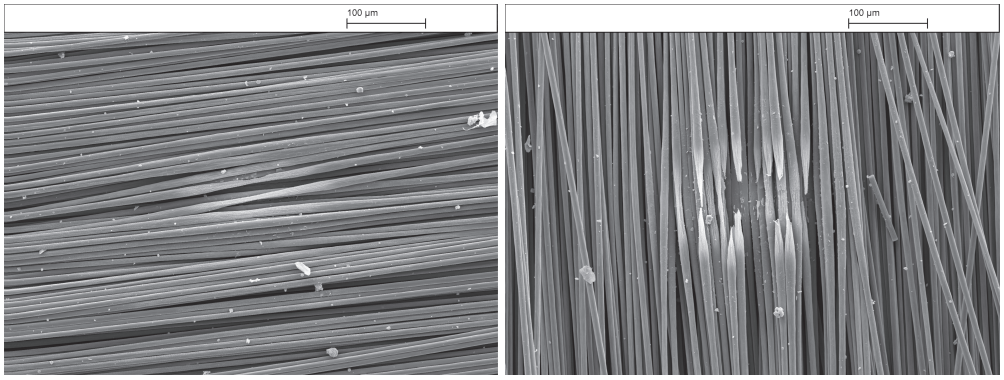

(a) **(b)**

Figure 5.4: SEM images of carbon fibre ablation sites using an RF CO_2 laser, each processed with a pulse fluence of $31.5 \pm 2.7 \mathrm{J\,cm^{-2}}$ and a spot radius of 136.4µm. (a) shows the damage to the fibres when the polarization of the RF CO_2 laser is parallel to the fibre orientation, and (b) shows the damage to the fibres when the polarization is perpendicular to the fibre orientation.

the Gaussian beam profile, where the fluence is highest, the fibres have decomposed partially and 'thinned'. Moving from the centre, the fibres become less thinned until they are a similar width to a fibre which has not been irradiated. Beyond this, at moderate fluences, the fibres have 'swelled', and the fibres are visibly wider; they have approximately doubled in diameter to 14µm. As the fluence drops at greater distances from the centre the swelling decreases and the fibres appear entirely unaffected. Figure 5.4b shows a similar result, but with more damage. In the centre where the fluence is highest, more energy has been absorbed by the fibres which are now perpendicular to the polarization of the laser beam, which means that the induced temperature rise has been high enough to fully decompose them. Further from the centre of the laser spot, the fibres have come to a point at the threshold for full decomposition of the fibre; even further from the centre the fibres gradually get wider as the absorbed energy drops, when the energy is low enough they become swollen. Eventually the absorped energy drops to the point where they are undamaged. This behavior was consistent throughout the repeats at this fluence, and other fluences also show significantly increased damage when the polarization is perpendicular to the fibre orientation.

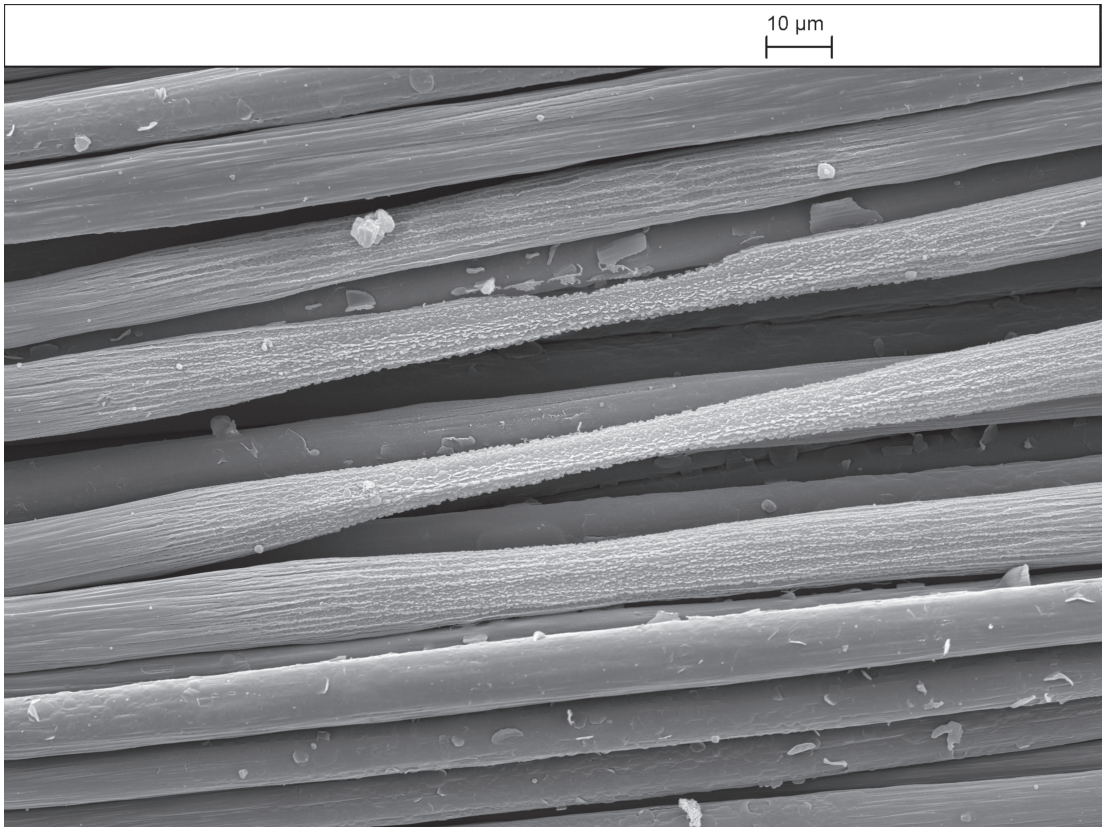

Figure 5.5: An SEM image of RF CO_2 laser irradiated carbon fibre weave, which demonstrates the thinning of fibres at moderate fluence levels, and the swelling beyond the original 7µm diameter at lower levels of fluence.

Fibre swelling has been previously observed during laser irradiation of PAN fibres[58, 5] and has been attributed to the high laser induced heating rates of the fibres causing rapid volitization of non-carbon impurities. The fibre thinning and swelling at irradiance levels which will not fully machine through fibres is shown in figure 5.5.

Measurements were taken in the X-axis and Y-axis for each site, using an optical microscope. The damage diameter was measured from where visible damage was apparent (the fibres looked 'blackened' when examined with an optical microscope, but look lighter in the SEM images presented). At each fluence and polarization orientation, 5 repeats were taken. The average damage diameter for each axis at particular fluences and fibre orientations with respect to the laser's polarization is shown in figure 5.6.

Figure 5.6 demonstrates that the damage for the carbon fibre weave is consistently higher when the polarization is perpendicular to the fibres. It should be noted that

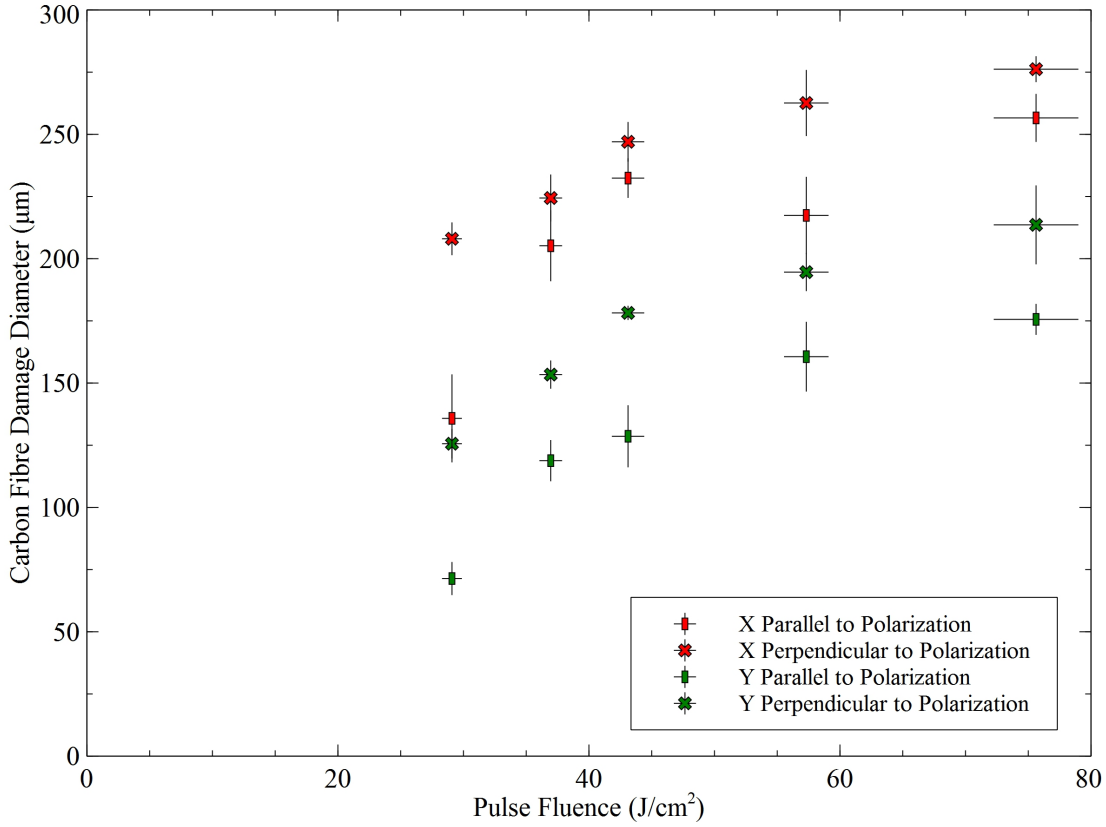

Figure 5.6: A graph of the average damage diameter of carbon fibre weave processed with an RF CO_2 laser, measured in two axes, and at parallel and perpendicular RF CO_2 laser polarizations with respect to the fibres, for various laser fluences.

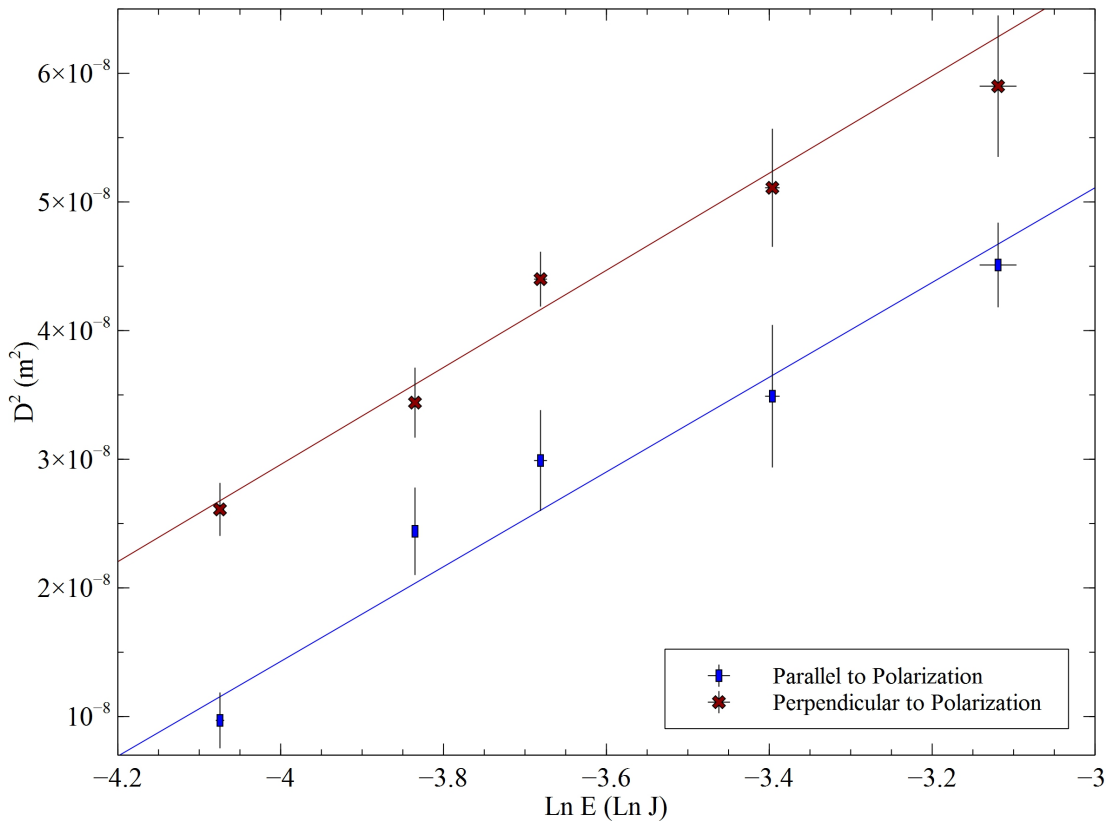

Figure 5.7: A graph of the damage diameter of RF CO_2 laser processed carbon fibre squared against the natural logarithm of the laser pulse energy, for laser light polarized parallel and perpendicular to the fibre direction.

when the polarization is parallel to the fibre orientation there will be increased heat flow in the X-direction, and increased heat flow in the Y-direction when the light is perpendicularly polarized. This means that the gap between the data for the two polarizations (figure 5.6) is greater in the Y direction because it has additional energy absorbed into the fibres, and also a larger heat affected zone in the direction of the measurement.

This data can also be used to calculate the damage threshold of the fibres with each polarization orientation using equation 5.3 as before. In order to do this the damage area was estimated by using the measurements in each axis to calculate the area as an ellipse. The diameter for a circle of equivalent area was then calculated. The results were then plotted and are shown in figure 5.7.

From figure 5.7, the information presented in table 5.2 can be extracted. From this

Table 5.2: A table of the spot size, threshold energy and threshold fluence for carbon fibre weave parallel and perpendicular to the polarization of the RF CO_2 laser used to ablate it.

	Parallel polarization		Perpendicular polarization	
	Value	Uncertainty	Value	Uncertainty
Spot size (μm)	130.8	6.5	131.5	4.2
E_T(mJ)	11.5	5.1	7.7	2.4
F_T (J cm^{-2})	21.3	11.2	14.3	5.5

data, it can be seen that the spot size derived for the two polarization orientations are almost identical, as expected. They are also close to the value measured for the cast epoxy resin, as might be expected as the experimental setup is the same; however, the value in table 5.1 was used to calculate the fluence from the energy in this set of results, due to the lower uncertainty because of the more uniform sample used.

The fluence threshold for carbon fibres parallel to the polarization is around 1.5× the value when the fibres are perpendicular to the polarization, suggesting the energy being absorbed in the fibres is reduced by 1.5× when the polarization is parallel to the fibres. The uncertainties on these values are relatively large, however, mainly because of the logarithmic axis used to determine the incercept; therefore when combining the uncertainties, any small changes in the gradient result in large alterations in the value from the intercept. It can be seen that the two gradients are parallel, as expected, and that the damage diameters are consistently higher when the polarization is perpendicular to the fibres, which is also corroborated by the SEM images, such as those in figure 5.4. For this reason it can be said with confidence that the threshold fluence is higher when the fibres are parallel to the polarization.

CFRP

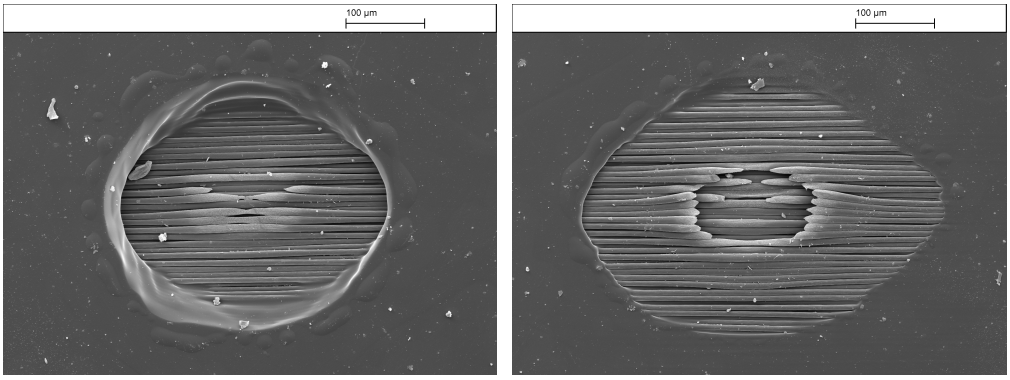

(a) 47µm epoxy depth

(b) 7µm epoxy depth

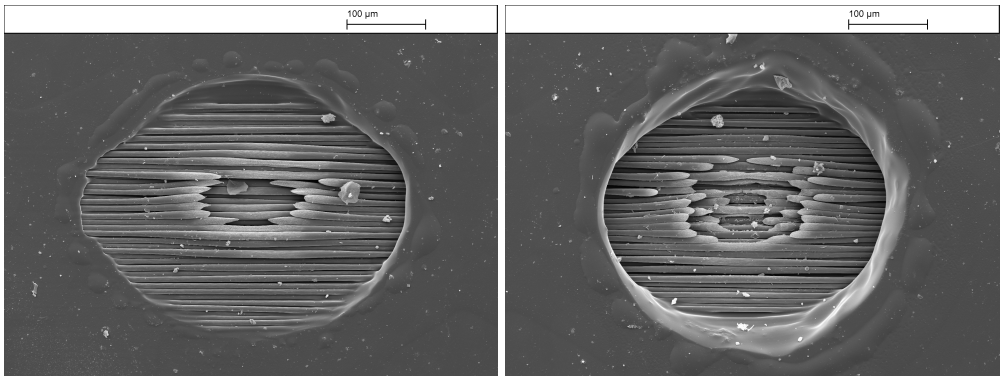

(c) 22µm epoxy depth

(d) 50µm epoxy depth (3 consecutive ablations)

Figure 5.8: SEMs of epoxy ablated with an RF CO_2 laser at a fluence of $75.6 \pm 3\,\mathrm{J\,cm^{-2}}$, with varying thicknesses of epoxy on top of the carbon fibres, displayed below each image.

RF CO_2 laser ablation of carbon fibre composites becomes more complex because in addition to considering the polarization of the incident light on the fibres and the direction of heat flow, the variation in the thickness of the epoxy on top of the fibres should also be considered. Figure 5.8 shows SEM images of the damage to the material with a variation in epoxy overcoating thickness at a fluence of $75.6 \pm 3\,\mathrm{J\,cm^{-2}}$. A graph of the variation in damage diameters for the epoxy and the fibres for both fibre directions at this fluence is plotted in figure 5.9a. When analysing our results the variation in spot size for the X and Y directions must not be forgotten.

When the epoxy damage diameter measurement (figure 5.9a) is perpendicular to the

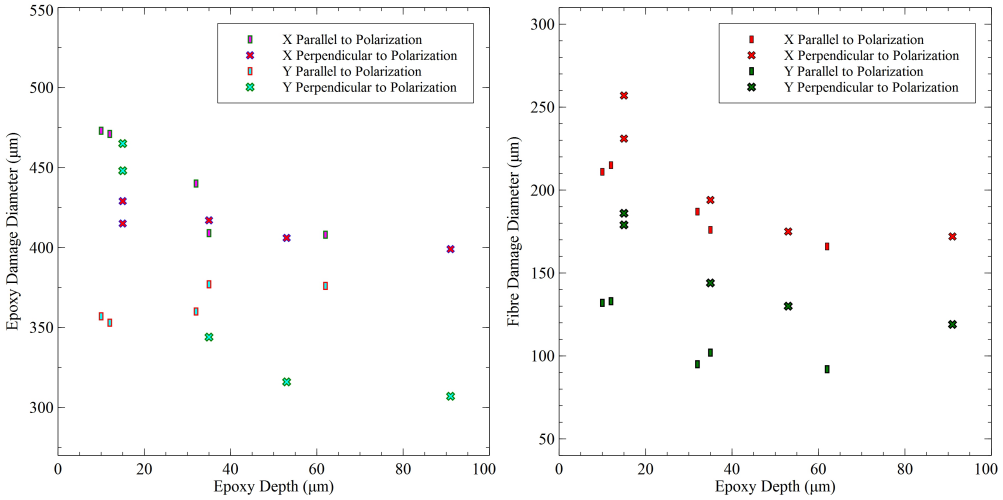

(a) Epoxy damage in CFRP

(b) Fibre damage in CFRP

Figure 5.9: Plots of the damage diameter in the X and Y direction for epoxy (5.9a) and carbon fibre weave (5.9b) for fibres which are parallel and perpendicular to the polarization of the RF CO_2 laser. A fluence of $75.6 \pm 3\,\mathrm{J\,cm^{-2}}$ was used for these plots.

fibre direction, i.e. X direction with the fibres perpendicular to the polarization and Y direction with the fibres parallel to the polarization, the plots are relatively straight. This is because any energy that is coupled into the fibres will mostly flow in the direction of the fibres, so even when the epoxy is thin and more energy is coupled, an increased damage range in this direction is not seen.

When the epoxy damage diameter measurement is parallel to the fibre direction, i.e. X direction with the fibres parallel to the polarization and Y direction with the fibres perpendicular to the polarization, it can be seen that there is a significant increase in epoxy damage when the depth is thinner than the absorption depth of 26.8μm (section 4.8). This is due to heat flow along the fibres as when the epoxy is thinner the fibres will get hotter, which increases this effect for two reasons: the first is the epoxy is thinner in places than the optical absorption depth so energy will be absorbed by the fibre from the start of the interaction (also any reflected energy at this stage will also be absorbed by the epoxy increasing the absorbed energy density), and the second is that only a thin layer of epoxy needs to be removed before the fibres are exposed to the full irradiance of the laser; this can happen during the 1ms pulse, as will be discussed

in chapter 6. The heat flow effect is increased when the fibres are perpendicular to the polarization because more energy is absorbed by the fibres (section 4.7).

When the epoxy is much thicker than the optical absorption depth, the heat flow does not affect the epoxy damage diameter in either direction. This is due to very little energy being transmitted through the epoxy to the carbon fibres, and the epoxy taking much longer to decompose, therefore leaving the fibres exposed but not damaged. Any heat which is conducted along the fibres is likely to be too deep to affect the surface of the epoxy, though internal damage may occur. It can also be noted that at thicker epoxy depths, in the Y direction, the epoxy damage diameter is larger when the fibres are perpendicular to the measurement direction (parallel to the polarization). This can be observed at other energies (Appendix A), but they are not as pronounced as this result. One theory for this increase in damage is reflections from the fibres being absorbed by the epoxy. Because the polarization is parallel to the fibre direction, over 81.1% of the energy is reflected, the reflectivity is also much higher at the edges of the fibre in this polarization (section 4.7), where the reflected light would be directed across the sample and would be incident on adjacent fibres or epoxy resin. The same effect cannot be observed in the X direction; this would support the theory because less energy is reflected in this orientation, and also the reflectivity decreases towards the edges of the fibres (section 4.7).

Another basic way to explain this effect is with equation 2.4, i.e. when the fibres are closer to the surface, the ratio of fibres to epoxy is greater, therefore the conductivity increases, thus yielding a larger HAZ.

The damage to the fibres is similar to that observed earlier in the bare fibre experiments, but the damage diameter for all four configurations decreases at a similar rate when the epoxy thickness increases, as shown in figure 5.9b. Fibre swelling is observed as before (figure 5.10). A full graph of all the data for fibre damage against epoxy thickness for various fluences in the four configurations is shown in Appendix A.

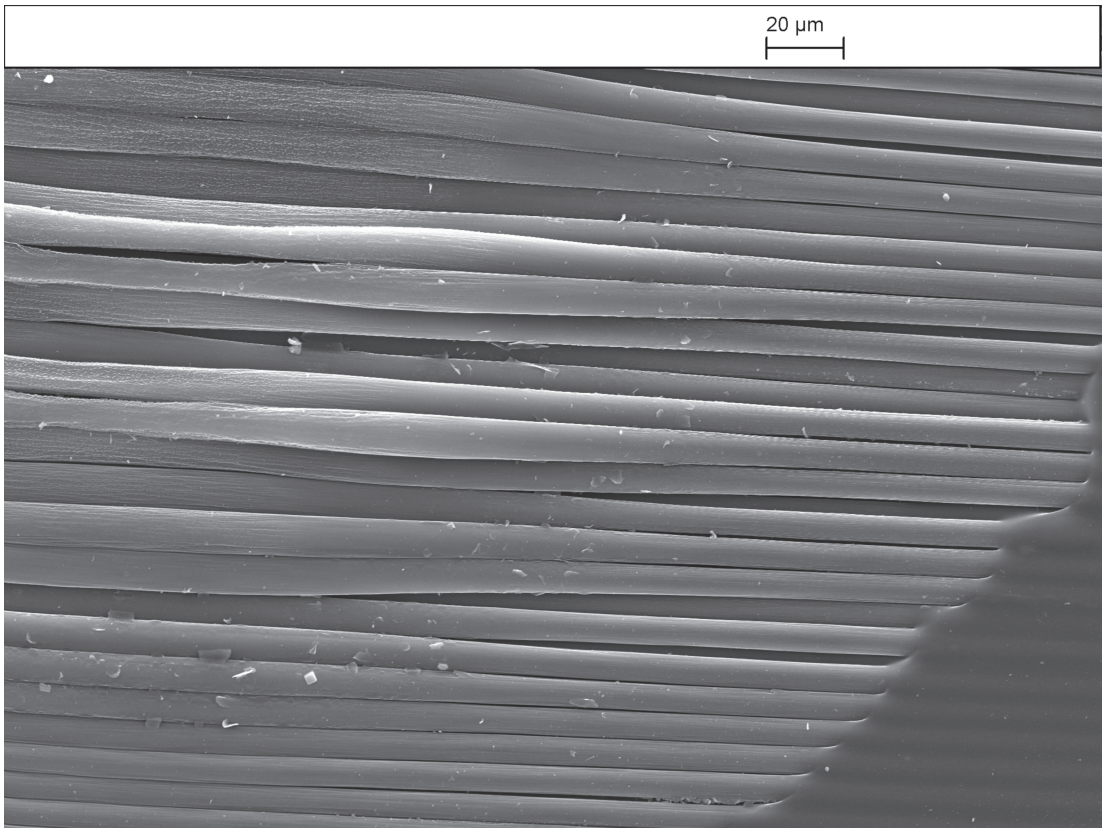

Figure 5.10: An SEM image of CFRP processed with an RF CO_2 laser. Fibres can clearly be seen thinning in the top left of the image where the fluence is highest, swelling as the fluence drops further from the centre of the spot, and finally at even lower fluences at the edges of the damage area the epoxy resin matrix is stripped but the fibres appear unaffected.

5.3 Fume content of laser processed CFRPs

5.3.1 Isokinetic sampling & GC-MS

Isokinetic sampling is a technique used to capture fume from a continuous extraction system. An extraction system typically has a large diameter tube with a high volumetric flow rate in order to direct any harmful particulates or gases to a capture or filter system. When sampling isokinetically, a nozzle with a flow velocity matched to the extraction tube is inserted into the main pipe to collect the fume. The flow rate is matched so that it samples the same level of airbourne material as the main flow and can be used for quantitative measurements. The captured fume can then be analysed, in this case by gas chromatography-mass spectrometry (GC-MS).[70]

To set up an isokinetic sampling system, a tube with a smaller diameter nozzle was inserted into the extraction pipe. This nozzle was attached to a separate pump unit, and the volumetric flow rate was adjusted so that the particle flow speed is matched to the speed in the extraction system. The flow velocity of a tube can be calculated using equation 5.4.

$$V_x = \frac{Q_x}{\pi(D_x/2)^2} \tag{5.4}$$

where V_x is the flow velocity ($\mathrm{m\,s^{-1}}$), Q_x is the volumetric flow rate ($\mathrm{m^3\,s^{-1}}$) and D_x is the diameter of the pipe (m). This can be used to derive the isokinetic condition described in equation 5.5[139].

$$\frac{Q_n}{Q_p} = \frac{{D_n}^2}{{D_p}^2} \tag{5.5}$$

where Q_n is the flow rate of the sampling nozzle, Q_p is the flow rate of the extraction system, ${D_n}^2$ is the diameter of the nozzle and ${D_p}^2$ is the diameter of the extraction

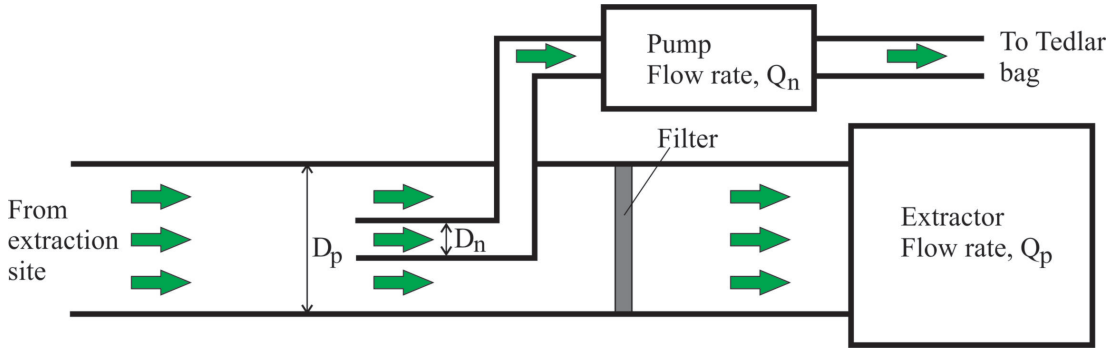

Figure 5.11: A diagram of an isokinetic sampling setup, used to extract a small section of the fume flowing in an industrial fume extraction system to a Tedlar bag so that it can be analysed by GC-MS.

pipe, as shown in figure 5.11.

In order to use this technique to analyse the fume from RF CO_2 laser processed carbon fibre composites, a Sator commercial marking system[140] was used. The system has a 200W RF CO_2 laser tube, directed by mirror galvanometer, and is focussed with a scan lens. Throughout this chapter the laser was set to a 50% duty cycle. This system was used because it had the ability to produce a large volume of fume continuously.

A Purex 400i extraction system[141] was used to extract the fume from the ablation site via a 50mm diameter hose at a flow rate set to $127 m^3 h^{-1}$, yielding a calculated flow velocity of $18 m s^{-1}$ at the extraction point. This was checked with a hot-wire anemometer, which gave a measured flow rate of $17.5 m s^{-1}$. The isokinetic sampling nozzle, with a diameter of 1.37mm, was inserted into the flow $\sim$ 1.5m downstream of the fume extraction point. This was to ensure as close to laminar flow as possible for the fume-bearing gas flow. The fume extracted using the battery pump was then directed into a 1L Tedlar bag.[142] The flow rate of the battery pump was adjusted to $1.5 L min^{-1}$ to give an isokinetic configuration. The flow rate meant that the pump would need to run for 40s to fill the Tedlar bag, which meant that more than 50s of continuous fume was required in order to allow the fume flow to settle to a constant rate in the extraction tube and then fill the Tedlar bag. The extraction system also had a filter in the hose to capture particles which were ejected from the surface and this is discussed in section 5.3.3.

The Sator system was set up to mark a 100×100mm square of CFRP with a 6×6 grid of squares. Each square had a series of concentric squares of different sizes within it. The pattern would repeat once the first pass was finished. Each pass had a duration of 17.5s, yielding fume from the epoxy and also the carbon fibres because there would be multiple passes of the same sites. The Sator laser was started and after a delay of 5 seconds it was expected that the fume has stabilised in the tube. The small pump was then switched on and the Tedlar bag was filled and sealed.

Fume which has been sampled isokinetically can be analysed using gas chromatography-mass spectrometry (GC-MS), which directs captured molecules through a heated column.[70] The time the molecules take to travel through the column is called the retention time. The eluted molecules are then ionized by the mass spectrometer and their charge to mass ratio is determined. Using the two methods in series helps to remove uncertainties in the results. A solid phase micro extraction (SPME) fibre was inserted into the Tedlar bag, and the bag was placed in an oven at 333K for 1 hour, allowing the condensed fume to volatilise and adsorb to the SPME fibre. The SPME fibre was then placed into a GC-MS machine and reheated to release the fume[143, 144], and the result shown in figure 5.12 was obtained.

From figure 5.12 it can be seen that the detector was saturated at a retention time of around $6-7$min. The software matched the result to a database of spectra and found that the fume is primarily phenol, which has a retention time the same as the saturated section of the graph. This is not unexpected as the aromatic ring with a direct bond to a hydroxyl group is a key precursor and component of epoxide resins, and similar results have been found in literature for thermal decomposition.[72, 71] The spikes in the graph at later times are assorted long chain hydrocarbons.

5.3.2 FT-IR gas-phase fume analysis

A Fourier transform infra-red spectrometer (FT-IR)[70] is a device which directs a wide spectrum of mid infra-red light through a cavity and onto a detector at the other

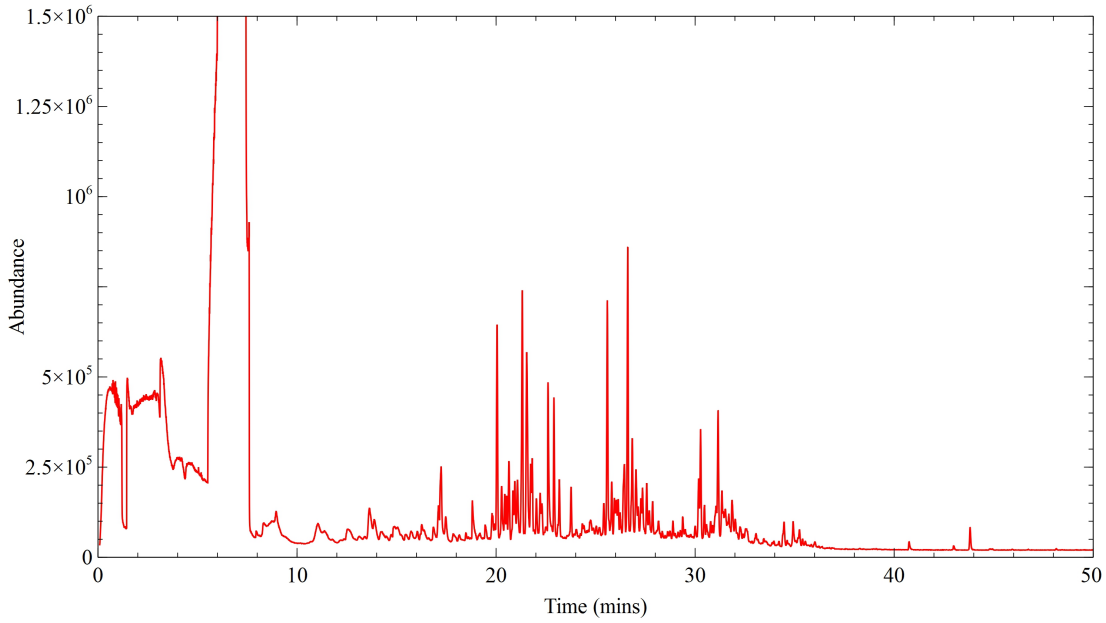

Figure 5.12: A GC-MS spectrum of the fume from an RF CO_2 Sator laser processed composite, sampled isokinetically in a Tedlar bag, and then adsorbed to an SPME fibre.

side. It then uses a Fourier transform to convert the collected data to an absorbance spectrum. A Thermo-Nicolet NEXUS 670 FT-IR[124] was used in this section. From the absorption lines and bands on the spectra molecules can be identified. This is because only certain photon energies can be absorbed by the molecules, based on the transition between its quantized vibrational energy levels.[92] In this section a gas-phase spectra is used, which typically has sharp peaks compared to liquid-phase as damping of the vibrational resonance is less, to deduce the fume contents from CFRP and its constituents.

A chamber was designed and built which allowed laser material processing in a controlled background gas atmosphere and to capture fume from the interaction. Figure 5.13a shows a rendering of the chamber, figure 5.13b shows an 'exploded' view of the chamber and figure 5.13c shows a 'sliced' view of the chamber. The cell was a cube with six ports. The bottom port had a block of aluminium to place samples on for processing. This meant that the samples could be removed easily and replaced without the need to disturb any optical elements. The top port had a retaining ring to hold an NaCl window in place; this meant that a sample could be processed in the cell using an IR

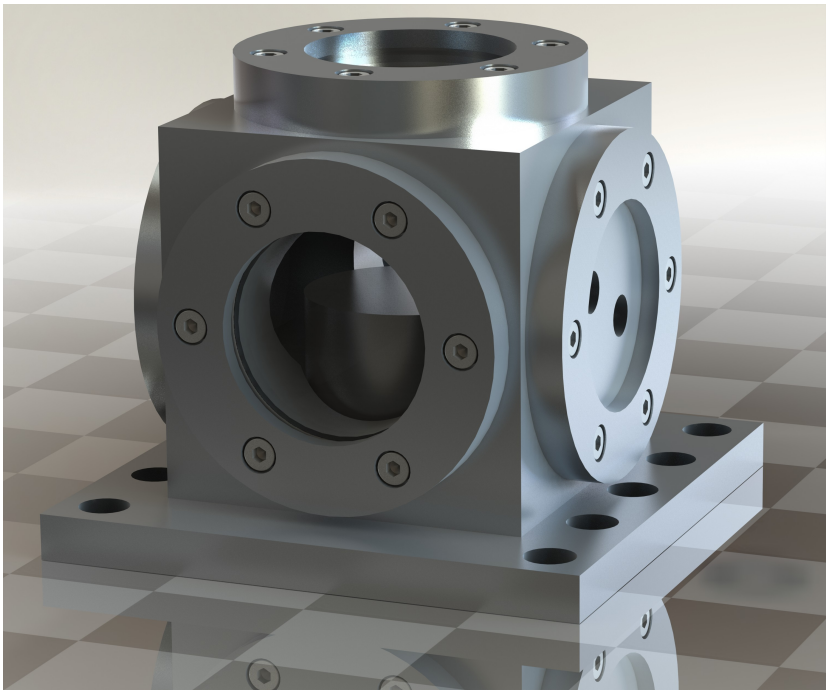

(a)

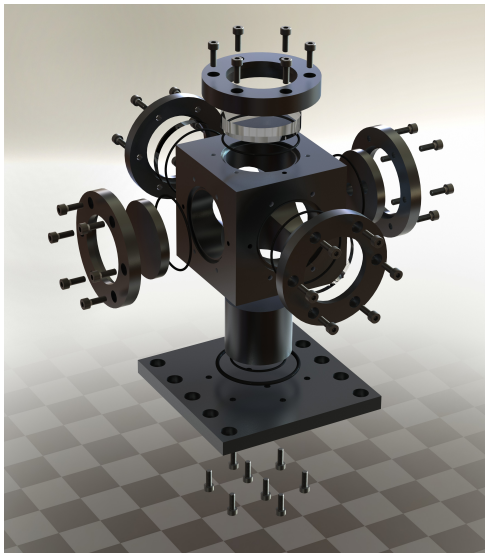

(b)

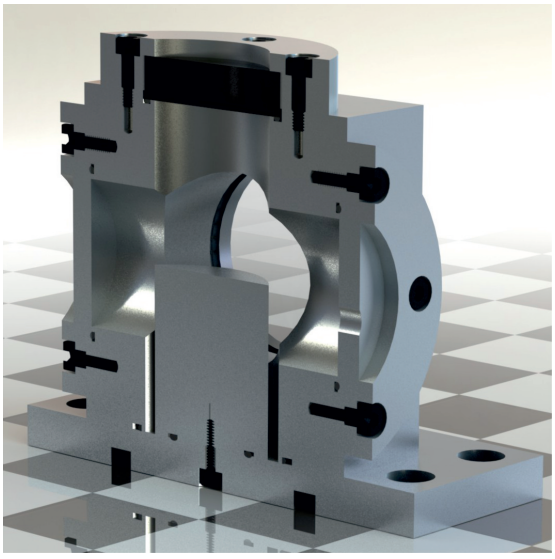

(c)

Figure 5.13: SolidWorks 2011 Education edition renderings of an aluminium chamber designed to capture fume processed within the cell; the atmosphere within the cell could be controlled. The cell has NaCl windows for laser processing at a wavelength of 10.59μm, and also FT-IR gas analysis.

laser. Two of the ports on opposite sides also had NaCl windows in them to allow FT-IR analysis. Another side port had an aluminium disk with two NPT threaded holes so that gas connections could be fitted. The remaining side had a blank aluminium disc inserted. O-rings were used throughout the cell to ensure that gas could not move between the cell and the lab once it was closed. This configuration meant that the chamber could be evacuated and filled with bottled compressed gas. Samples could then be processed in various atmospheres, and FT-IR analysis could be performed on the captured fume.

Cast epoxy resin, carbon fibre weave and CFRP were separately analysed using this cell. The material under test was loaded into the cell and the gas fittings were closed, sealing laboratory air into the cell. A background FT-IR spectrum was taken through the NaCl windows. The sample was processed inside the cell using the Sator RF CO_2 laser (described in section 5.3.1) by marking concentric squares on the surface by scanning the pattern across three times. Note that the squares were much smaller than those in section 5.3.1 because the FT-IR detector is very sensitive so smaller quantities of gas were sufficient. Having subtracted the background spectrum for the empty cell, the fume for each sample was analysed using the FT-IR spectrometer, yielding the results shown in figure 5.14.

Figure 5.14 shows that epoxy resin and carbon fibre have different absorption spectra, and CFRP has a spectrum which is a combination of the two components; there are no new absorption features as a result of the material being a composite. Some of the absorption peaks appear on both the epoxy and the carbon fibre, and some appear on one or the other. The significant absorption bands in the CFRP spectrum have been identified and annotated with a reference letter, and will be discussed in detail below.

Region A shows the absorption characteristics of methane (figure 5.15). The features in the methane absorption are very distinctive and the experimental spectrum shows an exact match to those in literature.[145, 146] From figure 5.14 it can be seen that the methane is due to the epoxy in the composite because it is not present in the carbon

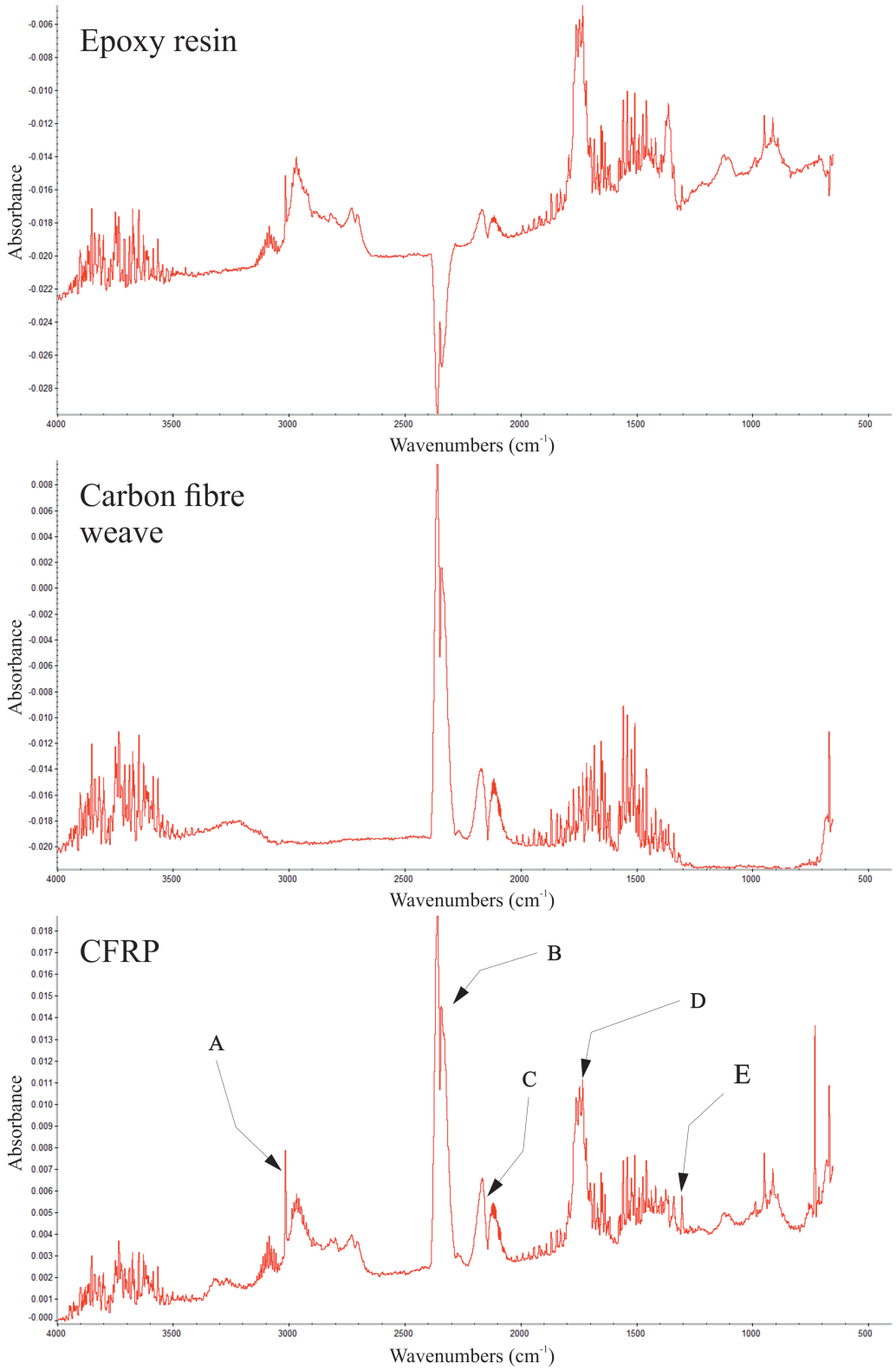

Figure 5.14: Infra-red spectra, taken using an FT-IR spectrometer, for RF CO_2 laser processed cast epoxy resin, carbon fibre weave and CFRP in laboratory air.

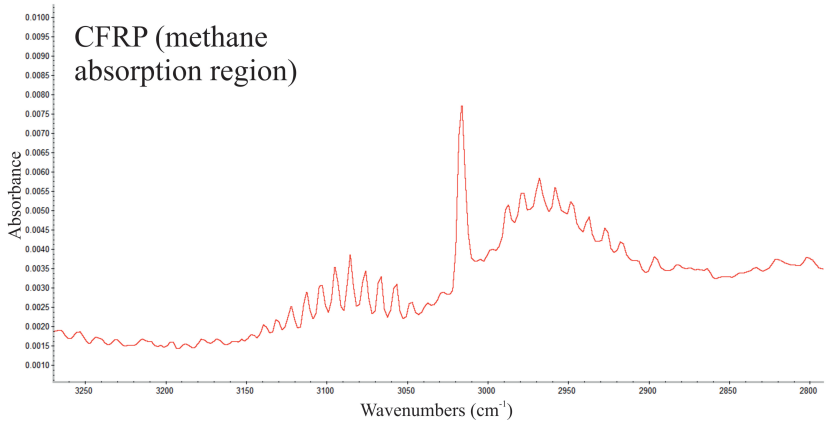

Figure 5.15: Region A in the CFRP absorption spectrum of figure 5.14, showing the vibration-rotation structure caused by the presence of methane.

fibre spectrum.

The methane gives two broad absorption envelopes of many closely spaced peaks, with a peak in the centre; this is around the region where it would be expected to find C-H bonds.[147] This structure is typical of a vibration-rotation spectrum[92]; the absorption region involves a transition from the ground to excited state for a single vibrational mode, with substructure due to rotational energy levels. Rotational energy levels are more closely spaced, and these are superimposed as sharper peaks. The two peaks arise from the rotational energy levels moving to a more or less excited state, and the higher absorbance in the centre of the peaks is due to a greater abundance of molecules in the higher energy levels. The central peak is a transition from a ground rotational and vibrational state to an excited vibrational level with a ground rotational level; this central feature is not a permitted transition for all molecules giving vibration-rotation absorptions, but it is allowed in methane.[146]

It would also be expected for methane to show a similar absorption from another vibrational mode around 1285cm^{-1}. It is possible that the central peak of this absorption at region E is visible; however most evidence of it has been masked by the presence of water vapour in the atmosphere which causes the large amount of 'noise' from absorptions between $1250-1750\text{cm}^{-1}$ (the noise at $3500-4000\text{cm}^{-1}$ is also due to water vapour).[148] The water vapour is present on all of the spectra, and is likely to be due

to fluctuations in the laboratory atmosphere; some water may be produced by the laser processing, but it is not visible on these spectra.

Region B shows a double absorption band which corresponds to the vibration-rotation asymmetric stretch of CO_2.[149, 146, 147] This is a commonly observed absorption band and fluctuates due to the laboratory atmosphere. The epoxy absorption spectra shows a negative absorption of CO_2 which results from the changes in the CO_2 concentration before the background subtraction. From the results presented, and also previous repeats of this experiment, it can be deduced that epoxy does not produce a significant quantity of CO_2 in comparison to background fluctuations. However, the carbon fibre does, in part, decompose to CO_2 because a more significant absorption can be seen; this result has been repeatable.

Region C shows another double absorption band which can be correlated to the vibration-rotation stretching of CO.[150, 146] This absorption is visible in all of the spectra above, indicating that both the epoxy and the carbon fibre produce CO.

Region D shows a relatively large absorption at $1730 - 1760\text{cm}^{-1}$ which is visible amongst the absorption caused by water in the atmosphere. This region relates to a C=O bond stretch vibration.[147] The most likely source for this absorption is formaldehyde, which would show a significant absorption here[151, 147]; however as other molecules also demonstrate absorption in this region, other tests would be required to unambiguously assign this to formaldehyde. An absorption band around this area has been found in previous thermal decomposition experiments for an epoxy resin and in that experiment it was also concluded that it was likely to be formaldehyde.[72]

In order to analyse a higher fume concentration and better mimic an industrial setup, the Sator laser was used to produce a large quantity of fume in the cell by scanning three $\sim$ 50mm long lines 100 times to cut through the CFRP. The cell was visibly filled with a dense brown ‘smoke’. The FT-IR analysis is shown in figure 5.16. From this it can be seen that the majority of the fume is CO_2 due to the very large absorption which is close to saturating the detector, and far in excess of background fluctuations. The CO

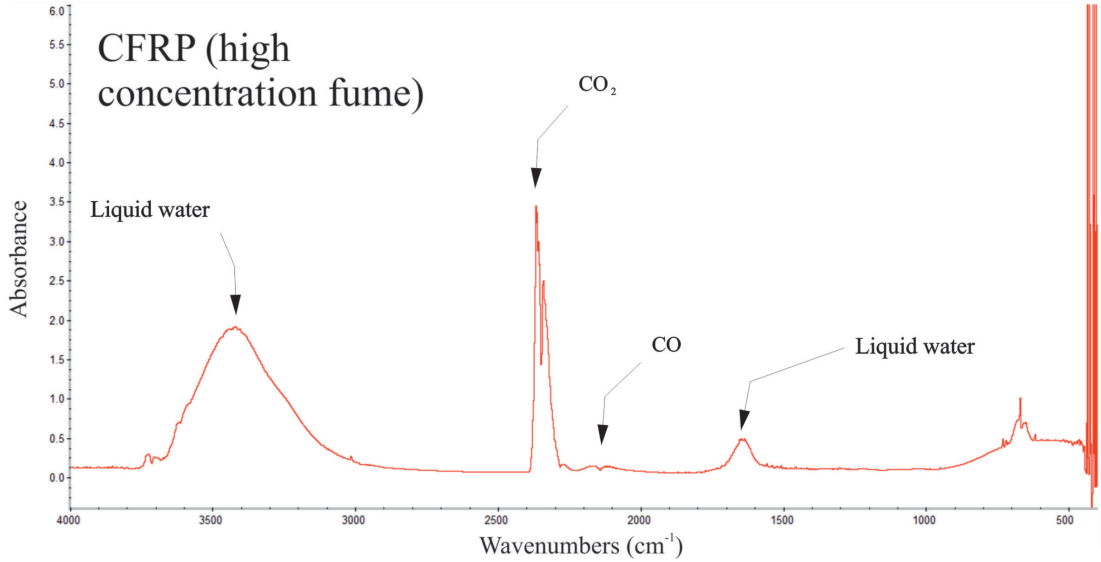

Figure 5.16: FT-IR analysis of a high concentration of fume produced from using a Sator laser to cut three $\sim$ 50mm slots in a CFRP sheet.

absorption is still visible on an expanded scale which means that a significant quantity of CO is produced, although it is much less abundant than the CO_2. For the higher quantity of fume, broad absorptions around $\sim 3400 cm^{-1}$ and $\sim 1650 cm^{-1}$ can also be seen, which are due to liquid water.[148] This suggests that the fume contains water vapour which condenses on the windows. The broad condensed water absorptions are likely to mask evidence of methane and formaldehyde in the spectrum.

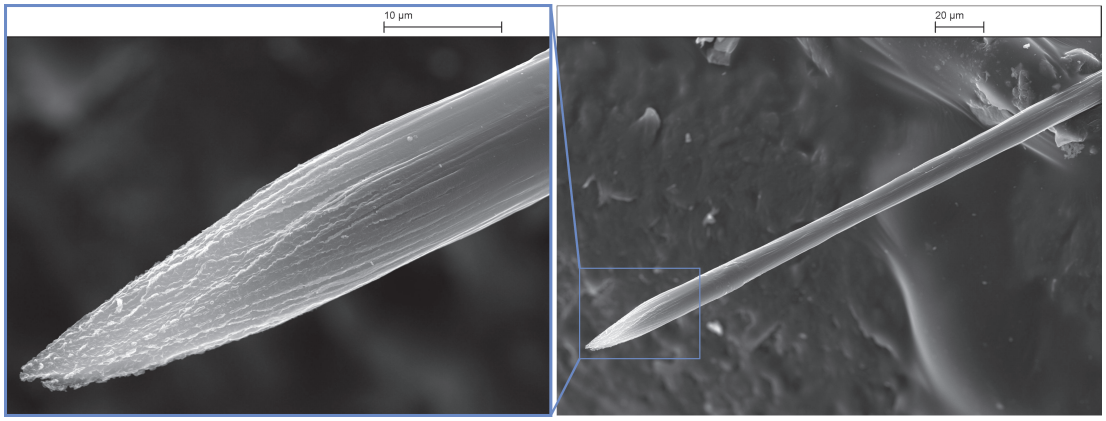

Figure 5.17: SEM of a fibre found around the ablation sites for carbon fibre weave processed with an RF CO_2 laser.

5.3.3 Particle fume capture

After laser processing the CFRP in section 5.2 the sites were examined for debris using an optical microscope. Little was found, though loose fibres were occasionally discovered around the ablation sites for carbon fibre weave, but not the CFRP. A fibre released from the surface of the carbon fibre weave was examined using SEM (figure 5.17). It can be seen that it is pointed at the ends and also has a swollen region next to the point, which was also observed at the edges of the damage sites in section 5.2. After this point the fibre shows no damage, and still has a 7µm diameter. The other end of the fibre looks similar to this. This suggests that the fibre has only been irradiated at its ends, which means that the middle section has not been exposed to the laser energy. From this it can be deduced that the fibre was released from between ablation sites, and the pointed end and swelling is due to the energy from the edges of the Gaussian profile laser beam. The fibre can be released because there was no epoxy to hold the fibre in place, whereas on the CFRP the epoxy would hold a fibre in the sample.

The filter from the CFRP analysis on the isokinetic sampling setup was observed with an optical microscope (figure 5.18). In this image the mesh of the glass fibre filter can be seen. The filter itself is mostly covered in a material which looks like ‘soot’ from the laser interaction (the filter was visibly black). In the filter a few carbon fibre fragments can also be seen, and are identifiable because they are very narrow and straight, and

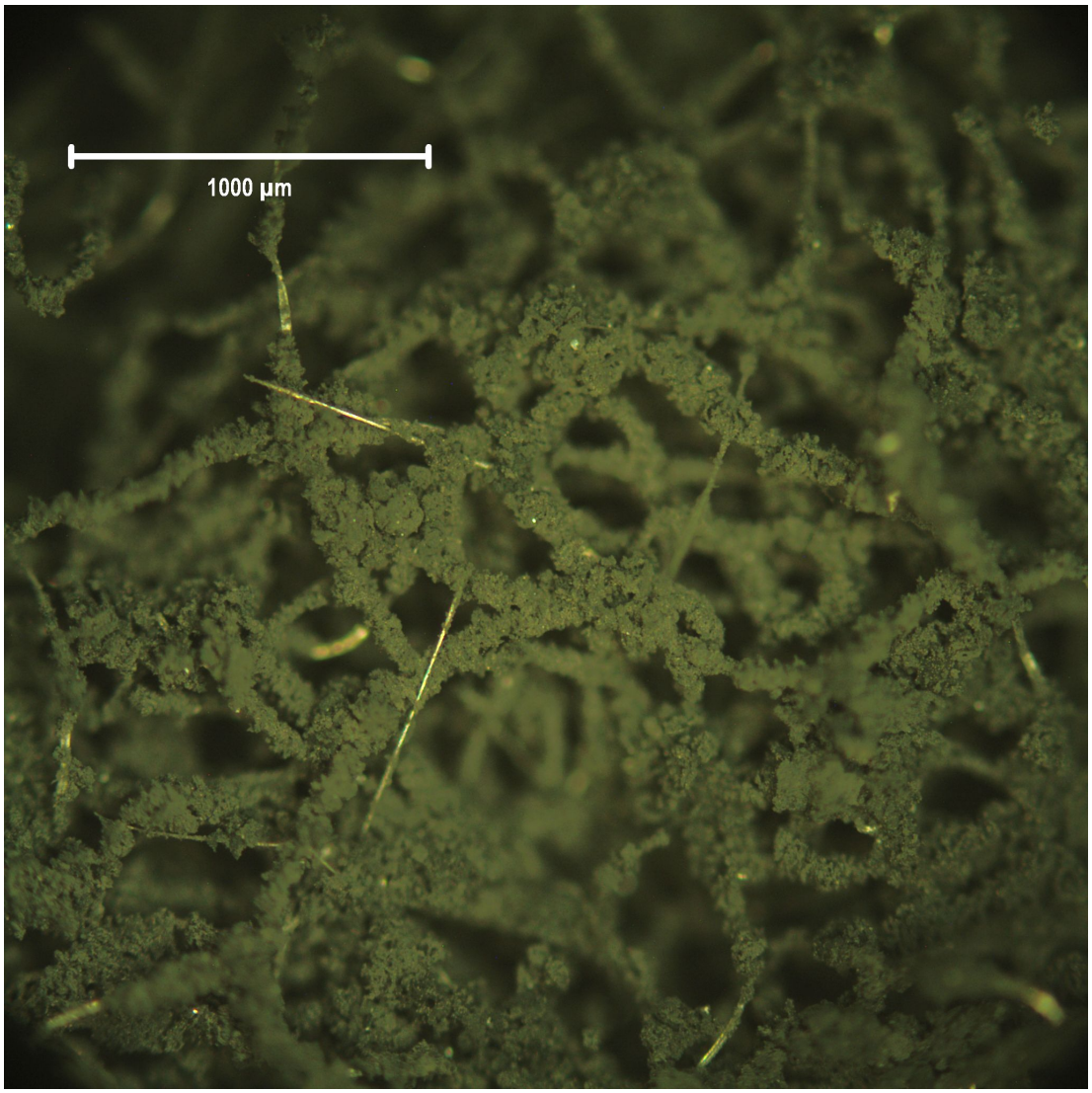

Figure 5.18: An optical micrograph of carbon fibre fragments trapped in a glass fibre filter. This is the result of processing CFRP with an RF CO_2 laser in a Sator system. The location of this filter is shown in figure 5.11 in the larger diameter extraction tube.

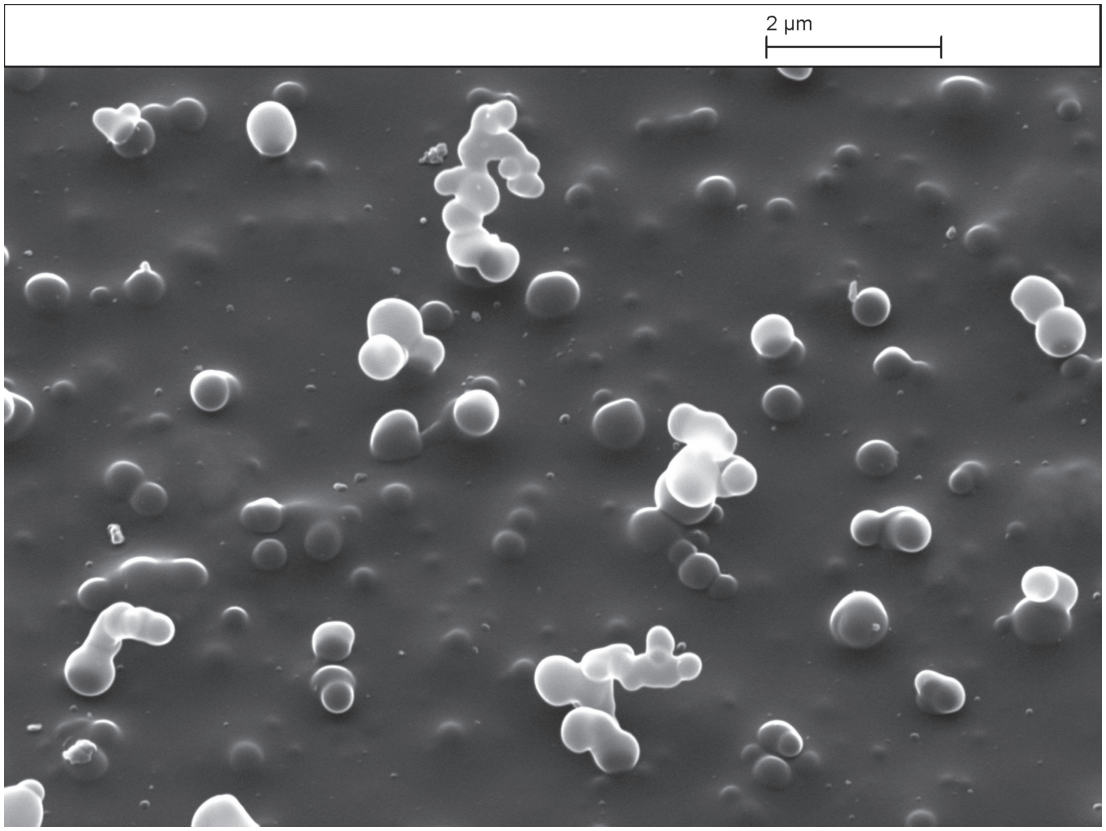

Figure 5.19: An SEM image of the fume from RF CO_2 laser ablation of CFRP deposited onto an SEM stub that had been coated with adhesive.

generally are not covered in the soot which the rest is. From the previous results the carbon fibre decomposes to gas phase material, so the soot is likely to be from the epoxy. This would suggest that the fibres are released after the epoxy has been mostly removed, which would mean that they are no longer held in place by it. Fibres could be released by being 'chopped' at either end, due to the closely spaced concentric squares. Examining the sample after it had been processed, it was revealed that the epoxy had decomposed between the ablation strips, due to the HAZ of the Sator laser.

The 'sooty' deposits which were found on the filter, have also been described in the literature when a gas assist is used during laser cutting of CFRPs.[21] In order to examine them the RF CO_2 laser was focussed onto a sample which was placed at 45° to the optical axis of the laser. An SEM stub with an adhesive pad was placed parallel to the surface and spaced $\sim$ 10mm from the sample. The laser ablated the CFRP with 10 pulses in order to interact with both epoxy and carbon fibres, and ejecta

were deposited onto the SEM stub. The SEM image is shown in figure 5.19. From this $<$ 500nm spheres on the surface can be seen. From previous results it is likely that they are either spheres of phenol which have condensed from the vapour, or soot from the thermal decomposition. It is also evident that there is a very fine particle coating covering some spheres. From previous experiments it is possible to assert that this is not simply the adhesive. This may be a finer carbon deposition from the fibres.

5.4 Conclusions

In this chapter the spot size of the laser has been measured through damage studies, and it will be taken to have a radius of 136 ± 3µm throughout this thesis. The fluence threshold for RF CO_2 laser ablation of RS-M135 epoxy resin was found to be $4.2 \pm 0.5\,\mathrm{J\,cm^{-2}}$. The carbon fibres have been shown to thin before full decomposition under relatively high fluences. At moderate fluences the fibres swell; the combination of these two processes means that when the fibres are ablated with an RF CO_2 laser they have an easily identifiable pointed end. The fluence threshold for the T300 carbon fibres is strongly dependent on the orientation of the fibres with respect to the laser polarization. The ablation threshold is $21.3 \pm 11.2\,\mathrm{J\,cm^{-2}}$ when the fibres are parallel to the polarization, and $14.3 \pm 5.5\,\mathrm{J\,cm^{-2}}$ when the polarization is perpendicular to the fibres. This shows that the energy absorbed by the fibres when the polarization is perpendicular to the fibre direction is $1.5\times$ that of when the fibres are parallel to the polarization, and agrees with the absorption predictions made in chapter 4.

It has been shown that the primary vapour phase fume product of CFRP ablated with an RF CO_2 laser is phenol. The gas phase product is mainly carbon dioxide, but also contains carbon monoxide, methane, and it is likely, formaldehyde. When a large quantity of the composite is cut there is also water vapour present in the fume. Detached fibres have been found around the carbon fibre weave ablation sites, and also caught in the filter in the fume extraction pipe for CFRP. It is likely that these have been ‘chopped’

between ablation sites, but it is not possible to specify because the fibres are difficult to find after the processing is complete.

Both phenol[152] and formaldehyde[153] are hazardous in the case of skin contact, eye contact, ingestion and inhalation. Methane is a flammable, colourless and odourless gas; it presents and immediate fire hazard when concentrations in air are greater than 5%. Methane is also an asphyxiant.[154] Carbon monoxide is a colourless and odourless gas which is extremely toxic when inhaled.[155] Carbon dioxide is an asphyxiant.[156] From this, it is clear that the fume from RF CO_2 laser processing of CFRPs must be treated. It was found that fibres in the fume had been swollen, as opposed to thinned; it follows that released fibres were greater than 7μm in diameter, and therefore not inhalable.[73]

Chapter 6

Laser Processing of CFRPs Part II: Fume dynamics

6.1 Introduction

In this chapter the fume dynamics when an RF CO_2 laser interacts with an epoxy resin, carbon fibre and CFRP are examined. This is achieved by using ultra-fast imaging techniques, the first of which is shadowgraphy, which allows us to directly observe particulate phase fume as it leaves the sample.[75] The second technique is time resolved interferometry, which has been shown to increase the sensitivity of the imaging system, and will enable us to observe gas phase fume via changes in the refractive index.[9] The combination of these techniques will show when the fume starts to leave the sample, which indicates the start of the decomposition, at what velocity the fume is travelling, in addition to allowing the composition of the fume to be observed.

First, the high magnification optical imaging system and the shadowgraphy setup are discussed. Results from this are presented and conclusions drawn from them. Then, how the system was modified to improve its sensitivity by setting it up to form a time resolved interferometer is detailed. Results are presented and analysed. The experimental results are then compared to theoretical predictions from a temperature rise

decomposition model, which uses the thermal and optical characteristics of the epoxy resin which were measured in chapter 4.

6.2 Shadowgraphy

6.2.1 Experimental arrangement

Shadowgraphy is a technique which allows us to observe at high magnification, ultra-fast events in a time resolved fashion[81, 9]. The fundamental idea of the technique is to focus a camera on an area of interest, a short pulse then illuminates the scene while the shutter is held open. In this way the exposure duration is set by the length of the pulsed light source, not the shutter speed.

In our setup the area of interest was an RF CO_2 laser ablation site, and the ultra-fast visible light to expose the camera was provided by a collimated pulse from a dye laser, with a pulse duration of τ_{exp}, see figure 6.1. The RF CO_2 laser, described in section 3.2, was directed perpendicularly to the top of the table via a Au coated mirror. This meant that the target could be placed onto a stage without having to fix it in place. The camera's physical shutter was opened for a duration of τ_{cam}. While the shutter was open, a pulse from the RF CO_2 laser ablated the target. During or after the ablation pulse, at a time delay of t from the start of the RF CO_2 laser pulse, the collimated laser pulse from an excimer laser pumped dye laser, described in section 3.3, was directed through the plume and into the camera to expose it. A full diagram of the shadowgraphy setup is shown in figure 6.2.

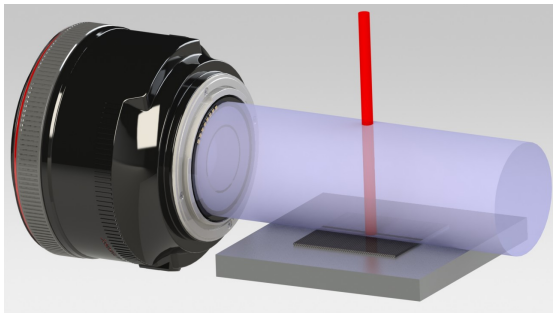

Figure 6.1: A simplified diagram of the ultra-fast shadowgraphy technique. A camera focuses upon the area above an RF CO_2 laser ablation site and a collimated pulse from a dye laser is directed through the ablation plume and into the high magnification camera system.

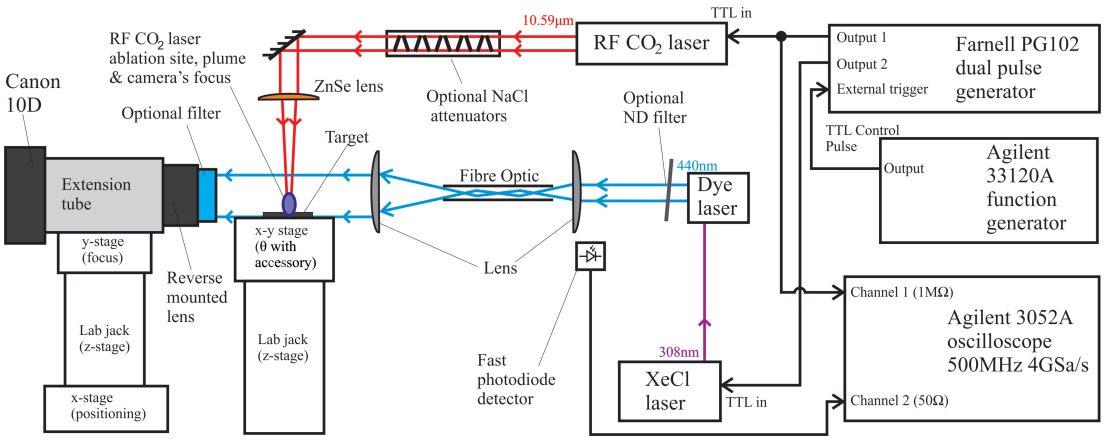

Figure 6.2: A diagram of a shadowgraphy experimental setup. A visible laser pulse is generated from an excimer pumped dye laser; this pulse is collimated and directed through a plume from an RF CO_2 laser interacting with a material and into a high magnification imaging system. The control system to govern the laser timings is also shown.

For the high magnification macro imaging system a Canon EOS 10D DSLR camera was attached to the back of a variable length extension tube. A lens was reverse mounted to the front of the extension tube, forming a macro imaging system. Adjusting the length of the extension tube changed the magnification of the system. The tube was lined with black card to stop reflections in the tube. There was also an optional filter accessory which could be attached to the front of the system and hold a $1''$ diameter band-pass filter. A Centon F/1.8 50mm prime lens and a Carl Zeiss F/3.5 135mm prime lens were available. The aperture on both lenses could be adjusted. A low F/number ($f\#$) allows more light into the system but reduces the depth of focus, whereas a higher $f\#$ reduces the light entering the system but increases the depth of focus. The diffraction limited resolution improves as the $f\#$ is reduced, but at the same time the optical performance is compromised due to an increase in spherical aberration. The Canon EOS 10D[157] had a 6.3 megapixel CMOS sensor with dimensions of 22.7mm by 15.1mm. The electronic gain of the sensor could be varied by changing the ISO setting on the camera. High gain can introduce unwanted electrical noise. The camera was remotely operated by a laptop for convenience and also to aid mechanical stability. An optical diagram of the high magnification system is shown in figure 6.3.

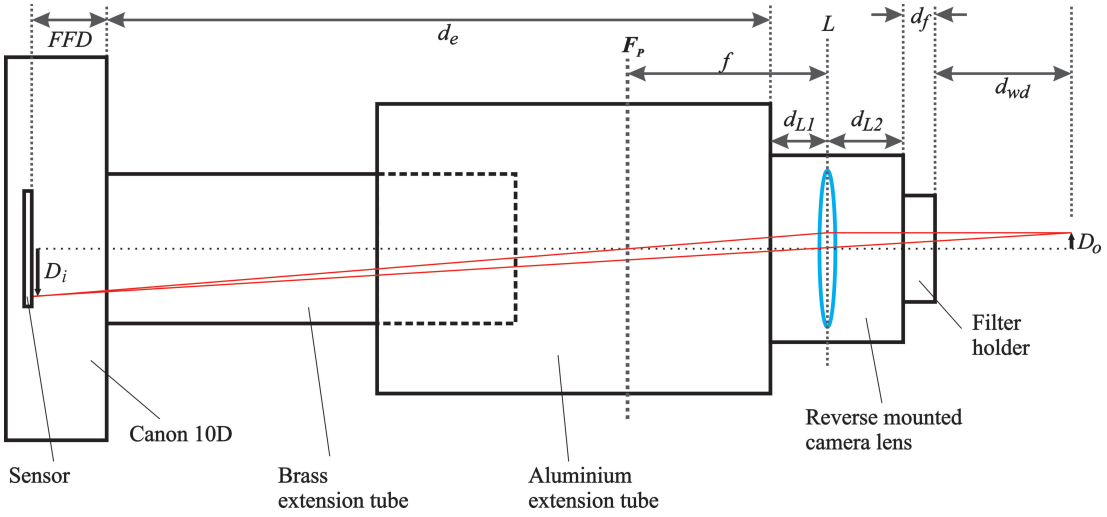

Figure 6.3: An optical diagram of the high magnification imaging system. A lens, with a focal length f, is reverse mounted on an extension tube of length d_e. The lens is simplified to be treated as a single thin lens at a position L. The object, D_o, is magnified onto the camera's sensor to form an image D_i. The magnification of the system, $M = {}^{D_o}/_{D_i}$, and the working distance, d_{WD}, are calculated using the thin lens formula.

The camera prime lenses are systems of multiple lenses within a plastic/metal body. These systems can be simplified to be treated as a single thin lens with the two principal planes located at position L within the body, at a distance of d_{L1} from the conventional front of the lens, and a distance of d_{L2} from the conventional rear. d_{L1} and d_{L2} were measured for each lens by focussing a parallel source of light on to white paper with the lens facing each direction in turn and measuring the distance from the edge of the lens body to the focussed image with a ruler. The length of the body of the lens was also measured. Assuming that the focal length is the same in both directions, $d_{L1}$and d_{L2} and therefore position L could be found. This technique also allowed the focal length, f, to be confirmed for each lens (50mm and 135mm). From this it is clear that the front focal length of the camera is $f - d_{L1}$ and the back focal length is is $f - d_{L2}$.

The focal position, F_P, was a distance of f from L. In both directions f was 50mm from one lens and 135mm from the other. The length of the extension tube, d_e, was measured with a ruler (excluding a section which locks into the body of the camera, and a section which goes into the filter thread on the lens) and could be adjusted between $255 - 370$mm. A ruler was used to measure the thickness of the filter holder, d_f, to be

25mm. The flange focal distance (FFD) is the distance from the mounting flange on a camera body, which allows lenses to be attached, to its sensor. The Canon EOS 10D uses an EF lens mount which has an FFD of 44mm[158].

The Gaussian imaging formula[87, 159, 95, 86], equation 6.1, was used to describe the optical arrangement.

$$\frac{1}{f} = \frac{1}{s_o} + \frac{1}{s_i} \tag{6.1}$$

where s_o is the object distance and s_i is the image distance. The magnification, M, is calculated with equation 6.2.

$$M = -\frac{s_i}{s_o} = \frac{D_i}{D_o} \tag{6.2}$$

where D_i is the image size and D_o is the object size.

The measured values for each lens were used to calculate values for s_i as shown in equation 6.3.

$$s_i = FFD + d_e + d_{L1} \tag{6.3}$$

This allowed s_o and M to be calculated from equations 6.1, 6.2 and 6.3. Finally the working distance, d_{WD}, could be calculated with equation 6.4.

$$d_{WD} = s_o - d_{L2} - d_f \tag{6.4}$$

The theoretically calculated values for several configurations are shown in table 6.1.

The range of accessible fields of view (FoV) and working distances were measured experimentally by focussing the system onto a sheet of paper with a grid with 0.5mm

Table 6.1: A table showing the measured image parameters of the high magnification imaging system for various configurations compared to the theoretical values calculated using the Gaussian imaging formula.

f (mm)	d_e (mm)	Measured			Theoretical		
		FoV (mm)	M	d_{WD} (mm)	FoV (mm)	M	d_{WD} (mm)
50	360	3.0×2.0	7.6	22	3.0×2.0	7.7	22
	235	4.2×2.8	5.4	27	4.4×2.9	5.2	25
135	360	13.0×8.7	1.7	85	11.2×7.4	2.0	92
	235	21.5×14.0	1.1	137	20.6×13.7	1.1	147

divisions printed on it and verified by inspection with a microscope. The paper was illuminated and an image was taken; image processing software was used to calculate the distance to pixel ratio for the particular magnification and image size. A ruler was used to measure the distance from the front of the filter accessory to the grid which the system was focussed to, i.e. d_{WD}. The magnification was calculated from the ratio between the measured FoV and the camera's sensor dimensions. The results are shown in table 6.1.

A Thor Labs[160] 30mm cage system was used to direct light through the interaction. In the initial high magnification setup, the dye laser output was coupled into a BFH-22-200-CUSTOM 0.22NA, high-OH ($190 - 1200$nm), 200µm core, SMA to SMA optical fibre.

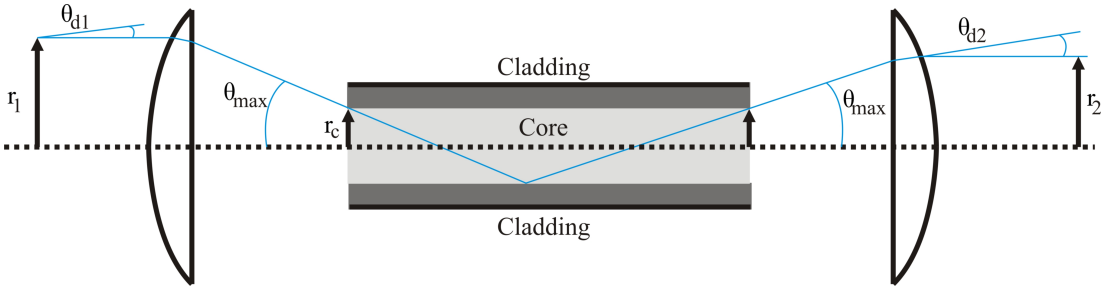

Figure 6.4: A diagram of light being coupled into an optical fibre, and being collimated after it exits it. θ_{max} is the maximum acceptance half angle, which is governed by the numerical aperture of the fibre. r_c is the fibre core radius. r_1 and r_2 are input and output collimated beam radii. θ_{d1} and θ_{d2} are input and output beam divergences.

Figure 6.4 is a diagram of the light from a collimated source being coupled into a fibre optic. The numerical aperture of the fibre was 0.22. This meant that the maximum acceptance half angle, θ_{max}, was 0.22rad. Due to the geometric configuration, equations 6.5 and 6.6 can be written.

$$r_1 = \theta_{max} \cdot f \tag{6.5}$$

where r_1 is the maximum beam radius that can be coupled to a fibre with an acceptance angle of θ_{max}, using a lens with a focal length of f.

$$\theta_{d1} = \frac{r_c}{f} \tag{6.6}$$

where θ_{d1} is the maximum divergence for beam to be coupled with a lens of focal length f, to form a spot smaller than the core radius of the fibre optic, r_c.

The angle at which the light exits the fibre was also governed by the numerical aperture of the fibre, which meant it was also θ_{max}, so the light exited the fibre optic at a half angle of 0.22rad. Substituting r_1 for r_2 in equation 6.5 meant that the collimated output diameter could be calculated for a particular lens. Substituting θ_{d1} for θ_{d2} in equation 6.6 meant that the divergence of the collimated output beam could be calculated in a similar way.

The dye laser was coupled to the fibre using using an AC254-050-A-ML achromatic doublet lens, with a focal length of 50mm and an AR coating suitable for light with a wavelength of $400-700$nm. The focal length of 50mm meant that a beam with a diameter of 22mm or less, coupled using this lens, would have a half angle which fell within the acceptance angle of the fibre. A beam with a divergence of less than 2mrad would have a spot size less than the 100µm radius of the fibre core. The fibre and lens were spaced at a distance of 50mm, and the fibre was attached to a ST1XY-A/M XY translation stage, which meant that the fibre could be aligned to optimize the light

coupled into the fibre. From the results in chapter 3 it can be seen that this system is suitable for use with the dye laser.

The fibre output was collimated with an AC254-100-A-ML achromatic doublet lens with a focal length of 100mm and was coated with an AR coating suitable for light with a wavelength of $400-700$nm. At a distance of 100mm between the fibre and the lens, the collimated light would theoretically have a diameter of 44mm; however, the lens had a diameter of 25.4mm. This meant that the intensity of the collimated beam was reduced due to losses around the edge; however it resulted in a more uniform beam and lower divergence, which was calculated to be 1mrad.

In this configuration the collimated output beam was large enough to illuminate the imaged area. At all times the dye laser had enough energy to use the camera at an ISO value of 100, minimizing noise. A variety of neutral density (ND) filters could be used to attenuate the intensity of the light which reached the camera's sensor if it was overexposed at the lowest ISO available.

The minimum resolvable feature for the shadowgraphy setup was calculated from the diffraction limit formula[95, 86], equation 6.7.

$$r_{diff} = 1.22\lambda f\# \tag{6.7}$$

where r_{diff} is the radius of the airy disc produced from a diffracted point source and λ is the wavelength of the light.

Throughout the experiments the lenses were at their lowest $f\#$, in order to reduce the effects of diffraction. In a standard imaging system this would increase the spherical aberration and decrease the depth optical depth of focus (DoF)[161]; however in a shadowgraphy system the diameter of the collimated pulse of light, $2r_2$, defines the effective aperture (provided that the collimated light is smaller than the aperture opening).[75].

For the 50mm F/1.8 lens the airy disc radius from a point source was 1µm; for the 135mm F/3.5 lens the airy disc radius was 2µm. The airy discs' radii were magnified onto the camera's sensor. Their new radii were calculated and are shown in table 6.2. The maximum resolvable particle velocity (V_{max}) was calculated by considering the velocity at which the circle of confusion's[1] diameter (d_{con}) for the camera sensor would be exposed by the airy disc in the 5ns dye laser pulse, see figure 6.5. The circle of confusion for the APS-C sensor of the Canon 10D was 18µm. This was chosen as the maximum acceptable blur for an image. The maximum velocities for each magnification are shown in table 6.2.

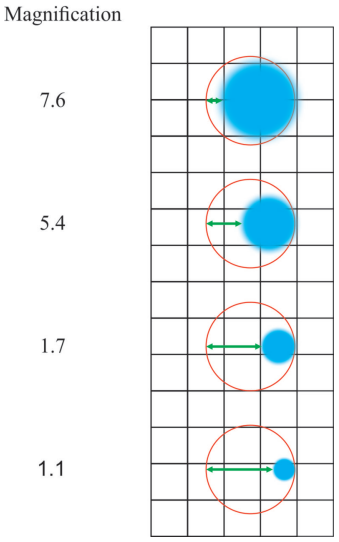

Figure 6.5: A diagram showing the diffraction limited airy disc for various magnifications (blue circles), compared to the circle of confusion (red circles) and the size of the pixels in the background. The green arrow shows the distance which the airy disc would have to move to cross the diameter of the circle of confusion. From this distance, and using the dye laser pulse duration, the maximum resolvable velocity was calculated.

The optical depth of focus, (DoF) for a shadowgraphy system is calculated with equation 6.8.[75]

$$DoF = 2 \cdot d_{con} \frac{f}{2r_2} \frac{M+1}{M^2} \tag{6.8}$$

The calculated values are shown in table 6.2.

The target was placed upon an x-y stage with micrometer barrel adjustment. This was in turn mounted on a lab jack that allowed the sample to be brought into the focal plane

[1]The circle of confusion is commonly defined as $1/1500$ of the diagonal size of the camera sensor. This is the maximum acceptable size for a point source to appear on the sensor, so it is used to define the parameters for acceptable sharpness.[162, 95]

Table 6.2: A table showing calculated diffraction limitations of the camera in various configurations, and the corresponding maximum resolvable velocities. The depth of focus is also shown; it should be noted that the depth of focus here is calculated with measured values.

Camera configuration	r_{diff} (µm)	V_{max} ($m\,s^{-1}$)	DoF (µm)
50mm F/1.8 max. mag.	7.6	560	11
50mm F/1.8 min. mag.	5.4	1440	16
135mm F/3.5 max. mag.	3.4	2240	181
135mm F/3.5 min. mag.	2.2	2720	335

of the RF CO_2 laser as described in section 3.2. Once the laser's focus was found, the camera's focus could be moved to the ablation site. This was achieved by marking a target with the RF CO_2 laser to locate the ablation spot, and placing the printed calibration grid at this point, ensuring that the paper was flat and perpendicular to the line of site of the camera.

The camera's field of view was moved to the ablation site with the x and z axes of the camera's stage.The depth of focus was very small so a fine micrometer barrel activated y-stage was used to focus the camera to the pattern. If the band-pass filter was added or removed, the optical path length changed, and therefore it was necessary to refocus the system.

Once the system was aligned, a reference point in the viewfinder of the camera was set to line up with the surface of the target and the lab jack locked in place. Thicker or thinner samples could then be moved to the reference point using the lab jack holding the target, thus ensuring that the RF CO_2 laser was focussed correctly and that the laser spot size was consistent for all experiments and samples. The target stage's x-y micrometer barrels were used during experiments to move to fresh ablation sites.

During shadowgraphy experiments, various sources of stray light needed to be considered. The first was ambient light from within the room. With a regular camera lens in an illuminated room, a 2s exposure would generally saturate the sensor. Using the high magnification system little ambient light reached the sensor, but with the main

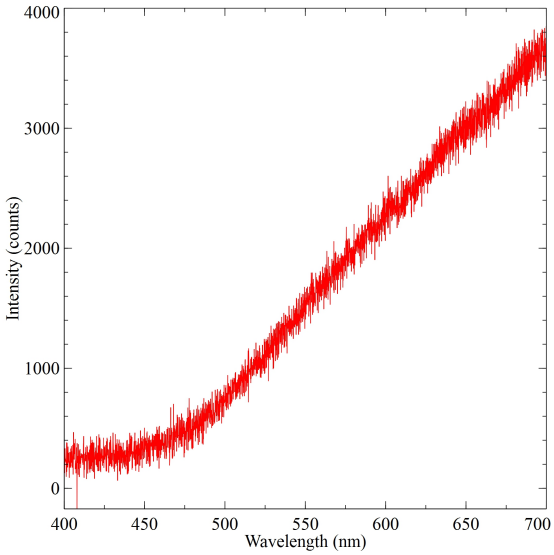

Figure 6.6: A plume spectroscope graph of carbon fibre weave being processed with an RF CO_2 laser. The integration time on the spectrometer is 1*s* and the laser was set to a *PRR* of 10Hz.

room lights on white hazes were seen on images, originating primarily from reflections off Al surfaces. Dimming the main lights in the laboratory and working with a desk lamp was sufficient to eliminate this.

The other source of light was from the laser interaction itself, such as flames and plasmas. Usually the light from the plume was blocked with an optical band-pass filter centred at the dye laser wavelength because it could hide details and was not time resolved. However, this light also carried useful information and was sometimes allowed to co-expose the scene together with the dye laser pulse. Care was taken to choose a dye laser wavelength that did not coincide with a strong emission from the plume so that the two 'signals' could be extracted.

Self illuminating plumes from laser ablated carbon fibres had been observed on earlier, unfiltered shadowgraph images in preliminary experiments as yellow/orange ($\lambda \sim$ 600nm). To get a more accurate representation of the self illuminating plume emission spectrum, plume spectroscopy was used. An Ocean Optics USB4000 spectrometer with a 1200mm^{-1} grating was directed so that its aperture faced the ablation site. The integration time was set to 1s. The lights were dimmed and a background spectrum recorded and subtracted. The RF CO_2 laser was pulsed at 10Hz processing carbon

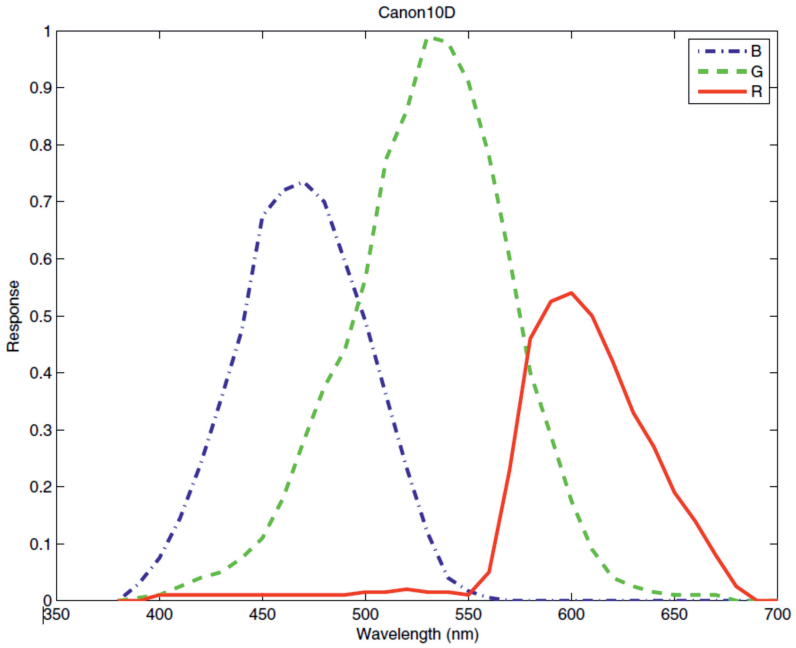

Figure 6.7: A plot of the red, green and blue pixel sensitivities of the CMOS sensor used in the Canon 10D.[163]

fibre weave. The sample was moved using the x-y stage while it was being processed. From this, the spectrum in figure 6.6 was acquired.

From figure 6.6 it can be seen that the optical emission from the plume is towards the red end of the spectrum, so a dye laser with an output wavelength of 440nm (blue), used with a corresponding filter, was a suitable choice for our experiments. The wavelength was also a suitable choice for maximizing the sensitivity of the blue pixels in the Canon 10D sensor (figure 6.7). The filter chosen was a Thor Labs FB440-10 which had a peak transmission of 45% at 440 ± 2nm and a bandwidth with a FWHM of 10 ± 2nm.

A graph of the lasers' pulse timings is shown in figure 6.8. Triggering the pulsed excitation of the dye laser and also gating the RF generator for the CO_2 laser was achieved using a Farnell PG102 dual pulse generator, as it can control and output two pulses and the delay between them. One pulse output, with a pulse duration of τ', controlled the RF CO_2 laser pulse width, τ, shown in more detail in section 3.2. The second output was a short pulse which triggered the XeCl laser. The width of this did not affect the pulse duration of the XeCl laser, the important part being the delay with

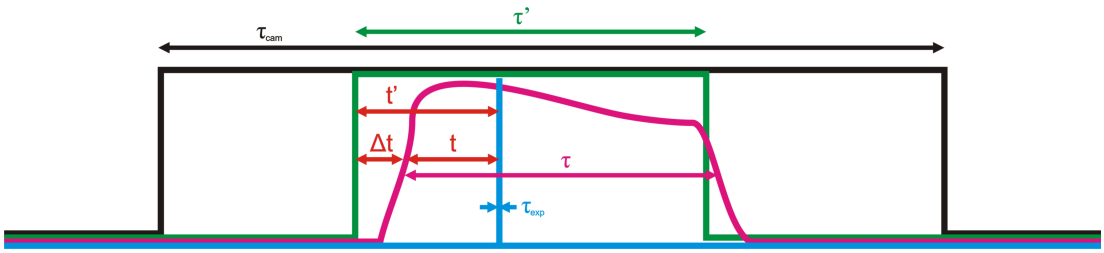

Figure 6.8: A timing graph of the system inputs and outputs used in the shadowgraphy setup (not to scale). τ_{cam} is the Canon 10D DSLR physical shutter duration. τ' is the pulse from the output of the dual pulse generator to the input of the RF CO_2 laser used to control its pulse duration, τ. τ_{exp} is the dye laser duration, as measured with a photodiode so there is no delay to be corrected. Δt is the delay between the start of the input from the dual pulse generator and the start of the optical emission from the RF CO_2 laser. t' is the time between the start of input pulse from the dual pulse generator and the dye laser pulse, measured on the oscilloscope. t is the corrected time between the start of the RF CO_2 laser pulse and the dye laser pulse ($t = t' - \Delta t$).

respect to the RF CO_2 laser input pulse. This delay was varied to achieve the required delay between the start of the RF CO_2 laser pulse and the dye laser pulse. The dye laser pulse was monitored using the fast photodiode described in section 3.3, rather than the input pulse to the XeCl laser to eliminate uncertainties caused by a delay between the input pulse and the gas laser discharge. The timing between the start of the input pulse to trigger the RF CO_2 laser and the pulse from the fast photodiode was measured using an Agilent InfiniiVision DSO-X 3052A oscilloscope; this is defined as t'. The timing delay, Δt, shown in section 3.2, was subtracted from t' to get the time through the laser interaction, t, at which the camera was exposed. The pulse generator was triggered using an Agilent 33120A function/arbitrary waveform generator; this was chosen because the *PRR* can be set to < 1Hz.

To carry out the shadowgraphy experiment a labelled sample was placed on the target holder. The camera's exposure time was set to $\tau_{cam} = 2$s. The output from the RF CO_2 laser was blocked with a slab of graphite. The function generator was set to run at a frequency of 0.5Hz with laser pulse durations of $\tau = 1$ms. The RF CO_2 and XeCl/dye laser systems were operated at a fixed frequency to improve consistency between pulses. This rate was chosen because it meant that one exposure could be

recorded while the camera's shutter was open for 2 seconds. When a shadowgraph image was to be taken, the camera was triggered in between sets of laser pulses (in the 2s gap). The graphite slab was moved aside allowing one RF CO_2 pulse through. After the ablation and illumination pulses the slab was placed across the RF CO_2 laser path to block it again. The value of t' for the image was recorded, along with a reference to the digital image file for analysis. Through the experiment t' was varied to get a range of delays. The target was moved to a new ablation site between images. The NaCl windows discussed in section 3.2 were used to vary the power, pulse energy and irradiance of the RF CO_2 laser in order to take sets of data as a function of these parameters. The images were made clearer by processing them to greyscale.

6.2.2 Results & analysis

Shadowgraphy results of cast epoxy resin being laser processed at an irradiance of $69.9 \pm 7.5 \text{kW cm}^{-2}$, using an RF CO_2 laser and a magnification of 7.6 on the optical imaging system are shown in figure 6.9. In figures 6.9a, 6.9b and 6.9c it can be seen the fume from the epoxy progresses as the time after the start of the laser pulse increases. Figure 6.9d shows the plume much later in the interaction. This is as far as the epoxy fume can be traced at this irradiance; if images are taken at greater times through the laser pulse, the fume does not appear to progress any further. Disturbances in the speckle pattern in the illumination would suggest that there is fume there, but it cannot be resolved by the shadowgraphy system.

Figure 6.10a shows a plot of fume propagation distance with time through a 1ms laser pulse for various irradiances incident on cast epoxy resin. Each point on the graph has been obtained from a shadowgraph image like those in figure 6.9. The plume progression distances were measured in pixels for each image, and were converted to a physical distance using the calibration in section 6.2.1. The time through the interaction was recorded using the oscilloscope and corrected for the offset shown in figure 6.8. The maximum resolvable height (distance from the sample) of the plume

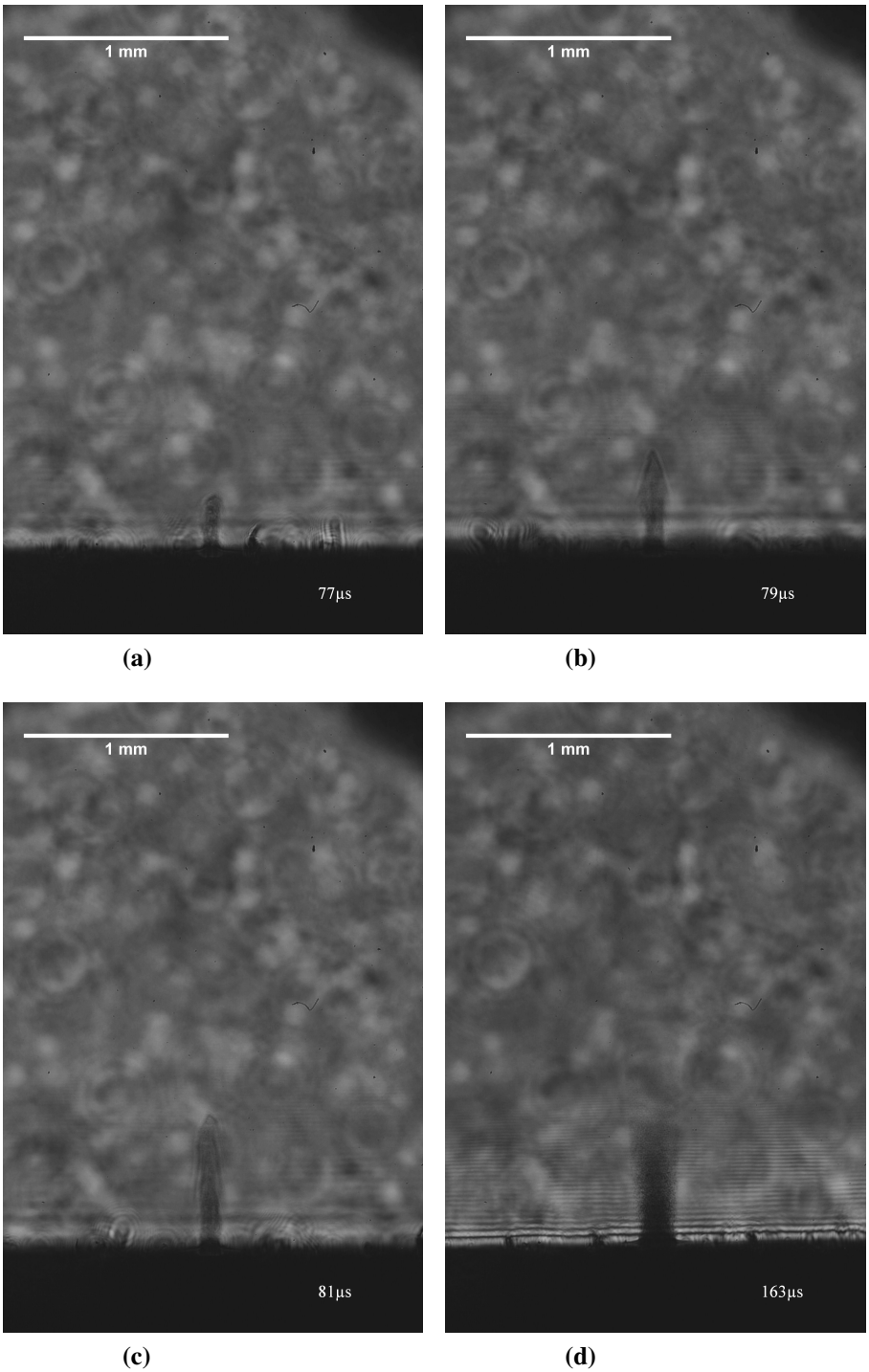

Figure 6.9: Shadowgraph images of cast epoxy resin processed with an RF CO_2 laser at an irradiance of 69.9 ± 7.5kW cm^{-2}. 6.9a is 77µs through the laser interaction and the fume has travelled 278µm. 6.9b is 79µs through the interaction and has travelled 506µm. 6.9c is 81µs through the interaction and has travelled 668µm. 6.9d is 163µs through interaction and the fume which is visible to the imaging system has travelled 923µm; however, there is evidence to suggest that the fume has progressed further than this.

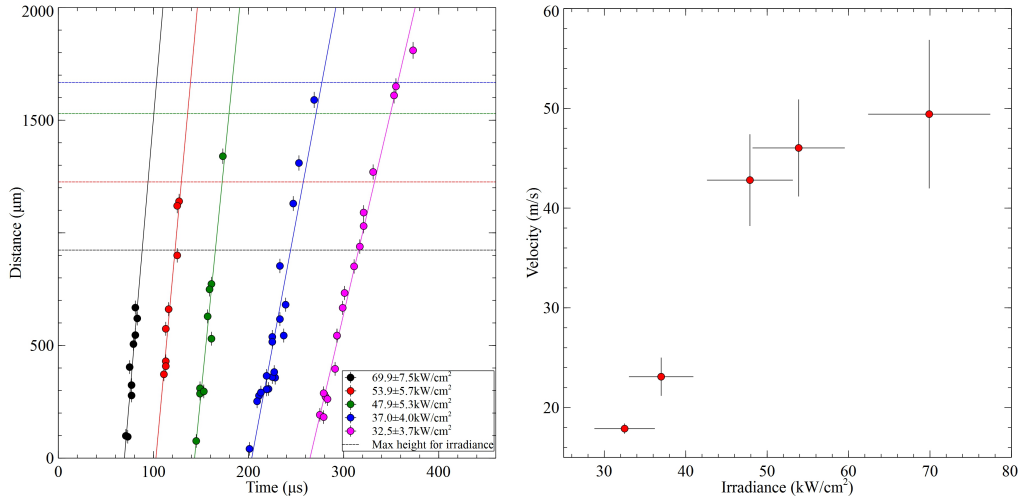

Figure 6.10: 6.10a is a graph of the propagation of the fume from an RF CO_2 laser ablating cast epoxy, with respect to time through the interaction, for various irradiances. Each point on the graph is determined from an image like those shown in figure 6.9. The maximum distances from the sample for which the fume is visible to our imaging system for the particular irradiances are also shown. 6.10b shows the velocity of the plume leaving the surface of the sample for various irradiances.

is also shown on the graph for each irradiance, calculated from figure 6.9d and the equivalent for other irradiances. Beyond this disturbances can be seen which could be gas, temperature gradients or particulates which were too small for the camera system to resolve.

The velocity of the plume expansion was calculated from the gradient of the regression line as a function of irradiance in figure 6.10a and the results are shown in figure 6.10b.

From figure 6.10a it can also be seen that the x-intercept, i.e. the time until the fume starts to leave the sample, varies significantly with irradiance (figure 6.11a). This is not surprising because when the irradiance is lower, it will take longer to deliver the same fluence; however, plotting figure 6.11b it is clear that the fluence delivered before the material starts to decompose also varies with irradiance. This means that the mechanism is not a simple energy loading process.

Figure 6.12 shows results for T300 carbon fibre weave processed with an RF CO_2 laser

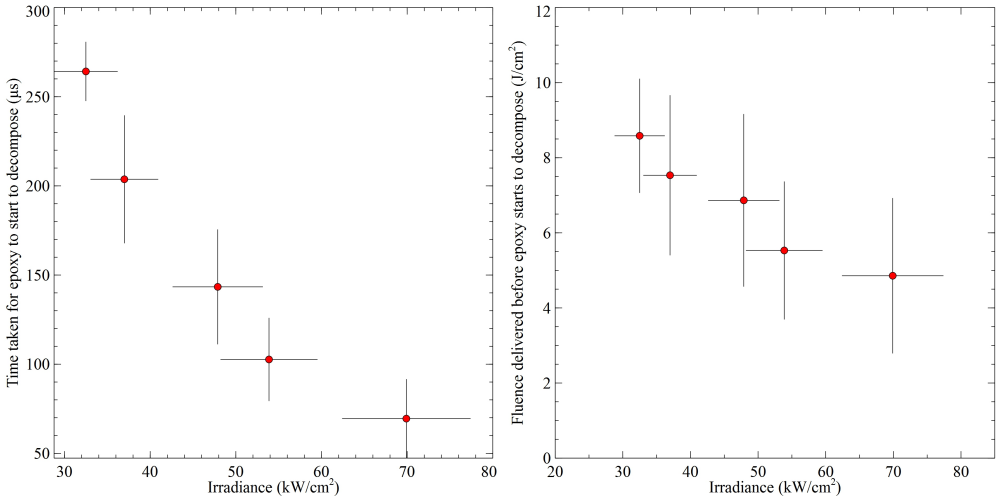

Figure 6.11: 6.11a shows the time taken for epoxy to start to decompose when ablated with various irradiances using an RF CO_2 laser. 6.11b shows the corresponding fluence delivered before the epoxy starts to decompose.

at an irradiance of $60.6 \pm 3.0 \text{kW cm}^{-2}$. The band-pass filter was attached for these results because a luminous plume from the laser interaction with the carbon dominated the images if it was not blocked from exposing the camera. In figure 6.12a it can be seen that the system was not sensitive enough to observe any fume, either gas or particulate phase. However, fibres were occasionally observed being released from the surface, as shown in figures 6.12b, 6.12c and 6.12d. This was not a frequent occurrence, however. It should be noted that the fibres leaving the surface were observed after the 1ms laser interaction had ended.

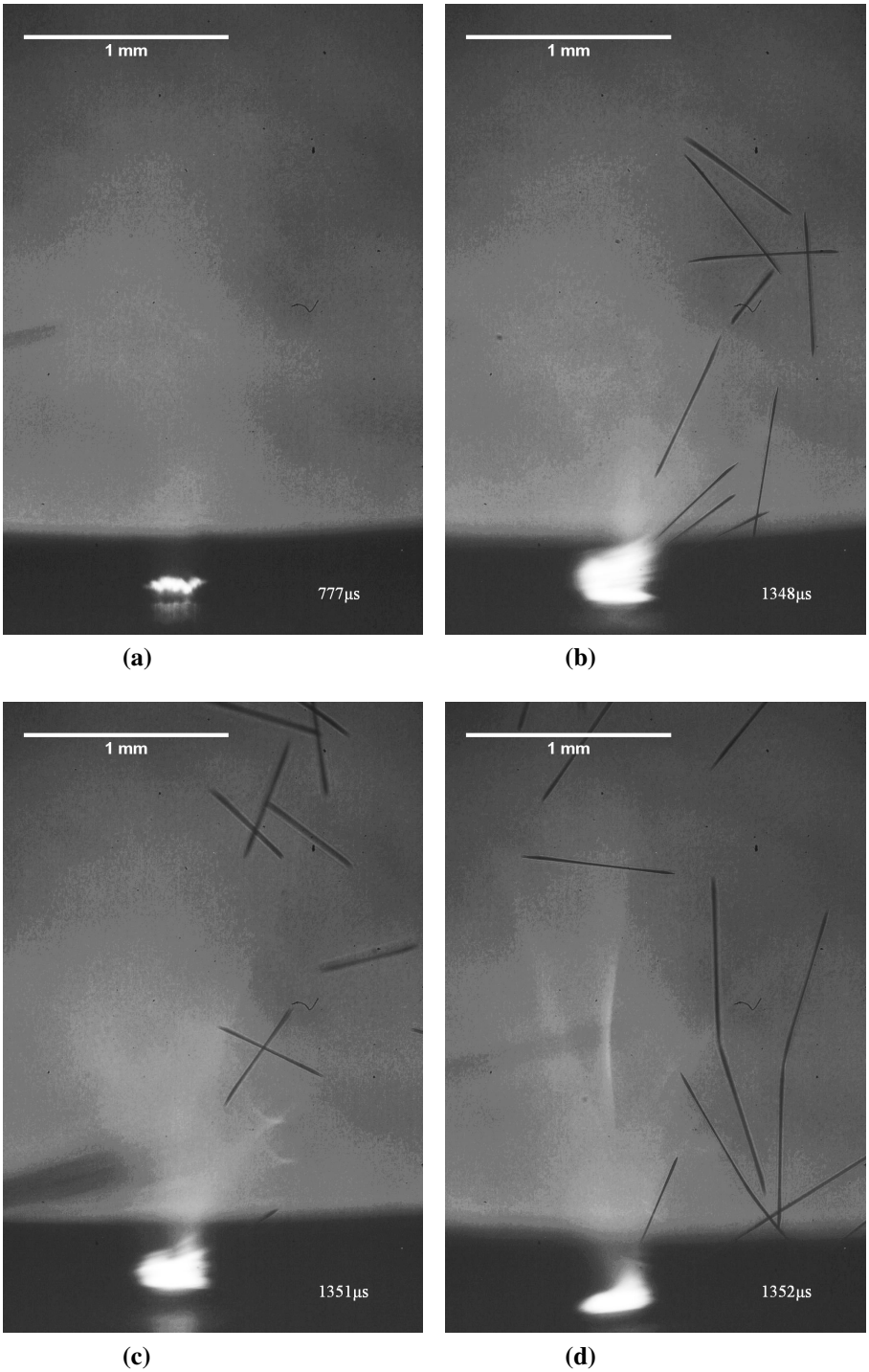

Figure 6.12: Shadowgraph images of T300 carbon fibre weave being processed with an RF CO_2 laser at an irradiance of $60.6 \pm 3.0\text{kW}\,\text{cm}^{-2}$. 6.12a is a typical shadowgraph image of what is seen when laser processing carbon fibre weave; this image is 777µs through the laser interaction. 6.12b, 6.12c and 6.12d show fibres being ejected from the surface. These images are all around 1350µs after the laser pulse has begun (note that this is 350µs after the laser pulse had finished).

6.2.3 Discussion

From the shadowgraphy results it can be deduced that the sensitivity of the system is not high enough to observe fume from epoxy past a particular distance (governed by irradiance) from the surface. Comparing images, a disturbance in the speckle pattern in the shadowgraphs in areas where it would be expected to see fume suggest that fume is present but is not resolvable. This could be due to the epoxy fume itself decomposing as it left the sample to either gas phase, or particulate phase which was too small to be resolved by the imaging system. Therefore information may be missing about the plume dynamics. It is not of interest to reduce the magnification and increase the field of view for epoxy using a shadowgraphy setup, as the optical resolution would decrease, and it is known that all of the resolvable fume can be viewed for the chosen irradiances used in a small field of view.

Under normal circumstances the fume from laser processing the carbon fibres is not visible. However, as with epoxy, disturbances point to unresolvable fume being present, either due to it being gas phase, or a very fine particulate ejecta. Carbon fibre fragments being released from the surface can be observed; however, it is rare to capture such an occurrence using a small field of view.

For these reasons, it would be beneficial to reduce the magnification of the system, while keeping the optical resolution as high as possible; at least 7µm resolution is required so that the carbon fibre with a diameter of 7µm can be resolved. It would also be beneficial to increase the sensitivity of the system so that gas phase and fine particulate phase fume can be observed. All these criteria were expected to be fulfilled using the time resolved interferometry system described in the next section.

6.3 Time resolved interferometry

6.3.1 Experimental arrangement

The shadowgraphy setup in section 6.2 was modified to create a time resolved interferometry system (TRI), (figure 6.13). The fundamental components behind the system remained the same; however, the collimated output from the dye laser was directed into a Michelson Interferometer, and the target for the RF CO_2 laser interaction was in one of its arms. The imaging system could then focus on the ablation site through the beamsplitter, and observe the plume via disturbances in the interference fringes, see section 2.6. The 135mm F/3.5 lens was used to image the scene in order to increase the field of view for the system. It also significantly increased the working distance; this was important for the time resolved interferometer as the camera needed to observe through the beamsplitter to the area of interest.

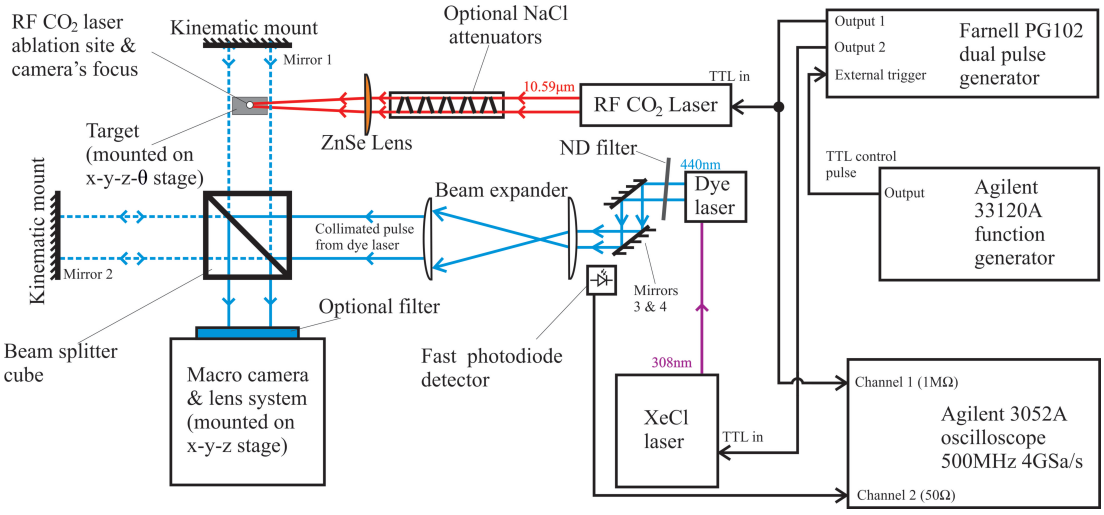

Figure 6.13: A diagram of the fast photography system, modified using an interferometer to make a fast, time resolved interferometer to observe the gas and particulate fume from an RF CO_2 laser interacting with a material.

The Michelson interferometer was arranged using a 30mm cage system with parts from Thor Labs[160], see figure 6.14. The beamsplitter was a non-polarizing 50:50 beamsplitter cube with an AR coating to minimize reflections in the wavelength range

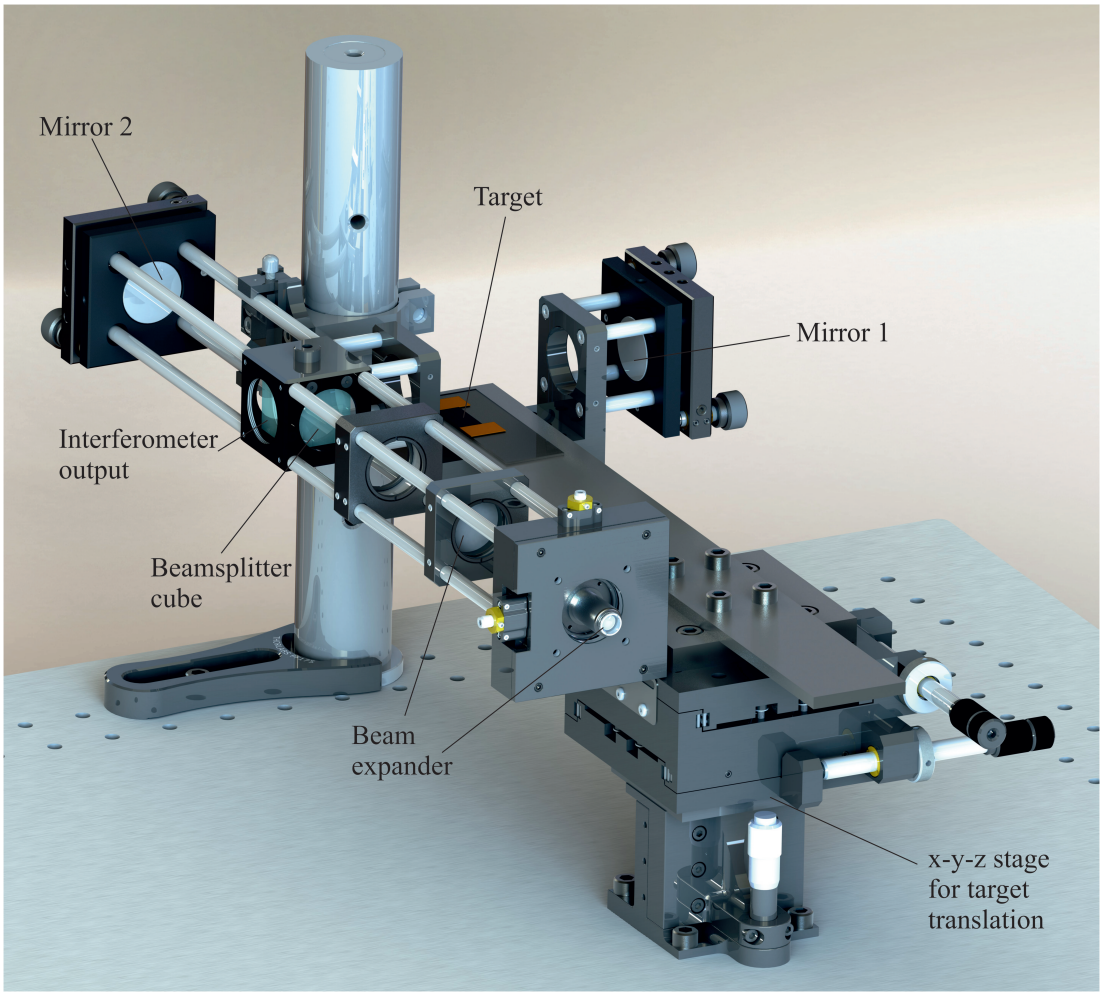

Figure 6.14: A render of the time resolved interferometry, setup using a Thor Labs 30mm cage system, created using SolidWorks 2011 Education Edition.

of $400-700$nm. The beamsplitter had 4 apertures with $1''$ diameters. Two $1''$ diameter broadband dielectric mirrors, suitable for light with a wavelength of $400-750$nm, were mounted in kinematic mounts, and attached to arms to reflect the light back to the beamsplitter cube. One kinematic mirror was spaced from the beam splitter cube with rods, and this is labelled as 'Mirror 2' in figures 6.13 and 6.14. The other was spaced using rods and a U-bench, and is labelled as 'Mirror 1' in figures 6.13 and 6.14. This formed an interferometer with a space in one of the arms, created by the U-bench, to place samples for analysis. The interferometer was then securely mounted to the optical table with a $1.5''$ diameter post.

For the time resolved interferometry setup, the dye laser beam was directed into a

beam expander[159] which was directly attached to the beamsplitter cube of the interferometer. The beam expander was made from a 13.86mm focal length aspheric lens and an achromatic doublet lens, with a focal length of 100mm; both lenses had an AR coating suitable for light with a wavelength of $400-700$nm. The lenses were mounted in cage plates and spaced at a distance of 113.86mm initially. This meant that the beam expander would collimate the beam and expand it by 7.2 times. This was sufficient to expand the dye laser beam, at a distance of 1m between the laser and the beam expander, to fill the $1''$ aperture of the interferometer with a uniform beam.

Two UV enhanced aluminium mirrors, which were suitable for wavelengths of $250-450$nm, were mounted in kinematic mounts. These are labelled as 'Mirrors 3 & 4' in figure 6.13. These mirrors were used to align the dye laser through the centre of the beam expander (and Michelson interferometer system). By removing the fibre optic beam delivery the optical quality of the system increased because the 'speckle' interference pattern from the fibre was reduced. It also made alignment easier.

The same x-y-z-ϑ stage as in section 6.2.1 was used, but with a $350 \times 40 \times 5$mm steel bar attached to it to place the sample in the U-bench (figure 6.14. The steel bar and stage was separate from the interferometer so the alignment wasn't changed when moving the sample. The RF CO_2 laser was focussed to a point in the middle of the collimated beam of light. The camera was then directed into the output of the beamsplitter cube and focussed to the RF CO_2 laser ablation site by placing a pin at that location. It should be noted that the working distance of the camera changed when observing a point through the beamsplitter cube due to the change in optical path length.

The collimation of the dye laser was finalised by observing output on the camera. At this point it was noted that the beam entering the camera was not collimated as before. At position L on figure 6.3 the diameter of the beam was 16mm. Using equation 6.8, the depth of focus increased to 283.8μm. Mirror 1 was aligned so that it was perpendicular to the collimated dye laser beam. Mirror 2 was then used to setup interference fringes, first with a Coherent Inc. HeNe laser[98] with a long coherence length

Figure 6.15: A cropped section of an interferometry image taken for this set of experimental results, and used to calculate the fringe visibility.

to find the fringes initially. Using the dye laser the coherence length was predicted to be $70-90\mu$m (section 3.3), so vernier callipers were used to make the distances from the beamsplitter to the mirrors as close as possible, before 'walking' mirror 2 to find the fringes. A high quality optical mount was required so that the mirrors could be aligned within the coherence length (a KC1/M mount was used)[160]. When the fringes were of as high a contrast as possible, the final adjustment to get the fringes straight, horizontal and spaced as required could be performed.

Due to the change in collimation of system, the image mm:pixel ratio was recalibrated using a pin at the camera's focus. The pin was measured in several places along it using a micrometer, and this was compared to the diameter in pixels on the image.

A more detailed explanation of the interferometer and its setup procedure is included in appendix B.

The 'direction' of the fringes was calibrated by replacing mirror 1 with an SM1Z fine translation stage. The dye laser was pulsed at a *PRR* of 10Hz and the interference fringes were observed as the optical path length was adjusted using the stage. It was found that in the configuration used in this thesis, a fringe shift 'downwards' corresponded to a reduction in optical path length.

The visibility of the system is a way to quantify the contrast between the light and dark fringes, and could be measured using the technique described in section 2.6. A blank TRI image from the system was used to measure the visibility of the system. A section of the image was cropped and is shown in figure 6.15. The image was processed using Mathematica by averaging the intensity of the pixel columns, and plotting the average column intensity against the x-position pixels. This is shown in figure 6.16. The intensity is the sum of the red, green and blue pixels for that position, with 1 being

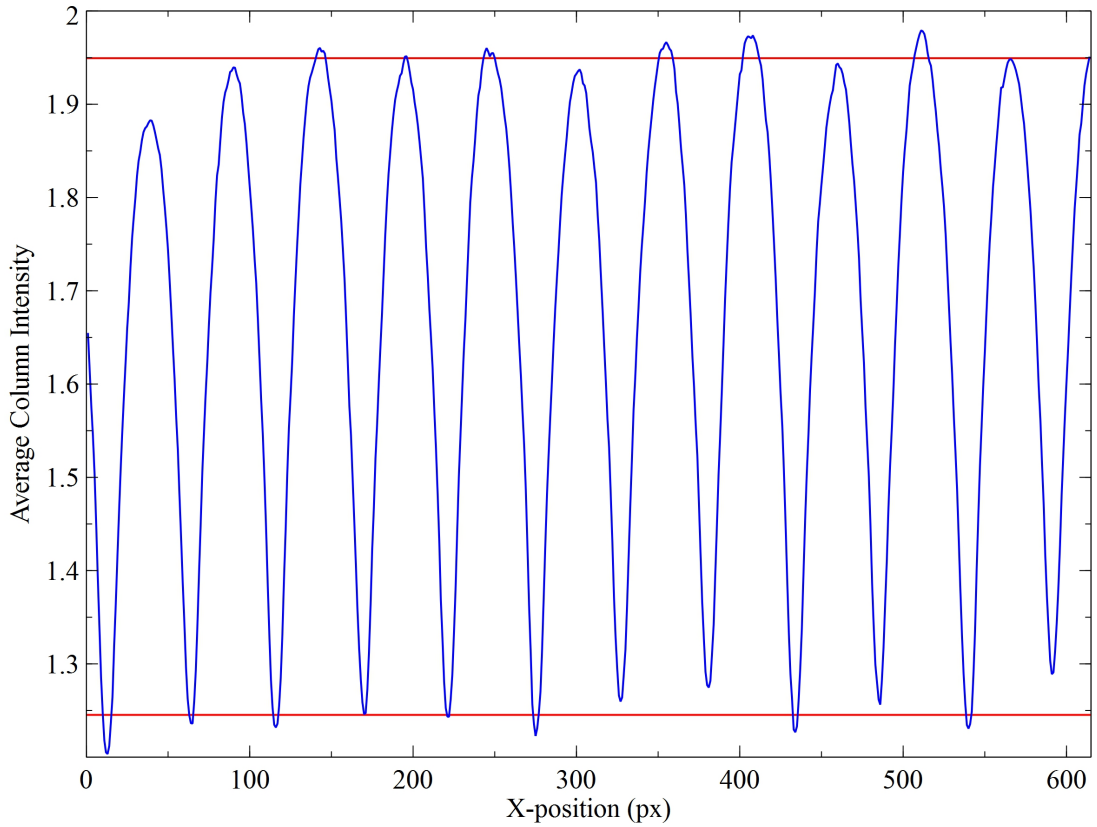

Figure 6.16: A graph displaying the average column intensity for x-position pixels for the image in figure 6.15. The average maxima and minima intensity is shown on the graph by the red lines.

the maximum intensity for a pixel colour, and therefore a fully white pixel's intensity would be 3.

The maxima and minima of figure 6.16 were averaged and are displayed as red lines on the graph. These values were then used to calculate the fringe visibility from equation 2.6 as 0.22.

The time resolved interferometry fume analysis experiments were carried out in the same way as section 6.2.2, but with samples processed with the RF CO_2 laser placed on the U-bench in the interferometer.

6.3.2 Results & analysis

Epoxy resin

Time resolved interferometry results of cast epoxy resin being laser processed at an irradiance of $72.2 \pm 1.6\text{kW cm}^{-2}$, using an RF CO_2 laser and using a magnification of 1.7 on the optical imaging system are shown in figure 6.17. Note that the images were not filtered. Due to the increased sensitivity by using the interferometer, the fume can be traced to the edge of the field of view, which is a distance of $\sim$ 10mm; at a similar irradiance using a shadowgraphy setup the fume could not be resolved past a distance of $\sim$ 1mm.

The technique was used to take a series of images at different times through the interaction and the distance travelled by the fume was measured. A graph of distance vs. time was plotted for various RF CO_2 laser irradiances, shown in figure 6.18a.

It can be seen from figure 6.18a that the propagation of the plume no longer appears linear. The fume is released from the surface at a particular velocity after a time delay for the irradiance used. The plume slows as it gets further from the sample. Towards the edge of the field of view it can be seen that the gradient, and therefore velocity, of the graph is approaching zero, i.e. the fume would be diffuse and under the influence of gravity and air turbulence.

In order to calculate the time through the laser interaction with the material when the material starts to leave the sample, and its velocity the results from fume distances of $<$ 5mm from the surface have been expanded and presented in figure 6.18b. It was assumed that the fume in this region was progressing linearly. From figure 6.18b the average velocity in the first 5mm which the plume travelled was extracted, shown in figure 6.18c. The value at which the line of best fit crossed the x-axis was calculated; this was defined as the time at which the epoxy started to decompose as it was the time when material began to leave the sample. The time at which the epoxy starts to

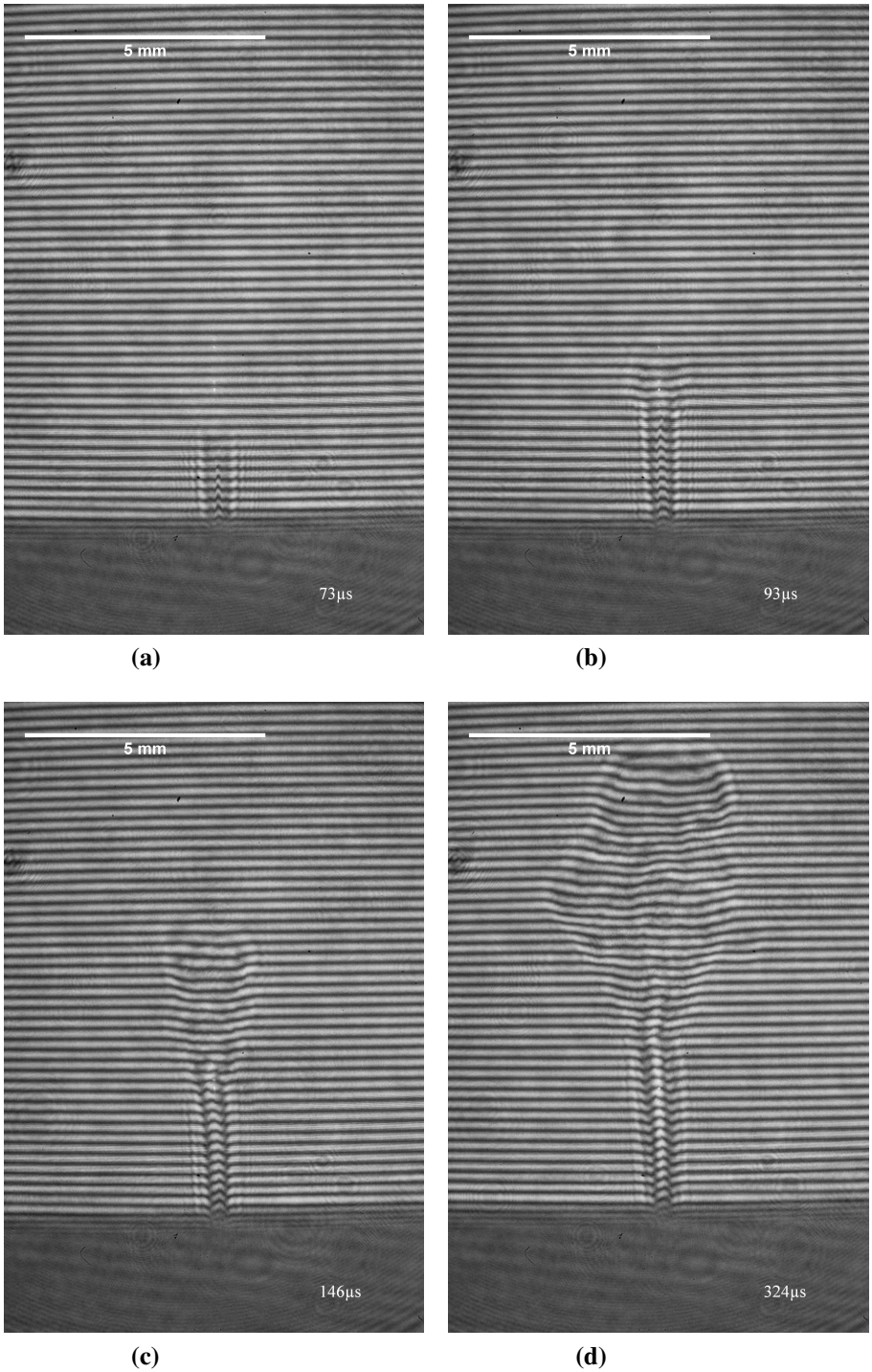

Figure 6.17: Time resolved interferometry results of cast epoxy resin ablated with an RF CO_2 laser at 72.2 ± 1.6kW cm^{-2}. Figure 6.17a is 73µs through the laser interaction with the epoxy and the fume has propagated 1726µm. Figure 6.17b is 93µs through the interaction and the fume has propagated 3389µm. Figure 6.17c is 146µs through the interaction and the fume has propagated 6138µm and figure 6.17d is 324µs through the interaction and the fume has propagated 9923µm.

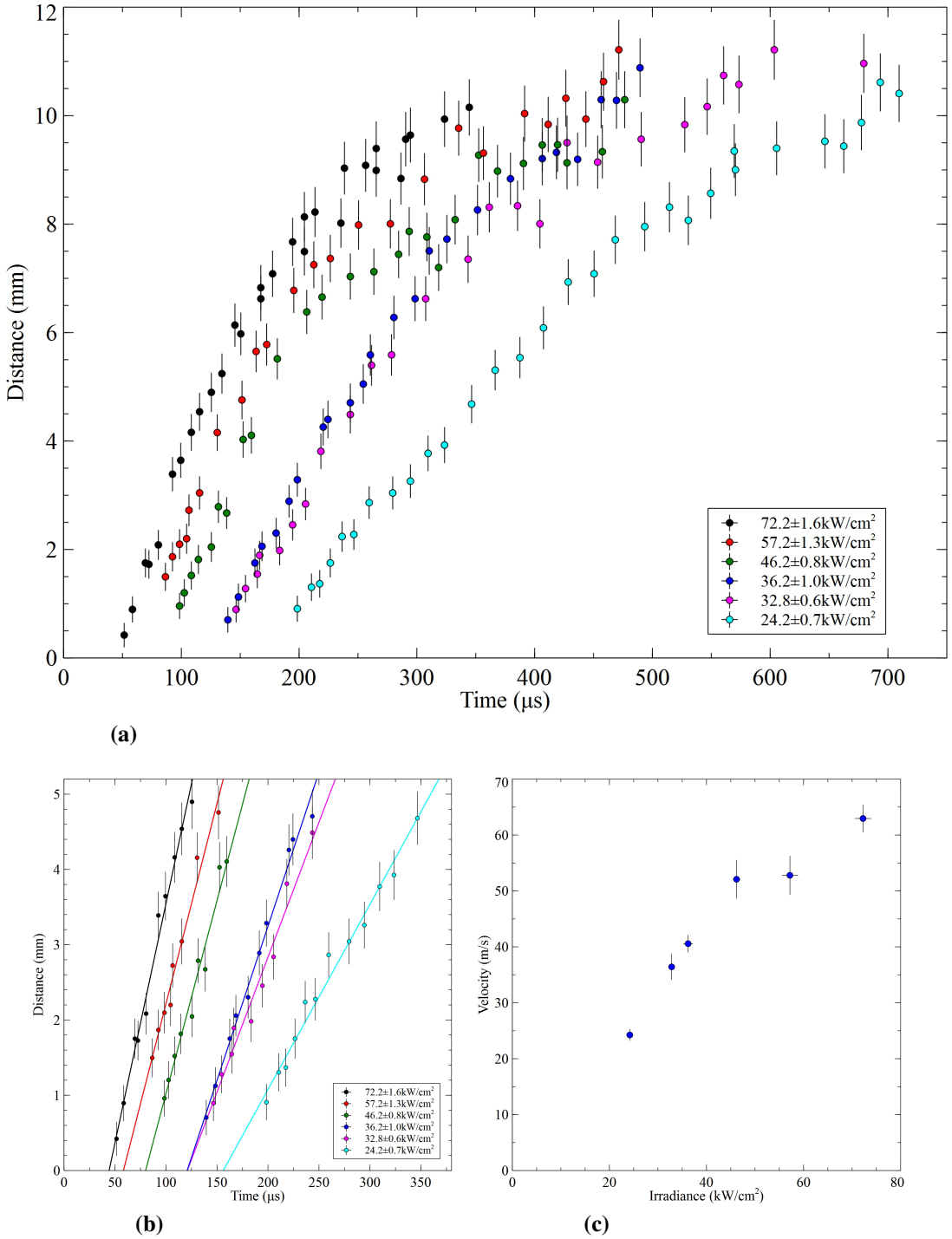

Figure 6.18: Graphs of the propagation of the fume from an RF CO_2 laser ablating cast epoxy, with respect to time through the interaction, for various irradiances. The distances have been measured using time resolved interferometry. 6.18a is a graph of the full set of results. 6.18b is a graph of the 'linear' region, for distances < 5mm. 6.18c is the average velocity versus irradiance for the first 5mm which the plume travels.

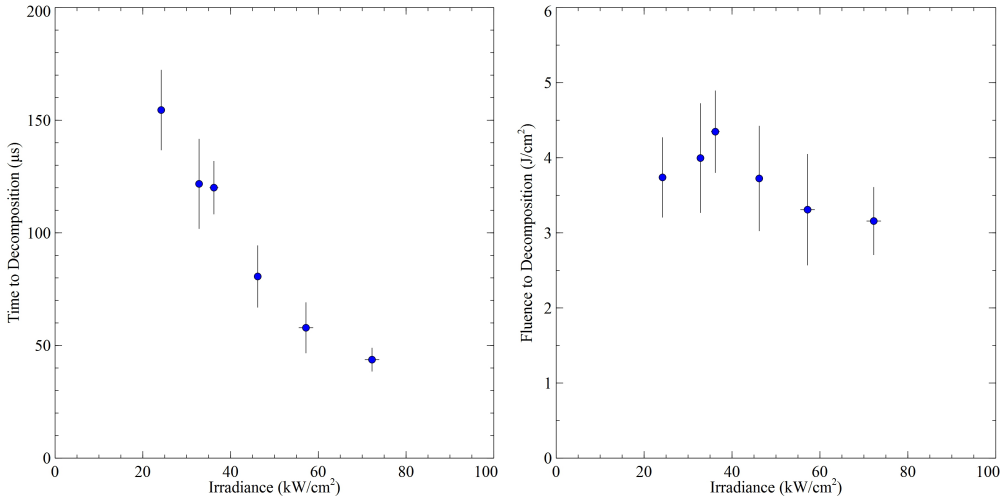

Figure 6.19: 6.19a shows the time taken for epoxy to start to decompose when ablated with an RF CO_2 laser at various irradiances. 6.19b shows the fluence delivered to the cast epoxy resin sample before it starts to decompose.

decompose with respect to irradiance is shown in figure 6.19a. From this, the fluence delivered to the epoxy up to the time it starts to decompose was calculated and is shown in figure 6.19b. It can be seen that the fluence delivered, i.e. the 'threshold' fluence varies with irradiance, but it would not be unreasonable to extract a constant threshold fluence over this range of irradiances.

T300 carbon fibre

T300 carbon fibre was processed using an RF CO_2 laser at an irradiance of $70.7 \pm 2.1 \mathrm{kW\,cm^{-2}}$. Results were taken using the time resolved interferometry technique.

Figure 6.20a shows a typical result when laser processing T300 carbon fibre weave at 874µs through the laser interaction. This result was not filtered, so the luminous plume is present in the image. A large uniform disturbance in the fringes is seen above the interaction site. The fringes have been displaced 'downwards' in the image, which means that the optical path length was reduced, as discussed in section 6.3.1. Therefore this can be interpreted as a reduction in the local refractive index.

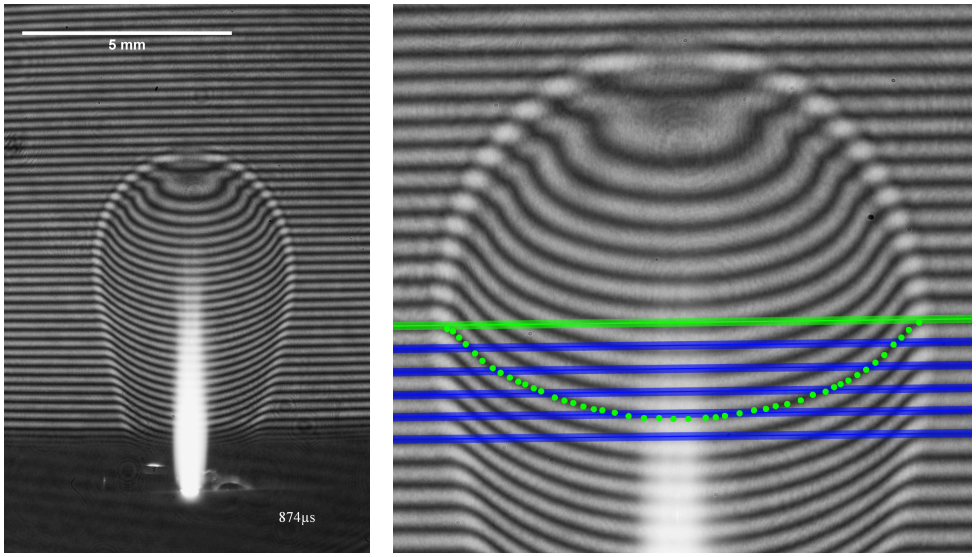

(a) (b)

Figure 6.20: Time resolved interferometry images of carbon fibre weave being processing with an RF CO_2 laser at an irradiance of $70.7 \pm 2.1 \mathrm{kW\,cm^{-2}}$. 6.20a shows the original image - no fibres are visible in the image and there are no streaks in the luminous plume. 6.20b shows the image being processed for fringe shift analysis.

Figure 6.20b shows the image processing technique used to calculate the number fringe shifts through the plume. The plume was assume to be circular in a plane parallel to the sample, so the distance through the centre of the plume was the same as its width. The plume was measured to be 4.7mm in diameter, and had 4.25 fringe shifts at this point. Using the technique described in section 2.6, the refractive index was calculated to be 1.00007356, compared to 1.00027249 of the air in the room.[164] The change in refractive could be due to different gases, temperatures or pressures which means that it is very difficult to decipher the exact cause. However, the change in refractive index with respect to temperature at atmospheric pressure is shown in figure 6.21a, and the refractive index with respect to pressure at room temperature is shown in figure 6.21b.[164] It can be seen that the refractive index decreases with an increase in temperaure, and increases with an increase in pressure. Using these two relations, the formula can be solved for the permissible temperature and pressure for the refractive index found for the plume (figure 6.21c); this plot shows temperature increases below that which the carbon fibre would be expected to sublime at, from atmospheric pres-

sure up to five times atmospheric pressure. These parameters are realistic for a laser plume, which gives confidence in the refractive index measured; however, with the large number of variables any further information cannot be extracted.

Figure 6.22 shows images of fibres being released from the surface, the areas of interest such as released fibres and fringe disturbances have been highlighted with orange rings. Figures 6.22a and 6.22b are towards the end of the 1ms RF CO_2 laser pulse. The fibres can be seen emerging from the luminous part of the plume, and are around the edge of the main fringe disturbance. Figures 6.22c and 6.22d are after the RF CO_2 laser pulse has ended. It can be seen that the fibres have progressed past the main fringe disturbances. Also, minor fringe disturbances are visible around the released fibres, which could be due to the fibres heating the surround air.

The plume in these images is different to that in figure 6.20a; bright streaks emerge from the ablation site. Examining these images and others, the fibres can be seen to line up with the streaks, suggesting that hot, incandescent fibres are causing these. Their rotation can also be observed in the streaks. This was a useful result as it assisted in the identification of images displaying the release of fibres in a non time resolved fashion. This in turn meant that the parameters causing the release of the fibres could be investigated more easily as the images with fibres are immediately identifiable.

By comparing TRI images of the ejecta from the carbon fibre weave to microscope images of the ablations sites, it was found that fibres were released when the fibres in the weave were ‘chopped’ at either end by separate laser pulses, so a single pulse is not sufficient to release fibres. This meant that their length depended on the distance between the irradiation sites. Figure 6.23 shows a micrograph image of three RF CO_2 laser ablation sites on a T300 carbon fibre weave, labelled 1, 2 and 3 in figure 6.23a. The sites were ablated in the numbered order. 6.23b was the first ablation site. It follows that because it was the first ablation site on the horizontal part of the fibre weave, no fibres could be released from the surface, because a second site is required to ‘chop’ fibres at each of the released section. The luminous plumes from 6.23c and

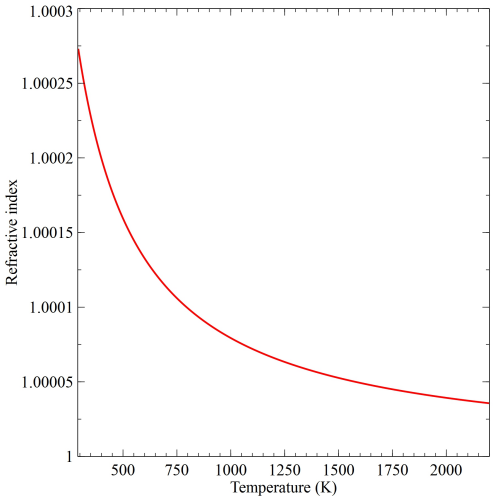

(a) A plot of the refractive index of air with respect to temperature (atmospheric pressure).

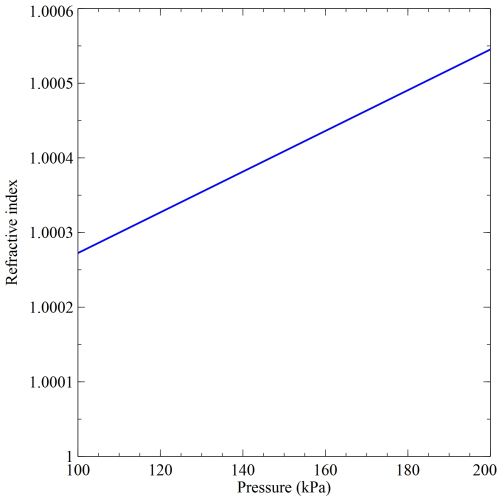

(b) A plot of the refractive index of air with respect to pressure (room temp).

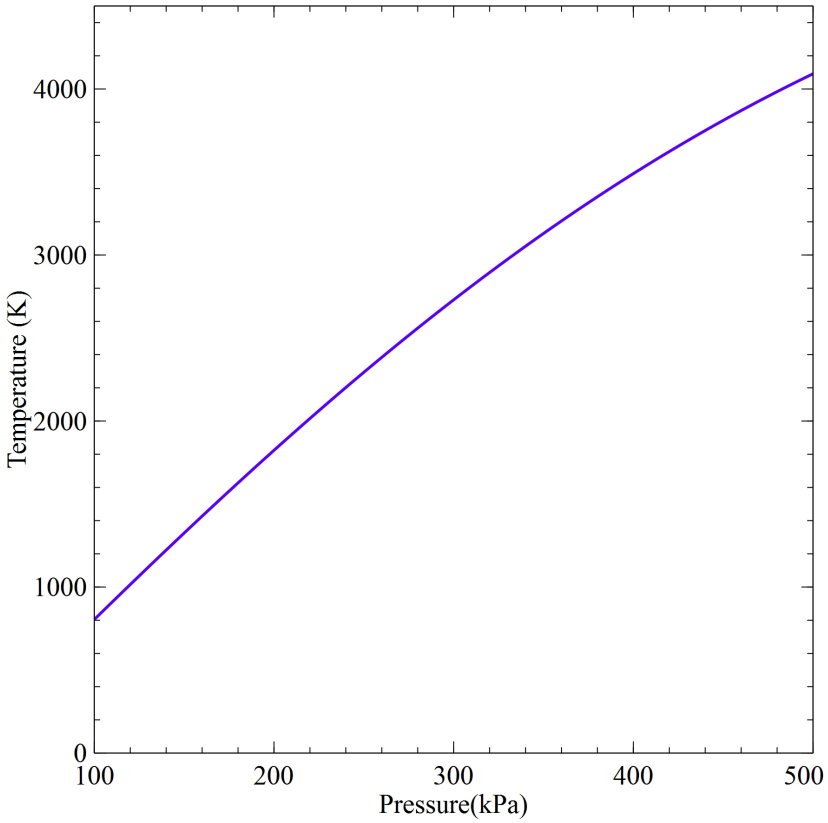

(c) A graph of the pressure and temperature of air which would give a refractive index of 1.00007356.

Figure 6.21: Plots of the refractive index of air, and also a temperature vs pressure plot for a refractive index of 1.00007356.

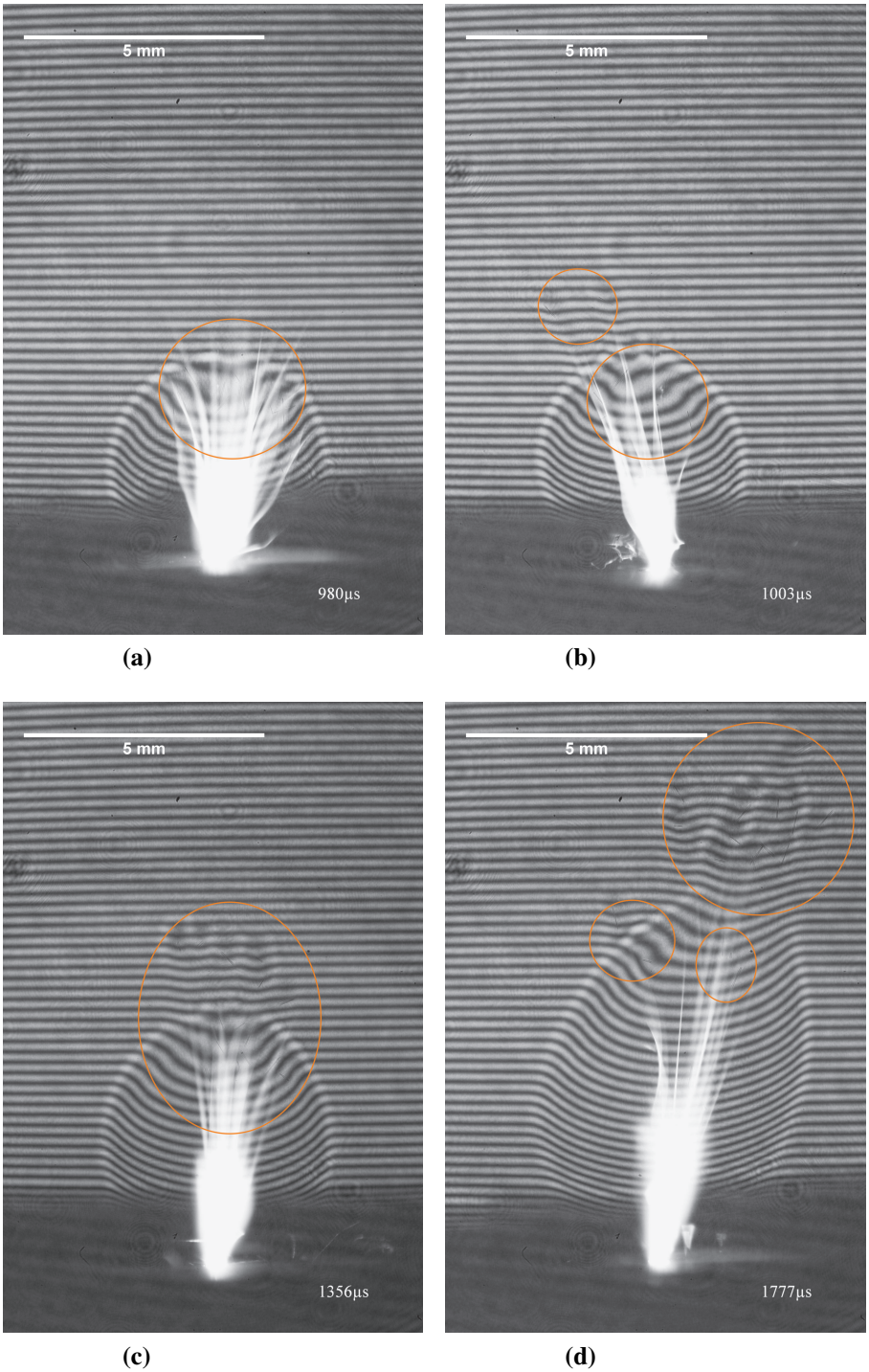

Figure 6.22: Time resolved interferometry images of carbon fibre weave being processed with an RF CO_2 laser at an irradiance of $70.7 \pm 2.1 \mathrm{kW\,cm^{-2}}$, fibres and fringe disturbances have been highlighted by orange rings. 6.22a and 6.22b show fibres being released towards the end of the pulse. 6.22c and 6.22d show fibres being released after the pulse has ended. In all images a streaky self illuminating plume can be seen. The streaks are caused by hot, incandescent fibres being released and exposing the camera.

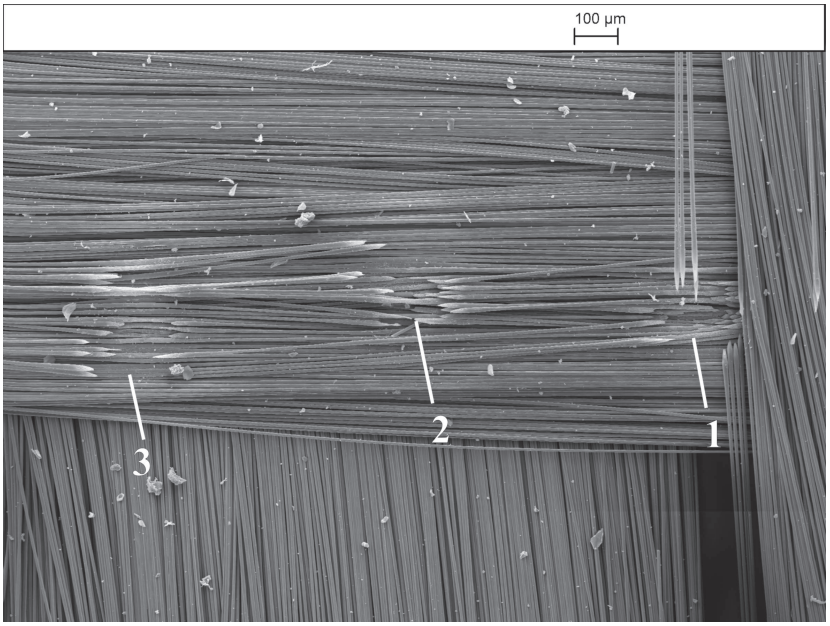

(a)

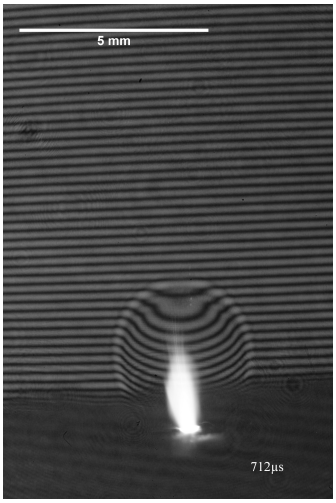

(b) Site 1

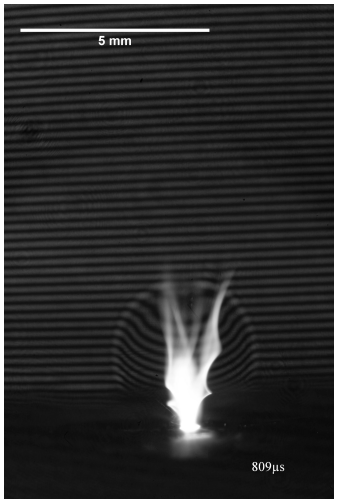

(c) Site 2

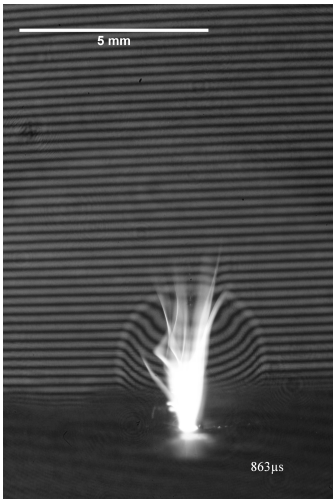

(d) Site 3

Figure 6.23: 6.23a shows an SEM of three RF CO_2 laser ablation sites on a T300 carbon fibre weave, labelled 1, 2 and 3; they were ablated in the numbered order at an irradiance of $70.7 \pm 2.1 \mathrm{kW\,cm^{-2}}$. The TRI image for ablation site 1 is shown in 6.23b. The plume shows that no fibres are released. The images from sites 2 and 3 are shown in figures 6.23c and 6.23d; the plume in these images shows that fibres were released. Fibres can also be seen if the images are examined carefully.

6.23d show evidence of fibres being released, due to their streaky nature. On closer examination fibres can be observed in the plume.

The fibres released from the surface in figure 6.23c were measured to have lengths of 632 ± 31µm, 644 ± 31µm, 503 ± 29µm and 645 ± 31µm. In figure 6.23a the smallest distance between laser damage around sites 1 and 2 is 438.85µm. A single fibre is visible in figure 6.23d, which has a length of 488 ± 29µm, compared to the 444.38µm between the sites. The fibres can be longer than the smallest distance between the sites because they may be 'chopped' by the top or bottom edges of the damage area.

In contrast to this result, figure 6.24a shows ablation sites when no fibres were released. In figure 6.24 there are two ablation sites, 1 and 2, which are spaced just 213.33µm apart. Due the fact that the fibres are vertical in the image, but the target was translated horizontally, no fibres were released, as shown in figures 6.24b and 6.24c. In these the characteristic streaky plume from when fibres are observed is not seen, and no fibres are visible when closely examining the images.

So far the effects of fibres being released have been observed, however many of the visible fibres are masked by the luminous plume. To order to view the fibres being released from the surface more clearly, the interferogram was filtered using the 440nm filter and further results were taken at an irradiance of $60.2 \pm 1.3\text{kW}\,\text{cm}^{-2}$. The interferograms, and the corresponding micrograph of the ablation site are shown in figure 6.25.

Figure 6.25a shows fibres being released from the surface of a carbon fibre weave. The corresponding ablation sites are shown in figure 6.25b. In the same way figures 6.25c and 6.25d correspond, and figure 6.25e is linked to figure 6.25f. In figures 6.25b, 6.25d and 6.25f a measurement of the smallest distance between the ablation sites where the fibre is 'chopped' is shown. The end of the measurement bar with the white dot indicates the ablation site at which the interferogram was taken.

The length of the released fibres in the images has been measured and is plotted in figure 6.26; the blue bar represents the range of distances between the ablation at which

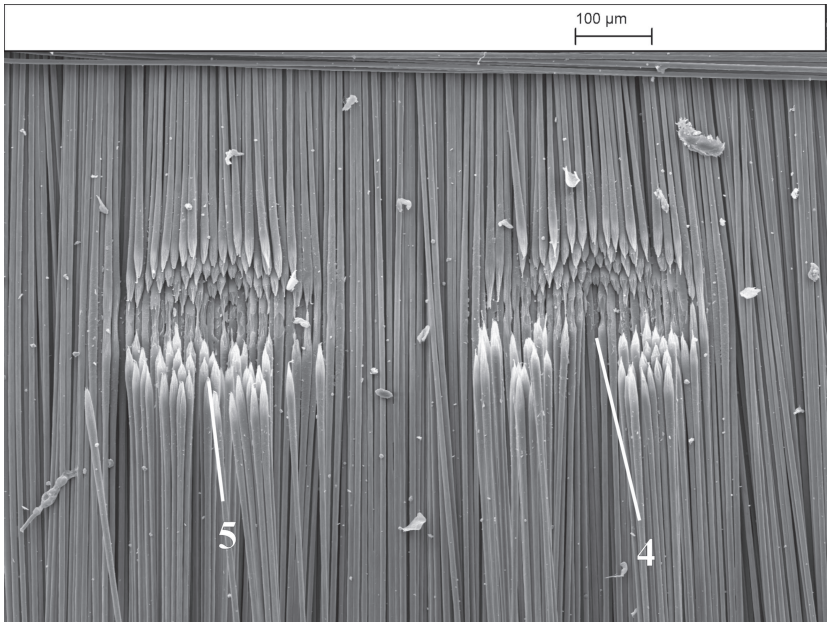

(a)

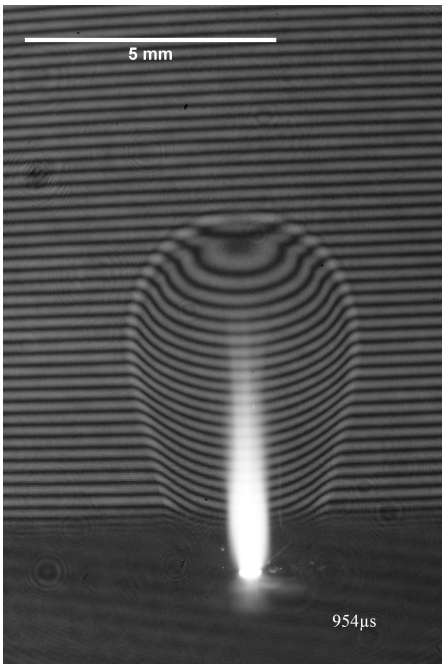

(b) Site 4

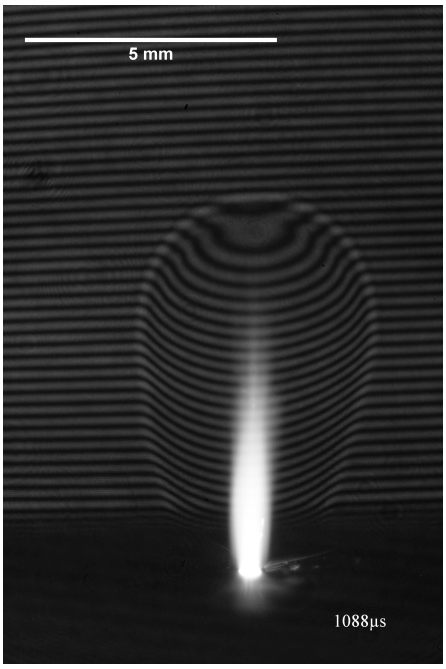

(c) Site 5

Figure 6.24: 6.24a shows an SEM of two RF CO_2 laser ablation sites on a T300 carbon fibre weave, labelled 4 & 5; they were ablated in the same order. The TRI image for both ablation sites are shown in figures 6.24b and 6.24c. The plume suggests that no fibres were released, and none are visible in either image.

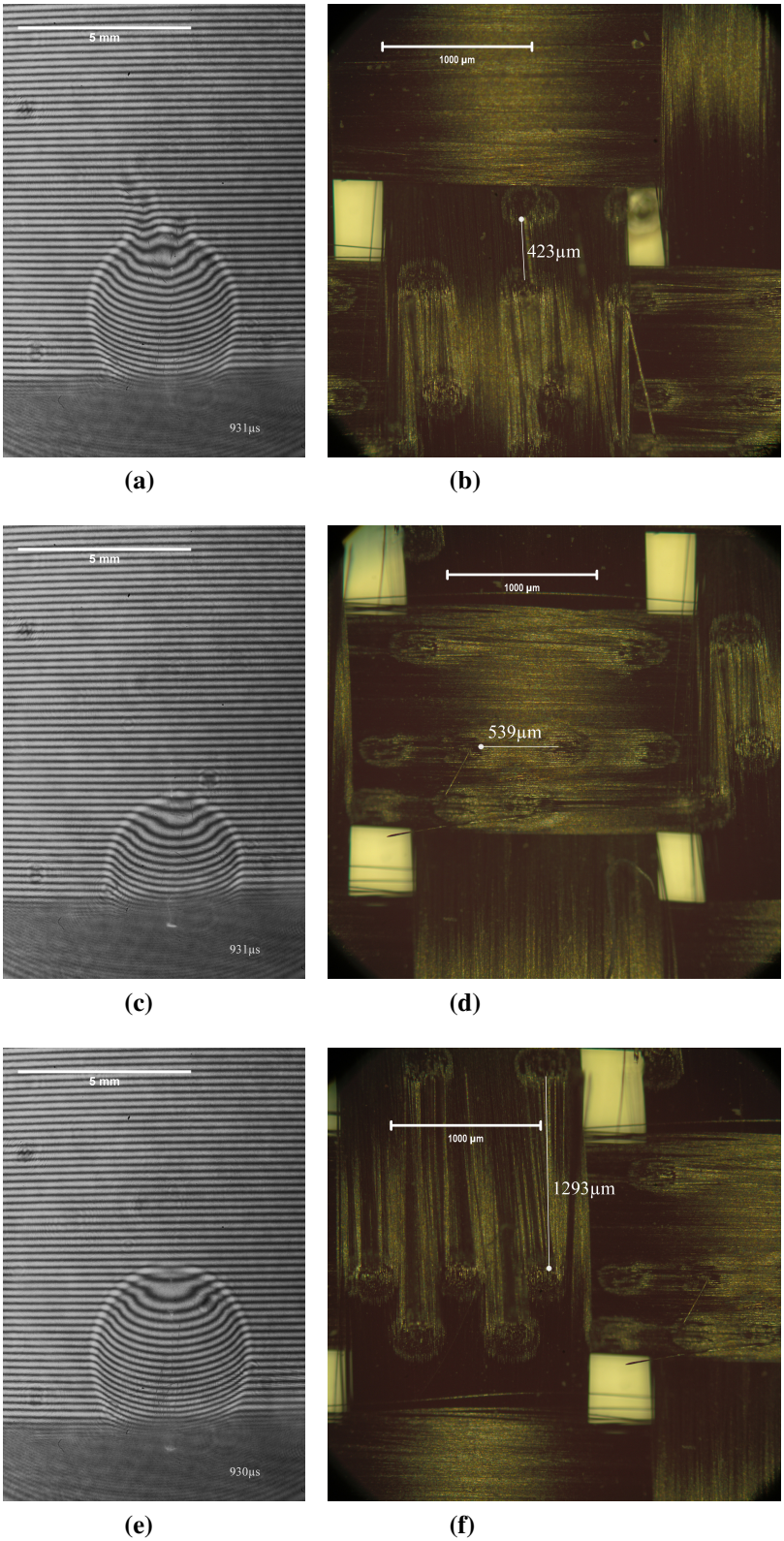

(a) **(b)**

(c) **(d)**

(e) **(f)**

Figure 6.25: Filtered TRI images and their corresponding damage sites for pure carbon weave processed with an RF CO_2 laser at $60.2 \pm 1.3\text{kW cm}^{-2}$. Fibres can be observed leaving the samples.

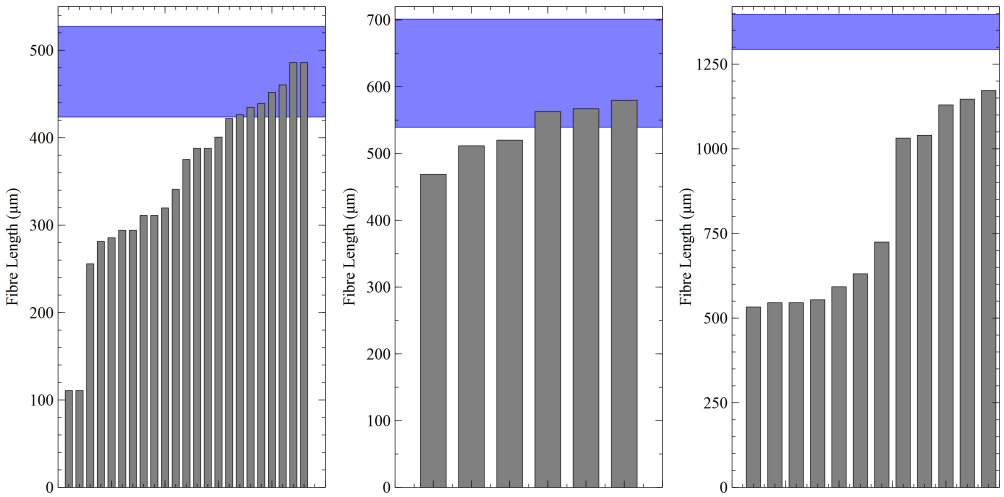

(a) From figure 6.25a.

(b) From figure 6.25c.

(c) From figure 6.25e.

Figure 6.26: Measurements of the fibres visible in figures 6.25a,6.25c & 6.25e. Each bar represents the length of a single fibre, sorted from the smallest to the largest. The blue bar represents the range distance between the two ablation sites where the fibres have been 'chopped', as measured in figures 6.25b, 6.25d & 6.25f.

the fibres could be cut out, i.e. from the shortest length between the sites to the longer distances at the edges of the them, which is an increase of approximately one damage diameter. From the graphs in figure 6.26 it can be seen that the length of the released fibres is related to the distance between the ablation sites. In figure 6.26b it is seen that all of the fibres were similar in length to the measured distance between the ablation sites, with half of the fibres falling in the measured range. The other fibres were shorter than the measured shortest point. This was likely to be due to a slight rotation in flight about an axis perpendicular to the optical axis of the camera causing a foreshortening of the image; however, from the results it would appear that the fibres in this image had less rotation about this axis than the results in figures 6.26a and 6.26c. This was likely to be due to the optical axis of the camera (which is from the bottom to the top of images 6.25b, 6.25d and 6.25f) being perpendicular to the direction of the fibres which were released.

In figures 6.25b and 6.25f it can be seen that the fibres released were parallel to the

optical axis of the camera, and therefore rotated about the axis perpendicular to it more than the fibres in figure 6.25d. This can be seen in figures 6.26a and 6.26c because many fibres appear to be significantly shorter than the shortest point between the two ablation sites. If the images are examined carefully, it can be seen that the shorter fibres are slightly less in focus compared to the longer ones. A certain amount of blurring may be caused by a fast rotation of the fibres; however because the fibres which appear to be longer are in better focus this is unlikely to be the case. The decrease in the focus of the apparent short fibres is likely to be due to the ends of the fibres moving out of the focal depth of the camera by rotation. It can be seen that the length of some of the released fibres is greater than the optical system's depth of focus.

By comparing the images in figure 6.25 it is clear that the fibres which were parallel to the optical axis of the camera do not appear to 'spread out' as much as the fibres which are perpendicular to the optical axis of the camera. This suggests that the fibres may be released at angles on a plane which is parallel to the direction of the fibres, as opposed to being released in the direction of the surface normal. This means that the fibres running parallel to the optical axis of the camera are more likely to change their distance from the lens and they could move out of the depth of focus of the optical system.

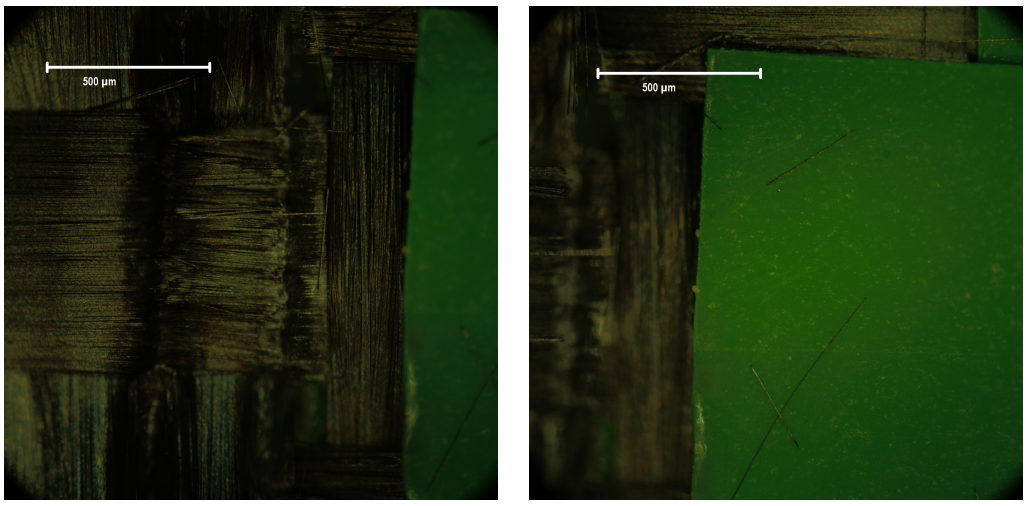

(a) **(b)**

Figure 6.27: Microscope images of fibre debris scattered about a site where two parallel lines were processed using a Sator laser.

These results were supported by processing carbon fibre with two parallel lines, spaced by approximately 400µm using a Sator laser[2] and examining the area under a microscope (figure 6.27); fibres of this length can be seen distributed around the area.

CFRP

The composite of T300 carbon fibre in RS-M135 epoxy matrix was also processed with an RF CO_2 laser and analysed using the TRI technique. Results at an irradiance of $67.3 \pm 1.4 \text{kW cm}^{-2}$ are shown in figures 6.28, 6.29, 6.30 and 6.31. The results were not optically filtered.

From section 5.2 it is known that the thickness of the epoxy matrix on top of the carbon fibres affects the damage to both the epoxy and the fibres. Figure 6.28a shows the TRI image from a section of the CFRP which had an epoxy matrix thickness of 47µm, measured using the focus stage on an optical microscope; the site is shown in figure 6.28b. It can be seen that the fume looks very similar to the results from the cast epoxy block. The distance travelled in the specified time is in agreement with what was observed in figure 6.18a.

In contrast to this, figure 6.28c shows a plume which is similar to that observed from pure carbon fibres. The ablation site is shown in figure 6.28d, and the epoxy depth was 7µm. The epoxy depth at this ablation site is less than the optical absorption depth of the epoxy at 10.59µm, as discussed in section 4.8. This means that the carbon fibres would be absorbing laser energy from the start of the interaction, so a higher fluence will be delivered to the fibres. The epoxy will also take less time to fully decompose from above the fibres. This means that the fibres will start to decompose earlier in the interaction; it follows that the observed fume is primarily a carbon plume, with some distortion from the epoxy which is ablated.

Figure 6.28e shows a plume from a site, shown in figure 6.28f, which had an epoxy depth of 22µm. This is slightly smaller than the the absorption depth of the laser light,

[2]The Sator laser is a galvanometer scanned 200W RF CO_2 laser.[140]

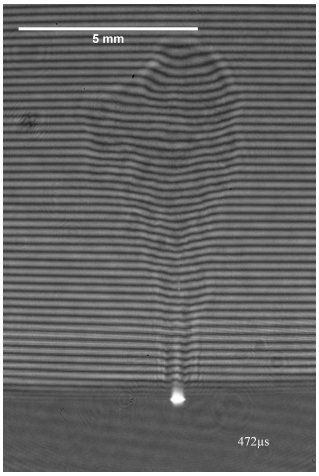

(a)
Site 1

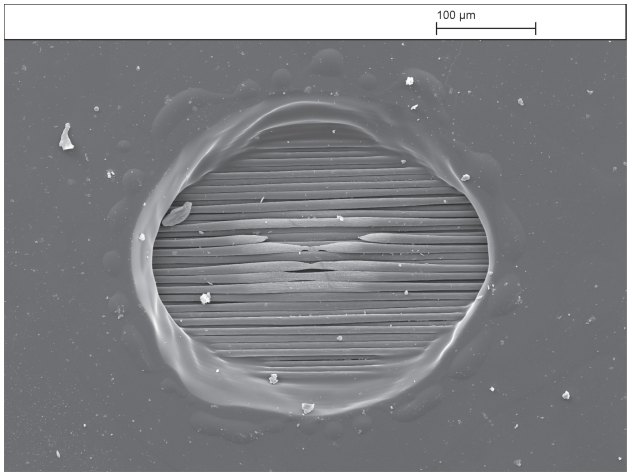

(b) Site 2

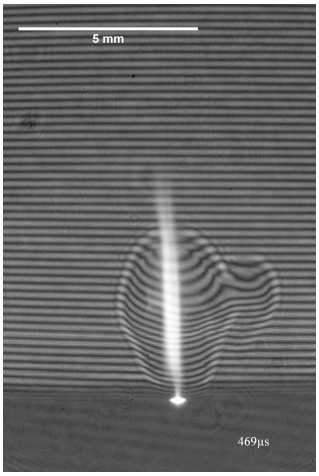

(c)
Site 3

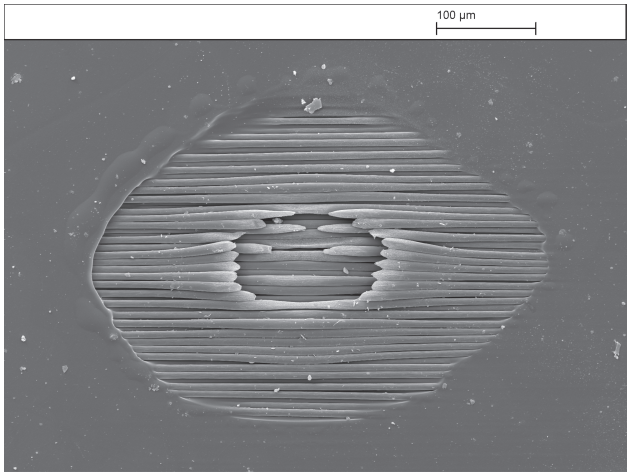

(d)

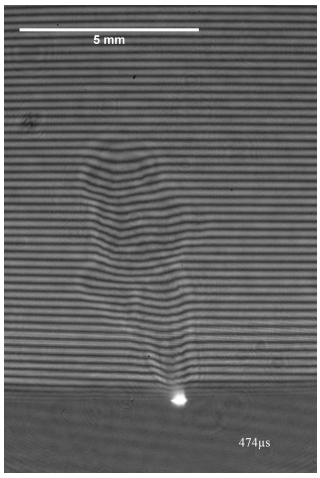

(e)

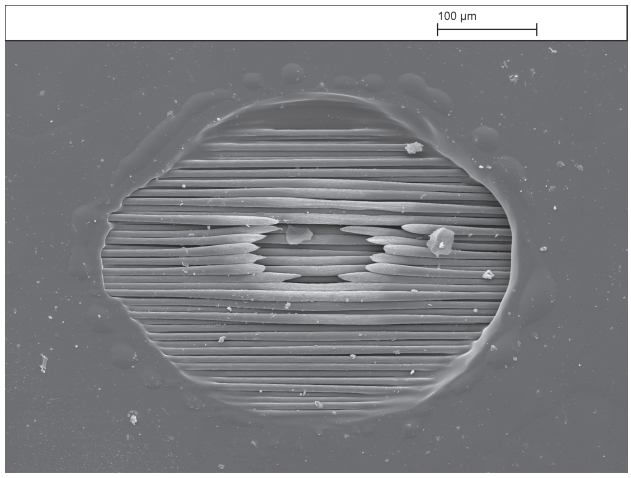

(f)

Figure 6.28: These figures show TRI images and the corresponding SEMs of CFRP processed with an RF CO_2 laser at an irradiance of $67.3 \pm 1.4\text{kW}\,\text{cm}^{-2}$. Figures 6.28a & 6.28b show results for an epoxy surface layer thickness of 47µm. Figures 6.28c & 6.28d had an epoxy thickness of 7µm. Figures 6.28e & 6.28f had an epoxy thickness of 22µm.

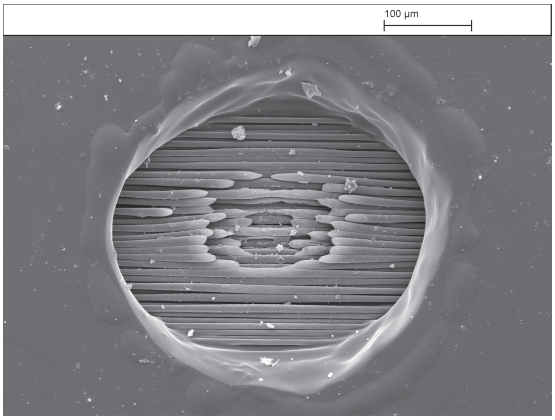

(a) Site 4

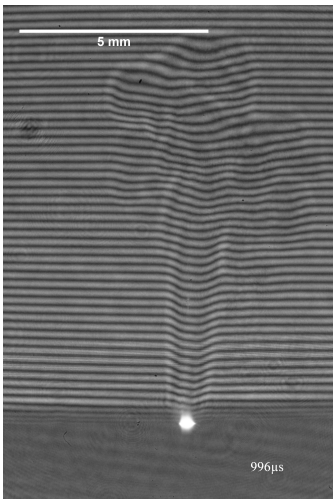

(b) First ablation

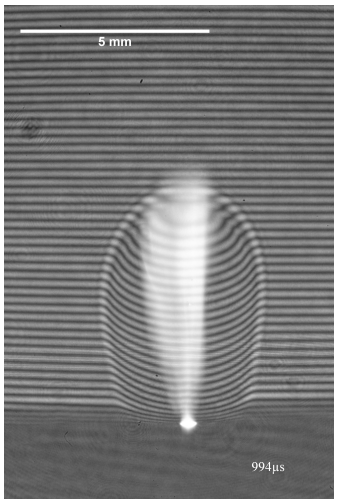

(c) Second ablation

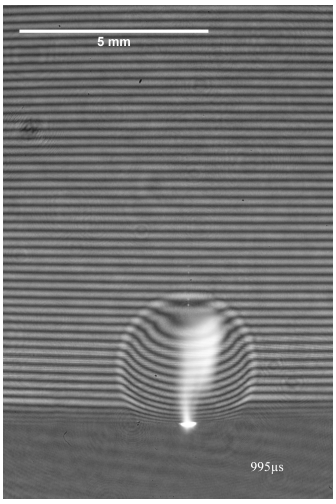

(d) Third ablation

Figure 6.29: Figure 6.29a shows an SEM of an ablation site which has been irradiated three times with 1ms pulses at an irradiance of $67.3 \pm 1.4\text{kW}\,\text{cm}^{-2}$. Figures 6.29b, 6.29c & 6.29d show TRI results for the 1st, 2nd and 3rd pulses.

which means some energy would penetrate through the epoxy to the carbon before the polymer was ablated. The plume is similar to the one observed with cast epoxy, and at this point no evidence of carbon decomposition is visible. However, by comparison with figure 6.18a, the distance travelled by the plume is less than would be expected at this fluence. This may be due to the fibres aiding thermal diffusion from the ablation site, thus lowering the volumetric energy density.

Figure 6.29a shows ablation site 4, which has a layer of epoxy matrix which is 32µm thick. Figure 6.29b shows the first TRI image of the ablation plume towards the end

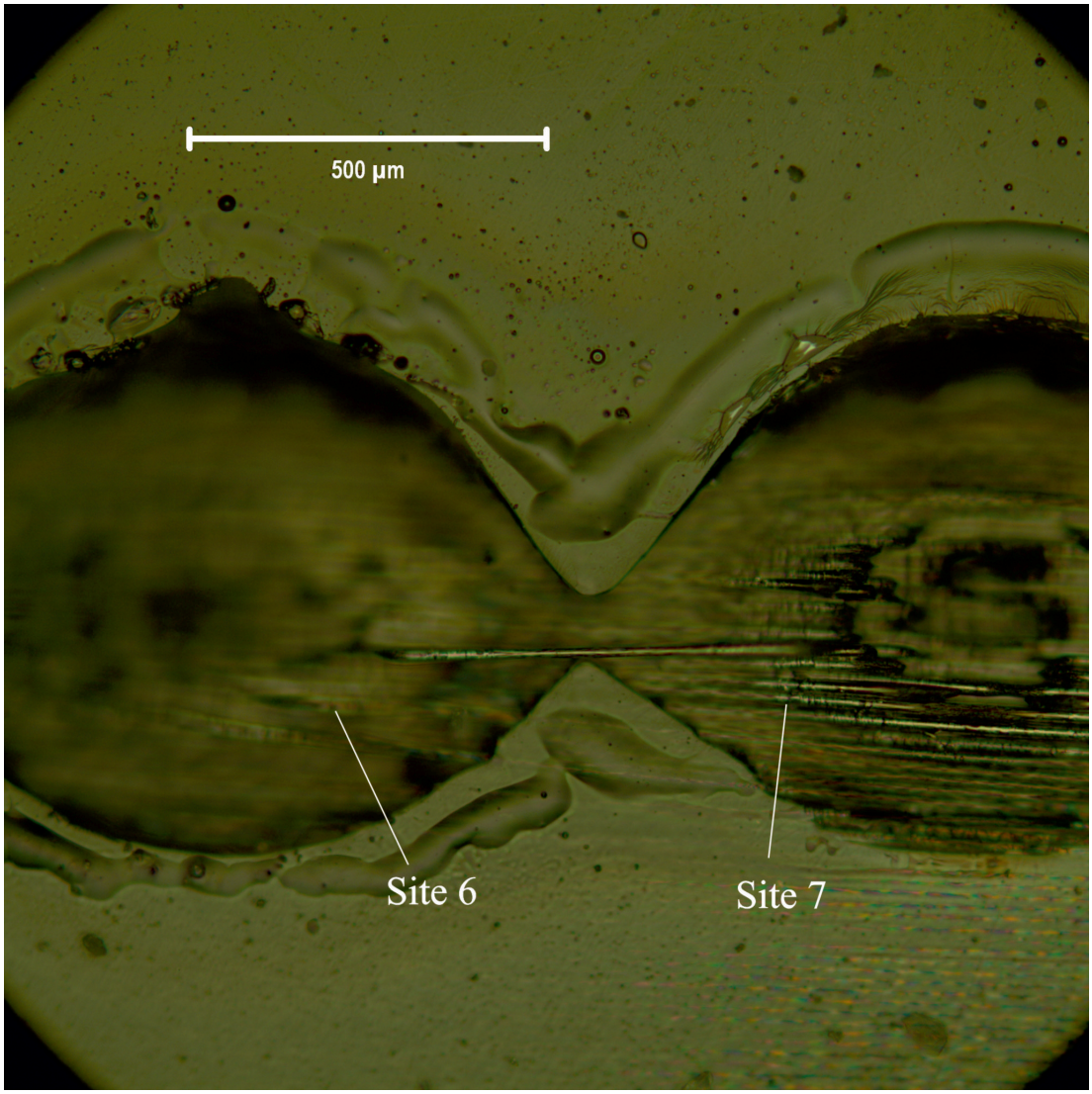

Figure 6.30: Two ablation sites which have each been irradiated with three 1ms pulses at an irradiance of $67.3 \pm 1.4\text{kW cm}^{-2}$. The edges of the epoxy damage sites overlap, and a loose fibre is visible between the carbon damage regions.

of the pulse. As before, the plume looks similar to the cast epoxy resin results, but the plume has not travelled as far as would be expected at this time. Figure 6.29c shows the second laser ablation at the same site; this looks like a pure carbon fibre ablation because at this point most or all of the epoxy will have been ablated leaving bare fibres after the first ablation. Figure 6.29d shows the plume for the third laser pulse at the same site. This also looks like a pure carbon fibre plume, but it is smaller than with the second laser pulse because some of the carbon will have been removed after the first pulse, and the projected fluence incident of the carbon will be lower.

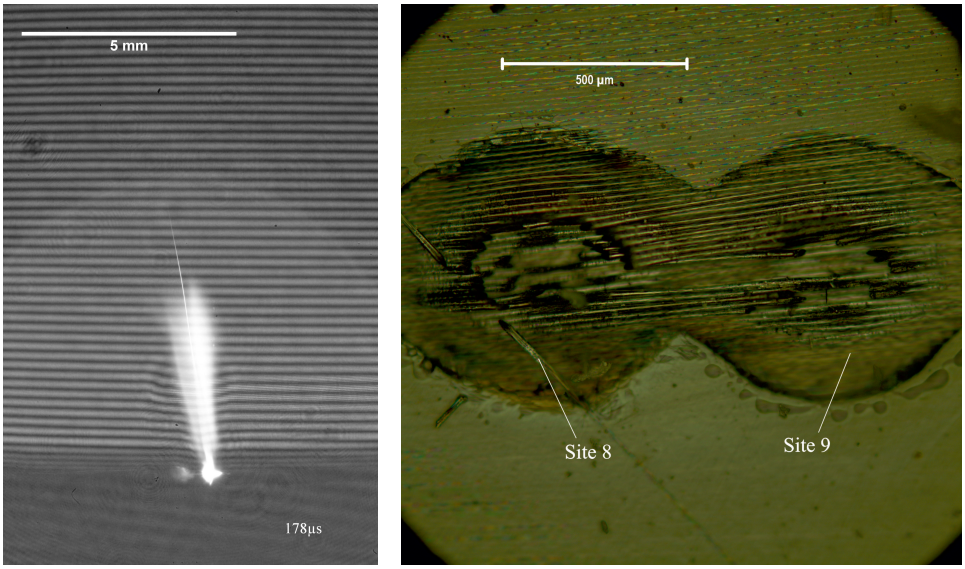

(a) Site 9 **(b)**

Figure 6.31: Figure 6.31b shows 2 ablation sites which have each been ablated with an RF CO_2 laser at an irradiance of $67.3 \pm 1.4 \text{kW cm}^{-2}$. The epoxy damage areas overlap and a fibre released from the surface can be see in figure 6.31a.

Figure 6.30 shows two laser ablation sites which are close to each other, where each site has been exposed to three laser pulses. Under this specific regime the epoxy damage areas, which are described in detail in chapter 5, overlap. The fibres, which are running horizontally, are fully exposed between the areas where they were damaged with the two laser ablation sites. This is due to the fluence threshold being much lower for epoxy compared to the carbon fibre, as discussed in chapter 5. This means that the epoxy can be entirely removed exposing fibres. The centre of Gaussian pulses has a high enough fluence to damage the carbon fibres, which can result in a fibre being 'chopped'. In this figure the area where a fibre has been cut out of the weave is seen, but the fibre remains on the sample. No evidence of fibres being ejected from the sample are visible in the TRI images. This may be due to the overlap between the epoxy damage areas being small, and some epoxy having remained on the free fibre, preventing it from being ejected.

Figure 6.31b shows two laser ablation sites which have a large overlap in their epoxy damage areas. From this microscope image an area where fibres have been removed between the areas where the carbon fibre has been ablated is visible. The TRI image from site 9 is shown in figure 6.31a. On this image a sharp, self illuminating streak is visible, which from experiments on pure carbon fibre it can be deduced that it is caused by a hot fibre being released from the surface.

6.3.3 Discussion

From the time resolved interferometry results the epoxy fume, which was previously unresolvable, has been traced to the edge of the field of view of an optical system with a lower magnification than used in section 6.2. The optical quality of the system has also been improved. From this the epoxy fume progression with time has been mapped out for particular irradiances. These results have been used to find the time at which the material starts to decompose, and also the fluence delivered up to the start of decomposition (i.e. the threshold fluence).

The plume from carbon fibres which could not be observed using shadowgraphy was resolvable using TRI. A large plume with uniformly distorted fringes was observed, and this allowed its refractive index to be calculated as 1.00007356, compared to the 1.00027249 for air at standard temperature and pressure.

A technique for finding fibres quickly and easily in a time-resolved and non time-resolved way has been discussed. This technique has been used to find specific regimes under which carbon fibres can be released from the surface for both pure carbon fibre weave and also a carbon fibre and epoxy composite.

6.4 Conclusions

In this chapter the fume from a cast block of RS-M135 epoxy resin, T300 carbon fibre weave and CFRP have been observed with shadowgraphy. The fume from the epoxy has some particulate phase products, but as the irradiance increases less of the fume is visible, either because it is gas phase or because it the particulates are too small for the system to resolve. The fume from carbon fibre weave cannot be resolved by shadowgraphy, though fibres were occasionally observed leaving the sample.

Time resolved interferometry was used to increase the sensitivity of the system, which meant that a large disturbance in the fringes could be seen when the carbon fibre weave was ablated. This is a distinctive plume which enables us to recognise when fibres are being damaged in a CFRP weave, compared to an epoxy plume. Fibres were also observed leaving the sample with this system, and disturbances around the fibres suggested that they were hot when in flight. In addition to this, yellow streaks were visible in the wake of the fibre, which not only reinforces that they are hot (incandescent), but also provided a non-time resolved method of quickly identifying when fibres were ejected from the surface. The results from this technique led to the conclusion that the fibres were released when they were 'chopped' at either end, and a single ablation site was not sufficient to release fragments of fibres (edge effects excluded). It was also found that fibres could be ejected from CFRP under a specific set of circumstances when the HAZ of the epoxy overlapped with another epoxy damage site, exposing bare fibres which could then be cut out as before. Due to the swelling of the fibres at the ends, and the way in which the fibres are released, a very specific regime would be required to release a fibre which had been thinned and cut out so that it was respirable (i.e. a diameter $< 3\mu m$). This is particularly unlikely with a Gaussian beam because the irradiance incident on the fibre would rapidly change from a regime where it was decomposing the fibre to when the fibre was swelling.

The fume propagation with time has been mapped out for epoxy resin using a time

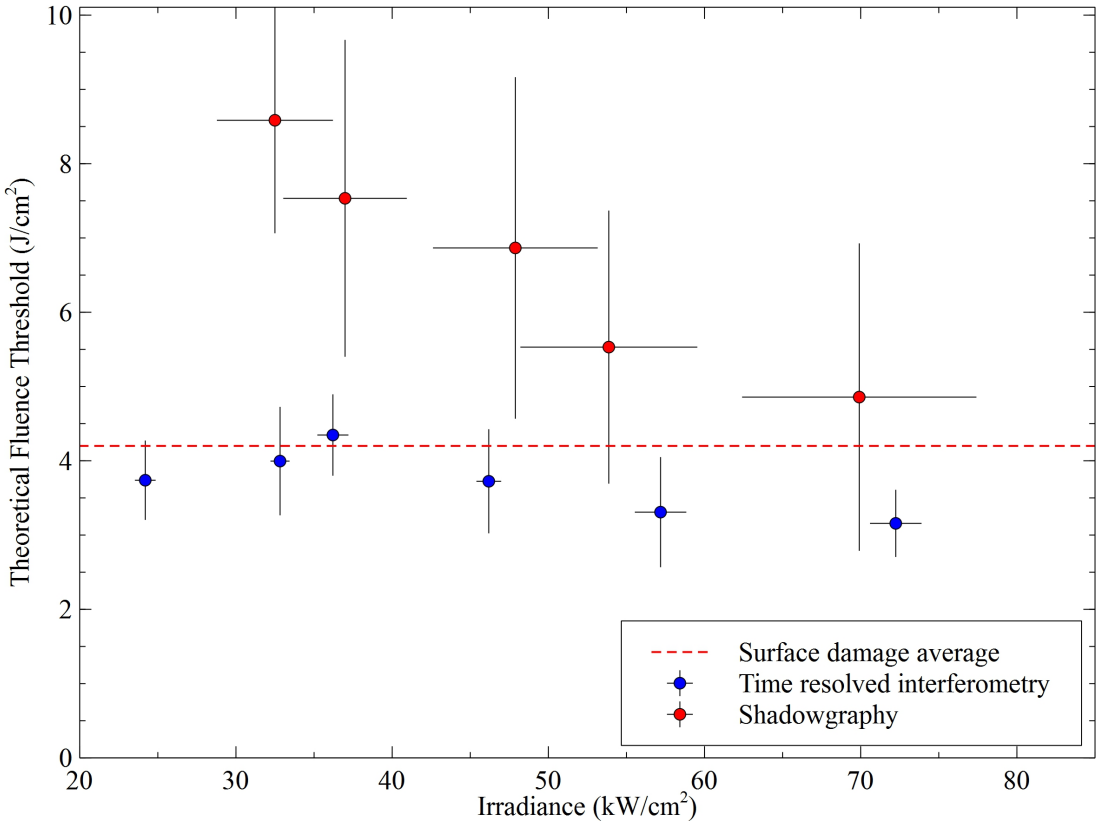

Figure 6.32: A graph comparing the fluence threshold for the RS-M135 epoxy resin calculated using shadowgraphy, TRI and also the average threshold fluence using the surface damage studies described in chapter 5.

resolved interferometry system. From this the initial velocities and the time for the start of the material decomposition have been estimated with respect to irradiance, although it is clear from the plots that the gradient is not linear and therefore the velocity is not constant. Figure 6.32 shows the fluence threshold for RS-M135 epoxy resin against irradiance derived using shadowgraphy (section 6.2), TRI (section 6.3) and also the average threshold fluence measured from the surface damage in chapter 5. From this it can be seen that the TRI provides a reasonable agreement with the fluence calculated by measuring the damage diameters at various fluences. The shadowgraphy shows a higher fluence threshold compared to the other two methods, particularly at lower irradiances. This is likely to be due to early fume being missed by the optical system because its sensitivity is too low. The thresholds and time which the epoxy takes to decompose will be compared to theoretical models in chapter 7.

Chapter 7

Laser Processing of CFRPs Part III: Theoretical Analysis

7.1 Polymer decomposition model

The time taken for polymers to decompose has been modelled. The calculation of the heat rise in the polymer was simplified by using a uniform source of irradiance, as opposed to a Gaussian profile. Only one-dimensional heat flow into the material was considered because the absorption depth of the 10.59μm wavelength light in epoxy is much smaller than the spot size in our experiments, so lateral heat flow can be ignored.[25] The specific heat capacity, density and thermal conductivity were all assumed to be independent of temperature. First, equation 7.1 can be written, stating that the temperature of the polymer, $T(z,t)$ (K) is equal to the temperature of the room, T_0 (K) plus a heat rise function, $\Delta T(z,t)$ (K) which will depend on the depth into polymer, z (m) and the time through the interaction, t (s).

$$T(z,t) = T_0 + \Delta T(z,t) \tag{7.1}$$

The heat rise in the polymer during a laser pulse was determined by using a semi-

analytical solution to the heat diffusion equation for a semi-infinite solid[50], shown in equation 7.2.

$$\begin{aligned}\Delta T(z,t) &= \frac{I_a}{K}\{\delta \cdot ierfc(\frac{z}{\delta}) - (\frac{1}{\alpha})e^{-\alpha z} \\ &\quad +(\frac{1}{2\alpha})e^{(\frac{\alpha\delta}{2})^2} \cdot [e^{-\alpha z}erfc(\frac{\alpha\delta}{2} - \frac{z}{\delta}) \\ &\quad +e^{\alpha z}erfc(\frac{\alpha\delta}{2} + \frac{z}{\delta})]\}\end{aligned} \tag{7.2}$$

where

$$\delta = 2\sqrt{D_H t} \tag{7.3}$$

and

$$D_H = {}^{K}/_{\rho c_p} \tag{7.4}$$

Here, I_a is the absorbed irradiance ($\mathrm{W\,m^{-2}}$), δ is the thermal diffusion length (m), K is thermal conductivity ($\mathrm{W\,m^{-1}\,K^{-1}}$), α is the optical absorption coefficient ($\mathrm{m^{-1}}$), D_H is the thermal diffusivity ($\mathrm{m^2\,s^{-1}}$), t is the pulse duration, ρ is the density ($\mathrm{kg\,m^{-3}}$) and c_p is the specific heat capacity ($\mathrm{J\,kg^{-1}\,K^{-1}}$). For the purposes of this model the temperature rise of the surface is used, so equation 7.2 can be simplified for $z = 0$ to give:[50]

$$\Delta T(0,t) = \frac{I_a}{K}\{\frac{\delta}{\sqrt{\pi}} - \frac{1}{\alpha}[1 - e^{(\frac{\alpha\delta}{2})^2}erfc(\frac{\alpha\delta}{2})\} \tag{7.5}$$

Then, an Eyring solution to the Arrhenius equation[89, 165, 90] is used to calculate the photothermal decomposition of the polymer, using the temperature rise calculated using equation 7.5. The rate constant for this pyrolysis, κ ($\mathrm{s^{-1}}$), can be calculated with

equation 7.6.

$$\kappa = \frac{k_B \cdot [T(0,t)]}{h} \cdot Exp[\frac{-E_T}{\overline{R} \cdot [T(0,t)]}] \tag{7.6}$$

where k_B is the Boltzmann constant ($m^2\,kg\,s^{-2}\,K^{-1}$), $\overline{R}$ is the gas constant ($kJ\,K^{-1}\,mol^{-1}$), h is Planck's constant ($m^2\,kg\,s^{-1}$) and E_T is the activation energy ($kJ\,mol^{-1}$). The fraction of bonds remaining, N_B, can then be calculated for a particular time through the interaction with equation 7.7.

$$N_B = e^{(-\kappa t)} \tag{7.7}$$

Figure 7.1 shows an example of a plot of the decomposition characteristics for a particular fluence and polymer following the Eyring model. From this the time to decomposition was defined as the time when the fraction of bonds remaining fell to 0.5 for the particular material and fluence.

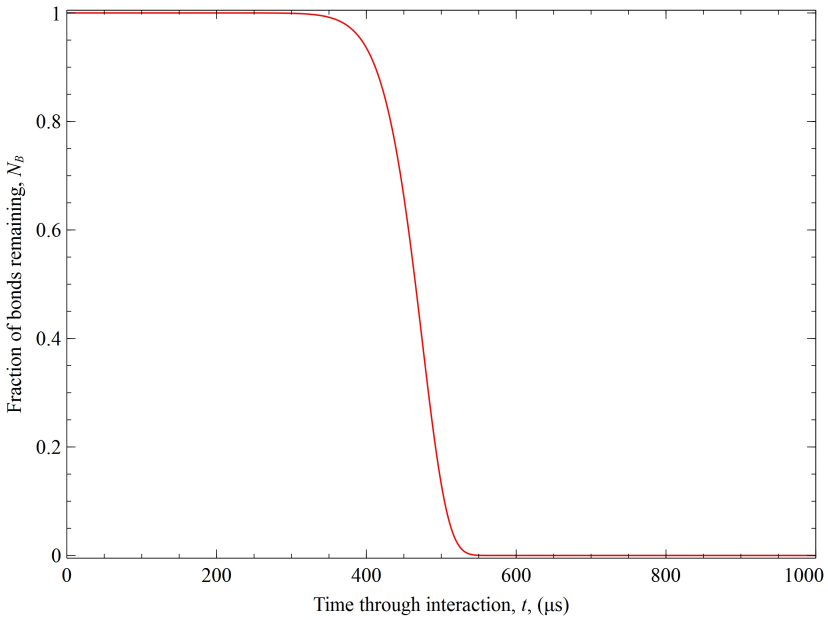

Figure 7.1: An example plot of the fraction of bonds remaining against the time through a laser pulse of a particular fluence using an Eyring solution to the Arrhenius equation.

The model was applied with the material parameters obtained in chapter 4 to determine

the theoretical time to decomposition for an RF CO_2 laser ablating an RS-M135 epoxy resin system, with respect to irradiance.

7.2 Results and Discussion

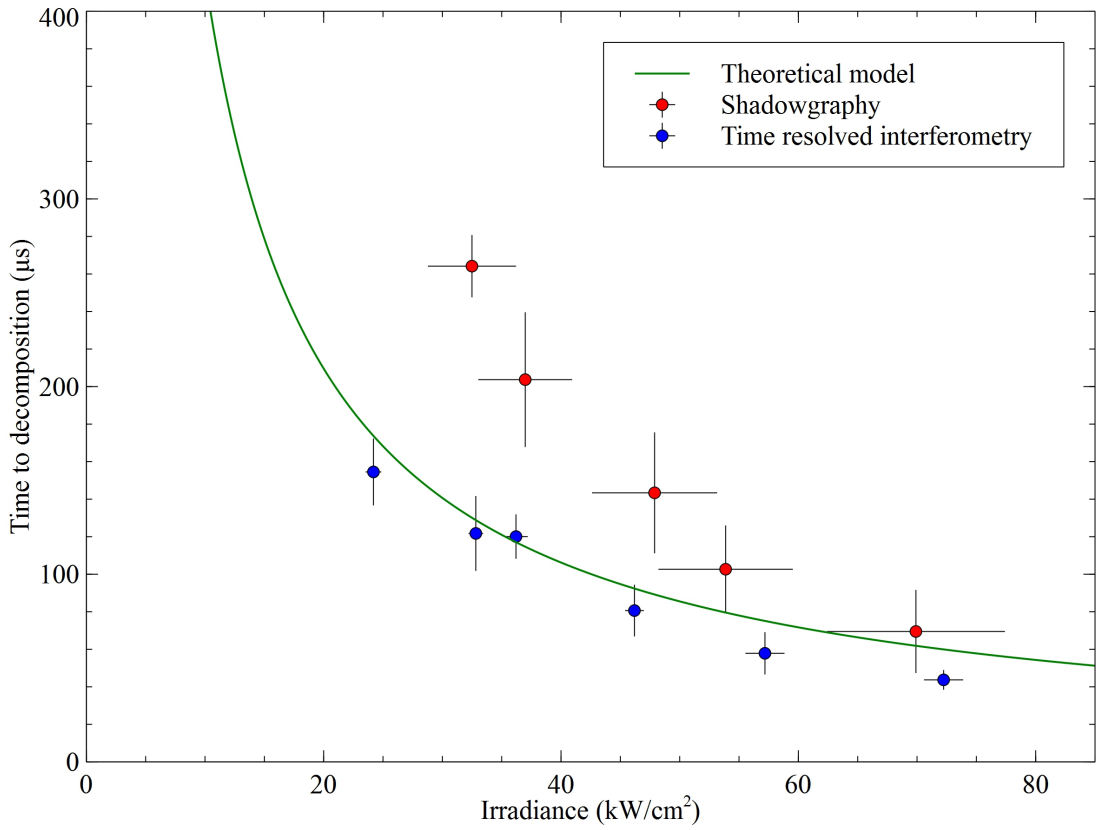

Figure 7.2: A graph of the time to decomposition for RS-M135 epoxy resin, ablated with an RF CO_2 laser with respect to irradiance. A line has been plotted from the theoretical model described in section 7.1, using material parameters obtained in chapter 4. This is compared with results obtained from tracing the plume back to the sample in order to measure the time at which the decomposition starts, using shadowgraphy in section 6.2 and time resolved interferometry in section 6.3.

The theoretical time to decomposition with respect to irradiance for RS-M135 epoxy resin ablated with a laser with a wavelength of 10.59µm is shown in figure 7.2. The theoretical prediction is shown together with the time to the start of decomposition obtained using shadowgraphy (section 6.2) and time resolved interferometry (section 6.3). From this it can be seen that the theoretical model shows good agreement with

results obtained using TRI. The shadowgraphy predicts that the decomposition starts later in the interaction, a result that can be attributed to the system not being sensitive enough to detect the lower level of fume present, particularly at lower irradiances. At higher irradiances the two methods converge, which is likely to be due to the higher heating rate meaning that a quantity of fume great enough for shadowgraphy to resolve is released soon after the decomposition begins, and any lower density fume which may be missed does not affect the timescale significantly.

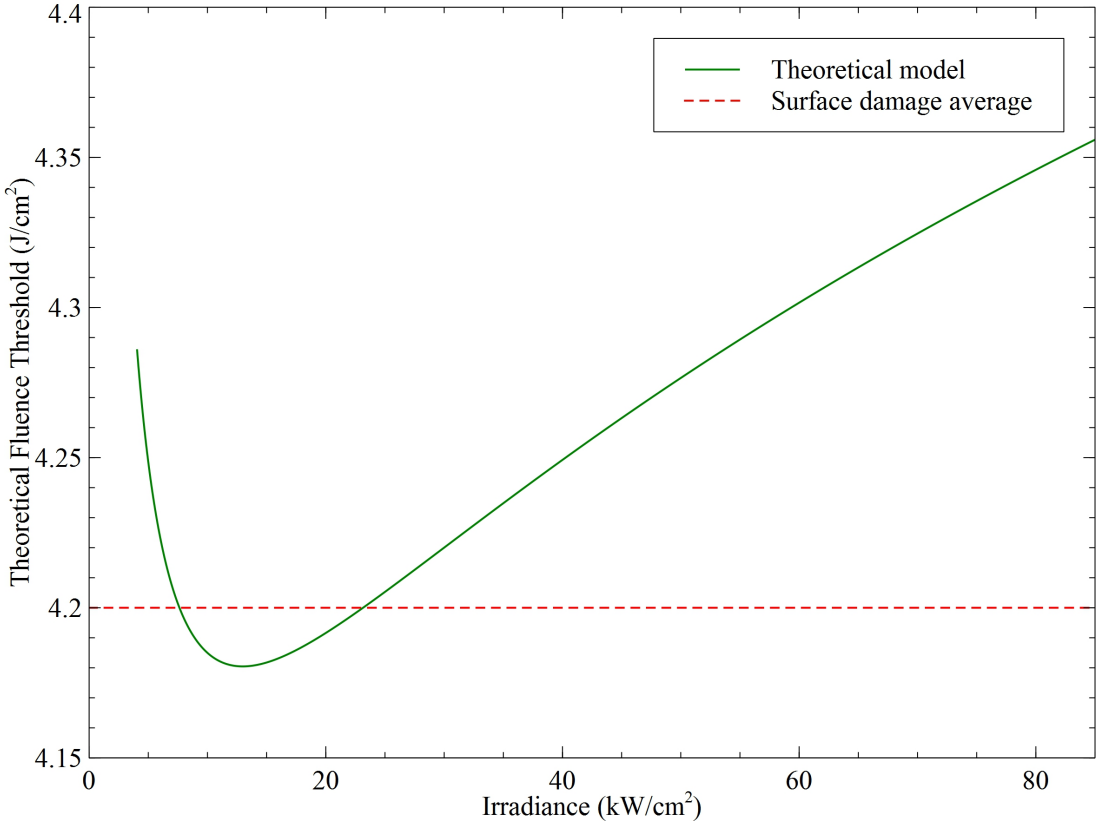

Figure 7.3: A graph showing the theoretical fluence threshold against irradiance for RS-M135 epoxy resin, ablated with an RF CO_2 laser. This is calculated from the fluence delivered in the time to decomposition in the theoretical modelling results shown in figure 7.2. The average fluence threshold which was measured for irradiances of $24 - 72\text{kW}\,\text{cm}^{-2}$ in section 5.2 is also shown on the plot

The theoretical time to decomposition can also be used to plot a theoretical fluence to decomposition, by calculating the energy delivered before the epoxy starts to decompose (figure 7.3). From this it can be seen that the threshold fluence varies with two competing processes. At low irradiances the thermal diffusivity dominates, so if

the heating rate is slower, the amount of heat lost from the surface into the sample is higher because the time scale is longer and as a result the fluence threshold is raised. As the irradiance increases the heat loss into the sample is less significant and the thermal decomposition kinetics dominate, so at higher heating rates, the temperature of decomposition is greater, raising the threshold. In other words, more rapid heating allows for larger temperature excursions before significant decomposition occurs. The result of this is an optimum processing irradiance of $13\text{kW}\,\text{cm}^{-2}$ in terms of the efficiency of the laser beam energy to resultant epoxy damage; however, it is important to note the scale on the plot as the percentage variation over this range of irradiances is low.

The average fluence threshold for the epoxy of $4.2 \pm 0.5\text{J}\,\text{cm}^{-2}$, which was measured for irradiances of $24 - 72\text{kW}\,\text{cm}^{-2}$ in section 5.2, is also shown on the plot. The measured value intersects the theoretical model, and also the predictions by the model all fall within the experimental uncertainty of the measured fluence over this range of irradiances.

The theoretical threshold fluence as a function of irradiance plotted with a wider range of fluences is shown in figure 7.4. This plot demonstrates more strongly that the variation over the range of irradiances is not significant, and while there is an optimum processing irradiance, the threshold is approximately constant for the range of irradiances which the RF CO_2 laser provides using this spot size. It also demonstrates that the model shows very good agreement with the average fluence threshold measured in section 5.2. The plot has also been compared to experimental results from sections 6.2 and 6.3. Here it can be seen that as before, shadowgraphy does not fit the theoretical results particularly at low fluences, and therefore is not suitable for determining the fluence threshold for polymers using long pulse, moderate irradiance lasers. The time resolved interferometry results show good agreement with the theoretical models, particularly at lower irradiances. In general the TRI predicted thresholds are lower than the measured average value and the theoretical model, which could be due to the linear approximation of the velocity. At higher fluences the fume has a higher initial

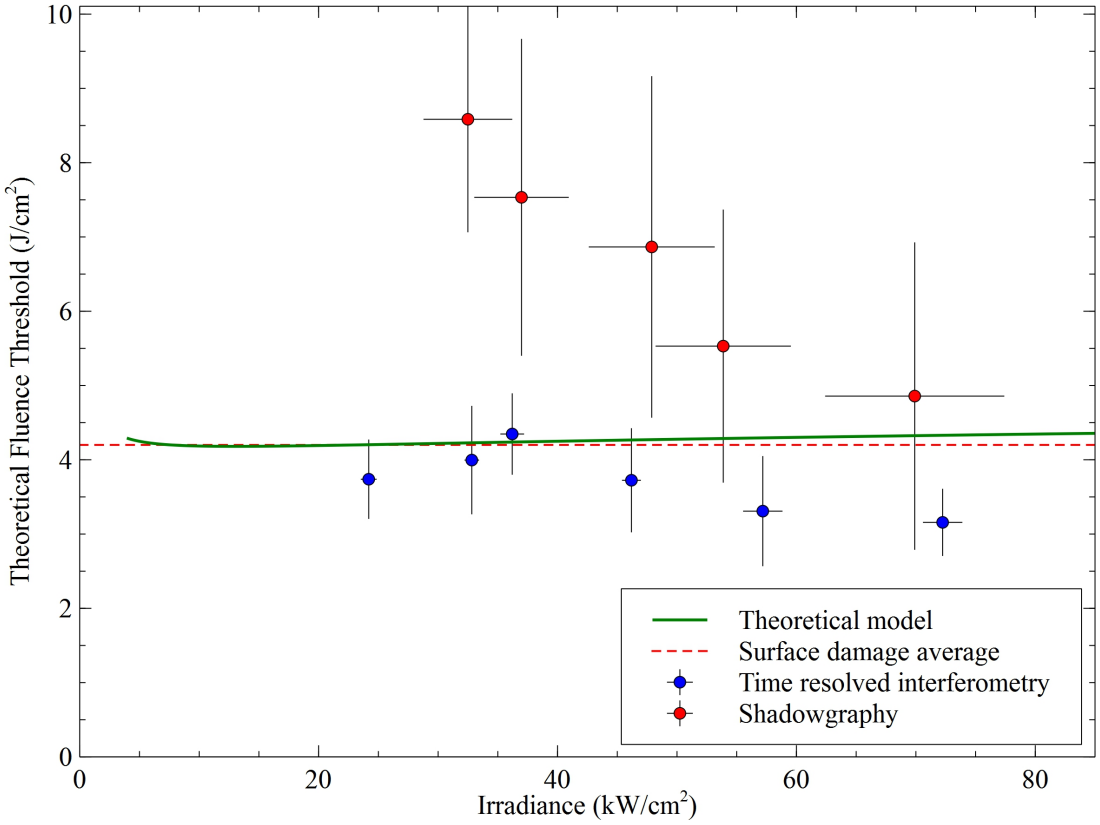

Figure 7.4: A graph of the theoretical threshold compared to experimental decomposition results measured in sections 6.2 and 6.3, and also the average threshold for the irradiance range $24 - 72\text{kW}\,\text{cm}^{-2}$, measured in section 5.2.

velocity, resulting in a greater drag, thus the linear approximation used is less valid as the irradiance increases.

Decomposition has been modelled and plotted over a wider range of irradiances in order to make predictions for more powerful industrial CO_2 lasers (figure 7.5). Estimating a spot size of 250μm and neglecting losses in optical elements, irradiances of $\sim 4\text{MW}\,\text{cm}^{-2}$ and $\sim 10\text{MW}\,\text{cm}^{-2}$ are achievable with a 8kW Rofin[166] DC series SLAB CO_2 laser and a 20kW Trumpf[167] TruFlow CO_2 laser respectively. The theoretical time to decomposition for this range is plotted in figure 7.5a and the theoretical threshold fluence is plotted in figure 7.5b. The heating rate induced with the Rofin 8kW laser would give a theoretical time to decomposition of 1.34μs and a predicted fluence threshold of $5.4\text{J}\,\text{cm}^{-2}$. The Trumpf 20kW laser yields a time to decomposition of 0.57μs with a fluence threshold of $5.7\text{J}\,\text{cm}^{-2}$.

It should be noted that this analysis is only valid for the onset of decomposition. Once volatilized material begins to emerge from the laser heated spot, coupling of the laser light can change due to plume absorption, scattering, ignition (flames) and plasma formation.

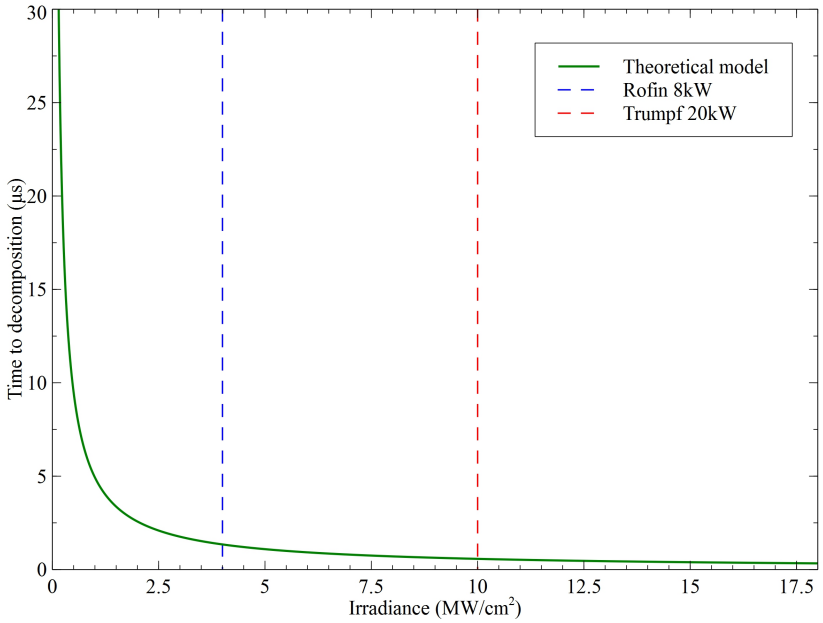

(a) Time to decomposition

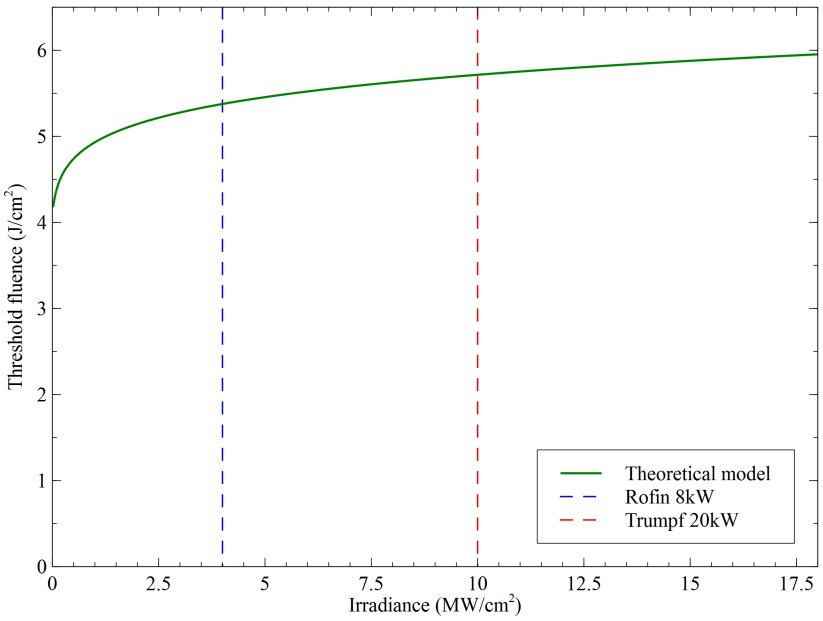

(b) Threshold fluence

Figure 7.5: Theoretical modelling predictions beyond the range of irradiances achievable by the RF CO_2 laser used in this thesis in order to cover some higher power industrial CO_2 lasers. Irradiances achievable by a Rofin 8kW laser and a Trumpf 20kW laser focussed to a spot with a radius of 250µm are shown on the plot. The time to decomposition is shown in figure 7.5a, and the threshold fluence is shown in figure 7.5b.

7.3 Conclusions

In this chapter the thermal decomposition of RS-M135 epoxy resin irradiated with an RF CO_2 laser has been modelled; good agreement is obtained with the average threshold fluence measured from the damage in chapter 5, and also the time to decomposition which was measured using time resolved interferometry in chapter 6. The parameters used in the model were based entirely on experimental data, due to the lack of thermal and optical properties in the literature for the specific epoxy resin.

The model is also suitable for predicting an optimum processing irradiance due to the two competing processes: thermal diffusion into the sample, and the effect of heating rate on the temperature of decomposition, as discussed in section 4.4, i.e. the greater the heating rate, the higher the decomposition temperature, thus the more energy required before the sample starts to decompose. It should be noted that over the range of fluences provided by the RF CO_2 laser the change in threshold fluence is relatively small for this low thermal conductivity material.

The model has also been used to predict the time to decomposition for this polymer using higher power CO_2 lasers, but experimental data is not currently available to confirm the validity of the model in this regime.

From the results here, it can be inferred that the fluence threshold with respect to laser irradiance can be predicted for a polymer without prior knowledge of its characteristics. This could be achieved by first using the techniques outlined in this thesis to measure the thermal and optical properties of the material, and subsequently using the obtained values in the model described in this chapter, yielding the fluence threshold.

Chapter 8

Conclusions

8.1 Conclusions

RF CO_2 laser processing of CFRPs has been investigated in order to develop an understanding of the interaction and particularly the contents of the resultant fume and the dynamics of this ejected material.

The RF CO_2 laser was characterised first in terms of spot size, pulse duration and pulse energy, which was important so that fluences and irradiances could be stated and used in models accurately. The delay in the optical output of the laser with respect to the control signal was also characterised because measurements involving time resolved fast imaging techniques were used extensively. The dye laser used for shadowgraphy and TRI was also characterised in pulse duration, linewidth and wavelength as these parameters govern the temporal resolution (effective shutter duration) of the imaging system, the interferometer coherence length, and the response of the camera's detector. The dye laser was suitable for the imaging systems and produced high quality shadowgraphs and interferograms.

The CFRP, carbon fibre weave and RS-M135 epoxy resin were then individually characterised. The epoxy resin was characterised using TGA, DSC and 'Lees' discs' to

measure the activation energy, specific heat capacity and thermal conductivity respectively, these values were obtained from literature for the carbon fibre weave. The thermal conductivity of the CFRP could be calculated knowing the epoxy matrix to carbon fibre ratio and the conductivity of each. TGA and DSC were used to describe the decomposition of the CFRP and carbon fibre weave in an air atmosphere and also a nitrogen atomosphere.

The reflectance and absorption coefficient of the epoxy was measured using FT-IR; the absorbance experiment required a thin slice of epoxy to be cast due to its high absorption coefficient at the RF CO_2 laser wavelength of 10.59μm. The complex refractive indices of carbon fibre are available in literature and these values were used with a model to calculate the reflectivity of the carbon fibre at the laser processing wavelength, and therefore the percentage of the laser light absorbed by the fibres. The reflectivities were found to be high and to depend on the polarization orientation of the incident light with respect to the fibre direction; when the polarization was perpendicular to the direction of the fibres the absorption was $1.6\times$ the value when it was parallel to the fibres. The parameters measured in chapter 4 were used to explain the laser processing results by calculating the thermal diffusion length and the optical absorption coefficient of the carbon fibres, and the two showed good agreement. The parameters were also used in theoretical models to predict the time to decomposition and threshold fluence for the RF CO_2 laser irradiation of epoxy resin.

The CFRP and its separate components were laser processed, and the results were analysed, aided by the thermal and optical measurements on the materials. It was found that the HAZ of the CFRP in the direction of the fibres was greatly increased as compared to the perpendicular direction. This was expected because of the anisotropic thermal conductivity leading to differences in the thermal diffusion length. The depth of the epoxy on top of the fibres in the CFRP, which was observed to vary over the surface of the sample, had a big impact on the HAZ. A thinner epoxy resin layer meant the visible HAZ was much larger. This is due to more energy being transmitted to the highly conductive carbon fibres through the epoxy, which can be as thin as 7μm, (i.e.

much less than the optical absorption depth for the epoxy of 26.8μm), and also because the epoxy will decompose sooner in the long pulse interaction, exposing the fibres. It can also be explained by the ratio of carbon fibres to epoxy resin being higher when the epoxy is thinner, increasing the contribution of the fibre conductivity, which is much higher than the epoxy, particularly in the direction of the fibres. The average fluence threshold for decomposition of the epoxy resin was measured to be $4.2 \pm 0.5 \mathrm{J\,cm^{-2}}$ in the range of $24 - 72 \mathrm{kW\,cm^{-2}}$, which was later found to be consistent with results from TRI and a theoretical decomposition model. The bare carbon fibre weave was found to have a threshold fluence of $21.3 \pm 11.2 \mathrm{J\,cm^{-2}}$ when the polarization of the laser is parallel to the direction of the fibres, and $14.3 \pm 5.5 \mathrm{J\,cm^{-2}}$ when the polarization is perpendicular to the fibres. Thus, when the incident light polarization is not in its optimal configuration, the fluence threshold is $1.5\times$ that of when it is in the optimal configuration, a result which is in close agreement with the predictions based on the reflectivity results. Fibre swelling during laser processing was also found. At low irradiances (which may be high enough to ablate epoxy) the carbon fibres were not damaged, at moderate irradiance levels the fibres swelled, and at higher irradiances the fibre thinned before decomposing fully and breaking. Due to the Gaussian profile of the laser irradiance the transition from high, to moderate, to low irradiance is experienced across the spot radius. This meant that the cut ends of the fibres were found to be swollen and pointed, which later made identification of fibres which had been laser processed easier.

The fume from the RF CO_2 laser processed CFRP was captured and analysed using FT-IR, GC-MS and SEM. It was found that the primary vapour phase fume product was phenol. The permanent gas phase product was mainly carbon dioxide, but also contained carbon monoxide and methane with some evidence of a formaldehyde component. When a large quantity of the composite was cut there was also water vapour present in the fume. A few fibres were found distributed around the ablation sites and in the filter from an extraction unit, and the fibres had characteristic swollen pointed ends which meant that they had been cut at either end by the laser. Many of the fume

contents were potentially hazardous to human health, and must be treated accordingly.

In order to gain a greater understanding of the release mechanism for the fibres, fast imaging was used. Fibres were observed leaving the sample ablation site with shadowgraphy and TRI. They could also be observed leaving the sample in a non-time resolved way by removing the optical band pass filter. Hot, incandescent fibres were self-luminous and exposed the camera with a 'yellow' streak, which was different from the usual self-luminous plume observed with the ablation of carbon fibres. The method was confirmed by observing fibres lining up with the yellow streak. The cut fibres also disrupted the Michelson fringes surrounding them, suggesting that they were hot. The fibres were confirmed as being released by being cut at either end, which means that they are released readily if a bare carbon fibre weave is processed with holes or cuts along the direction of the fibres. Fibres were also observed to be released from a CFRP under the specific condition that the epoxy HAZ from two ablation sites overlap exposing bare fibres which could then be cut. Due to the swelling of the fibres at the ends, and the way in which the fibres are released, is unlikely that a Gaussian beam would release a respirable fibre. This is because the irradiance incident on the fibre would rapidly change from a regime where it was decomposing the fibre, to where it induced fibre swelling. It is therefore unlikely that a fibre would be thinned along it's length to a diameter of $< 3\mu m$ and released. Interferometry was also used to measure the refractive index of the plume from CFRP, which was found to provide a realistic value, but no further conclusions could be drawn from it.

The fast imaging technique was also used to map out the trajectory of the plume from the ablated epoxy with respect to irradiance. In doing so the time delay before the interaction begins to produce fume could be plotted with respect to irradiance and also the velocity at which it leaves the sample. The velocity could be estimated by fitting a line of best fit to the first 5mm of the expansion above the surface of the sample assuming a linear distance-time relationship applied. The TRI results also gave a second method of measuring the threshold fluence with respect to irradiance, by calculating the fluence which was delivered to the sample before it began to decompose. The threshold

fluence over the range provided by the RF CO_2 laser was found to be relatively linear, and showed good agreement with the average threshold fluence measured by damage to the epoxy.

Finally, a theoretical model for the temperature rise and subsequent decomposition of the epoxy was presented, based on opto-thermal values which were measured in the thesis. This yielded the time to decomposition and the fluence threshold with respect to irradiance. The model showed good agreement with the fluence threshold measured using the two methods, and also the time to decomposition from TRI. The model was also used to predict these parameters for other higher power commercial long pulse CO_2 lasers. From the results it would be expected that these predictions could be made for any long pulse laser and given polymer with no previous knowledge of its characteristics.

8.2 Future work

The work presented here demonstrates techniques to gather fume information from laser processed CFRPs in a general way, and details of the likely fume content were set out in section 5.3. Due to the large variation in composites and laser processes the general techniques should be applied to the process to be used. For a specific laser process, the fume should be sampled isokinetically, as described in section 5.3.1. Using the data in this thesis on the likely fume content, appropriate gas detection systems, such as Dräger tubes[168], could then be used to gather quantitative 'parts per million' data for a particular process. In chapter 5 is was found that the fume content from laser processed CFRP were potentially hazardous; therefore, quantitative data for a specific process should be compared with local health and safety guidelines; subsequently, appropriate fume treatment should be selected. Fume gathered by isokinetic sampling could also be analysed for particulate size distribution using standard equipment which uses techniques such as laser diffraction or light scattering.

To take the work in this thesis further, the fume's effect on the laser process could be investigated. The absorption/scattering of the laser beam within the plume could be analysed by splitting the RF CO_2 beam and directing it through the area above the ablation site; measuring the transmitted energy in a time resolved way could provide useful data for laser processing. This technique, along with probe beam deflection, could also yield information about potential lensing effects due to the plume of changed refractive index which was found during carbon fibre ablation. It would also be of interest to investigate the degree of ionization in the plume using spectroscopy coupled with ion probe measurements. This would give an opportunity to assess the impact of plasma formation on the interaction.

Appendix A: CFRP and Carbon Fibre Weave Laser Processing Results

In this appendix, full sets of data from the RF CO_2 laser processing of CFRP performed in chapter 5 are presented. The epoxy damage diameter is plotted with respect to the epoxy thickness on top of the fibres in figure 1. The fibre damage diameter is plotted against the epoxy layer thickness in figure 2. The results are measured in the X and the Y direction and are separated into pulse energies and polarizations with respect to the fibre direction. The 'X direction' refers to the direction which is parallel to the polarization of the laser, and 'Y direction' refers to the direction which is perpendicular to the polarization. The trends discussed in chapter 5 can be seen across the range of pulse energies.

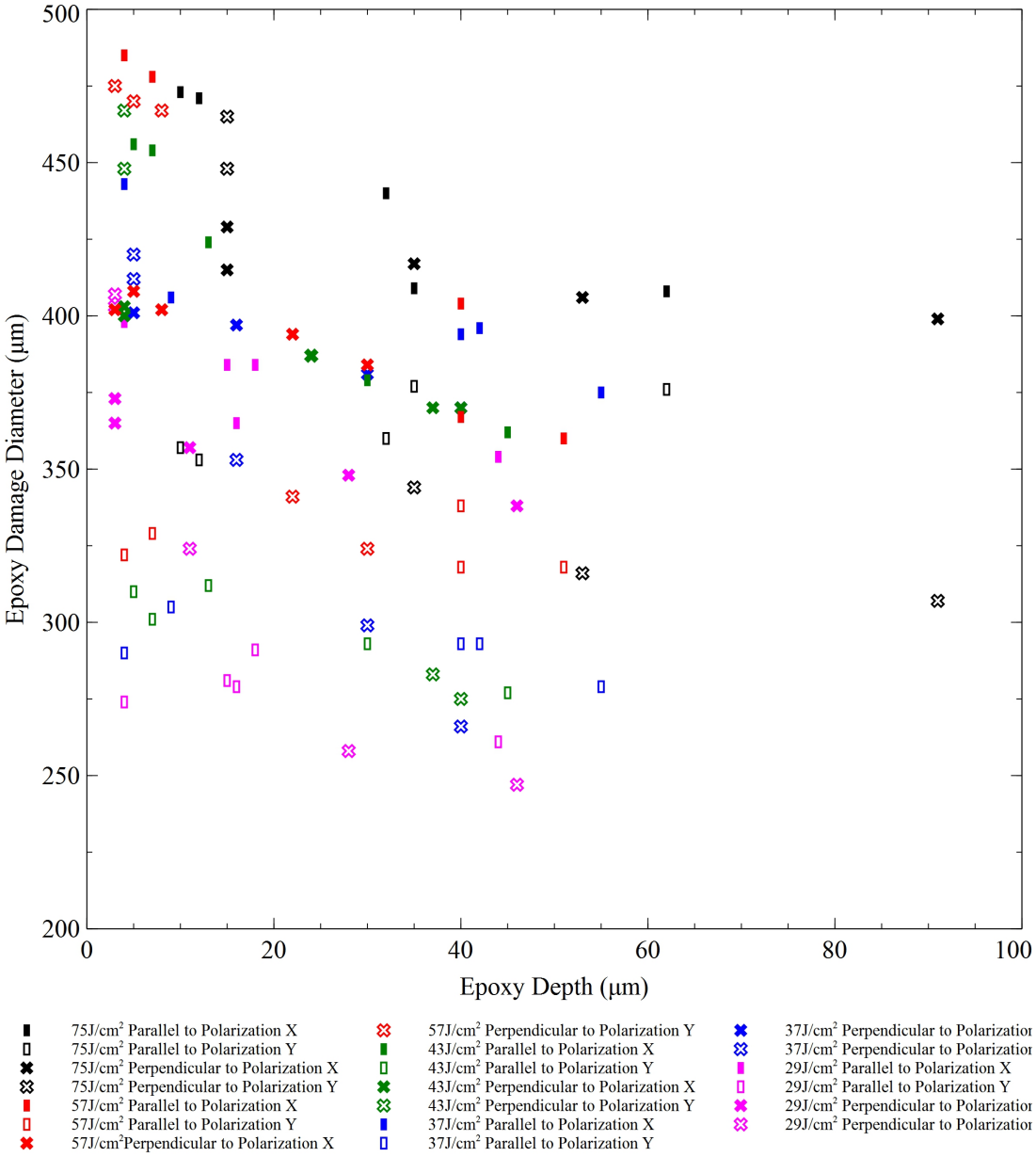

Figure 1: Results for the epoxy damage diameters for various irradiances and polarizations, with respect to the epoxy thickness on top of the fibres for carbon fibre reinforced composite processed with an RF CO_2 laser.

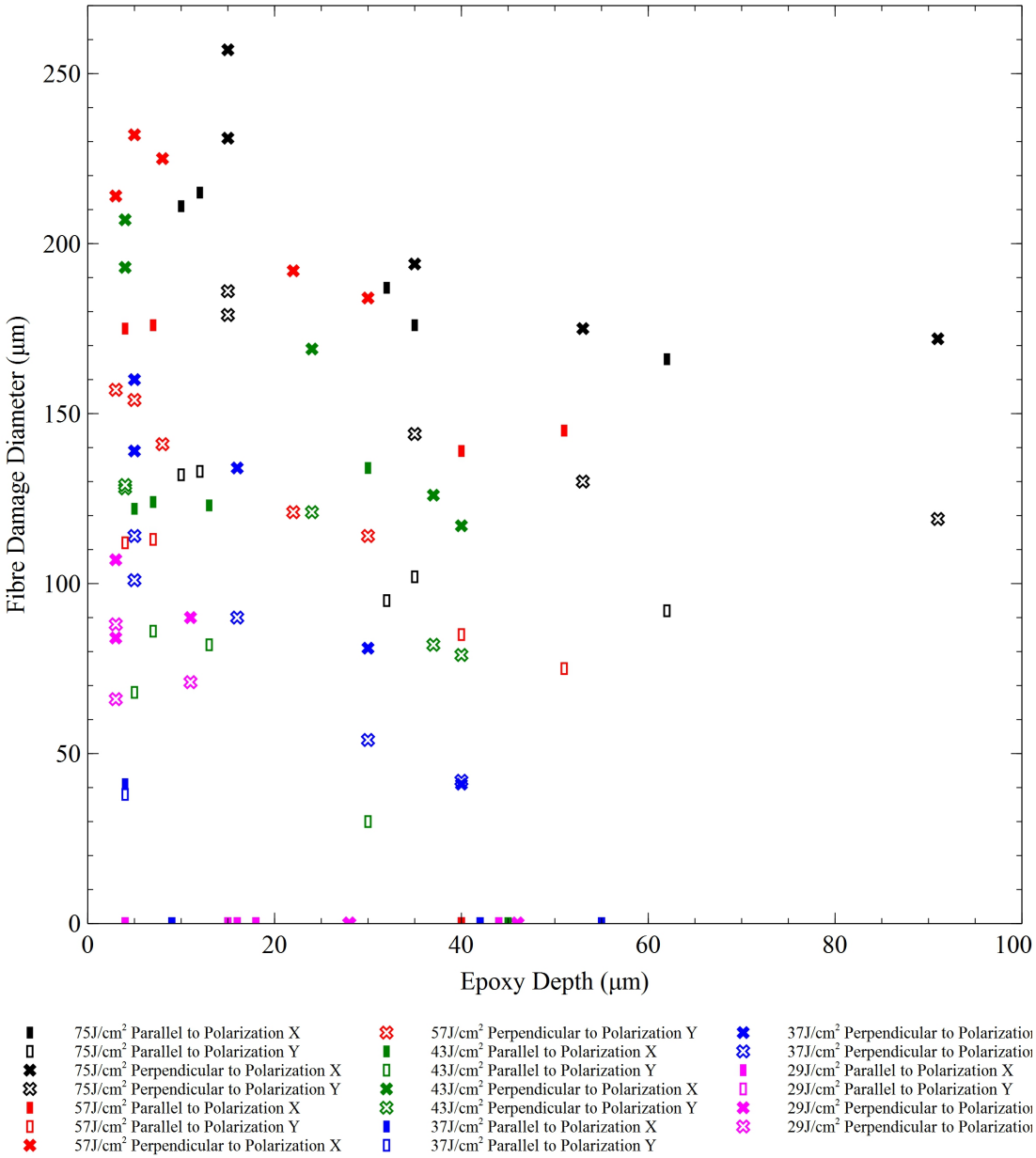

Figure 2: Results for the fibre damage diameters for various irradiances and polarizations, with respect to the epoxy thickness on top of the fibres for carbon fibre reinforced composite processed with an RF CO_2 laser.

Appendix B: Interferometer Parts List and Setup Procedure

Time resolved interferometry setup

The Michelson interferometer was arranged using a 30mm cage system with parts from Thor Labs Inc.[160] The primary component was a non-polarizing 50:50 beam-splitter cube, and the mirrors and collimating optics were spaced accordingly using rods ranging in size from ER90A 1.131″ rods, to ER6 6″rods, (figure 3). The high magnification camera system and stage to move the target were independent of the interferometer. The beam from the dye laser was directed into the interferometer via two PF10-03-F01 UV enhanced aluminium mirrors which were suitable for wavelengths of $250-450$nm, mounted in KM100 kinematic mounts on optical poles.

A render of the TRI setup, with the corresponding parts list is shown in figure 3. All of the parts number are from Thor labs Inc.[160]

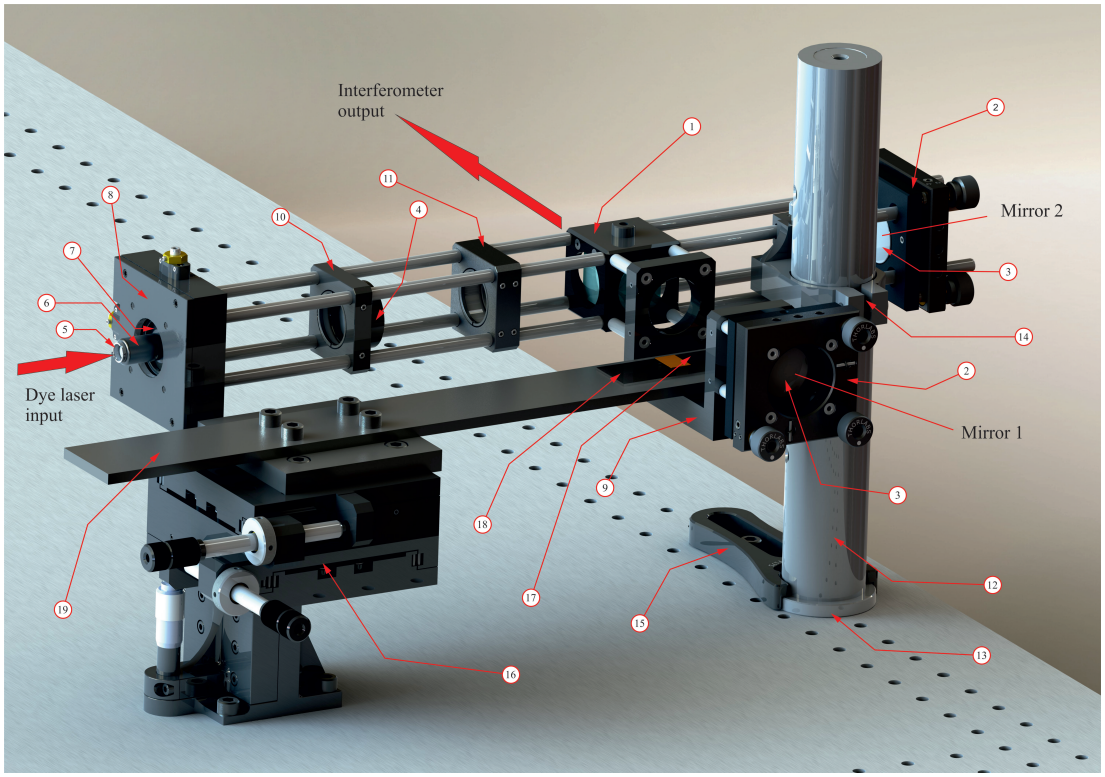

Figure 3: A render of the time resolved interferometry, setup using a Thor Labs 30mm cage system, the render was created using SolidWorks 2011 Education Edition.

Item	Part number	Description
1	CM1-BS013	Non-polarizing 50:50 beamsplitter cube, $400-700$nm
2	KC1/M	Kinematic mount
3	BB1-E02	$\varnothing 1''$ broadband dielectric mirror, $400-750$nm
4	AC254-100-A-ML	$\varnothing 1''$ achromatic doublet lens, $f = 100$mm, $400-700$nm
5	C560TME-A	$\varnothing 5.10$mm geltech aspheric lens, $f = 13.86$mm, $400-600$nm
6	E09RMS	Extended RMS to M9 $\times$ 0.5 adapter
7	SM1A3	Adapter with external SM1 threads and internal RMS threads
8	ST1XY-A/M	XY translator with 100 TPI drives, metric, ± 3mm travel
9	CB1/M	30mm cage system U-bench
10	CP02/M	SM1-threaded 30mm cage plate, $0.35''$ thick
11	CP02T/M	SM1-threaded 30mm cage plate, $0.5''$ thick
12	P250/M	$\varnothing 1.5''$ 250mm mounting post
13	PB4	Studded pedestal base adapter
14	C1526/M	30mm cage clamp for $\varnothing 1.5''$ posts
15	PF175	Clamping fork for $\varnothing 1.5''$ pedestal post
16	-	x-y-z micrometer driven target translation stage
17	-	Target
18	-	Microscope slide which target is mounted on
19	-	Steel bar

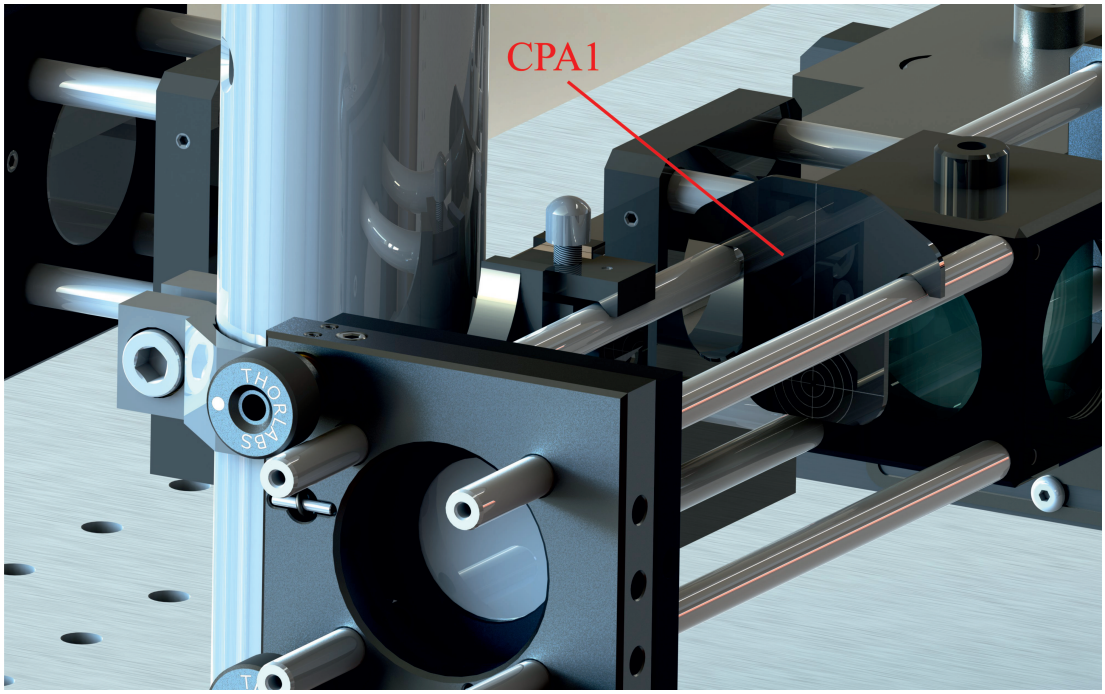

Figure 4: A render of the interferometer with a CP1 beam alignment tool in one of the arms.

Alignment procedure

The initial dye laser beam alignment through the system was performed by first removing the optics from the collimator, which had an initial spacing of 113.86mm as discussed in section 6.3.1. The UV enhanced mirrors which directed the dye laser though the interferometer were used to 'walk' the beam so that it passed through the centre of the beam splitter and was perpendicular to it. This was aided by a Thor Labs CPA1 beam alignment tool, (figure 4). The beam alignment tool could be placed into the 30mm cage system at any point, and had a 1mm hole through the middle. When the dye laser beam passed through the hole when the tool was placed at any point in the interferometer, the dye laser input alignment was complete.

Mirrors 1 and 2 were then aligned so that they were perpendicular to the dye laser beam. This was achieved with a home made alignment tool. A laser cutter was used to create a $1''$ clear acrylic disc with a 1mm hole in the centre. One side of the disc

was finely sanded so that it was 'frosted'. This was inserted into the interferometer between the beamsplitter and either mirror 1 or 2. The reflected beam of light could then be observed on the disc from both sides, and aligned so that it went through the hole in the centre. The optics in the collimator were then replaced.

The RF CO_2 laser was focussed to a point in the middle of the collimated beam of light and a pin was placed at that location. The camera was then directed into the output of the beamsplitter cube and focussed to the pin at the RF CO_2 laser ablation site. It should be noted that the working distance of the camera changed when observing a point through the beamsplitter cube due to the change in optical path length.

The interferometer was setup to observe interference fringes by adjusting mirrors 1 and 2. Throughout this part of the alignment process the camera body was removed from the extension tube and the output was observed on a piece of white paper. For the first stage the arm which held mirror 2 was blocked to increase contrast, and mirror 1 was used to align the collimated beam so that it was perpendicular to optical axis of the camera. This was achieved by using the pin at the ablation site as a reference point. Moving the mirror made two shadows of the pin move with respect to each other. At this stage the final setup of the collimator was performed. Changing the collimation by adjusting the distance between the lenses made the images of the pins change size with respect to each other. When the two images of pin were the same size the collimation was correct. The images of the pin could then be aligned with mirror 1 so that the two images were on top of each other.

Mirror 2 was then adjusted to form interference fringes. The mirror was initially set at around the same distance from the beam splitter cube as mirror 1, the distances were as close as was possible using vernier callipers and locked onto the cage bars. A Coherent Inc. HeNe laser[98] was then directed through the interferometer. A HeNe laser was chosen because it has a very narrow linewidth and therefore long coherence length, as discussed in section 2.6, which made fringes very easy to find and set up. The kinematic mount was used to adjust the angle of the mirror until large, clear fringes

were observed. The HeNe laser was removed and the dye laser was set to a PRR of 10Hz so that the output could be observed easily by eye on the paper. The final adjustment of the mirrors was achieved by 'walking' the mirror with the 3 adjustment screws of the kinematic mount; very small adjustments while trying to keep the angle constant were required as the coherence length was very short. When the fringes were as high contrast as possible, the final adjustment to get the fringes straight, horizontal and spaced as required could be performed.

Glossary

Symbol	Description
A	Surface area of sample in Lees' discs (m^2)
A_A,A_B,A_C,A_H	Surface area exposed to environment for copper disc A, B, C and the heater disc (m^2)
c_P	Specific heat capacity ($J\,kg^{-1}\,K^{-1}$)
$c_P(T)$	Specific heat capacity with respect to temperature ($J\,kg^{-1}\,K^{-1}$)
D	Damage diameter (m)
d	Sample thickness in Lees' discs (m)
d_{con}	Circle of confusion diameter (m)
d_e	Extension tube length (m)
d_f	Filter holder thickness (m)
d_g	Line spacing of grating (m)
D_H	Thermal diffusivity ($m^2\,s^{-1}$)
d_{L1},d_{L2}	Distance from front and rear of lens body to thin lens position (m)
D_n,D_p	Diameter of nozzle and extraction pipe (m)
D_o,D_i	Object and image size (m)
D_r	Column of refractive index n_2 diameter (m)
d_{WD}	Working distance (m)
D_x	Diameter of pipe (m)
DoF	Depth of focus (m)
E	Pulse energy (J)
E_a	Activation energy ($J\,mol^{-1}$)

E_T	Threshold energy (J)
f	Focal length (m)
$F(r)$	Fluence as a function of r ($\mathrm{J\,m^{-2}}$)
$f\#$	F/number
F_0	Peak fluence ($\mathrm{J\,m^{-2}}$)
F_P	Focal point
F_T	Threshold fluence ($\mathrm{J\,m^{-2}}$)
FFD	Flange focal distance (m)
$G(T)$	DSC calibration function (temperature dependent)
I	Current (A)
I_0,I_T	Initial and transmitted intensity
I_a	Absorbed irradiance ($\mathrm{W\,m^{-2}}$)
I_{max},I_{min}	Maximum and minimum intensity of interferometer fringes
K	Thermal conductivity ($\mathrm{W\,m^{-1}\,K^{-1}}$)
k	Imaginary part of complex refractive index $\tilde{n}$ (extinction coefficient)
k_o,k_e	Imaginary part of ordinary and extraordinary complex refractive indices (extinction coefficients)
K^p_{CFRP},K_m,K^p_f	Thermal conductivities of: the unidirectional CFRP parallel to the direction of the fibres, the resin matrix and the carbon fibres parallel to the direction of the fibres ($\mathrm{W\,m^{-1}\,K^{-1}}$)
l_c	Coherence length (m)
L	Thin lens position
M	Magnification
m	Order number
m_s	Sample mass (kg)
n	Real part of complex refractive index $\tilde{n}$
$\tilde{n}$	Complex refractive index
n_1	Refractive index of air
n_2	Refractive index of column in interferometer

N_B	Fraction of bonds remaining
n_o,n_e	Real part of ordinary and extraordinary complex refractive indices
$\tilde{n_o}$,$\tilde{n_e}$	Complex ordinary and extraordinary complex refractive indices
PRR	Pulse repetition rate (Hz)
Q_x	Volumetric flow rate ($m^3\ s^{-1}$)
Q_n,Q_p	Volumetric flow rate of nozzle and extraction pipe ($m^3\ s^{-1}$)
R	Reflectance
r	Spatial position (m)
r_1,r_2	Input and output collimated beam radii (m)
R_a,R_q	Surface roughness and RMS surface roughness (m)
r_c	Fibre core radius (m)
r_d	Radius of fume sphere (m)
r_{diff}	radius of airy disc (m)
r_{ss},r_{pp}	Amplitude reflection coefficients for s and p-polarized light incident on a basal plane
R_{ss},R_{pp}	Reflectance for s and p-polarized light incident on a carbon fibre
s_o,s_i	Object and image distance (m)
t	Delay between start of RF CO_2 laser optical emission and dye laser pulse (or time through laser pulse) (s)
t'	Delay between start of RF CO_2 laser trigger pulse and dye laser pulse (s)
$T(z,t)$	Temperature of sample at depth z and time t (K)
T_0	Room temperature (K)
T_A,T_B,T_C,T_H	Temperature of copper discs A, B, C and the heater disc (K)
T_D	Decomposition temperature at a particular degree of decomposition (K)
t_d	Time to decomposition (s)
T_{trans}	Fractional transmitted intensity
V	Voltage (V)

v_0	Initial velocity ($\mathrm{m\,s^{-1}}$)
V_m,V_f	Volumetric fraction of matrix and fibres in a CFRP
V_{max}	Maximum resolvable velocity ($\mathrm{m\,s^{-1}}$)
v_t	Terminal velocity ($\mathrm{m\,s^{-1}}$)
$V_{visibility}$	Visibility of interferometer
V_x	Flow velocity ($\mathrm{m\,s^{-1}}$)
w	Fringe spacing (m)
w_r	Peak fringe displacement of a column of refractive index n_2
z	Distance into sample (m)
$z(t)$	Fume propagation from the sample with respect to time t (m)
α	Optical absorption coefficient ($\mathrm{m^{-1}}$)
β	Fibre radial co-ordinate (m)
β_f	Fibre radius (m)
γ	Fractional degree of decomposition
Δt	Delay between start of RF CO_2 trigger pulse and optical emission (s)
$\Delta T(z,t)$	Temperature rise of sample at depth z and time t (K)
$\Delta\Theta$	Divergence full angle (rad)
$\Delta\lambda$	Linewidth (m)
$\Delta\lambda_t$	Theoretical linewidth (m)
$\Delta\nu$	Frequency bandwith (Hz)
δ	Thermal diffusion length (m)
ζ	Constant to be determined
θ_{d1},θ_{d2}	Fibre input and output beam divergences (rad)
θ_i	Angle of incidence (rad)
θ_r	Angle of refraction (rad)
θ_L	Littrow angle (rad)
θ_{max}	Maxium fibre acceptance half angle (rad)
θ_m	Angle of refraction at order m (rad)
κ	Rate constant ($\mathrm{s^{-1}}$)

λ	Wavelength (m)
λ_0	Peak wavelength (m)
ξ	heat transfer coefficient ($\mathrm{W\,m^{-2}\,K^{-1}}$)
ρ	Density ($\mathrm{kg\,m^{-3}}$)
ρ_{air}	Density of air ($\mathrm{kg\,m^{-3}}$)
ρ_d	Density of fume sphere ($\mathrm{kg\,m^{-3}}$)
τ	RF CO_2 laser pulse duration (s)
τ'	Laser trigger pulse duration (s)
τ_c	Coherence time (s)
τ_{cam}	Camera physical shutter duration (s)
τ_{exp}	Camera physical shutter duration (s)
χ	TGA heating rate ($\mathrm{K\,s^{-1}}$)
ψ	Angle displacement of mirror 2 in interferometer (rad)
ω_0	Spot radius (m)
$\partial\theta_m/\partial\lambda$	Total dispersion of system (rad)
dQ/dt	Heat flow (W)
dT/dt	DSC heating rate ($\mathrm{K\,s^{-1}}$)
dT/dx	Temperature gradient across sample in Lees' discs ($\mathrm{K\,m^{-1}}$)
$\overline{R}$	$8.31446\mathrm{J\,K^{-1}\,mol}$
c	$3.00 \times 10^8 \mathrm{m\,s^{-1}}$
g	$9.807\mathrm{m\,s^{-2}}$
h	$6.62606957 \times 10^{-34} \mathrm{m^2\,kg\,s^{-1}}$
i	$\sqrt{-1}$
k_B	$1.3806488 \times 10^{-23} \mathrm{m^2\,kg\,s^{-2}\,K^{-1}}$

References

[1] W.F. Smith. *Principles of materials science and engineering*. McGraw-Hill, New York, NY, 3rd edition, 1986.

[2] A. Abrao, P. Faria, J. Rubio, P. Reis, and J. Davim. Drilling of fiber reinforced plastics: A review. *Journal of Materials Processing Technology*, 186(1-3):1–7, 2007.

[3] D. Iliescu, D. Gehin, M.E. Gutierrez, and F. Girot. Modeling and tool wear in drilling of CFRP. *International Journal of Machine Tools and Manufacture*, 50(2):204–213, 2010.

[4] W.M. Steen. *Laser Material Processing*. Springer-Verlag, London, 1991.

[5] C.F. Cheng, Y.C. Tsui, and T.W. Clyne. Application of a three-dimensional heat flow model to treat laser drilling of carbon fibre composites. *Acta Materialia*, 46(12):4273–4285, 1998.

[6] P.E. Dyer, S.T. Lau, G.A. Oldershaw, and D. Schudel. An investigation of XeCl laser ablation of polyetheretherketone (PEEK)-carbon fiber composite. *Journal of Materials Research*, 7(05):1152–1157, 1992.

[7] Z.L. Li, P.L. Chu, H.Y. Zheng, and G.C. Lim. Process development of laser machining of carbon fibre reinforced plastic composites. *SIMTech technical reports*, 10(1):10–14, 2009.

[8] A. Riveiro, F. Quintero, F. Lusquiños, J. del Val, R. Comesaña, M. Boutinguiza, and J. Pou. Experimental study on the CO2 laser cutting of carbon fiber reinforced plastic composite. *Composites Part A: Applied Science and Manufacturing*, 43(8):1400–1409, 2012.

[9] P.E. Dyer, D.M. Karnakis, P.H. Key, and J.P. Tait. Excimer laser ablation of low and high absorption index polymers. *Applied Surface Science*, 96-98(95):596–600, 1996.

[10] A. Adamson. *A Textbook of Physical Chemistry*. Academic Press Inc., London, 1973.

[11] A.A. Michelson. The relative motion of the Earth and of the luminiferous ether. *American Journal of Science*, 1881.

[12] M.P. Groover. *Fundamentals of modern manufacturing: materials processes, and systems*. John Wiley & Sons Inc., New York, NY, 2nd edition, 2007.

[13] In Young Yang, Joo Yeong Jeong, and Ji Hoon Kim. Fracture toughness of CFRP laminated plates according to resin content. *International Journal of Precision Engineering and Manufacturing*, 11(2):309–313, 2010.

[14] C. Soutis. Carbon fiber reinforced plastics in aircraft construction. *Materials Science and Engineering: A*, 412(1-2):171–176, 2005.

[15] Airbus SAS. Innovative materials. *http://www.airbus.com/innovation/proven-concepts/in-design/innovative-materials/*.

[16] W.C. Chen. Some experimental investigations in the drilling of carbon fiber-reinforced plastic (CFRP) composite laminates. *International Journal of Machine Tools and Manufacture*, 37(8):1097–1108, 1997.

[17] J. Davim. Study of delamination in drilling carbon fiber reinforced plastics (CFRP) using design experiments. *Composite Structures*, 59(4):481–487, 2003.

[18] U.A. Khashaba. Delamination in drilling GFR-thermoset composites. *Composite Structures*, 63(3-4):313–327, 2004.

[19] R. Stone and K. Krishnamurthy. A neural network thrust force controller to minimize delamination during drilling of graphite-epoxy laminates. *International Journal of Machine Tools and Manufacture*, 36(9):985–1003, 1996.

[20] H. Hocheng and C.C. Tsao. Comprehensive analysis of delamination in drilling of composite materials with various drill bits. *Journal of Materials Processing Technology*, 140(1-3):335–339, 2003.

[21] P.W. French, M. Naeem, J. Clowes, and M.C. Sharp. Fibre laser material processing of Aerospace Composites. In *Proceedings of the Fifth International WLT-Conference on Lasers in Manufacturing*, pages 339–346, 2009.

[22] B. Rooks. Laser processing of plastics. *Industrial Robot: An International Journal*, 31(4):338–342, 2004.

[23] Y. Kawamura. Effective deep ultraviolet photoetching of polymethyl methacrylate by an excimer laser. *Applied Physics Letters*, 40(5):374, 1982.

[24] R. Srinivasan. Self-developing photoetching of poly(ethylene terephthalate) films by far-ultraviolet excimer laser radiation. *Applied Physics Letters*, 41(6):576, 1982.

[25] D. Bäuerle. *Laser processing and chemistry*. Springer-Verlag, Berlin, 2nd edition, 2000.

[26] National Physical Laboratory. 3.7.2 Bond lengths and dissociation enthalpies of diatomic molecules. *http://www.kayelaby.npl.co.uk/chemistry/3_7/3_7_2.html*.

[27] J.E. Andrew, P.E. Dyer, D. Forster, and P.H. Key. Direct etching of polymeric materials using a XeCl laser. *Applied Physics Letters*, 43(8):717, 1983.

[28] H.H.G. Jellinek and R. Srinivasan. Theory of etching of polymers by far-ultraviolet high-intensity pulsed laser- and long-term irradiation. *The Journal of Physical Chemistry*, 88(14):3048–3051, 1984.

[29] P.E. Dyer and J. Sidhu. Excimer laser ablation and thermal coupling efficiency to polymer films. *Journal of Applied Physics*, 57(4):1420, 1985.

[30] V. Srinivasan, Mark A. Smrtic, and S.V. Babu. Excimer laser etching of polymers. *Journal of Applied Physics*, 59(11):3861, 1986.

[31] R. Srinivasan, B. Braren, and R.W. Dreyfus. Ultraviolet laser ablation of polyimide films. *Journal of Applied Physics*, 61(1):372, 1987.

[32] Thomas Lippert. Interaction of Photons with Polymers: From Surface Modification to Ablation. *Plasma Processes and Polymers*, 2(7):525–546, 2005.

[33] P.E. Dyer. Excimer laser polymer ablation: twenty years on. *Applied Physics A*, 77(2):167–173, 2003.

[34] J.H. Brannon and J.R. Lankard. Pulsed CO2 laser etching of polyimide. *Applied Physics Letters*, 48(18):1226, 1986.

[35] Gad Koren. CO2 laser assisted UV ablative photoetching of Kapton films. *Applied Physics Letters*, 45(1):10, 1984.

[36] P.E. Dyer, G.A. Oldershaw, and J. Sidhu. CO2 laser ablative etching of polyethylene terephthalate. *Applied Physics B*, 48(6):489–493, 1989.

[37] R. Braun, R. Nowak, P. Hess, H. Oetzmann, and C. Schmidt. Photoablation of polyimide with IR and UV laser radiation. *Applied Surface Science*, 43(1-4):352–357, 1989.

[38] P.E. Dyer, D.M. Karnakis, G.A. Oldershaw, and G.C. Roberts. TEA CO2 laser ablation of Upilex polyimide. *Journal of Physics D: Applied Physics*, 29(10):2554–2563, 1996.

[39] P.E. Dyer, I. Waldeck, and G.C. Roberts. Fine-hole drilling in Upilex polyimide and glass by TEA CO2 laser ablation. *Journal of Physics D: Applied Physics*, 30(6):L19–L21, 1997.

[40] É.E. Said-Galiev and L.N. Nikitin. Ablation of polymers and composites when exposed to CO2 laser radiation (review). *Mechanics of composite materials*, (2), 1992.

[41] P. Cheo. *Handbook of molecular lasers*. Marcel Dekker, Inc., New York, NY, 1987.

[42] J. Powell. *CO2 laser cutting*. Springer-Verlag, London, second edition, 1998.

[43] F. Caiazzo, F. Curcio, G. Daurelio, and F. Minutolo. Laser cutting of different polymeric plastics (PE, PP and PC) by a CO2 laser beam. *Journal of Materials Processing Technology*, 159(3):279–285, 2005.

[44] A.J. DeMaria and T.V. Hennessey. The CO2 Laser: The Workhorse of the Laser Material Processing Industry. *SPIE Professional Magazine*, pages 1–27, 2010.

[45] P.A. Atanasov and M.G. Baeva. CW CO2 laser cutting of plastics. In *Proceedings of SPIE 3092, XI International Symposium on Gas Flow and Chemical Lasers and High-Power Laser Conference*, 1997.

[46] J. Paulo Davim, Carlos Oliveira, Nuno Barricas, and Marta Conceição. Evaluation of cutting quality of PMMA using CO2 lasers. *The International Journal of Advanced Manufacturing Technology*, 35(9-10):875–879, 2006.

[47] I.A. Choudhury and S. Shirley. Laser cutting of polymeric materials: an experimental investigation. *Optics & Laser Technology*, 42(3):503–508, 2010.

[48] S. Hashmi. *Comprehensive Materials Processing*. Elsevier Science Ltd., Amsterdam, 2014.

[49] J. Davim, N. Barricas, M. Conceicao, and C. Oliveira. Some experimental studies on CO2 laser cutting quality of polymeric materials. *Journal of Materials Processing Technology*, 198(1-3):99–104, 2008.

[50] M. Von Allmen and A. Blatter. *Laser-Beam Interactions with Materials*. Springer, Berlin, 2nd edition, 1998.

[51] William T. Silfvast. *Laser Fundamentals*. Cambridge University Press, 2nd edition, 2004.

[52] R. Rolfes and U. Hammerschmidt. Transverse thermal conductivity of CFRP laminates: a numerical and experimental validation of approximation formulae. *Composites science and technology*, 54(1):45–54, 1995.

[53] National Physical Laboratory. 3.11.1 Properties of polymers. *http://www.kayelaby.npl.co.uk/chemistry/3_11/3_11_1.html*.

[54] H. Niino, M. Nakano, and S. Nagano. Excimer laser ablation of polymers and carbon fiber composites. *Journal of Photopolymer Science and Technology*, 3(1):53–56, 1990.

[55] Christian Freitag, Volkher Onuseit, Rudolf Weber, and Thomas Graf. High-speed Observation of the Heat Flow in CFRP During Laser Processing. *Physics Procedia*, 39:171–178, 2012.

[56] Dirk Herzog, Peter Jaeschke, Oliver Meier, and Heinz Haferkamp. Investigations on the thermal effect caused by laser cutting with respect to static strength of CFRP. *International Journal of Machine Tools and Manufacture*, 48(12-13):1464–1473, 2008.

[57] Toray CFA Inc. T300 Carbon Fiber Data Sheet. *http://www.toraycfa.com/pdfs/T300DataSheet.pdf*.

[58] K. Voisey, S. Fouquet, D. Roy, and T. Clyne. Fibre swelling during laser drilling of carbon fibre composites. *Optics and Lasers in Engineering*, 44(11):1185–1197, 2006.

[59] T. Young and D. O'Driscoll. Impact of Nd-YAG laser drilled holes on the strength and stiffness of laminar flow carbon fibre reinforced composite panels. *Composites Part A: Applied Science and Manufacturing*, 33(1):1–9, 2002.

[60] J. Mathew, G.L. Goswami, N. Ramakrishnan, and N.K. Naik. Parametric studies on pulsed Nd:YAG laser cutting of carbon fibre reinforced plastic composites. *Journal of Materials Processing Technology*, 89-90(1-3):198–203, 1999.

[61] Z.L. Li, H.Y. Zheng, G.C. Lim, P.L. Chu, and L. Li. Study on UV laser machining quality of carbon fibre reinforced composites. *Composites Part A: Applied Science and Manufacturing*, 41(10):1403–1408, October 2010.

[62] R. Negarestani, M. Sundar, M.a. Sheikh, P. Mativenga, L. Li, Z.L. Li, P.L. Chu, C.C. Khin, H.Y. Zheng, and G.C. Lim. Numerical simulation of laser machining of carbon-fibre-reinforced composites. *Proceedings of the Institution of Mechanical Engineers, Part B: Journal of Engineering Manufacture*, 224(7):1017–1027, 2010.

[63] R. Negarestani and L. Li. Fibre laser cutting of carbon fibre-reinforced polymeric composites. *Proceedings of the Institution of Mechanical Engineers, Part B: Journal of Engineering Manufacture*, 227(12):1755–1766, 2013.

[64] A. Goeke and C. Emmelmann. Influence of laser cutting parameters on CFRP part quality. *Physics Procedia*, 5:253–258, 2010.

[65] J.F. Ready. *Effects of high-power laser radiation*. Academic Press Inc., New York, NY, 1971.

[66] T.J. Matthams. Mechanical properties of long-fibre thermoplastic composites with laser drilled microperforations 1. Effect of perforations in consolidated material. *Composites Science and Technology*, 59(8):1169–1180, 1999.

[67] E. Uhlmann, G. Spur, and H. Hocheng. The extent of laser-induced thermal damage of UD and crossply composite laminates. *International Journal of Machine Tools and Manufacture*, 39(4):639–650, 1999.

[68] J. Bliedtner, S. Remdt, H. Müller, and A. Petrich. Laser Cutting of Carbon Fibres. *Laser Technik Journal*, 10(5):45–48, 2013.

[69] P. Mucha, N. Speker, R. Weber, and T. Graf. Momentum and velocity of the ablated material in laser machining of carbon fiber preforms. *Applied Physics A*, 113(2):361–366, 2013.

[70] D.A. Skoog and D.M. West. *Principles of instrumental analysis*. Saunders College Publishing, Philadelphia, PA, 4th edition, 1980.

[71] K.L. Erickson. Thermal decomposition mechanisms common to polyurethane, epoxy, poly (diallyl phthalate), polycarbonate and poly (phenylene sulfide). *Journal of thermal analysis and calorimetry*, 89(2):427–440, 2007.

[72] N. Grassie, M.I. Guy, and N.H. Tennent. Degradation of epoxy polymers: Part 1-Products of thermal degradation of bisphenol-A diglycidyl ether. *Polymer degradation and stability*, 12(1):65–91, 1985.

[73] Tommy Hertzberg. Dangers relating to fires in carbon-fibre based composite material. *Fire and Materials*, 29(4):231–248, 2005.

[74] P.F. Holt and M. Horne. Dust from carbon fibre. *Environmental research*, 17(2):276–83, 1978.

[75] J.R. Castrejón-Pita. High speed shadowgraphy for the study of liquid drops. In *Fluid Dynamics in Physics, Engineering and Environmental Applications Environmental Science and Engineering*, pages 121–137. Springer, Berlin, 2013.

[76] M.E. Forney. *On the Appplication of a Laser to High Speed Photography*. PhD thesis, California Institute of Technology, 1963.

[77] P.E. Dyer and R. Srinivasan. Nanosecond photoacoustic studies on ultraviolet laser ablation of organic polymers. *Applied physics letters*, 48:445, 1986.

[78] G.M. Davis and M.C. Gower. Time resolved transmission studies of poly(methyl methacrylate) films during ultraviolet laser ablative photodecomposition. *Journal of Applied Physics*, 61(5):2090, 1987.

[79] J. Meyer, J. Kutzner, D. Feldmann, and K.H. Welge. Time-resolved experiments on the photoablation of polystyrene and PMMA by ArF-laser radiation. *Applied Physics B*, 12:7–12, 1988.

[80] P. Simon. Time-resolved ablation-site photography of XeCl-laser irradiated polyimid. *Applied Physics B: Lasers and Optics*, 256:253–256, 1989.

[81] R. Srinivasan, Bodil Braren, Kelly G. Casey, and Mildred Yeh. Ultrafast imaging of ultraviolet laser ablation and etching of polymethylmethacrylate. *Applied Physics Letters*, 55(26):2790, 1989.

[82] C.A. Puliafito and D. Stern. High-speed photography of excimer laser ablation of the cornea. *Archives of Opthalmology*, 105(9):1255–1259, 1987.

[83] P.E. Dyer, D.M. Karnakis, P.H. Key, and D. Sands. Fast photography of UV laser ablated metal films. *Applied Surface Science*, 109-110:168–173, 1997.

[84] R.E. Walkup, J.M. Jasinski, and R.W. Dreyfus. Studies of excimer laser ablation of solids using a Michelson interferometer. *Applied Physics Letters*, 48(24):1690, 1986.

[85] C.M. Vest. *Holographic interferometry*. John Wiley & Sons Inc., New York, NY, 1979.

[86] A. Lipson, S.G. Lipson, and H. Lipson. *Optical physics*. Cambridge University Press, Cambridge, UK, 4th edition, 2010.

[87] Eugene Hecht. *Optics*. Addison Wesley Longman Inc., Reading, Pa., 3rd edition, 1998.

[88] G.M. Odegard and A. Bandyopadhyay. Physical aging of epoxy polymers and their composites. *Journal of Polymer Science Part B: Polymer Physics*, 49(24):1695–1716, 2011.

[89] F.C. Burns and Stephen R. Cain. The effect of pulse repetition rate on laser ablation of polyimide and polymethylmethacrylate-based polymers. *Journal of Physics D: Applied Physics*, 29(5):1349–1355, 1996.

[90] A.L. Marchant and H.V. Snelling. Reciprocity in long pulse duration laser interactions with polymers. *Journal of Physics D: Applied Physics*, 45(21), 2012.

[91] K.J. Laidler. *Chemical Kinetics*. HarperCollinsPublishers Inc., New York, NY, 3rd edition, 1987.

[92] Peter Atkins and Julio de Paula. *Atkins' Physical Chemistry*. W. H. Freeman and Company, New York, NY, 10th edition, 2014.

[93] Universal Laser Systems. OEM ULR 30. *http://www.co2laser.com/*.

[94] Agilent Technologies Inc. Agilent InfiniiVision 3000 X-Series Oscilloscopes. *http://cp.literature.agilent.com/litweb/pdf/5990-6619EN.pdf*.

[95] D.C. O'shea. *Elements of modern optical design*. John Wiley & Sons Inc., New York, NY, 1985.

[96] Walter G. Driscoll, W. Vaughan, and Optical Society of America. *Handbook of Optics*. McGraw-Hill, New York, NY, 1979.

[97] Database of Optical Materials. Crystran. *http://www.crystran.co.uk/optical-materials*.

[98] Coherent Inc. 5100 Patrick Henry Drive, Santa Clara, CA 95054 USA. *http://www.coherent.com/*.

[99] D. Brewster. On the laws which regulate the polarisation of light by reflexion from transparent bodies. *Philosophical Transactions of the Royal Society of London*, 105:125–159, 1815.

[100] Donald C. O'Shea, W. Russell Callan, and William T. Rhodes. *An Introduction to Lasers and Their Applications*. Addison-Wesley Pub. Co., Reading, Pa., 1978.

[101] GSI Group Inc. Cosford lane, Swift Valley Rugby, Warwickshire, CV21 1QN. *http://www.gsig.com/*.

[102] Kodak. Optical Products. *Kodak Laboratory Chemicals*, 1987.

[103] CA Palmer, EG Loewen, and RGL Thermo. *Diffraction grating handbook*. Newport Corporation, 2005.

[104] Abdul Al-Azzawi. *Physical optics: principles and practices*. CRC Press, Boca Raton, FL, 2006.

[105] F.J. Duarte, P. Kelley, L.W. Hillman, and P.F. Liao. *Dye Laser Principles: With Applications*. Academic Press Inc., San Diego, CA, 2012.

[106] Ophir Optronics Solutions Ltd. BeamStar Beam Profiling System. *http://www.ophiropt.com/*.

[107] Ocean Optics Inc. USB4000 Spectrometer. *http://www.oceanoptics.com/products/usb4000.asp*.

[108] E G & G Judson. FND-100Q Datasheet. *http://www.datasheetarchive.com/dl/Scans-001/Scans-0026786.pdf*.

[109] Goodfellow Cambridge Ltd. Carbon/Epoxy Composite. *http://www.goodfellow.com/pdf/2929_1111010.pdf*.

[110] PRF Composites. Ultra Low Viscosity Epoxy System RS-M135. *http://www.prfcomposites.com/materials/resin/*.

[111] Buehler ITW Test & Measuement GmbH. In der Steele 2, 40599, Düsseldorf, Germany. *http://www.buehler.co.uk/*.

[112] Veeco Instruments Inc. 1 Terminal Drive Plainview, NY 11803. *http://www.veeco.com/*.

[113] J. Abrahamson. Graphite sublimation temperatures, carbon arcs and crystallite erosion. *Carbon*, 12(2):111–118, 1974.

[114] C.D. Doyle. Estimating isothermal life from thermogravimetric data. *Journal of applied polymer science*, 6(24):639–642, 1962.

[115] T. Ozawa. A new method of analyzing thermogravimetric data. *Bulletin of the Chemical Society of Japan*, 707(1952), 1965.

[116] J.H. Flynn and L.A. Wall. A quick, direct method for the determination of activation energy from thermogravimetric data. *Journal of Polymer Science Part B: Polymer Letters*, pages 323–328, 1966.

[117] J.H. Flynn. The isoconversional method for determination of energy of activation at constant heating rates. *Journal of Thermal Analysis and Calorimetry*, 27:95–102, 1983.

[118] National Physical Laboratory. 2.3.6 Specific heat capacities. *http://www.kayelaby.npl.co.uk/general_physics/2_3/2_3_6.html*.

[119] C.H. Lees. On the Thermal Conductivities of Single and Mixed Solids and Liquids and their Variation with Temperature. *Philosophical Transactions of the Royal Society A: Mathematical, Physical and Engineering Sciences*, 191:399–440, 1898.

[120] I. Newton. A Scale of the degrees of heat. *The Philisophical Transactions of the Royal Society of London*, 1701.

[121] Joseph Fourier. *The analytical theory of heat*. Cambridge University Press, Cambridge, 1878.

[122] Hyperphysics (R. Nave). Thermal Conductivity. *http://hyperphysics.phy-astr.gsu.edu/hbase/thermo/thercond.html#c1*.

[123] C. Kittel. *Introduction to solid state physics*. John Wiley & Sons Inc., New York, NY, 8th edition, 2004.

[124] Thermo Fisher Scientific Inc. 81 Wyman Street Waltham, MA, USA, 02451. *http://www.thermofisher.com/*.

[125] PerkinElmer Inc. Saxon Way Bar Hill, Cambridge, Cambridgeshire, CB23 8SL. *http://www.perkinelmer.co.uk/*.

[126] National Physical Laboratory. 2.5.9 Light reflection. *http://www.kayelaby.npl.co.uk/general_physics/2_5/2_5_9.html*.

[127] John E. Hatch. *Aluminum: Properties and Physical Metallurgy*. American Society for Metals, Russell Township, OH, 1984.

[128] E.D. Palik. *Handbook of optical constants of solids II*. Academic Press, San Diego, CA, 1998.

[129] Christian Freitag, Rudolf Weber, and Thomas Graf. Polarization dependence of laser interaction with carbon fibers and CFRP. *Optics Express*, 22(2):1474, 2014.

[130] J. Lekner. Reflection and refraction by uniaxial crystals. *Journal of Physics: Condensed Matter*, 3(32):6121–6133, 1991.

[131] J.V. Larsen and T.G. Smith. Carbon Fiber Structure. *Naval Ordnance Lab, White Oak, MD*, 1971.

[132] S.A. Kovalenko. Descartes-Snell law of refraction with absorption. *Semiconductor Physics, Quantum Electronics & Optoelectronics*, 4(3):214–218, 2001.

[133] Y.Y. Liu, H. Wei, S. Wu, and Z. Guo. Kinetic Study of Epoxy Resin Decomposition in Near-Critical Water. *Chemical Engineering & Technology*, 35(4):713–719, 2012.

[134] Jae Hun Lee, Kwang Seok Kim, and Hyo Kim. Determination of kinetic parameters during the thermal decomposition of epoxy/carbon fiber composite material. *Korean Journal of Chemical Engineering*, 30(4):955–962, 2013.

[135] Y.W. Song, H.S. An, M.J. Shim, and S.W. Kim. Thermal decomposition characteristics of DGEBA/MDA/GN system for insulating materials. *Proceedings of 1998 International Symposium on Electrical Insulating Materials*, 1998.

[136] Jiangbo Wang, Jianghua Fang, Jiarong Wang, and Haoqi Gao. Kinetics Study on Thermal Decomposition of Polyepoxyphenylsilsesquioxane/Epoxy Resin Systems. *Journal of Macromolecular Science, Part B*, 51(8):1525–1536, 2012.

[137] Chin-Lung Chiang, Ri-Cheng Chang, and Yie-Chan Chiu. Thermal stability and degradation kinetics of novel organic/inorganic epoxy hybrid containing nitrogen/silicon/phosphorus by sol-gel method. *Thermochimica Acta*, 453(2):97–104, 2007.

[138] National Physical Laboratory. 2.3.7 Thermal conductivities. *http://www.kayelaby.npl.co.uk/general_physics/2_3/2_3_7.html*.

[139] T. Reed and A. Das. *Handbook of biomass downdraft gasifier engine systems*. Biomass Energy Foundation, 1988.

[140] Domino UK Ltd. Trafalgar Way, Bar Hill, Cambridge, CB23 8TU. *http://www.dominolaser.com/en/index.html*.

[141] Purex International Ltd. Purex House, Farfield Park, Manvers, Rotherham, South Yorkshire, S63 5DB. *http://www.purex.co.uk/*.

[142] DuPont UK Ltd. Wedgwood Way, Stevenage, Hertfordshire, SG1 4QN. *http://www.dupont.com/*.

[143] A. Penalver, E. Pocurull, F. Borrull, and R.M. Marce. Trends in solid-phase microextraction for determining organic pollutants in environmental samples. *Trends in Analytical Chemistry*, 18(8):557–568, 1999.

[144] Benoît Thiébaut, Agnès Lattuati-Derieux, Moïra Hocevar, and Léon-Bavi Vilmont. Application of headspace SPME-GC-MS in characterisation of odorous volatile organic compounds emitted from magnetic tape coatings based on poly(urethane-ester) after natural and artificial ageing. *Polymer Testing*, 26(2):243–256, 2007.

[145] National Institute of Standards & Technology. Methane. *http://webbook.nist.gov/cgi/cbook.cgi?ID=C74828&Mask=1*.

[146] C.J. Pouchert. *The Aldrich library of FT-IR spectra*. Aldrich Chemical Company, Milwaukee, Wis., 1997.

[147] T. Shimanouchi. *Tables of Molecular Vibrational Frequencies Consolidated. Volume I*. National Bureau of Standards, Washington, D.C., 1972.

[148] D.L. Hansen. *Sprouse Collection of Infrared Spectra: Book 4: Common Solvents: Condensed Phase, Vapor Phase and Mass Spectra*. Sprouse Scientific Systems Inc, Paoli, PA., 1990.

[149] National Institute of Standards & Technology. Carbon Dioxide. *http://webbook.nist.gov/cgi/cbook.cgi?ID=C124389&Units=SI*.

[150] National Institute of Standards & Technology. Carbon Monoxide. *http://webbook.nist.gov/cgi/cbook.cgi?Name=co&Units=SI*.

[151] National Institute of Standards & Technology. Formadehyde. *http://webbook.nist.gov/cgi/cbook.cgi?Name=formaldehyde&Units=SI*.

[152] ScienceLab. Phenol MSDS. *http://www.sciencelab.com/msds.php?msdsId=9926463*, 2013.

[153] ScienceLab. Formaldehyde MSDS. *http://www.sciencelab.com/msds.php?msdsId=9924095*, 2013.

[154] Air Products Inc and Chemicals. Methane MSDS. *http://avogadro.chem.iastate.edu/MSDS/methane.pdf*, 1999.

[155] Praxair Technology Inc. Carbon Monoxide MSDS. *http://www.praxair.com/~/media/North%20America/US/Documents/SDS/ Carbon%20Monoxide%20CO%20Safety%20Data%20Sheet%20SDS%20P4576.pdf*, 2009.

[156] Air Products Inc and Chemicals. Carbon Dioxide MSDS. *http://avogadro.chem.iastate.edu/MSDS/carbon_dioxide.pdf*, 1993.

[157] Canon. Canon UK Ltd, Woodhatch, Reigate, Surrey, RH2 8BF. *http://www.canon.co.uk/*.

[158] Technical aspects of the Canon EF lens Mount. http://www.eflens.com/lens_articles/ef_lens_mount.html.

[159] W.J. Smith. Modern optical engineering. 1966.

[160] Thorlabs Ltd. 1 Saint Thomas Place, Ely, CB7 4EX. *http://www.thorlabs.co.uk/*.

[161] C. Woodhouse and R. Lambrecht. *Way Beyond Monochrome 2e: Advanced Techniques for Traditional Black & White Photography Including Digital Negatives and Hybrid Printing*. Focal Press, Waltham, MA, 2nd edition, 2010.

[162] H.H. Nasse. Depth of Field and Bokeh. *Carl Zeiss - Camera Lens Division*, 2010.

[163] C.P. Huynh and A. Robles-Kelly. Comparative colorimetric simulation and evaluation of digital cameras using spectroscopy data. *Digital Image Computing Techniques and Applications, 9th Biennial Conference of the Australian Pattern Recognition Society*, pages 309–316, 2007.

[164] K.P. Birch and M.J. Downs. Correction to the updated Edlén equation for the refractive index of air. *Metrologia*, 31(4):315, 1994.

[165] Arthur W. Anderson. *A Textbook of Physical Chemistry*. Academic Press, New York & London, 1973.

[166] ROFIN-SINAR UK Ltd. York Way, Willerby, Kingston upon Hull, HU10 6HD. *http://www.rofin.com/*.

[167] TRUMPF Ltd. President Way, Airport Executive Park,Luton, Bedfordshire, LU2 9NL. *http://www.uk.trumpf.com/en.html*.

[168] Drägerwerk AG & Co. Dräger sampling tubes and systems. *http://www.draeger.com/sites/en_uk/Pages/Chemical-Industry/Draeger-Sampling-Tubes-and-Systems.aspx*.